A discrete element model of orogenesis

Mark Naylor

Doctor of Philosophy
School of GeoSciences
University of Edinburgh
2004

Abstract

A computational Discrete Element Model (DEM) is developed to investigate the kinematic evolution of erosive and non-erosive doubly vergent wedges, focussing on the implications for the interpretation of field data.

Orogenic belts have long been the subject of significant scientific investigation, containing an integrated record of deep crustal tectonic and surface processes. Typically, orogenic systems are active for tens of millions of years. However, only a small subset of the data is available in the modern day snapshot, with observations often limited to incomplete records at the topographic surface and a sparse distribution of wells and seismic sections.

Many current field studies focus on attempting to identify a positive correlation between tectonic and surface processes. Techniques and observations include thermochronometry, geobarometry, geomorphology, structural reconstruction and syn-tectonic stratigraphy. In order to further constrain the evolution, analogue and computational modelling is required.

Modelling studies include analogue sandbox models and computational Finite Element Models (FEMs). Analogue models generate many emergent structural features, but cover a small range of parameter space and have poor reproducibility. FEMs provide poor structural resolution due to underlying continuum assumptions in their formulation, but are effective at investigating a wider range of parameter space, boundary conditions and erosive feedbacks. The DEM provides the opportunity to build on the best parts of both techniques, providing structural resolution on the sub-orogen scale. This thesis investigates the possibility that some of the discrepancies in the results may be resolved by basing the interpretation of this data on a DEM computational model that allows the emergence of displacements across discrete structures.

In order to achieve this, the thesis develops the DEM, highlighting the importance of formulating appropriate boundary conditions and emergent material properties. The role of particle shape, packing structure and inter-particle force parametrisation is investigated using angle of repose and singly vergent wedge experiments. Particles consisting of clusters of three random sized discs produce results most comparable with sandbox analogues and real accretionary prisms. This work demonstrates how the incorporation of thrust sheets of constant length (l) into the wedge at some constant convergence rate (v) introduces a second order time-scale related to the time required to completely incorporate successive thrust sheets where $t = l/v$. This thesis provides evidence that the discrepancies in field investigations searching for the erosive-tectonic signal may be masked by these emergent second order tectonic fluctuations.

Acknowledgements

I would like to thank Hugh and Patience for being fun supervisors, Geoff Batt and Nick Hulton for a constructive viva, my parents for being supportive throughout my time in Edinurgh and Lindsay for her patience and abstract comments.

Declaration

I declare that this thesis was composed by myself, that the work contained herein is my own except where explicitly stated otherwise in the text, and that this work has not been submitted for any other degree or professional qualification except as specified.

(*Mark Naylor*)

Table of Contents

List of Figures

List of Tables

Chapter 1

Introduction

A computational Discrete Element Model (DEM) is developed to investigate the kinematic evolution of erosive and non-erosive doubly vergent wedges, focussing on the implications for the interpretation of field data. This introductory chapter provides background information about the nature of the geological evidence available in orogenic systems, defines the system to be investigated and reviews previous analogue and computational models. The structure of the thesis is presented, highlighting the scientific focus of each chapter. Results from DEM modelling will be presented as figures in the thesis and as a set of interactive animations, stored on the CD at the back of the thesis. These can be accessed by loading Index.html in any web browser.

1.1 Introduction

The long-term ($10^6 - 10^7$ yrs) mechanical growth of mountain belts was first investigated through detailed mapping and dating of rocks in mountain belts such as the European Alps and North American Rockies. The recognition of crustal thickening was identified when the first thrust faults were documented (Heim, 1897), subsequently the study of negative gravity anomalies formed by the isostatic compensation of the thickened crust built upon this understanding (Karner and Watts, 1983). Once these observations had been integrated into a mechanical interpretation for the macro-scale form of mountain belts as a thrust wedge (Chapple, 1978), the foundations for numerical and analogue modelling of mountain systems were available. However, the expansive understanding of mountain belts as we see them today provides us with only a snapshot in time, and even then it can be difficult to resolve internal structures.

There is a wide range of different types of data available to provide geological evidence regarding the evolution of orogenic systems; these data can broadly be split into two categories. Firstly, there is data that relates to the modern day state of the system and data that forms an integrated record of the evolution of the orogen. Modern-day conditions are frequently

extrapolated back and used to constrain modelling attempts with poor justification (e.g. use of modern day precipitation rates or the use of modern day topography to estimate the perturbation of isotherms 20 Myr ago). Secondly, there is information that records the integrated history of a mountain belt which can be used to reconstruct the mechanical evolution of the system. One of the main difficulties in performing this type of reconstruction is finding good temporal constraints. Examples of both types of data can be found in Table 1.1.

Modern-day evidence	Integrated evidence
Topography	Sediment stratigraphy
GPS	Off-shore sedimentary record
Tectonic activity	Thermochronometry
Seismicity	Geobarometry
Reflection seismic lines	Paleomagnetic history
Erosion rate measurement	Glacial features
Precipitation distribution	Pollen record

Table 1.1: Examples of some of the modern day and time integrated evidence that is available in mountain systems

In order to further investigate the evolution of orogens, forward modelling is required to make predictions and to define possible endpoint scenarios that can be tested against real data to better improve assumptions used in modelling. Models that assume some initial set of conditions and boundary conditions and that are run to find best-fit endpoint scenarios, are termed *forward models*. They are run to generate output comparable with geological observations, thus allowing us to better constrain the initial conditions required to fit the observations. This involves iteratively re-running the model to invert the problem. There will always be geological complexity and it must be accepted that solutions will be non-unique. Currently, orogens are modelled through both sand analogues (Malavieille, 1984; Persson, 2001; Storti et al., 2000) and numerical finite element techniques (Willett et al., 1993; Beaumont et al., 1996). These techniques identify similar evolutionary schemes, but differ in the type of detail they resolve, the boundary conditions and the model parametrisation. Sandbox models generate individual structures but are limited by the range of parameter space available and the experimental repeatability. Finite element models have an appropriate gross parametrisation but their Coulomb continuum assumption excludes discrete thrusting and shear surface formation.

1.2 Aims and approach

This thesis develops an alternative modelling method based upon the Discrete Element Model (DEM) that combines appropriate parametrisation for the macro-scale form with the ability to accommodate shortening through discrete thrusting and shearing. I build upon the work started by Burbidge (2000), who applied DEMs to singly-vergent critical wedges. Understanding the feedbacks and processes involved in orogenesis presents a difficult challenge where the combined data can often be interpreted in different ways. This project develops a forward model that is used to make testable hypotheses and improves the interpretation of real systems. It is not our intention to try to reproduce interpreted cross sections, but rather focus upon the mechanisms involved in the evolution of the system.

The aims of this thesis are:

1. To investigate a suitable set of DEM boundary conditions for doubly-vergent wedge and orogenic modelling
2. To attempt a quantification of the natural variability of accretion and internal thickening in the maintainance of a critically tapered doubly-vergent orogen
3. To investigate the structural response of a discrete element model orogen to localised erosion defined by a threshold elevation
4. Relate the findings of this study to the interpretation of real orogens.

The main areas where this thesis makes advances are in discrete element modelling of crustal materials, understanding the mechanics of wedges using a discrete element model approach and providing new insights into orogenesis.

1.3 What defines a continent-continent collisional orogen?

Mountain belts are distributed across the globe, those that are still active (e.g. Himalaya, Taiwan, Andes, S.Alps) lying along convergent plate boundaries (Molnar, 1988). They fall into two types depending upon the composition of the over-riding and subducting plates (Dewey and Bird, 1970). Subduction of dense oceanic lithosphere beneath continental lithosphere produces Cordilleran orogens where a linear mountain belt lies on the overthrusting plate, parallel to the subduction zone. This project considers the second type, collisional mountain ranges, which are initiated by a change in the composition of the lithospheric material being brought to the trench, making it too buoyant to descend beneath the over-riding plate. The resulting continental collision closes the ocean and thickens a mountain belt. Continental collision marks the beginning of the cessation of convergence along a plate boundary and the initiation of new plate boundaries. This process has been documented in the Indian Ocean, in response to the

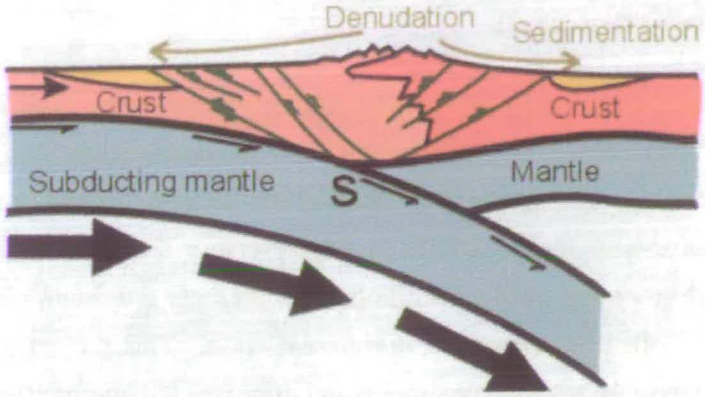

Figure 1.1: Subduction zone geometry

collision of India and Eurasia (Van Orman et al., 1995). Classical plate tectonics would see this as a geologically abrupt transition, when significant underthrusting of continental lithosphere is prevented by its buoyancy (McKenzie and Morgan, 1969). However this is an oversimplification not evident in observation, as exemplified by the Himalaya. This mountain chain is still undergoing rapid uplift across a broad zone (Molnar and Chen, 1982), and it may well be the case that slab pull continues to operate in some modified form to assist the northerly movement of India (Molnar, 1984). Mountain belts are preserved after the end of convergence (e.g. Appalachians , Urals, Alps and Pyrenees), until they are eroded away or become incorporated in new settings.

In purely kinematic terms, the growth of an active collisional orogen requires a velocity discontinuity at a plate boundary (Figure 1.1) where a significant amount of material is not subducted. Driven by convergence, this material is either accreted or underplated (Figure 1.2) into the orogen, accretionary complex or doubly vergent wedge and as more material is incorporated the wedge grows. If the wedge geometry was governed purely by bulk properties, it would be symmetric. Mountains and accretionary prisms are not symmetric; the direction of subduction introduces an asymmetry into the kinematics which accounts for the asymmetry in non-eroding models (Willett et al., 1993). Orogenesis and wedge formation is the accommodation of material that is not subducted.

1.4 Review of trends in orogenesis

In order to set the scene, a brief review of current trends in the field of orogenesis is presented. The thesis aims to test and explore ideas associated with the following topics:

- Approximation of orogens to Critical Wedge systems
- Climatic forcing driving tectonics - feedback between surface processes and tectonic

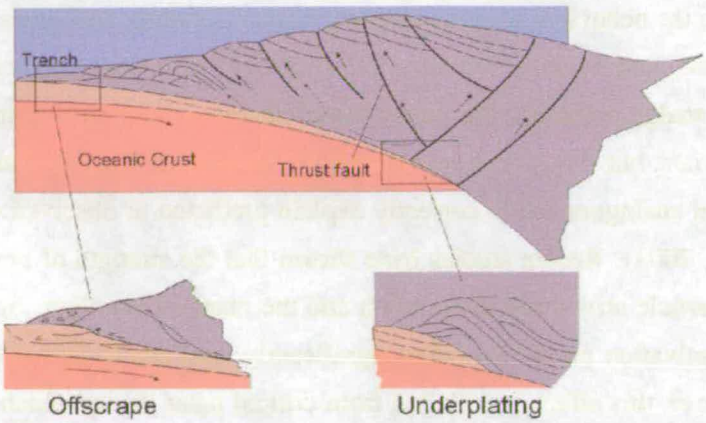

Figure 1.2: Processes of mass influx into an accretionary complex

boundary conditions

- Continuum forward modelling of particle trajectories to predict thermochronometric age distribution
- Treatment of orogens as steady state systems

1.4.1 Approximation of orogens to critical wedge systems

Critical wedge theory describes the force balance within a wedge that is being grown in a manner analogous to a bulldozer ploughing into a pile of sand. Solutions have been derived for both cohesive (Davis et al., 1983) and non-cohesive Coulomb materials (Dahlen et al., 1984), which predict self similar growth with some constant taper angle (surface slope + basal dip) which is purely a function of internal friction (μ_e), basal friction (μ_b) and cohesion (C) parameters. Thus for a convergent wedge, three dynamic states are predicted. In a critical state the wedge is at its stable taper angle, but the accretion of further material into the wedge pushes it out of its critical state. In a super-critical state, the wedge is greater than the stable taper angle. The wedge locks up and slides stably on the base, accreting material at the toe of the wedge to shallow the mean angle. In a sub-critical state, the wedge is below critical taper and must deform internally to increase taper to the stable state.

Many researchers use the critical wedge system to approximate boundary conditions that generate accretionary prisms and fold and thrust belts, where the bulldozer is some backstop and the driving force is provided by the subducting plate. The assumption that the material is at Coulomb failure is justified by the observation that fractures, micro-cracks and mechanical heterogeneities penetrate rocks at all orientations. Critical wedge theory has been applied qualitatively to real fold and thrust belts, accretionary wedges and non-accretionary wedges to explain their mechanics and evolution (Davis et al., 1983; Lallemand et al., 1994).

To investigate the behaviour of these systems further, sandbox analogues (Lohrmann et al., 2003) and finite element models (Willett, 1992; Fullsack, 1995) have been developed to simulate the critical wedge problem. The stress-strain curves of rocks are comparable with those of granular materials, but it has been recognised in mechanical analysis and experimental description that sand analogues fail to correctly explain predicted or observed wedge geometries (Lohrmann et al., 2003). Recent studies have shown that the strength of granular materials is sensitive to the particle size-shape distribution and the material handling. Sand analogue fault initiation and reactivation properties differ significantly, and this is also observed in rock experiments. However, this effect is excluded from critical taper theory which only uses one set of coefficients. It has long been known that undeformed materials have higher strengths than deformed materials (Brace and Byerlee, 1966; Byerlee, 1978; Paterson, 1978). The strength of rocks in geological settings is also dependent on strain rate, temperature, effective stresses and the roughness of the sliding surface (e.g. Rutter, 1972; Jaeger et al., 1996). Identifying important material characteristics within natural systems must motivate the choice of analogue (Lohrmann et al., 2003) and computational materials.

Generalising critical wedge theory to a double-sided wedge, accretionary prism or orogen requires the introduction of the velocity discontinuity at some point along the base of the slab rather than at a boundary so that the backstop is an emergent internal feature of the system and evolves as the wedge grows.

1.4.2 Climatic forcing driving tectonics

Having generated a conceptual model of how a wedge oscillates around some critical taper, it is easy to see how a process that redistributes mass within that system, e.g. erosion, can push it out of equilibrium. Removal of mass from the high parts of the wedge and depositing it at the toe will shallow the angle of the wedge. This feedback promotes internal deformation to mechanically regain the taper angle.

The scale on which localised erosion becomes important is controversial, as exemplified in the review by Molnar (2003) review of four contradictory papers (Burbank et al., 2003; Dadson et al., 2003; Reiners et al., 2003; Wobus et al., 2003). They each present very different assessments of the extent and nature of climatic influence on collisional orogens. Many studies (e.g. Montgomery et al., 2001) extrapolate modern day climatic conditions and configurations to some paleo-climate, which involves these problematic assumptions.

1.4.3 Continuum forward modelling of particle trajectories to predict thermochronometric ages

The introduction of continuum modelling motivated new descriptions of orogenic systems (Willett et al., 1993; Beaumont et al., 1996). The output from these models shows steady

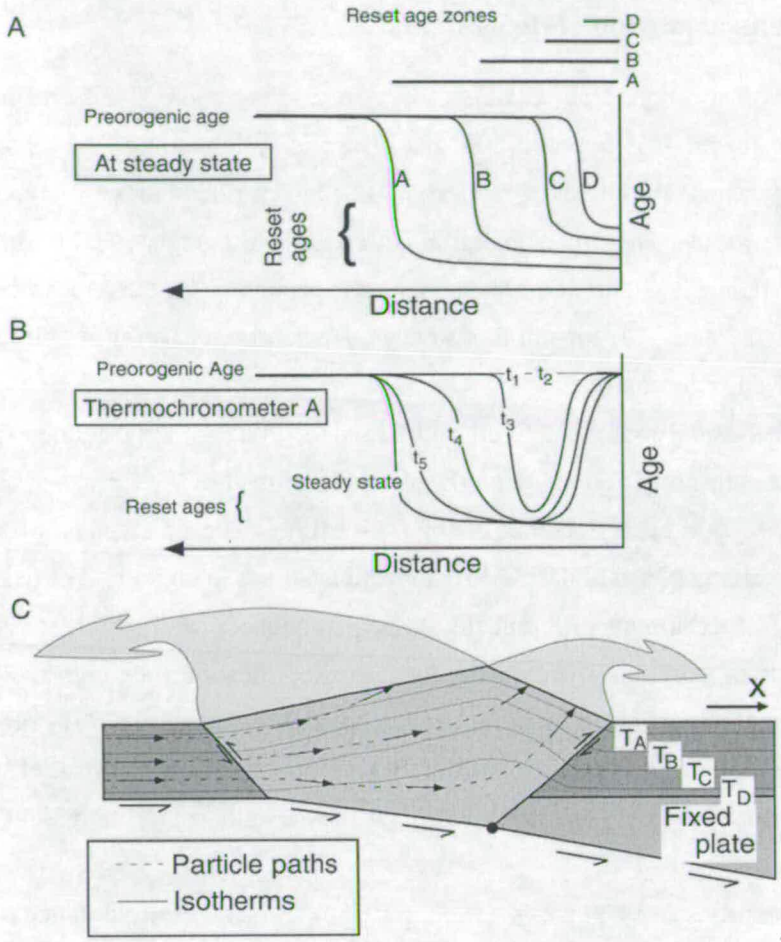

Figure 1.3: Evolution to exhumational steady state for thermochronometers. A: Surface pattern of ages from multiple thermochronometers at exhumational steady state. B: Time evolution of surface ages from thermochronometer A with closure temperature T_A assuming constant pre orogenic age. C: Particle paths and closure isotherms. (From Willett and Brandon (2002))

trajectory paths for parcels of rock which, when coupled with a thermal model, can predict a thermochronometric age distribution (Figure 1.3 A and B) (e.g. the Olympics in Willett and Brandon, 2002). If the age distribution reaches a steady state, this is referred to as an exhumational steady state, described below. These trajectories assume that discrete motions along individual thrusts average over time to some continuum deformation, producing smooth trajectory paths (Figure 1.3C). It is difficult to justify this assumption when we see structures with large discrete offsets across which different thermochronometric ages are measured (such as the MCT in the Nepali Himalaya, Burbank et al., 2003).

1.4.4 Orogens as steady state systems

The assumption that orogens can attain steady state allows a more significant interpretation of field data to be made. It is hypothesised that orogenic systems may be able to attain various dynamic steady states (Willett and Brandon, 2002), as described below:

Flux steady state - The flux of material added to the orogen is equal to the erosional flux out. The flux balance is slightly complicated when accounting for the deposition of the eroded material in the foreland. A wedge in flux steady state has a time averaged constant volume and thus constant wedge geometry.

Topographic steady state - Willett and Brandon (2002) strictly defined the topographic steady state to be the condition at which the elevation of the Earth's surface at all spatial points within a domain of interest does not change with time. The practicality of a real orogenic topography remaining constant despite erosion and tectonics in unlikely. For example, consider the complexity of exhuming different lithological sequences with different erodabilities. To achieve this true topographic steady state, local erosion must balance both the rock uplift rate and the horizontal advection of topography. Burbank and Anderson (2001) suggested that the most realisable definition is one where the system maintains constant relief, constant mean elevation and constant local base level, although the elevation of an individual point can vary through time.

Thermal steady state - There is a time invariant temperature field. The temperature field is dependent upon erosion and the velocity field, therefore for a thermal steady state to be achieved we must first attain a velocity field steady state. The existence or non-existence of a thermal steady state has large implications for surface distributions of thermochronometric ages.

Exhumational steady state - This refers to an invariant spatial distribution of thermochronometric ages across a surface. It is an important concept in predicting thermochronometric ages from forward models. It makes the assumption that over geological time-scales, the flux of material through an orogen averages to some time invariant continuum distribution. For this to hold, any episodicity in uplift must occur on a time-scale lower than the resolution of the thermochronometry.

Without being able to directly observe the time evolution of the system, it will always be difficult to justify the use of steady state assumtions in interpreting orogenic data.

1.5 Previous modelling approaches

This section provides a review of the application of critical wedge theory to orogenic systems and of current analogue and computational orogenic modelling techniques, highlighting where these models have been successful as well as important limitations.

1.5.1 Critical wedges

Huiqi et al. (1992) used sandbox models to simulate the evolution of foreland fold and thrust belts. The models generated imbricate thrust sheets at the front of the wedge that became back-rotated in the more internal parts of the wedge. The tapers produced in the models were consistently higher than those predicted from theory. This is not surprising as sand is a granular material and as such extra phenomena, such as dilation and arching, play important roles that are not a component of critical taper theory. However, despite this the wedges produced do try to sustain a constant taper angle.

Willett (1992) successfully compared critical wedge theory using a finite element model (FEM) with the analytic solution of Dahlen (1984) and was able to investigate the response of the wedge to a change in basal friction. The critical wedge was modelled by advancing a rigid, vertical, smooth backstop into the deformable plastic Coulomb material. To approximate the infinite wedge, the taper angle is measured away from the backstop. These models clearly demonstrated that deformation oscillates between internal thickening and frontal accretion to maintain the wedge taper and that weaker bases propagate information further away from the backstop generating shallower angles as compared with high basal frictions which localise uplift at the backstop.

The continuum deformation implied by Coulomb failure at every point in a critical wedge formulation does not permit the development of structures with large, discrete offsets and strain partitioning as is observed in many thrust wedges. A system at Coulomb failure everywhere has no memory of recent sliding, only of the mass distribution and boundary conditions. In contrast, a system which is only at Coulomb failure on discrete planes remembers recent deformation and has the option to re-exploit this weakened zone.

There are two main problems involved in using a critical wedge as an analogue for orogenic evolution. Firstly, the kinematic boundary conditions originally applied in critical wedge FEM's require a smooth backstop, which equates to a system with both plates moving at the same velocity towards a singularity (Figure 1.4) (Willett, 1992). Secondly, the critical wedge backstop is of infinite height, so there can be no transfer of material between the pro- and retro-sides. In reality, material derived from the pro-side is observed in the retro-wedge of many mountain belts. For example, the North Pyrenean Fault in the Pyrenees represents the suture zone between the colliding European and Iberian plates, but is now located approximately half-way down the retro-wedge (northern) side of the mountain belt (Munoz, 1992). Similar examples of the horizontal flux of material through the central divide of the mountain belts from the pro- to the retro-sides have been demonstrated from the Southern Alps New Zealand and Cascades, Washington State (Willett, 1999). Subsequent FEM's have utilised a doubly vergent geometry, and define the singularity as stationary with respect to the over-riding plate, a more realistic boundary condition.

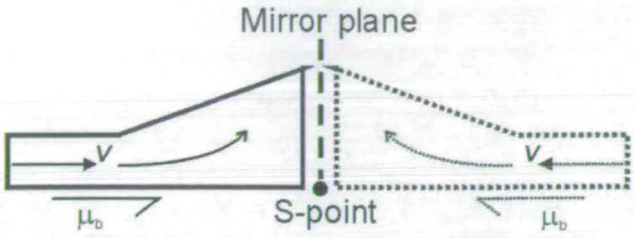

Figure 1.4: A kinematic comparison between critical wedge and doubly vergent wedge boundary conditions in a frame of reference with a stationary subduction point, the S-point. The only way to satisfy the zero friction on the vertical backstop boundary condition in generalising the singly vergent wedge to a doubly vergent context is for the system to be symmetric about the backstop, indicated by the dashed line mirror plane. v is the convergence rate at which material is introduced into the system from infinity, μ_b is the basal friction.

The strength of critical wedge theory concerns the dynamics and modes of accommodation of stress in the system. All things being equal, the slope will try to maintain a constant taper angle. If the wedge becomes too steep, it will slide stably on the base and be accreted at the toe, to make the slope shallower. If too shallow, material may be thrust under the wedge and become incorporated at the rear by underplating, causing a steepening of the wedge. If no material is added, the wedge can also thicken internally, through processes analogous to the back rotation of stacked imbricates, out-of-sequence thrusting and back thrusting (Platt, 1986). The basal and internal coefficients of friction regulate the duration the system spends in each of these possible phases.

1.5.2 Doubly vergent wedges

Here we outline the modelling approaches of several researchers who have used a variety of sandbox and finite element approaches. They all improve upon the critical wedge simulations for modelling real accretionary settings, as the boundary conditions are more geologically motivated.

Doubly-vergent wedges appear to follow an evolutionary scheme during their growth, involving three stages (Willett et al., 1993; Storti et al., 2000). These are characterised by the introduction of new deformation mechanisms that accommodate shortening. *Stage 1* is characterised by symmetric steep sided topography about a central ridge. Deformation is dominated by motion along a retro-vergent thrust and associated block uplift. There is no sliding along the base and material is fluxed to the S-point (Figure 1.5(a)). In *Stage 2* the wedge has now reached a threshold size where pro-wedge accretion occurs at the pro-wedge angle, and hence surface slope, is now dependent on the pro-side basal coefficient of friction; the wedge can now propagate stably on the pro-side (Figure 1.5(b)). At *Stage 3*, a further threshold is reached and

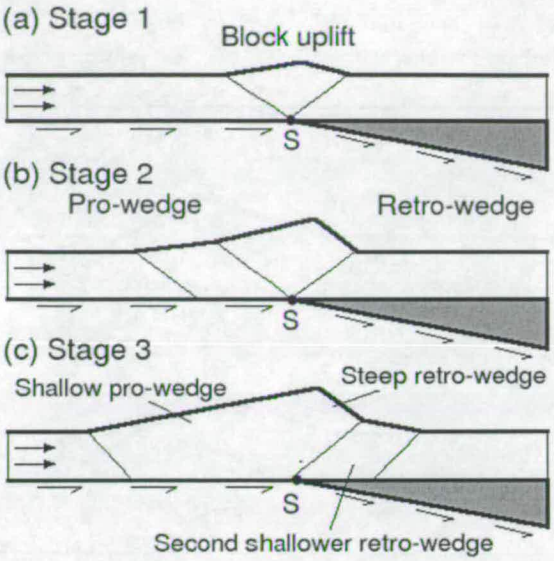

Figure 1.5: Illustration of the three characteristic stages in the evolution of a doubly vergent wedge. Modified from Willett et al. (1993).

a component of shortening is accommodated by stable sliding of the whole wedge on the pro and retro-sides and material is accreted at the toe of the steep retro-wedge, forming a second, shallower wedge on the retro-side (Figure 1.5(c)). All of the analogue, FEM and DEM models presented follow this scheme, but not all reach *Stage 3*.

1.5.2.1 Sandbox models

Dry sand is an excellent analogue for brittle deformation of the upper crust in the Earth's field of gravity. It has been shown that sand exhibits Navier-Coulomb behaviour similar to many sedimentary rocks (McClay, 1990). The angle of internal friction is just over 30^o and the apparent cohesive strength is approximately 1.05 kPa. Importantly, a layer of sand several centimetres thick can deform easily under its own weight, satisfying the scaling laws for body forces and surface forces. Faults that form within the models are not discrete fractures, but granular shear zones of finite width proportional to their grain size, forming by progressive dilation. They can now be imaged in scanners without the model being destroyed to obtain a 3D time evolution.

The properties of sand are complicated. Krantz (1991) noted that the density of a portion of sand is more dependent upon its physical handling than composition, and that the internal friction coefficient varies significantly depending upon the tightness of the packing. This makes it difficult to directly compare the work of different groups unless precise details of experimental set-up are given. Reactivated faults showed lower coefficients of friction in sand. Dilation in

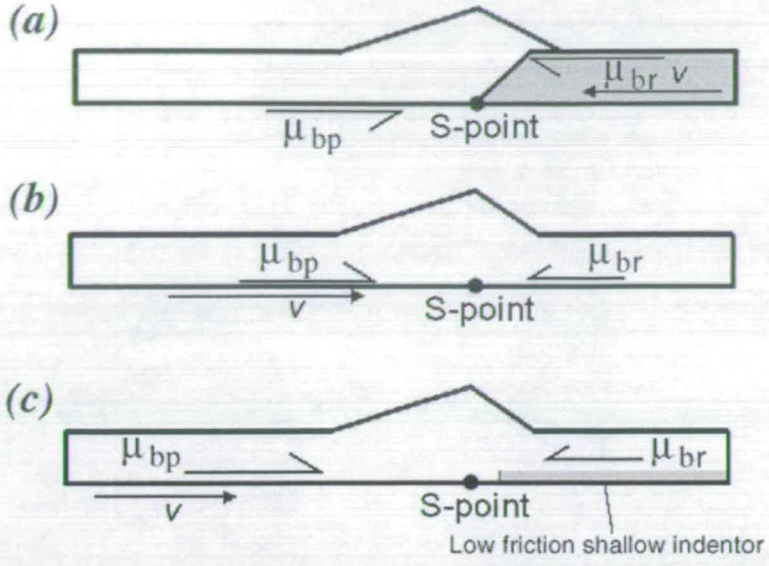

Figure 1.6: Boundary conditions for various doubly vergent sandbox experiments, v indicates the direction of convergence. μ_{bp}, μ_{br} and their corresponding half arrows indicate the presence pro- and retro-side basal friction. (a) Rigid indenters of various tapers intruding into deformable sand layer - Persson (2001), the frame of reference in this experiment has the subducting plate stationary with the retro-side indenter and S-point migrating into it. (b) Homogeneous medium with a weaker retro-side base, kinematic discontinuity is produced by drawing a sheet under the pro-side and drawing it out at the S-point - Malavieille (1984), Storti et al. (2000), in this frame of reference the S-point and over riding plate are stationary. (c) Homogeneous medium with a weaker retro-side shallow indenter - Wang and Davis (1996), in this frame of reference the S-point and over riding plate are stationary.

fault zones can be up to 13% (McClay, 1990), significantly larger than fault zones found in nature. Koyi (1995) showed that individual imbricate sheets exhibit an area loss of 12-13% during shortening by sandbox experiments. The elastic strain range of sand is significantly smaller than found in brittle rocks, which makes it unsuitable for investigating seismic events.

Persson (2001) used an analogue sandbox model to investigate how indenter geometry affects the rise of an orogenic wedge from an indented continent, and observes *Stage 1* and 2 deformation (Figure 1.6(a)). In her experiments a retro-vergent thrust, which rises steeply from the S-point and shallows towards the surface, is strongly localised near the S-point. When the angle of the indenter is approximately the same as the angle of the retro-vergent thrust, the thrust utilises the ramp. If the angle of the indenter is too shallow, a retro-vergent thrust is initiated at the base of the indenter with a steeper angle. This thrust partitions a region adjacent to the indenter which is not deformed further. A steep indenter requires the S-point to step

back from the toe of the indenter so that the thrust initiated is shallow and coincident with the top of the indenter. What is clear from these experiments is the persistence of a self-organising retro-vergent thrust.

Similar results were obtained in a homogeneous material with no indenter by Malavieille (1984) and Storti et al. (2000). A basal velocity discontinuity (Figure 1.6(b)) is sufficient to produce a similar retro-vergent structure. This suggests that the retro-vergent structure is a result of a common kinematic effect, as the presence of a stronger backstop is not a necessity for the formation of the structure. Both experiments effectively partition deformation across this structure so that no deformation occurs in the retro-wedge and thus *Stage 3* is never reached.

Wang and Davis (1996) introduce a weak surface above a shallow backstop in the retro-wedge to simulate the growth of thin-skinned contractional wedges over a strong backstop (Figure 1.6(c)). Experiments were performed for different basal coefficients of friction on the backstop's upper surface (μ_{br}). Weak surfaces on the backstop allowed deformation to propagate to the retro-side, ie. *Stage 3* growth. This suggests that the friction between the sand and the retro-base in the other experiments was too strong to allow progression to *Stage 3*. However, in the above case the indenter introduced is of a finite height and potentially introduces a further geometric complication that hinders a direct comparison with the other sand-box models (Malavieille, 1984; Storti et al., 2000).

1.5.2.2 Finite element models

The FEM's have been applied to critical wedge and doubly vergent systems. They have provided insight into the dynamics and controls upon such systems and allowed a full investigation of parameter space. They have also made it possible to investigate more complex feedbacks and couplings due to processes such as erosion (Willett, 1999), isostasy and temperature dependent rheology which were not previously accessible. They resolve the gross form and first order structures, such as the dominant retro-vergent thrust in the sandbox models. However, due to the assumption that the material deforms as a continuum, they find it difficult to resolve finer structures and must be forced to allow discrete thrust sheets to evolve (e.g. Beaumont et al., 2000b).

Willett et al. (1993) outlined a boundary arrangement for investigating doubly vergent wedges at active margins or during continent-continent collision. Beaumont et al. (1996) further developed this idea to vary the proportions of incoming material incorporated into the wedge versus that subducted. Willett (1999) presented an erosion coupled finite element model (Figure 1.7).

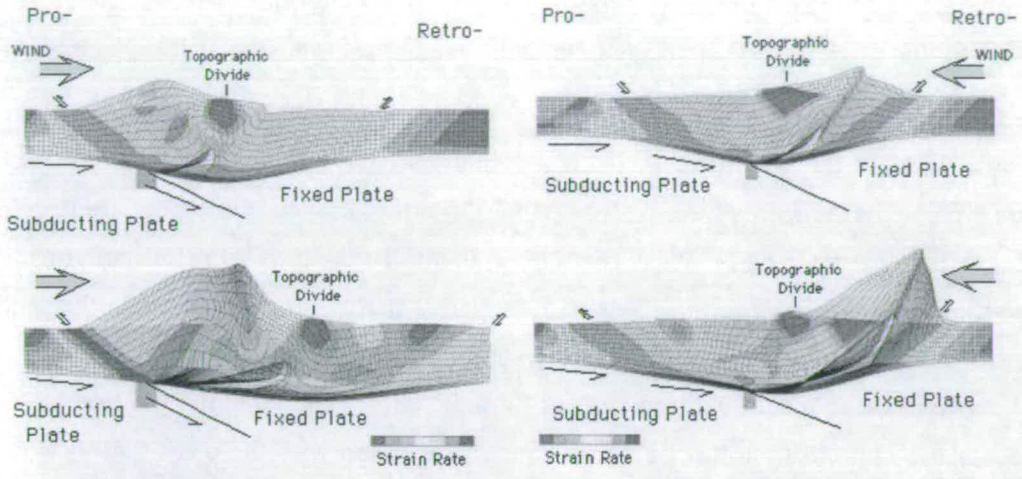

Figure 1.7: Coupled finite element model for deformation and erosion of an orogenic mountain range. In the left hand figures, precipitation and erosion are focussed on the orogenic wedge above the subducting plate (the pro-wedge). Orographic effect is the end member case of completely effective so that there is no precipitation on the leeward side of the mountains. Note progressive focussing of deformation into pro-wedge to the left and highest exhumation in the orogen interior. In the right hand figures, precipitation and erosion are focussed on the orogenic wedge above the overriding plate (the retro-wedge). Orographic effect is the end member case of completely effective so that there is no precipitation on the leeward side of the mountains. In contrast to model above, deformation remains focussed on each edge of orogen. Highest exhumation occurs at low elevation at the retro-wedge deformation front. Top to bottom shows model results with increasing time. (Taken from Willett, 1999).

1.6 Thesis structure

This chapter has presented a review of the current position of doubly-vergent wedge theory, analogue techniques and computational modelling that will be built upon in the rest of the thesis.

Chapter 2: A detailed description of the DEM developed for this study, based on the work of Cundall and Strack (1979), is provided.

Chapter 3: An appropriate DEM material to be used in the doubly-vergent wedge simulations must be justified. The material properties of a regular hexagonal packing, random single disc packing and random clustered disc packing will be investigated for a range of parameter space using angle of repose and singly vergent critical wedge experiments. This work builds upon the work of Burbidge and Braun (2002) which attempted to simulate the evolution of singly vergent wedges using a regular hexagonal packing.

Chapter 4: The singly-vergent boundary conditions will then be generalised to simulate doubly-vergent wedges. Two different boundary condition arrangements will be investigated motivated by (Willett et al., 1993). The results of these experiments compare with the range of results observed in the sandbox work of various authors.

Chapter 5: The Natural Variability of these systems will then be investigated to define the natural cycles of a non-erosive system. Departures from this background signal can then be identified as significant departures. Comparisons are drawn with the Pyrenees to support the mechanisms explored.

Chapter 6: Non-erosive systems do not expose deep material, so a simple erosional algorithm will be applied to test the steady state and continuum assumptions used in interpreting data from orogenic systems. The Pyrenees and a recent review by Molnar (2003) are re-assessed using insight gained from the modelling.

Chapter 7: This discussion chapter reviews the work of the thesis, highlighting the implications of the work with ideas for further studies.

Chapter 2

Discrete Element Model fundamentals

2.1 What is a DEM?

Many types of model rely on continuum assumptions in their solution, which impose constraints on the types of problem that can be easily investigated. Previous Finite Element Models have difficulty in resolving discrete displacement across individual structures as observed in real mountain belts and wedges. The solution presented by Willett and Brandon (2002), showing smooth and continuous trajectory paths for parcels of rock moving through the wedge, is a product of the underlying continuum assumption. The limitations of this assumption are investigated in Chapter 6.

A different type of model has been developed as part of this study that does not rely on such assumptions. I wrote the DEM code in Fortran and ran it on a dual processor AuthenticAMD 1.8Ghz using the NAGWare Fortran 95 compiler. The aim was for simulation to run for no longer than a week using a single processor. The Discrete Element Model (DEM) consists of a large array of individual elements (particles) that interact through micro-scale interactions. Information on position, velocity and force is recorded on the particle scale so that the equations of motion can be solved for each particle to update their velocities and positions. The DEM was first proposed by Cundall and Strack (1979) as an application to granular assemblies. Due to the level of computational power at the time, they could only realistically use ~ 10 discs in 2D simulations. Desk top computers can now realistically run simulations with $\sim 10^5$ to 10^6 particles in 2D. The technique is coming of age and is becoming a realistic alternative for some problems.

The maximum resolution of the system is on the same length scale as the size of the elements involved. Particles can be designed to represent individual grains of sand or some bulk mass of rock. Particles can be any shape, this study mainly uses discs and clusters of discs to simplify the problem. Graphical output can be coloured to highlight individual particle properties or averaged bulk properties. Generally, the individual particle mass does not change with

time and mass is conserved within the system.

The key flow within the model is summarised in Figure 2.1. Particle positions and velocities are used to evaluate local contact forces. In the simulations presented here, particle interactions are short range and limited to physical contact. Generally, DEMs can include long ranged particle interactions (e.g. electromagnetic). Boundary conditions and body forces also act on each element; the sum of all these interactions is integrated to generate the initial conditions for the next time loop. The product of these simple contact-contact interactions in many body problems is highly complicated, leading to non-linear results.

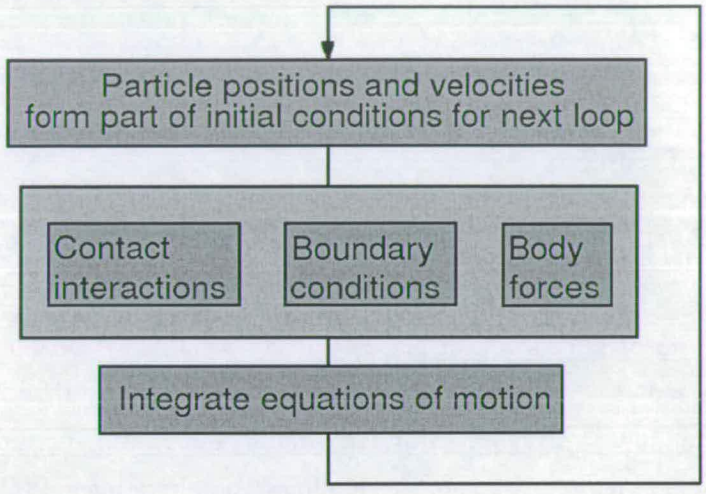

Figure 2.1: Flow of events within each DEM time-step. Each time-step the particle positions and / or velocities are used to determine the forces on each particle in that time-step. These are numerically integrated to determine the new positions and velocities for the next time-step.

2.2 Force summation

There are two types of force that can act on a body. *Surface forces* are caused by the direct contact of one body with the surface of another. Examples include concentrated (or point) loads, which are applied to a point on a body, and linearly distributed loads, in which case the surface loading is applied along a narrow area. *Body forces* are developed when a body exerts a force on another body without direct or physical contact between the bodies. Examples include gravitational and electromagnetic forces acting on a body. Each particle experiences contact interactions with other particles, body forces and boundary conditions. The force components resulting from these interactions are resolved into Cartesian co-ordinates and summed for each particle to determine the net forces and moments acting on each particle. The nature of the different interactions in this thesis are described below.

2.2.1 Contact interaction

The only inter-element forces employed in this study are surficial normal and tangential particle-particle contact forces that arise due to physical contact between the i^{th} and j^{th} elements.

2.2.1.1 Contact detection

Before the magnitude of the forces can be determined, we must establish which elements are touching. Computationally, the slowest process in running a DEM is contact detection. If every particle were to be compared with every other particle, the speed of the program would decrease approximately with the square of the number of particles. In optimising contact detection efficiency, the best that we could hope to achieve is for the total detection time taken to increase linearly with the number of particles.

By sorting the particles into a cell structure (Figure 2.2(a)), it is possible to reduce the number of comparisons made by only comparing the i^{th} particle with particles in the same or neighbouring cells. Firstly, the i^{th} particle is linearly sorted into columns, nx_i and rows, ny_i of widths dx and dy respectively (Figure 2.2(b)).

$$\left.\begin{aligned} nx_i &= 1 + INT\left(\frac{x_i}{dx}\right) \\ ny_i &= 1 + INT\left(\frac{y_i}{dy}\right) \end{aligned}\right\} \text{Sort into columns and rows} \tag{2.1}$$

It is now easy to construct lists of particles in the columns and rows near each boundary, to improve the efficiency of applying boundary conditions (Table 2.1). Ndx is the total number of columns in the x-direction within the model with width dx.

Column or row number	Boundary
$nx = 1$	left
$nx = Ndx$	right
$ny = 1$	bottom

Table 2.1: Column, nx, or row, ny, that coincides with a boundary.

Using the intersections of the nx_i^{th} column and ny_i^{th} row, a cell number, m_i can be allocated to the particle and stored in a Linked List (Allen and Tildesley, 1987).

$$m_i = nx_i + Ndx\, ny_i \tag{2.2}$$

It is now a simple procedure to compare particles in adjacent cells. Forces are equal and opposite, so we need only compare Cell A with Cell B and not the reverse (Figure 2.2(c)).

The size of the cell to attain the best performance is a balance between small cells which contain few particles but need updating after a short particle displacement and large cells which

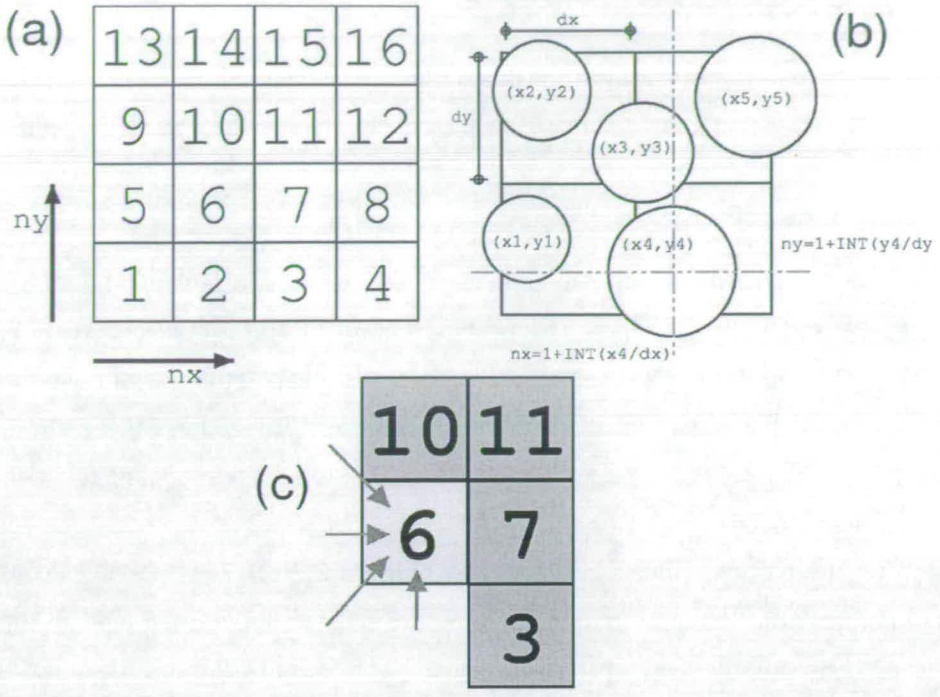

Figure 2.2: Illustration of how particles are linearly sorted into a cell structure to assist efficient contact detection. (a) Boxing of particles into columns and rows (nx and ny) are used to generate a unique cell number, (b) Discs are sorted into cell structure by linear sorting in the x and y directions into a unique cell, $m = nx + Ndxny$ and (c) Cells need only be compared once as forces are equal and opposite.

contains more particles but do not need to be updated as frequently. This scheme works well for a packing involving discs of similar sizes. A constant cell size may be inconvenient for particles with a large range of sizes, because the cell size must always be larger than the largest particle. In these circumstances, a dynamic cell size may be useful

2.2.1.2 Normal interaction

Once a reduced list of potentially touching particles has been generated, we can efficiently determine the definite contacts and the magnitude of the contact forces. We chose to use particles composed of discs, as this significantly simplifies the algebra, and thus improves the speed of the model. In order to give the particles angularity, some of the simulations use particles comprised of three discs clusters. The geometry of the normal problem between the i^{th} and j^{th} discs is shown in Figure 2.3.

Contact between two discs is determined by whether the absolute separation, Δ_r ,of the discs, is less than the sum of their radii, Δ_R. The absolute separation of the discs is given from Pythagoras as:

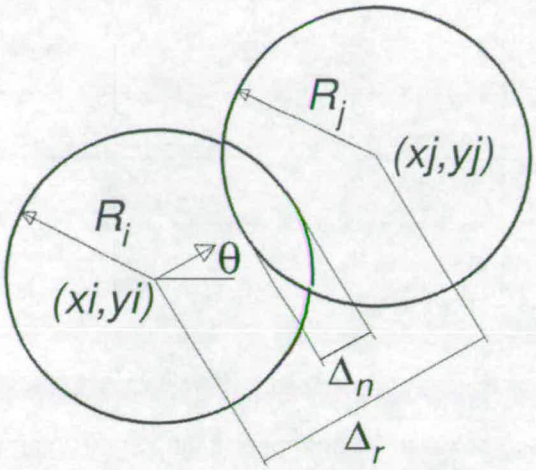

Figure 2.3: Key normal contact relations between i^{th} and j^{th} discs used to determine the normal contact force, F_n. θ is the angle between the centroids, (x_i, y_i) and (x_j, y_j), which are separated by an absolute distance Δ_r. The overlap, Δ_n, between the particles is exaggerated for clarity.

$$\left.\begin{array}{rcl} \Delta_x &=& x_j - x_i \\ \Delta_y &=& y_j - y_i \\ \Delta_r &=& \sqrt{\Delta_x^2 + \Delta_y^2} \end{array}\right\} \text{Centroid separations} \tag{2.3}$$

and the sum of the radii,

$$\Delta_R = R_i + Rj \tag{2.4}$$

A spring force law (Equation 2.5) where the magnitude of the normal force, F_n, is proportional to some very small overlap of the discs, Δ_n, (Figure 2.4(a)) is used. A strong spring constant, k_n, is chosen so as to ensure the discs are virtually rigid. This is appropriate for this study as it allows a detailed description of enduring contacts in a dense packing. Models that simulate energetic media with brief interactions and a long mean free path (distance travelled between collisions) can alternatively use a velocity based scheme.

$$\left.\begin{array}{lrcl} & \Delta_n = & \Delta_r - \Delta_R \\ \text{for} \quad \Delta_n < 0, & F_n = & -k_n \Delta_n \\ \text{else}, & F_n = & 0 \end{array}\right\} \text{Normal repulsive spring} \tag{2.5}$$

The normal contact interaction is damped proportional to the relative normal velocity between the two elements. This mechanism of damping is often referred to as a *dashpot*, after the elementary impedance element in mechanics which may be approximated mechanically by a plunger in a cylinder of air or liquid. This style of damped normal repulsive contact force,

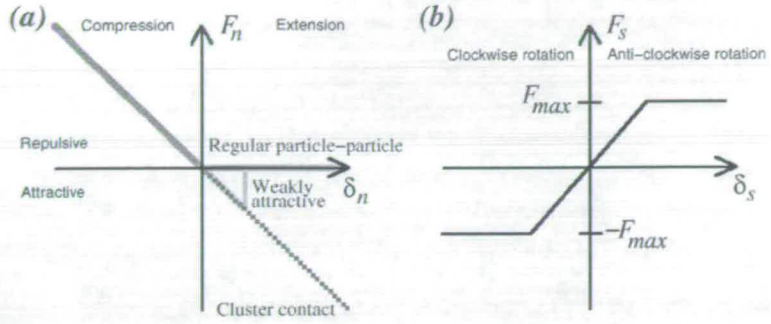

Figure 2.4: Force vs. displacement laws for normal and tangential components of particle contact force. (a) The normal force is purely repulsive under compression. Clusters of discs forming aggregate particles have strong attractive forces under extension. (b) The maximum tangential force is limited by a Coulomb failure criteria which is proportional to the Normal contact force.

known as the spring-dashpot model, is illustrated schematically in Figure 2.5, incorporating a tangential component limited by Coulomb friction described below.

The contact force law algorithm can be varied to produce different styles of disc interaction. The spring-dashpot interaction describes those contacts that occur between distinct particles. When particles are comprised of a cluster of discs, these interact through a cluster contact force law. Removing the constraint that $\Delta_n < 0$ in Equation 2.5 we get the cluster contact force law which is repulsive under compression and attractive under extension (Figure 2.4(a)), so that the discs remain fixed relative to each other. The discs between which cluster contacts exist do not change with time, so it is easy to exclude such contacts from the spring-dashpot evaluation, a list of cluster contacts can be iterated over separately. In order to simulate strain weakening, unbroken contacts could be made weakly attractive. The flexibility of the contact force law provides an opportunity to address some of the non-linear problems associated with the release of elastic strain energy within thrust wedges, as noted by Bombolakis (1994).

2.2.1.3 Tangential component

The tangential force law introduces frictional stick-slip and a Coulomb failure energy dissipation into the model. It resists any forces that would lead to a tangential acceleration and describes the way in which two discs slide across one another. The geometry of the rotational problem is shown in Figure 2.6. The magnitude of the force, F_s is proportional to the total amount of tangential displacement, Δ_t that has occurred since the contact was formed and retains the opposite sign to Δ_t so as to act as a restoring force. The total tangential displacement, Δ_t is made up from the relative tangential translation of the i^{th} and j^{th} discs, δ_t and the summation of the relative particle rotations acting at the contact, $R_i\delta_{\theta_i} + R_j\delta_{\theta_j}$. The signs are chosen

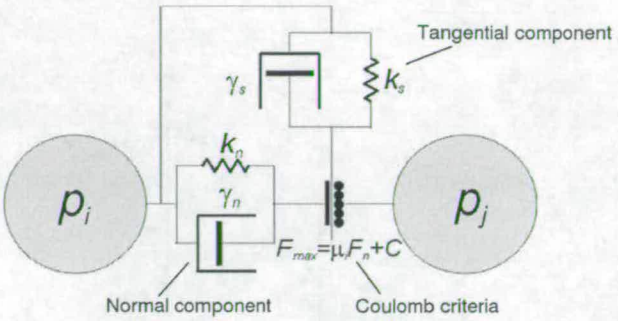

Figure 2.5: Spring dashpot model, a schematic representation of the p_i^{th} to p_j^{th} particle-particle contact forces applied in the discrete element model. The normal and tangential spring constants and damping coefficients are k_n, k_s and γ_n, γ_s respectively. F_{max} is the Coulomb failure limit.

by convention with anticlockwise rotation positive.

$$\left.\begin{aligned} \Delta_t &= \delta_t - R_i\delta_{\theta_i} - R_j\delta_{\theta_j} \\ F_s &= -k_s\Delta_t \end{aligned}\right\} \text{Tangential restoring spring} \tag{2.6}$$

The magnitude of the tangential force is limited by a Coulomb friction threshold above which slip occurs (Figure 2.4(b)) such that,

$$\text{if} \quad |F_s| > F_{max} \quad \text{then} \quad \left.\begin{aligned} |F_s| &= F_{max} \\ \text{where} \quad F_{max} &= F_n \tan\phi_i + C \end{aligned}\right\} \text{Coulomb failure} \tag{2.7}$$

The amount of resistance to sliding any tangential contact can provide is proportional to the magnitude of its normal contact force, the constant of proportionality is the Coulomb coefficient of friction. Cohesion, C, is neglected. A spring-dashpot normal contact with no normal force cannot preserve a tangential force so that whenever $\Delta_n^{i,j} > 0$, the corresponding $F_s^{i,j} = 0$. Some studies suggest that sliding contacts experience a lower coefficient of friction than static loads. This can be incorporated by introducing a hysteresis into the coefficient of friction.

The Coulomb friction resistance abruptly changes sign when the relative tangential velocity, v_t, changes direction. At a non-sliding contact, $v_t = 0$ and the static tangential frictional force can take any value between $\pm\mu_s F_n$.

This simple set of rules produces a very complicated behaviour. Aside from the energy dissipated through regular damping, energy stored in the tangential spring is lost whenever a normal spring-dashpot contact is broken. In a dense system, these interactions introduce a memory into the system that remembers which parts of the system have undergone deformation.

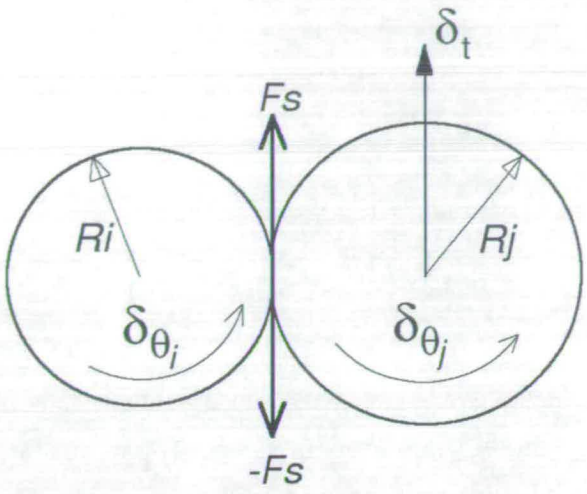

Figure 2.6: Key tangential contact relations between i^{th} and j^{th} discs used to determine the sheer force, F_s. The illustration is shown in a frame of reference where the i^{th} particle is stationary. δ_t is the tangential displacement of the j^{th} particle with respect to the i^{th}.

2.2.1.4 Resolving of contact forces into translational components

For discs, it is easy to geometrically obtain the sine and cosine of the angle, θ, between the x-axis in Cartesian frame of reference and the vector parallel to the normal contact direction.

$$\sin\theta = \frac{\Delta_y}{\Delta_r} \tag{2.8}$$

$$\cos\theta = \frac{\Delta_x}{\Delta_r} \tag{2.9}$$

In the Cartesian frame, the x and y components of the normal and tangential forces between the i^{th} and j^{th} discs now become,

$$F_x^{i,j} = F_n^{i,j}\cos\theta + F_s^{i,j}\sin\theta \tag{2.10}$$

$$F_y^{i,j} = F_s^{i,j}\cos\theta - F_n^{i,j}\sin\theta \tag{2.11}$$

which can be added, equally and oppositely to the i^{th} and j^{th} particle force summation.

The tangential force acting on each disc is equal and opposite. The torque, τ, it applies is proportional to the distance from its axis of rotation. Thus, discs of different radii experience different moments for a given tangential force. All of the moments acting on each disc are summed to formulate a rotational equation of motion.

$$\tau_i = \tau_i + F_s R_i \tag{2.12}$$

$$\tau_j = \tau_j - F_s R_j \tag{2.13}$$

2.2.2 Boundary conditions

The term *boundary conditions* refers to the way in which particles interact with regions of the model where they are not permitted to enter. Choosing the right boundary conditions is very important. In this chapter, a brief outline of the main issues and implementation will be given and Chapter 4 will investigate those appropriate to model the evolution of doubly vergent wedges.

An undeformable boundary across which a particle cannot travel will be termed *rigid*, the normal interaction is again modelled using a strong linear spring. For a general wall, where the closest points to the i^{th} particle are (x_b, y_b) the normal overlap is given by 2.14. A *smooth* wall imparts no tangential force at its contacts. A *rough* surface allows a tangential component which resists motion parallel to the surface through a frictional force law. A Coulomb failure criteria has been applied limiting the magnitude of the tangential component.

$$\delta_n = \sqrt{(x_i - x_b)^2 + (y_i - y_b)^2} - R_i \tag{2.14}$$

The mechanism by which the boundary interacts with the particle does not have to be via exerting a force. For example, a velocity condition can be imposed on those elements in contact with part of a wall. These particles form a pseudo boundary for those not forced by this velocity condition and act to drag the adjacent particles along. Due to the angularity of the particles, this interaction will not be a simple Coulomb interaction. Indeed the forced particles have fewer degrees of freedom than those constituting the bulk material and are thus stronger than the bulk material.

For some experiments, such as those investigating erosion, it may be necessary to completely remove particles from the model space. To avoid re-allocation of model arrays, a simple procedure is undertaken to store these eroded particles in a region outside the main model space at some unique location dependent upon particle number, setting their size and velocity to zero to ensure no particle movement. They can then be automatically excluded from the particle comparison lists. Similarly, this technique can be used to add particles to a system.

2.2.3 Body forces

The only body forces applied in this study arise from gravity, though generally they may arise from any background field. The mass of each particle is local and constant, so rather than

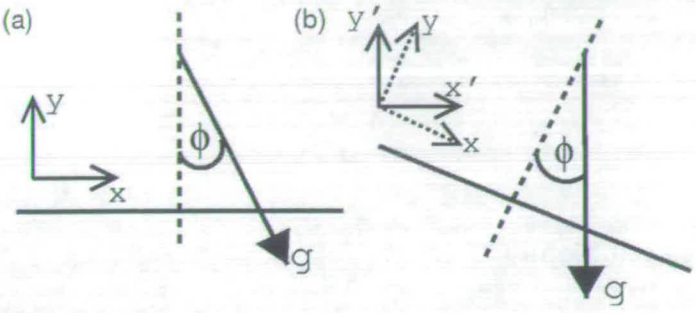

Figure 2.7: Transformation of body forces from Cartesian coordinates (x,y) to (x',y') by a rotation through an angle ϕ simplifies the boundary conditions for an inclined plane problem. (a) shows the model space with the gravity vector oblique to the slope surface (the x axis), (b) Model space transformed back to a frame where the gravity vector is vertical, parallel to y'.

resetting the Cartesian particle force summations to zero each time loop, we can set them to the resolved body forces such that,

$$\begin{aligned} \mathbf{F}_x &= 0 \\ \mathbf{F}_y &= -\mathbf{M}g \end{aligned} \tag{2.15}$$

For some problems it may be more useful to use a frame of reference that is rotated with respect to the gravity vector, for example a gravity driven granular flow down an inclined plane (Figure 2.7). In this case, it simplifies the contact search algorithm if the Cartesian frame of reference is parallel and perpendicular to the inclined surface rather than to gravity. Now the body force components are given by,

$$\begin{aligned} \mathbf{F}_x &= \mathbf{M}g\sin\phi \\ \mathbf{F}_y &= -\mathbf{M}g\cos\phi \end{aligned} \tag{2.16}$$

2.3 Integrate forces and update positions

Once the force components have been summed over all particles in a Cartesian frame of reference, the equations of motion can be evaluated to update the position and velocity of the particles. Using the equations of motion,

$$\begin{aligned} Force &= Mass \times Acceleration \\ Torque &= Inertia \times Angular\ acceleration \end{aligned}$$

$$\left.\begin{aligned} \mathbf{V}_x(t+1) &= \mathbf{V}_x(t) + \frac{\mathbf{F}_x dt}{\mathbf{M}} \\ \mathbf{V}_y(t+1) &= \mathbf{V}_y(t) + \frac{\mathbf{F}_y dt}{\mathbf{M}} \\ \mathbf{V}_\theta(t+1) &= \mathbf{V}_\theta(t) + \frac{\tau dt}{\mathbf{I}} \end{aligned}\right\} \text{Update velocities} \tag{2.17}$$

$$\left.\begin{aligned} \mathbf{X}(t+1) &= \mathbf{X}(t) + \mathbf{V}_x dt \\ \mathbf{Y}(t+1) &= \mathbf{Y}(t) + \mathbf{V}_y dt \\ \theta(t+1) &= \theta(t) + \mathbf{V}_\theta dt \end{aligned}\right\} \text{Update positions} \tag{2.18}$$

2.4 Particle geometry and packing structure

So far, the formulation discussed has fitted into a well defined mathematical framework. In continuum modelling, the next step is to make approximations that enable solutions to be found. These assumptions are a main source of error. A DEM exhibits emergent phenomena due to the geometry of the particles and packing, not present in continuum modelling. For example, if we think of friction as being some resistance to motion, the interlocking of angular grains of sand in a shear box will increase friction as compared with smooth round grains (Mair et al., 2001). Coulomb friction is adequate to describe the total frictional effect in continuum modelling. However in DEM modelling, friction is an emergent product of Coulomb, particle geometry and packing structure. These ideas will be explored in depth in Chapter 3.

Various regular and random particle geometries and packing structures have been investigated. These are generated using a packing program and allowed to settle under gravity before an experiment is run. If cluster particles are to be used, they are specified in the initial packing program. Several experiments can be run on the same initial packing.

2.5 Energy dissipation

There are two main energy dissipation mechanisms in the DEM. Normal and tangential contacts simulate irreversible internal deformation whilst friction dissipates energy during periods of slip governed by Coulomb failure. During relaxation of a normal contact, the energy stored in the tangential spring is lost as the slip threshold, F_{max} reduces.

2.6 Previous DEM applications

DEM studies fall into two general categories. Energetic problems which are best described by a velocity based scheme and static problems which use a force based scheme. This is due to the different descriptions underpinning the two regimes, for example normal energy being

dissipated through a coefficient of restitution in the former or a dashpot in the latter. These formulations are not inconsistent, but do use different language.

This study focusses on problems with dense packings and enduring contact. At the extreme end, a range of studies have focussed on the growth of piles of particles and the evolution of the resulting internal contact network (Silbert et al., 2002; Landry et al., 2003). These studies highlight that the internal stress distribution, and thus the resulting pile geometry is dependent upon how the pile was grown. Segregation and mixing of particles in industrial apparatus has been extensively modelled (Tsuji et al., 1992; Dury and Ristow, 1999). From a purely numerical perspective, friction and mobilization of contacts in granular numerical avalanches has been looked at by Staron et al. (2001).

Recently, DEMs have begun to be been applied within the Earth sciences. Obvious applications include fault gauge mechanics (Morgan and Boettcher, 1999; Morgan, 1999) and granular avalanches (). A numerical simulation of seismic waves was performed by Toomey and Bean (2000) with the aim of developing a tool to investigate wave propagation in multiphase media. Finch et al. (2003) investigated the resulting thinning strata associated with the propagation of a single blind thrust. Most relevantly to this study, Burbidge (2000) tackled the problem of a singly vergent critical wedge.

2.7 Numerical stability

In order to determine a 'ballpark' figure for the magnitude of model time-step, δ_t and to ensure the stability of the model at particle contacts we generate an inequality between the maximum permitted displacement, δ_x with the greatest gravitational displacement increment through a dimensional analysis (Equation 2.19). Taking unit mass,

$$\delta_x > g\,\delta_t^2 \tag{2.19}$$

Thus rearranging for the time increment, to be stable with respect to the normal increments,

$$\delta_t < \sqrt{\frac{\delta_x}{g}} \tag{2.20}$$

The amount of overlap, Δ_n at the bottom of a column of l particles is approximated by equating the repulsive force due to the compression of the a spring with spring constant, k_n with the total load above it,

$$k_n \Delta_n \approx \sum_l M_l g \tag{2.21}$$

$$\Delta_n \approx \frac{\sum_l M_l g}{k_n} \tag{2.22}$$

$$\delta_t < \sqrt{\frac{\sum_l M_l}{k_n}} \tag{2.23}$$

The expense of having a high spring constant, k_n, to ensure rigid particles, has an expense in the size of time-step required for stability of the model. If any part of the system fails this limit, the model is likely to explode as the instability propagates.

Efficiency of the model can be further improved using a dynamic time-step (Zhang and Whiten, 2001) which adjusts to use the largest *dt* possible at any stage. However, some workers had difficulty in implementing this so it was avoided in this study (Burbidge, 2000). Tsuji et al. (1992) noted that it is often necessary to check the simulation results using different time-step sizes.

2.8 Model output

Each of the individual iterations the model makes is termed a *model time-step*. One run typically consists of millions of model time-steps so it is impractical to record information every cycle. Instead, still frame snap-shots are dumped $\sim 25,000$ model time-steps, each one of these is called an *output time-step*. The difference between two successive output time-steps provides an integrated picture of deformation over that period. The main problem with presenting still frame images as figures is that they represent only a small subset of the model data and give a poor indication of the temporal evolution. For this reason, many of the figures are also presented as animations on the CD at the back of the thesis. These can be investigated interactively by running "Index.html" in any web browser. The animations are sub-divided into singly-vergent and doubly-vergent pages. Specific combinations are referenced at the top of the pages and a list of all animations is provided in table format. Alternatively, any combination of animations can be displayed using the drop down menus and submitting a combination. They animations are stored as gif's and can be loaded into a gif viewer, such as xanim, which provides more viewing options. For better performace, it is recommended that the contents of the CD are copied onto a hard-drive.

Many of the critical wedge results presented will be normalised by the depth of the undeformed incoming material. This allows the results to be easily scaled to different systems. Model time is replaced with the total amount of convergence accommodated per unit model depth. This can be scaled to real time assuming a convergence rate.

Chapter 3

Material Properties

This Chapter outlines some general properties of various DEM materials, defined by the initial particle size shape distribution. The chapter starts with a brief review of the properties of granular materials, as there are many parallels between DEM and granular materials. Then, a justification of the initial particle geometry employed for the rest of the study is given, by investigating angle of repose and singly-vergent critical wedge experiments for regular hexagonal, random single disc and random cluster DEM materials.

3.1 Granular materials

The properties of granular materials arise from the product of many simple contact-contact interactions. Wolf (1997) noted that dissipative particle-particle interactions give rise to unexpected effective friction properties on large length-scales compared to the particle diameter and long time-scales compared to the duration of one contact interaction. This is because the dynamic feedback between the static friction at the non-sliding contacts is dependent on the acceleration of the packing as a whole. He further characterised the dynamic properties of many particle systems by:

1. Irreversible particle-particle interactions
2. Translational and rotational excitation energies that are much greater than thermal energies
3. Hysteric behaviour (memory effects, stick-slip) such as static friction
4. Geometric constraints, expressing themselves through, for example, dilatancy and arching

For a material to be considered granular, we require that, under experimental conditions, the thermal energy is much less than the order of the change in gravitational potential energy

required to displace a particle, mgR, otherwise Brownian motion becomes important. This implies that grains must be larger than $\sim 1\mu m$ at room temperature. Providing that this condition holds, we can arbitrarily add thermal heat to the system with no change in the dynamics. This allows us to define a new thermodynamic variable *granular temperature*, which is the standard deviation of the grain velocity about some mean. Thus, regions with a high spread in velocity have a high granular temperature.

Such properties are present in many systems, not all of which might naturally be classified as granular problems, e.g. traffic flow which exhibits self organisation and non-equilibrium phase changes (Helbing, 1997).

3.1.1 Granular friction and particle angularity

Friction is the force that resists the relative motion of two contacting bodies. Thus, if we are measuring the bulk friction of a granular material, we are measuring the integrated resistance to motion due to all particle interactions. As such, the traditional concept of micro-scale atomic friction and the meso-scale interlocking of individual grains generate that resistance.

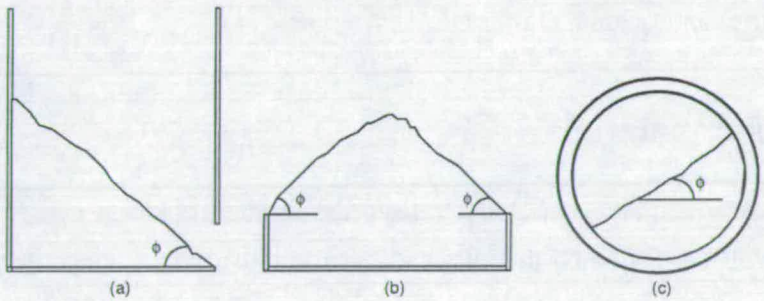

Figure 3.1: Examples of different experimental methods for measuring the angle of repose. (Modified from Oger et al. (1998))

The term *angle of repose* is ambiguous. It describes the maximum angle at which a surface is stable, but a given granular material exhibits different surface slope angles depending upon how the slope is generated (Figure 3.1). For example, three different angles will be found in the sequence; 1) Pour a pile of sand onto a flat plate and measure the surface angle, 2) Incline the plate slowly, recoding the angle at which failure occurs, 3) Once failure has occurred, measure the angle at which the slope comes to rest. For the case of a simple sand pile, Geng et al. (2001) demonstrated the dependence of the surface slope upon whether a point source or a careful layering is used to generate the pile. It is therefore unsurprising that particle morphology, which influences how particles mesh together, is important in determining bulk properties.

Interestingly, Roux (2000) notes that complete rigidity is only guaranteed in the case of spherical cohesionless grains. Otherwise the network of contacts (the packing) might deform

elastically in response to small load increments, without an apparent change in packing structure.

3.1.2 Arching effects

Arching refers to the effect where strain is taken up along a limited set of chains of particles within the packing (Duran, 1997). This produces a non-uniform load across the base of a sand pile, and a strain minima under the centre. This effect is analogous to the equilibrium within a key stone bridge (Figure 3.2). A similar phenomenon is also observed in dynamic systems.

Figure 3.2: Example of a key-stone structure, an arching effect. The downward force of the over-burden spreads out to the stones on either side of the keystone. The red lines indicate the direction of the inter-block normal forces.

3.1.3 Granular fluids

Generally, a change in *phase* is characterised by properties which change discontinuously, without a change in chemical composition. If a solid granular material has enough input of energy so that all the frictional contacts can be simultaneously broken, it will start behaving collisionally as a fluid (Umbanhowar, 2003). If more energy is added, it can then change phase into a granular gas and its behaviour becomes kinetic (D'Anna et al., 2003). These systems are of particular interest as they are far from equilibrium, with strong spatial and temporal variations in quantities such as density and local particle velocity. Traditional descriptions of liquids using equilibrium statistical mechanics derive a relation known as the fluctuation-dissipation theorem, it is therefore surprising that in many instances, non-equilibrium granular materials appear to behave like liquid (Jaeger et al., 1996).

3.1.4 Granular memory and dilatancy

Any hysteric behaviour retains some memory, as the current state is dependent on the path taken to get there. This is the same process by which magnetic materials retain information. Memory can be stored in the packing structure, and thus the normal force distribution, of a smooth granular material. For a granular material to deform from a static equilibrium, it must first dilate. The regions that dilate are looser and thus weaker, providing a mechanism to localise deformation. If the region does not completely regain an equilibrium equivalent to its initial state, the packing will be different in some way to the rest of the material. In this way past deformation can be remembered.

A frictional granular system has a second method for remembering past deformation. Each tangential contact can take any value between $\pm F_{max}$ (the Coulomb limit). Depending on the sequence in which the contacts were loaded, a given particle arrangement may have different values of tangential frictional forces, and thus a memory. Contacts which are at Coulomb failure are thus more likely to slip again, producing a strain weakening effect. A material defined to be at Coulomb failure cannot remember in this way.

A granular material can even remember how it has been handled, because internal friction varies depending upon whether sand used in experiments is sifted, poured or sprinkled (Krantz, 1991; Schellart, 2000).

3.2 DEM material properties - Particle shape and packing structure

Global friction is an emergent property of all the contact processes that result in a resistance to motion, i.e. the coefficient of internal friction, particle shape and packing geometry. Individual particle shape remains constant throughout the experiments presented, however the particle geometry and force network evolves in response to the applied boundary conditions (Lanier and Jean, 2000; Silbert et al., 2002). Through these mechanisms, the DEM material has some memory of past deformation. For example, a sheared granular material is less resistant to the initiation of subsequent shear events than it is for the first event.

Three different initial particle packings were considered (Figure 3.3). Each was generated by placing particles within some grid structure to ensure no overlap, and then allowed to settle under gravity to equilibrium. Where random sized balls were generated, they ranged between $0.7 - 1.0$ particle diameters with an even spread. Multiple angles of repose and singly-vergent critical wedge experiments for each packing are presented.

3.2.1 Angle of repose

The measurement of the angle of repose for free flowing, non-cohesive materials yields an approximation of the internal angle of friction. Roughly constant values have been reproduced in

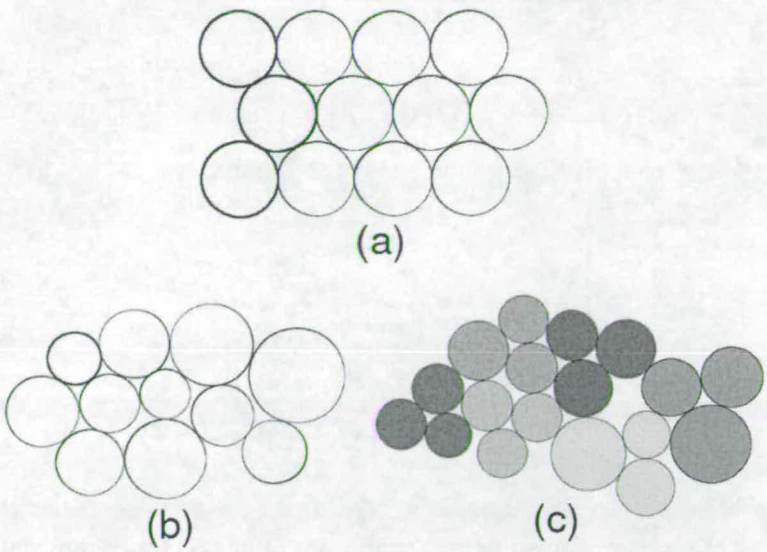

Figure 3.3: Particle packing structures investigated as part of this study. (a) The regular hexagonal packing (b) Random single disc packing (c) Random cluster packing.

the laboratory for a given experimental method (Terzaghi, 1943). The internal angle of friction measured in experiments can vary significantly depending upon experimental conditions (e.g. with confining pressure in the biaxial test), so the angle of friction should not be assumed to be identical to the angle of repose.

The boundary conditions applied are motivated by those used by Oger et al. (1998) to measure the angle of repose in the ledge simulation. Oger et al. (1998) found the angle of repose response to variations in the internal coefficient to be qualitatively similar to the results of the biaxial test (i.e. initially the angle of repose increases rapidly as contact friction is increased, until it becomes independent of internal friction when it reaches higher values, Figure 3.4). In other words, there is a limit up to which increasing the inter-particle contact friction will strengthen the packing, above this the angle is limited by processes other than contact friction.

The DEM material is allowed to settle in a square container. The lowermost particles are fixed in space and one of the retaining side walls removed. Particles are allowed to flow across this boundary and are removed from the system. The flow is clearly not behaving as a traditional fluid as flow only occurs in a thin surface layer. The experiment is run until the material comes to rest forming some surface profile. The angle of the surface is termed the *angle of repose*. These experiments have been run for each packing with four different internal coefficients of friction, $\mu_e = 0.30, 0.10, 0.03, 0.01$ to see the response of the packing to the internal angle. The output in Figures 3.6 to 3.17 are coloured in bands by the initial, settled, undeformed depth.

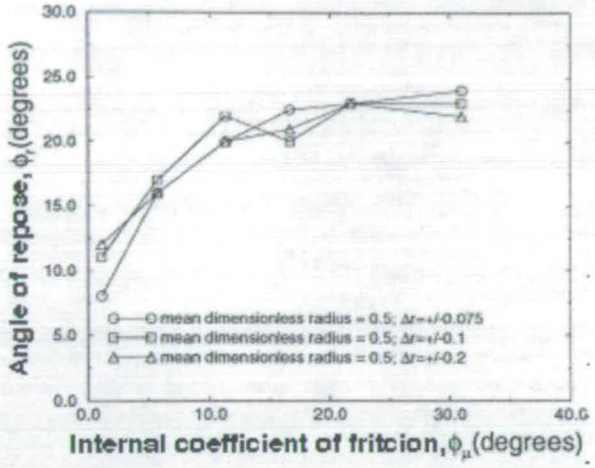

Figure 3.4: Angle of repose versus internal coefficient of friction for assemblies of about 1250 particles having different size distributions. (Modified from Oger et al. (1998))

3.2.1.1 Regular hexagonal packing

This packing is the densest possible formation for uniform, single disc particles and is thus the strongest. Each particle touches six other particles forming three linear contact planes. For any motion to occur, the material must dilate to allow one plane to slide over another. As illustrated in Figure 3.5(a), the horizontal and 60° planes require the least perpendicular displacement, $0.27R$, to allow one sheet plane to slide over the other. The vertical and 30° planes are formed by a zig-zag of particles and require a perpendicular displacement of one particle radius in order to slide (Figure 3.5(b)).

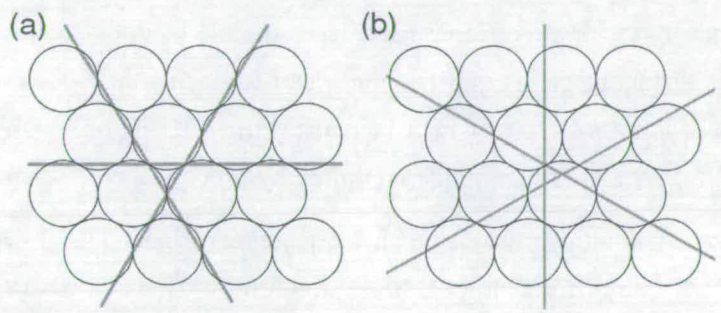

Figure 3.5: Detailed illustration of the regular hexagonal packing. (a) shows the primary planes of weakness that only require a displacement of $0.27R$ perpendicular to the plane for sliding to occur. The particles are also aligned in chains along these directions allowing stress to propagate long distances as there is no deviatoric component. (b) secondary planes of weakness that require a perpendicular displacement of $1.0R$ for sliding to occur.

In all cases (Timestep 1), the initiation of sliding starts by the formation of a narrow shear zone about two balls wide, along a 60° yield plane that initiates at the bottom open corner of the base. The normal faulted block rapidly exits the system (by Timestep 2). When the energy release is small and the inter-particle friction strong, the block remains intact, but as more energy is release the block becomes fluid and loses its structure (Figures 3.6 and 3.7). Lower values of the coefficient for internal friction result in this transition occurring sooner (Figure 3.9). The flow along the surface results in slope parallel retreat. The depth of flow tends to zero at the top of the packing and increases towards the open boundary for all experiments. The cessation of the flow and the beginning of the stable slope starts with the position of the upper zero flow depth smoothly migrating down a stabilising surface. A stable surface is attained when the flow has migrated out of the side of the model. This takes longer for the lower internal angle of friction experiments, as more material has to be removed to attain the lower stable surface slope. The packing beneath the rest surface is undisturbed, demonstrating the resistance of this packing to mobilisation, except where a particle is unsupported. In this case it will travel in free-fall. Figure 3.8 clearly illustrates this strength in the third frame, where a significant overhang develops before being undermined.

The resulting equilibrium slopes attained from these experiments do not have constant taper angles, but are concave. This is most clearly demonstrated in the lower internal angle experiments (e.g. Figure 3.9). However the development of a tail between Figures 3.6 to 3.7 suggests that this is an expression of the same effect. As the surface is concave, the slope is dependent on the x position of the measurement (Equation 3.1), and is not solely a product of the internal angle of friction. It is this extra x term that is imposed by the hexagonal packing.

$$\frac{dy}{dx} = f(\mu_e, x) \tag{3.1}$$

High internal angles of friction allow the angle of repose to be determined by the 60° plane in the hexagonal packing and very little material is removed. Indeed, the combination of hexagonal packing and high friction allows single balls that overhang the slope below to be supported.

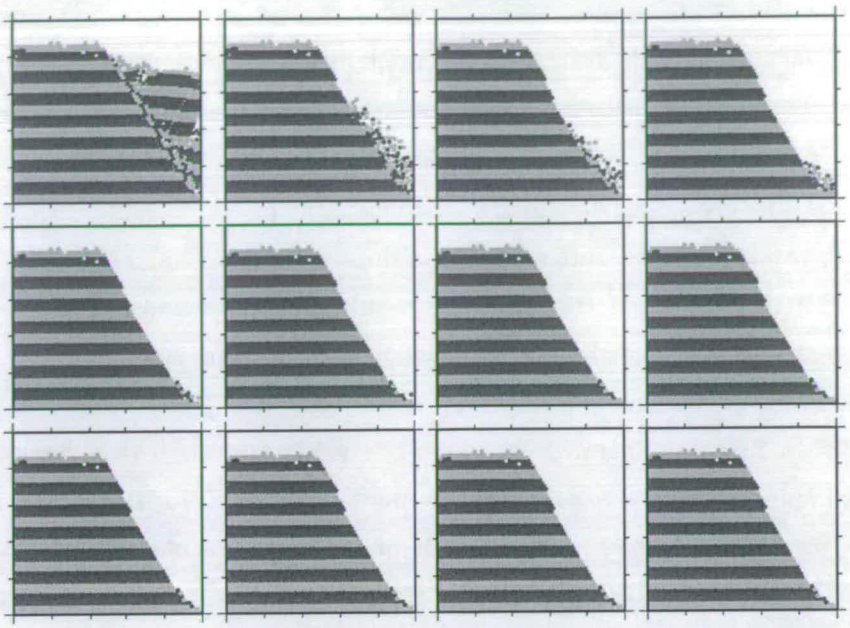

Figure 3.6: Slump angle of repose experiment for the regular hexagonal packing and $\mu_e = 0.3$, the surface slope is strongly controlled by the packing structure. Gravity acts vertically downwards.

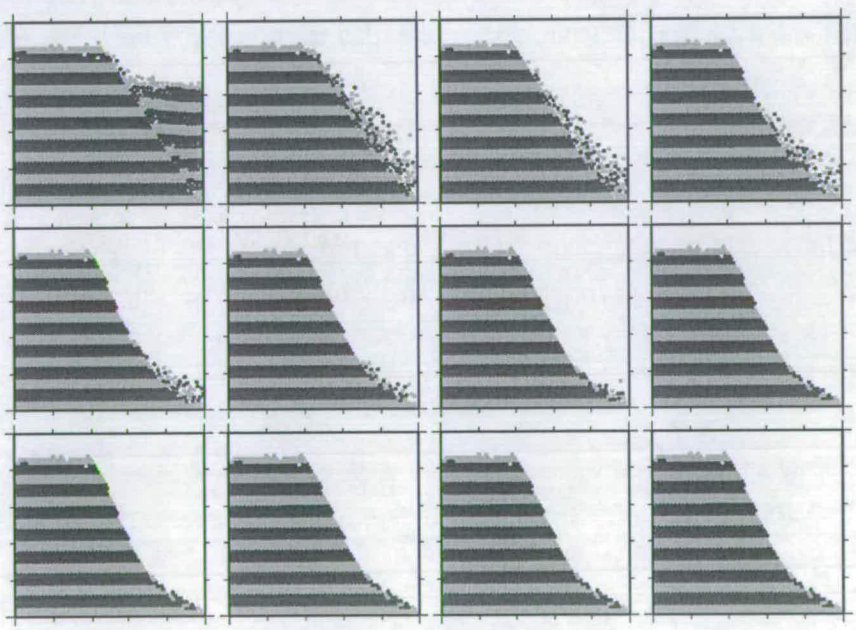

Figure 3.7: Slump angle of repose experiment for the regular hexagonal packing and $\mu_e = 0.1$.

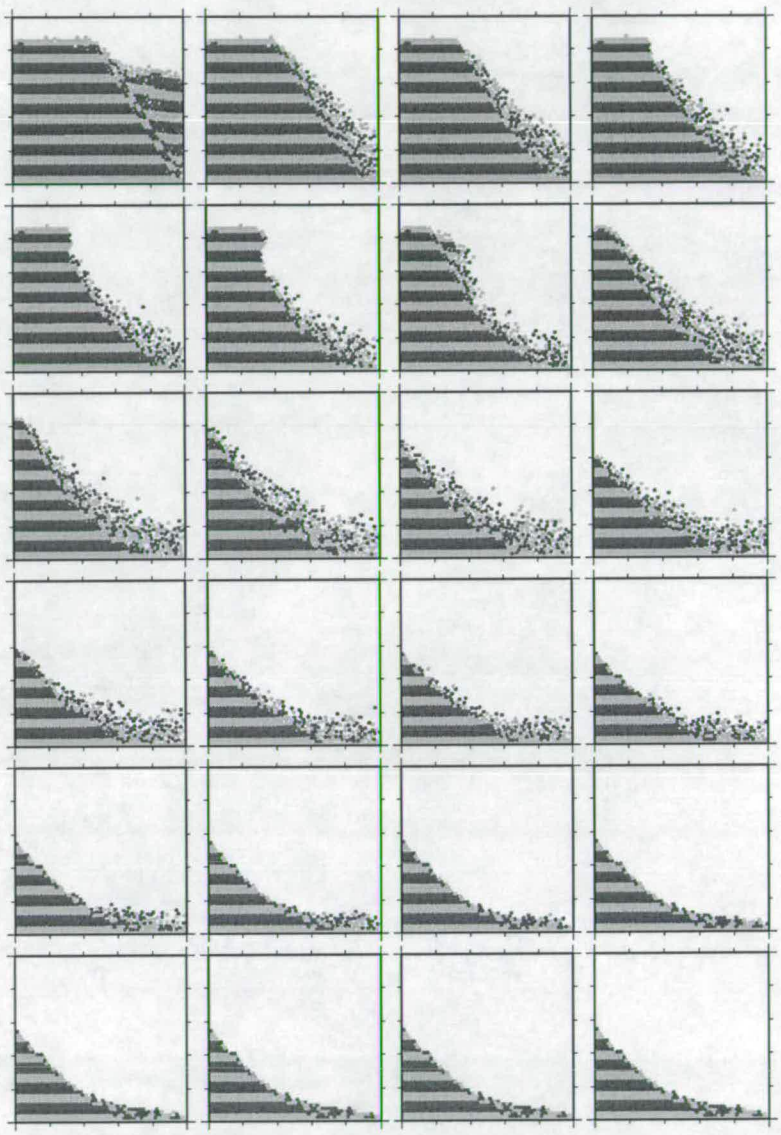

Figure 3.8: Slump angle of repose experiment for the regular hexagonal packing and $\mu_e = 0.03$, resulting in a concave surface profile. Gravity acts vertically downwards.

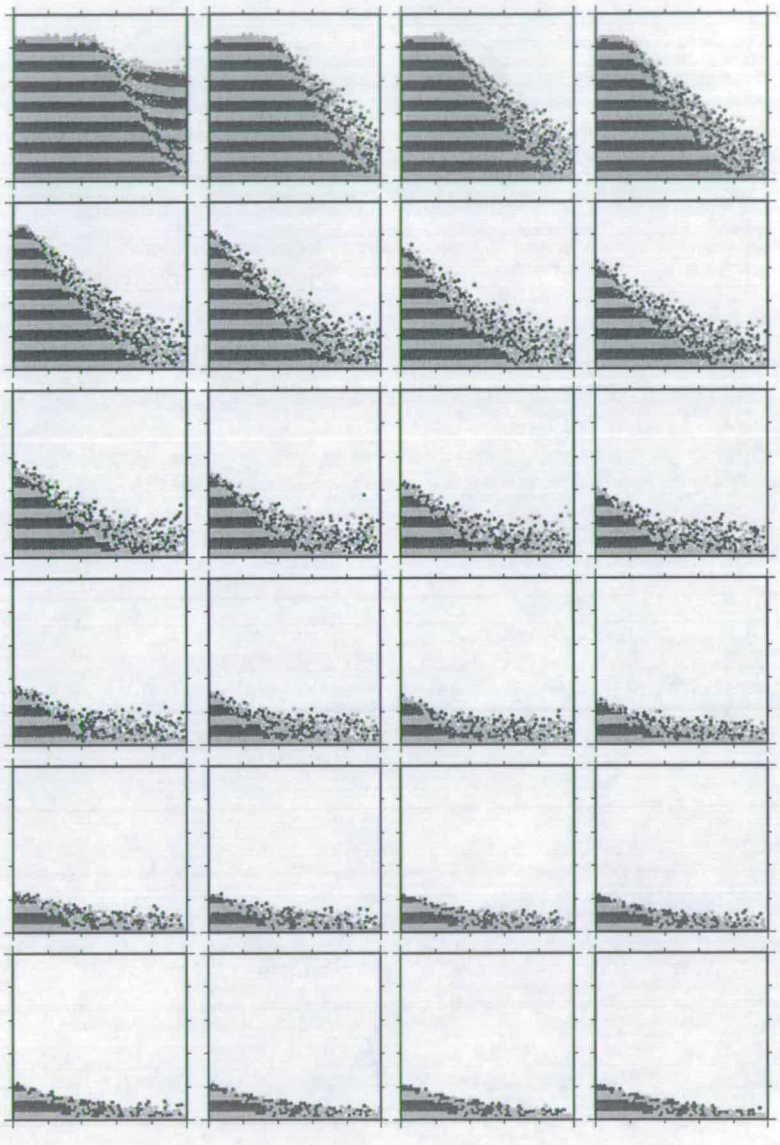

Figure 3.9: Slump angle of repose experiment for the regular hexagonal packing and $\mu_e = 0.01$. Gravity acts vertically downwards.

3.2.1.2 Random single disc

To address some of the dependence problems with the regular hexagonal packing, a random single disc packing was tested (Figure 3.3(b)), again using a suite of slump angle of repose experiments with different internal coefficients of friction (Figures 3.10 to 3.13). Vastly different behaviour is observed compared to those produced by the regular hexagonal packing. During the evolution of the system, we initially observe thinning of horizons towards the open boundary as GPE is released, this thinning region makes a transition into a mobile surface layer flow that detaches along the thinning plane where the kinetic energy is much greater than the energy required to displace a particle, as the thinning unit becomes thin. The weaker the internal angle, the further back into the packing this initial thinning extends. The depth of the flowing boundary layer is controlled in part by how easy it is to erode the undeformed lower surface. In other words, the depth required to disperse the kinetic energy. For the case of $\mu_e = 0.3$, we can see the sliding and thinning of a block as it cleaves off the top of the pile (Timesteps 6-7).

Compared to the hexagonal packing results, the angle of repose is significantly lower and transition between the upper boundary flow layer and the undeformed wedge is less distinct. The upper surface is more susceptible to abrasive erosion. Importantly, the upper surface is now much flatter, removing the dependence of slope on position and making it purely a product of the bulk properties of the material, specifically the internal coefficient of friction.

$$\frac{dy}{dx} = f(\mu_e)$$

Many authors have noted the problem of over-rotation in single disc particles (Ting et al., 1995). As there is no physical surface roughness to the particles, they can accommodate relative motion very easily through rotation and sliding. Early work with DEMs showed significantly lower angles of repose than their analogue counterparts. Mair et al. (2001) demonstrate through direct shear experiments, that this abnormally low friction is due to the absence of surface asperities. Thus, many studies have taken to using non-circular (or non-spherical in 3D) particles to deal with this phenomenon.

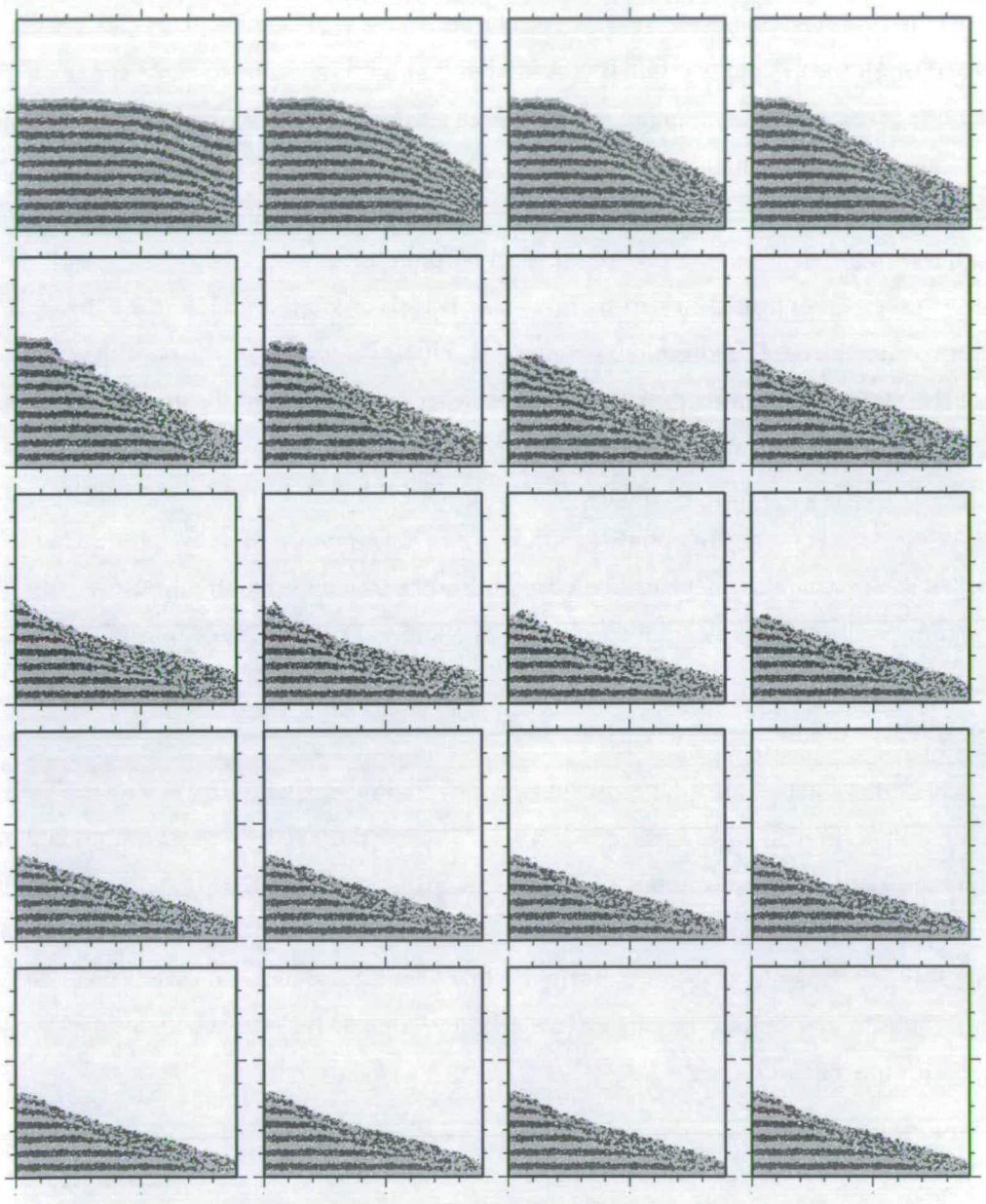

Figure 3.10: Slump angle of repose experiment for the random single disc packing and $\mu_e = 0.3$, the surface profile is linear. Gravity acts vertically downwards.

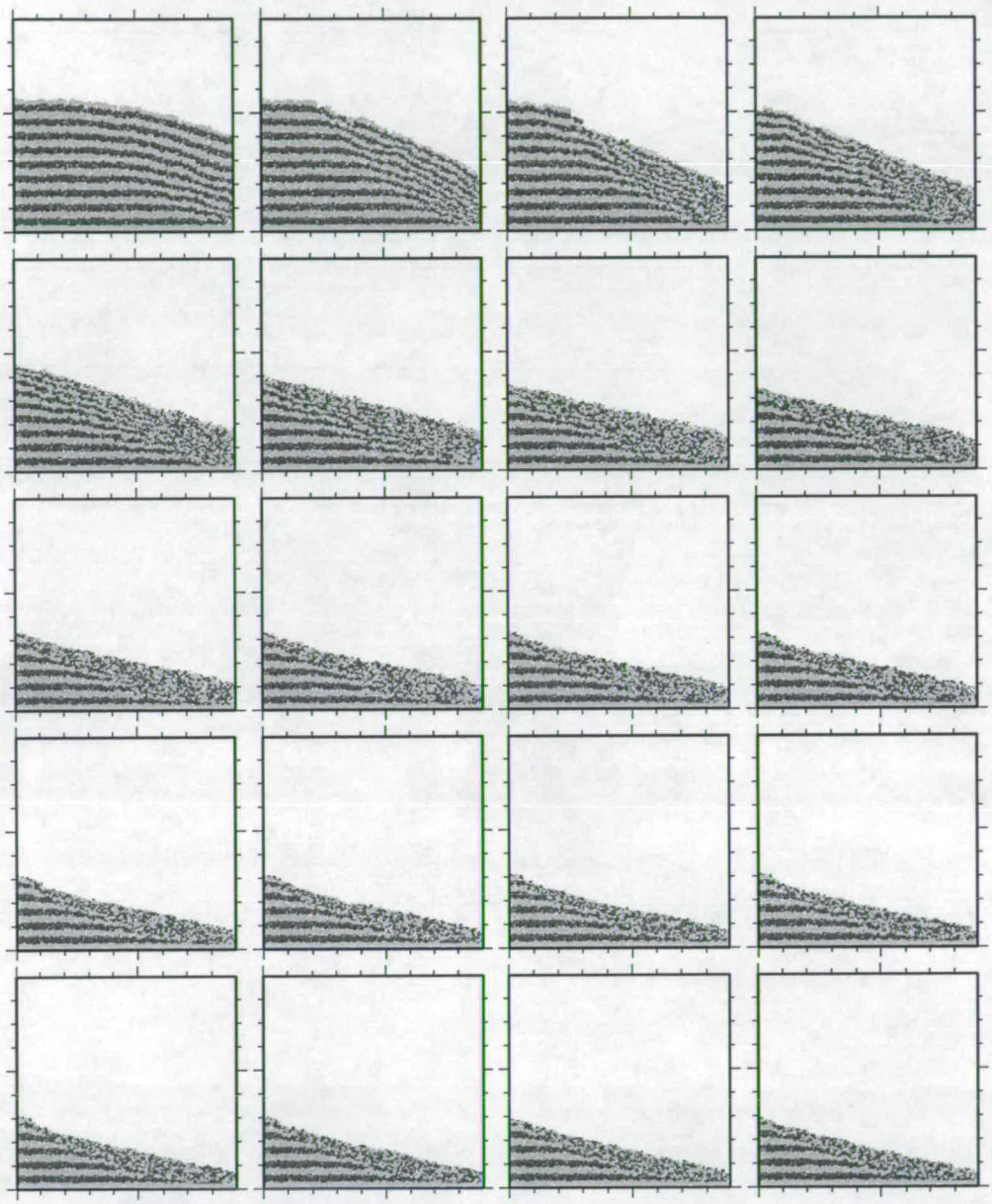

Figure 3.11: Slump angle of repose experiment for the random single disc packing and $\mu_e = 0.1$, the surface profile is linear. Gravity acts vertically downwards.

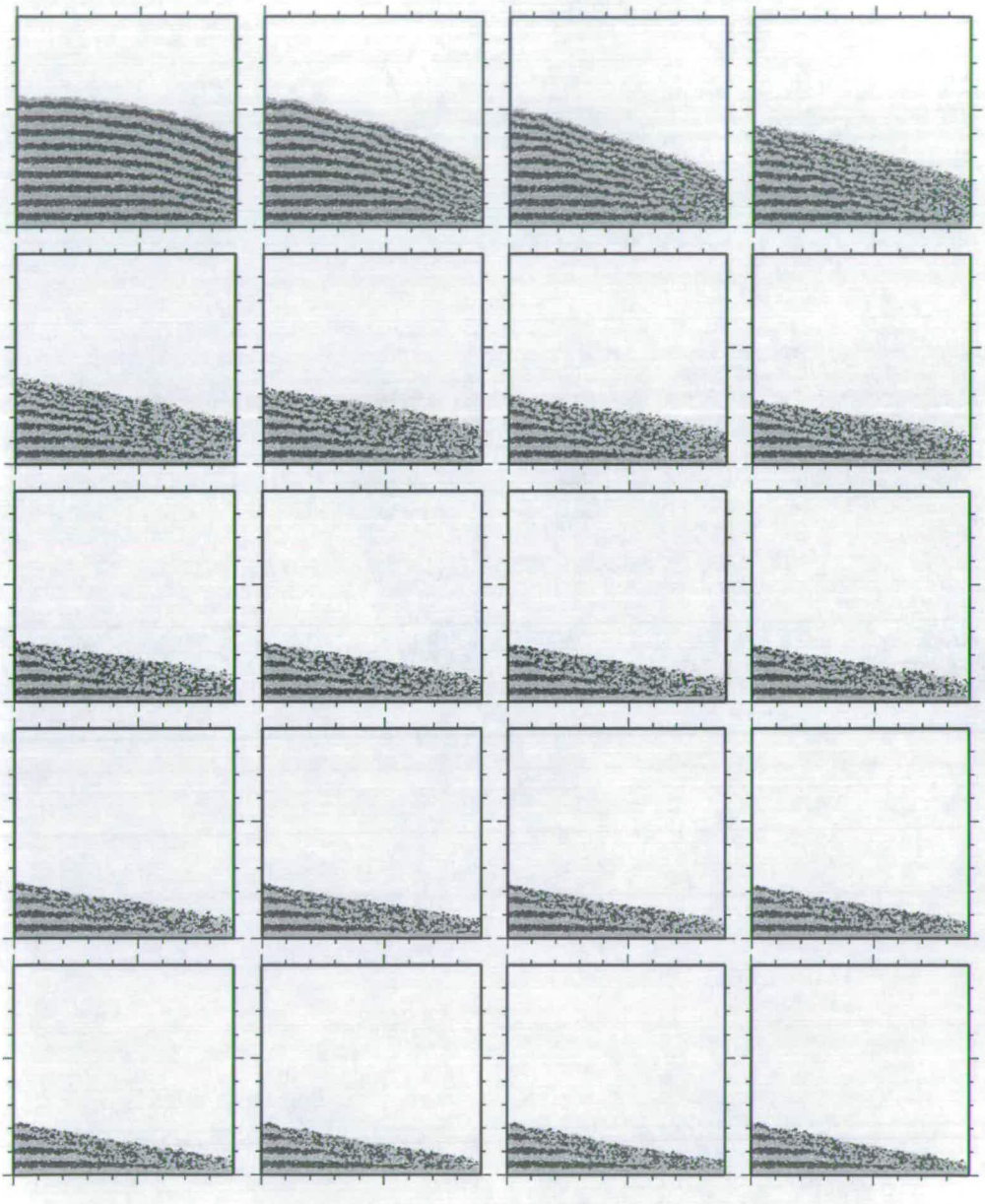

Figure 3.12: Slump angle of repose experiment for the random single disc packing and $\mu_e = 0.03$, the surface profile is linear.

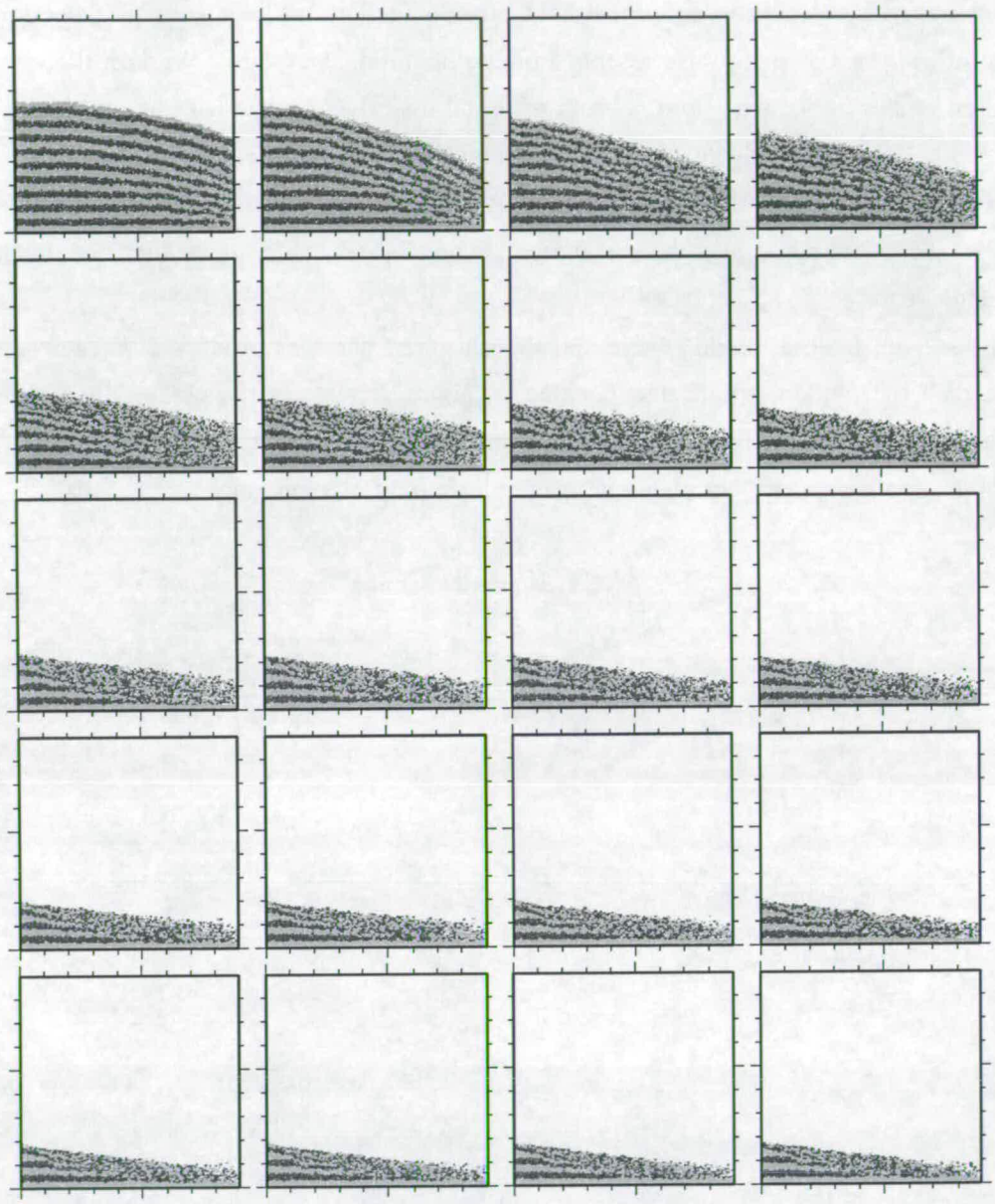

Figure 3.13: Slump angle of repose experiment for a random single disc packing and $\mu_e = 0.01$.

3.2.1.3 Random clusters

Ovular and polygonal particles have been used to overcome the problem of over-rotation associated with using purely round particles (Ting et al., 1993). The use of these shapes makes contact detection more difficult, as it is no longer possible to simply use Pythagoras and the sum of two constant radii to determine contact (see Section 2.2.1.1). Contact detection was already the slowest step, so this presents a big computational expense. We take the approach of Jensen et al. (1999), who used clusters of round discs to generate particle roughness (Figure 3.3(c)). This has the advantage that no new algorithms are required, we only need to specify which discs are permanently bound together. We used clusters of three discs of random size. This packing is less dense than the single disc packing as it is harder to pack clustered particles than single discs.

For a given internal angle of friction, the clustered particles produce a steeper angle of repose than the random single disc packing. This indicates that the global slump angle of repose is not only a product of the internal coefficient of friction, but also the particle shape. Global friction is an emergent phenomena of at least these two properties.

$$\frac{dy}{dx} = f(\mu_e, \text{Particle shape})$$

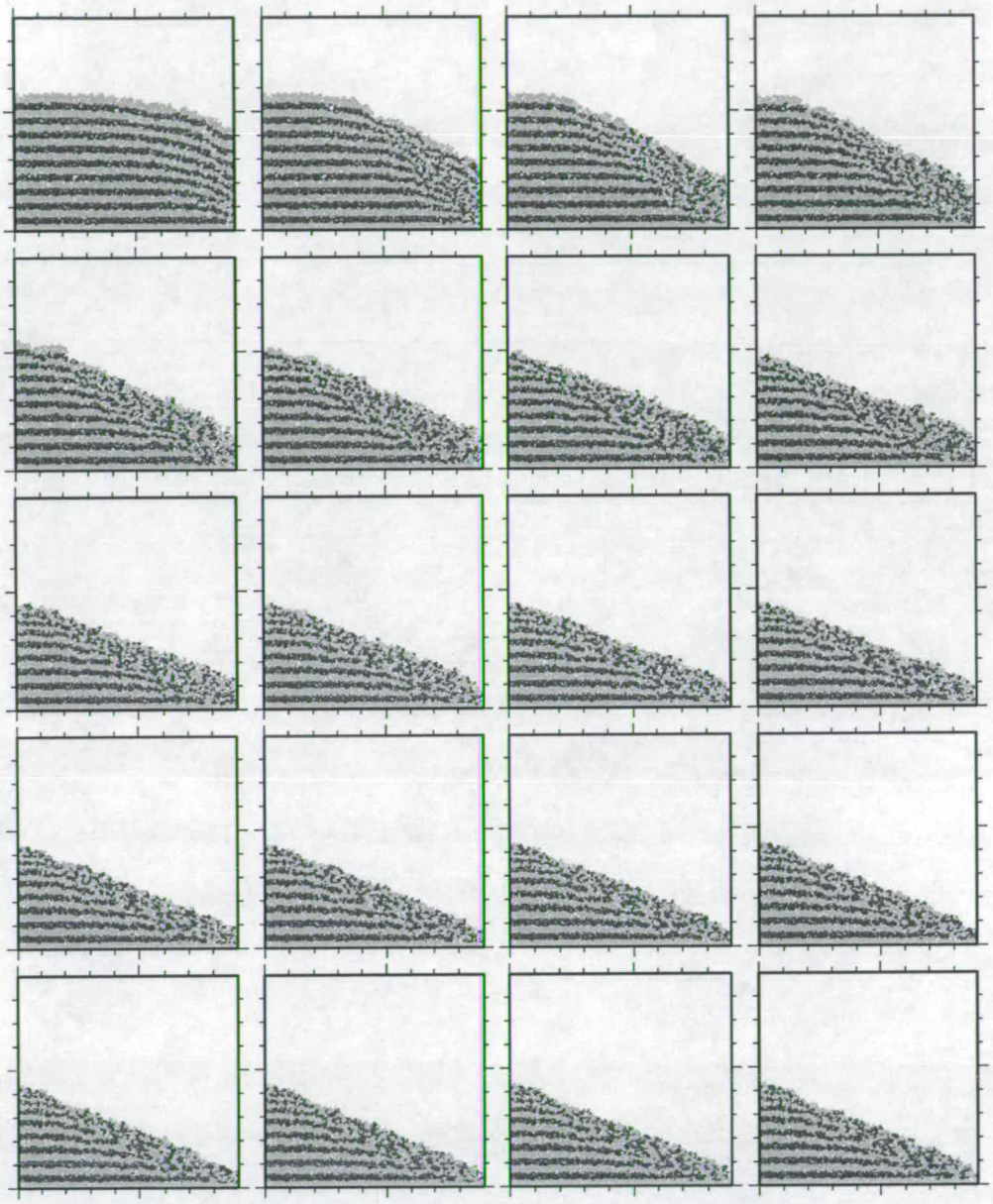

Figure 3.14: Slump angle of repose experiment for the random cluster packing with $\mu_e = 0.3$.

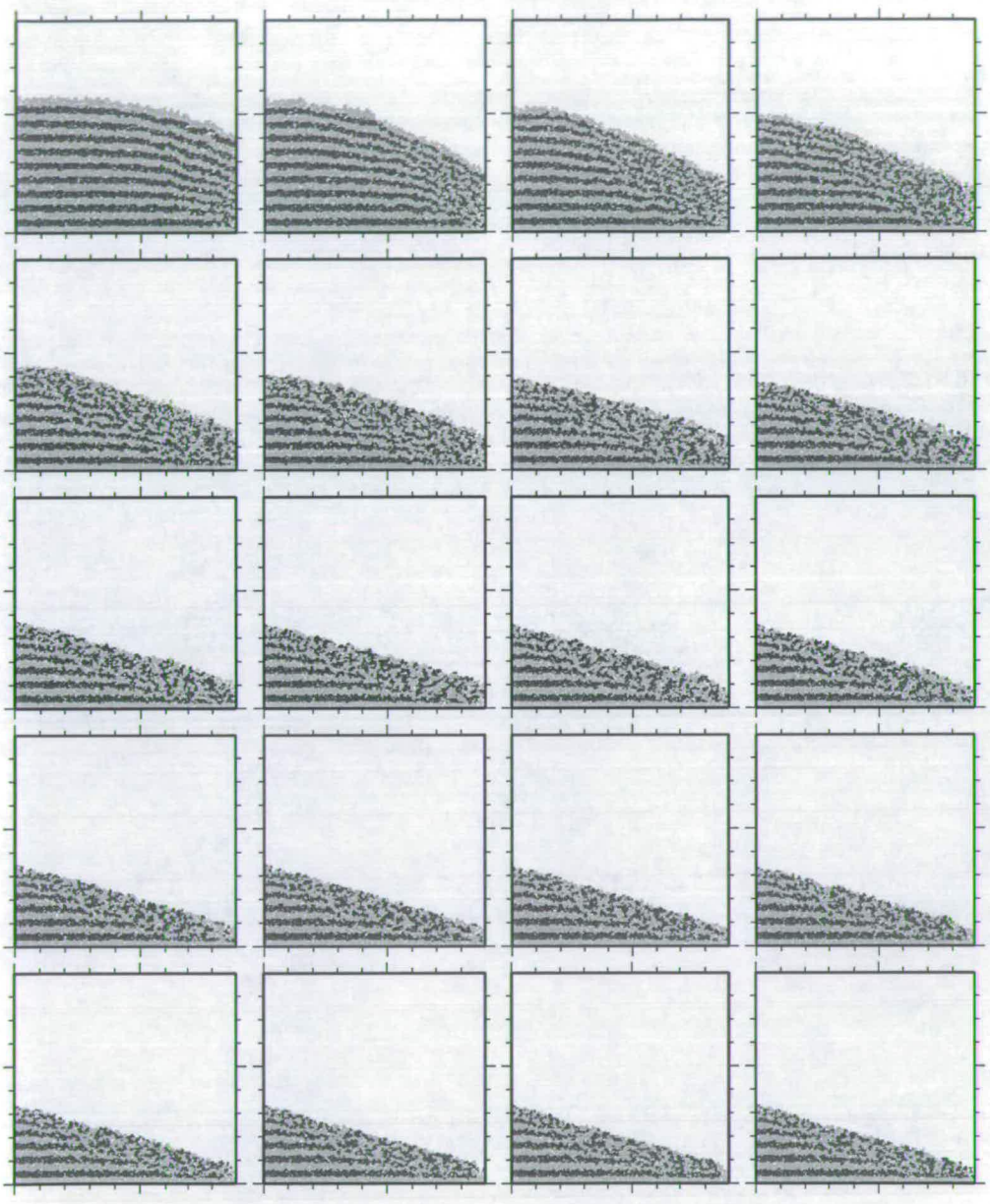

Figure 3.15: Slump angle of repose experiment for the random cluster packing with $\mu_e = 0.1$.

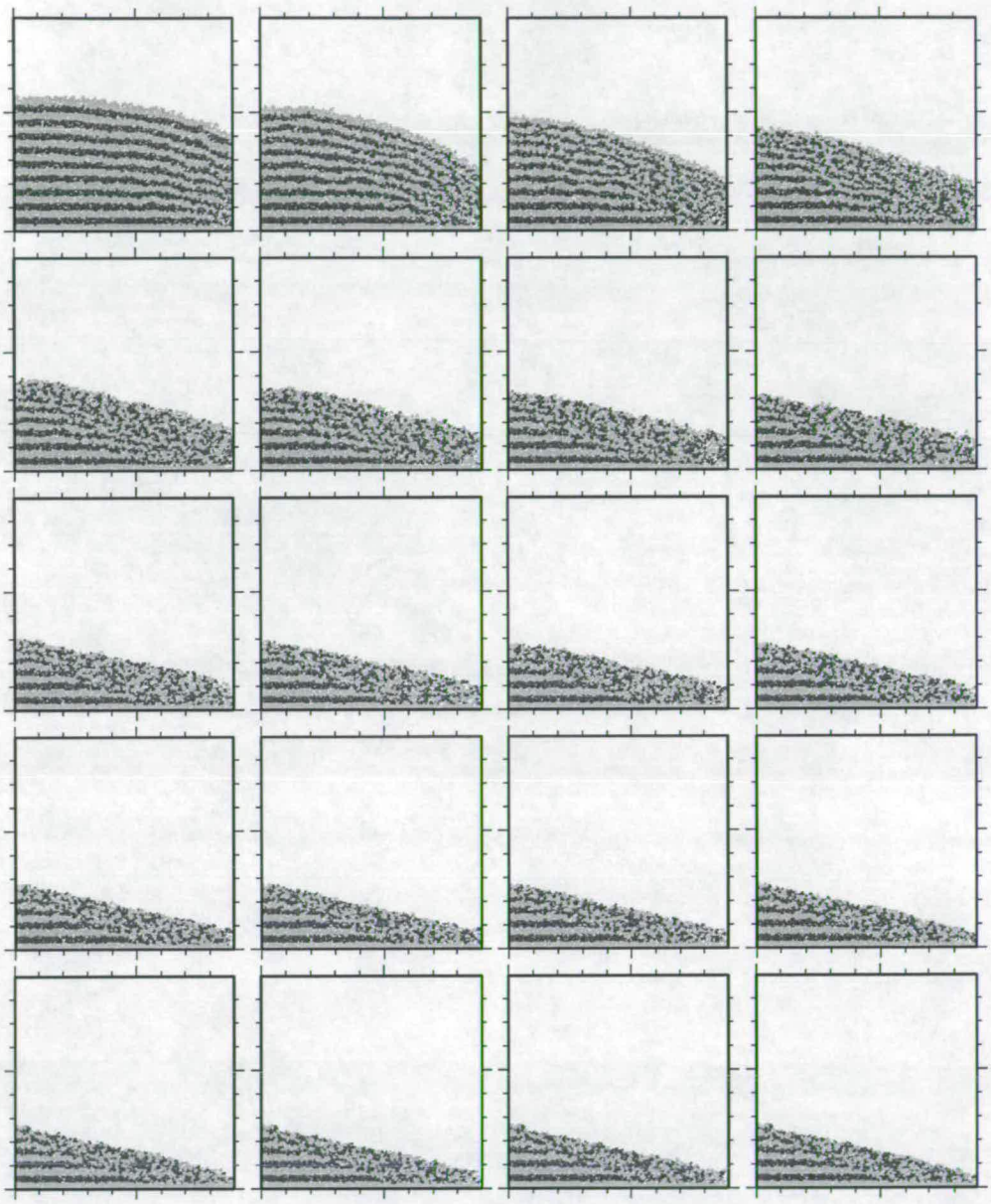

Figure 3.16: Slump angle of repose experiment for the random cluster packing with $\mu_e = 0.03$.

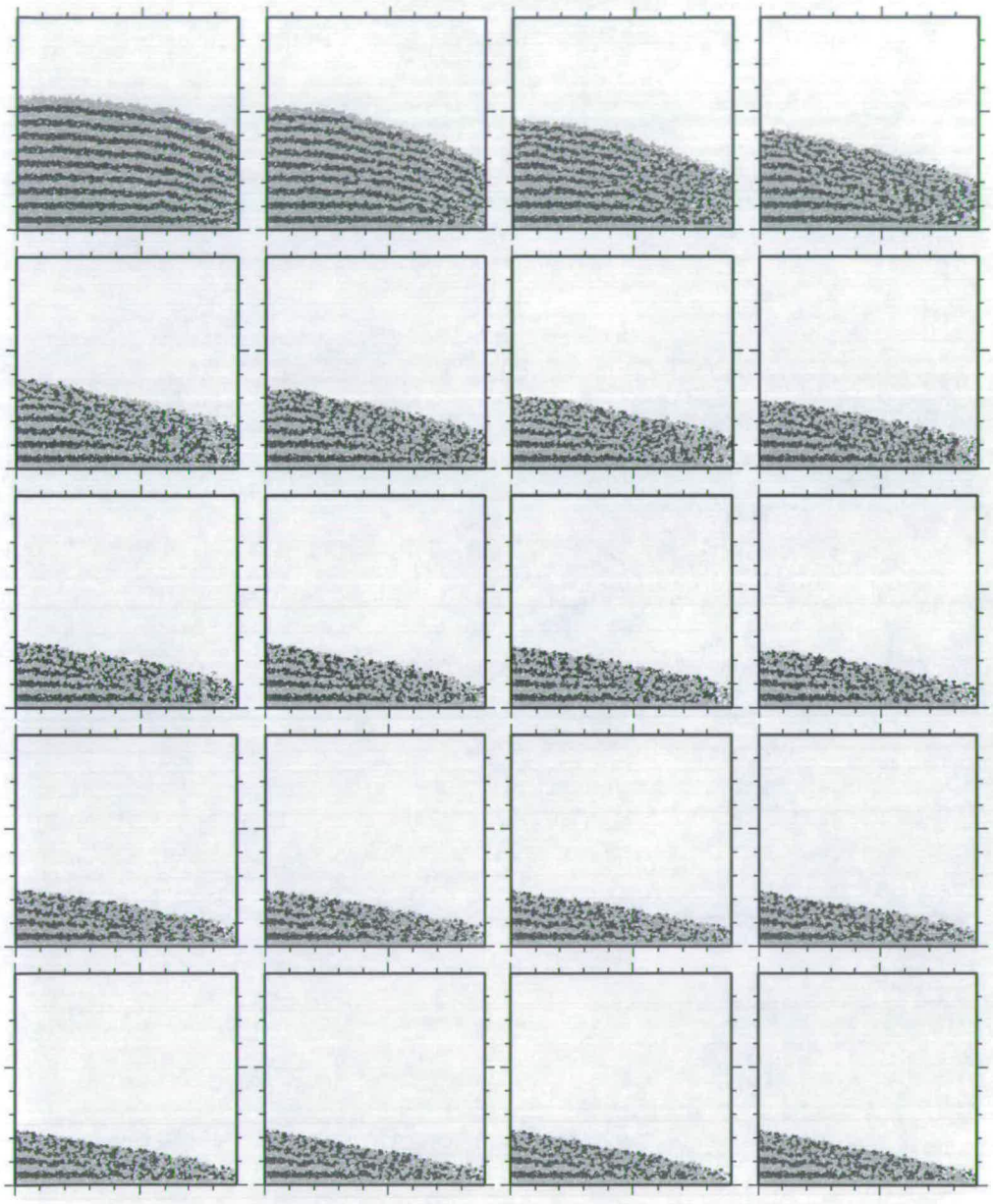

Figure 3.17: Slump angle of repose experiment for the random cluster packing with $\mu_e = 0.01$.

3.2.2 Alternative angle of repose experiment

A second angle of repose experiment is also investigated. This time the lower boundary is Coulomb, and 80% of the right most retaining wall is removed allowing particles to flow out of the system. The remaining part is formed by fixing the position of the particles in contact with the retaining wall (Figure 3.18). Initially, the evolution of the system is similar to that of the angle of repose experiments already presented, with flow confined to an upper boundary layer. The new boundary conditions permit a second process, internal deformation, to lower the taper angle. The whole pack rotates anticlockwise towards the lip of the retaining wall, causing thinning of the horizons towards the interior. The importance of this process increases for weaker internal coefficients of friction. By changing the boundary conditions on the slump angle of repose experiment, we have introduced another deformation mechanism. This highlights the importance of choosing and defining boundary conditions with care.

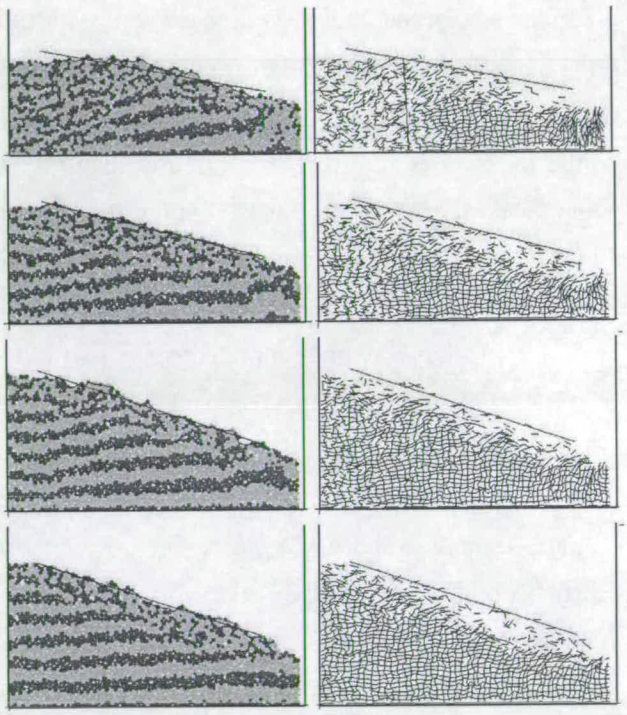

Figure 3.18: Different end members for the alternative angle of repose experiment with $\mu_e = 0.05, 0.1, 0.2, 0.27$. The barrier in this system is a fixed retaining wall at 20% the initial packing height. This system exhibits an extra degree of freedom compared to the experiments previously presented which allows the material to deform internally.

3.2.3 Singly-vergent critical wedge: Random and regular packing

The regular hexagonal packing structure was employed by Burbidge and Braun (2002) in their study of singly-vergent critical wedge evolution (Figure 3.19). They suggested that this is a good packing to choose as the horizontal layering simulates mechanical properties associated with horizontal bedding found in sedimentary rocks. The boundary conditions have been replicated here to test the dependence of their results on the particle geometry and packing structure of the DEM material used. The right hand side wall acts as a rigid indenter and is moved at a constant velocity into the packing, generating the boundary conditions necessary to form a singly-vergent critical wedge. We chose to use a backstop with no frictional component as the analytic and finite element solutions for the problem require a smooth indenter. The lower boundary behaves as a rough Coulomb surface across which the material can stick or slip depending upon the state of stress.

The results for the regular hexagonal packing compare well with those presented by Burbidge and Braun (2002) (Figure 3.20). Initially, deformation is localised on the indenter (right hand boundary). However, it soon propagates away from this boundary generating pop-ups at large distances from the indenter (i.e. at distances greater than the order of magnitude of the feature at the indenter). The relative displacement plots in Animation SVW-Hex (See CD) show how displacement is localised along horizontal planes as two rows side one over the other, the 60^o planes are also often highlighted. This behaviour is not observed if a random packing is used (Figures 3.21 and 3.22), as they are much more consistent with sandbox analogue models and analytic critical wedges than the regular hexagonal packing experiments. The random material localises deformation within a single wedge formed as the indenter ploughs into the packing. The wedge oscillates around some constant taper angle by either accreting at the toe of the wedge or thickening internally. The tip of the wedge accretes units of constant wavelength, which subsequently become rotated as they are incorporated into the wedge, this agrees well with the accretion of new thrust sheets observed in sandbox models.

The prescribed hexagonal geometry contains planes of weakness and long, linear chains of abutting particles (Figure 3.5). It is easy to transmit stress a long way down these chains, which explains the formation of pop-up structures at distance (Animation SVW-Hex). Further, in many of the experiments presented by Burbidge and Braun (2002), deformation became localised on the far (non-indenting) boundary. Again, this is due to horizontal chains finding it easier to transmit the stress from the indenter to the opposite boundary rather than accommodate the shortening internally (Figure 3.19). Once deformation has propagated to the far boundary, the system knows that it is in a confined container and the approximation of an infinite slab breaks down.

The structures within the hexagonal pop-ups have discrete displacements thrusting over the incoming material, which agrees well with observed geological structures. However, in terms

of simulating critical wedges, this does not compensate for the problems with localisation. The random packing experiments generate a periodicity in the deformed horizontal horizons due to the incorporation of constant wavelengths of new thrust sheets. However, the shearing is not as discrete as for the hexagonal case. Regions that have undergone shearing experience dilation and remember the deformation, the weakening associated with dilation provides a mechanism for preferential reactivation. The regular hexagonal packing is the tightest packing structure possible, thus the effects of dilation when using hexagonal packings will be proportionally greater than the random systems.

The random systems introduce more homogeneity to the DEM material, stress is no longer propagated along long linear chains due to the presence of a geometric devioric component within the force network. These systems evolve significantly more independently of the internal packing than with the regular hexagonal packing (Animation 3.1). Experiments have been run for a range of basal and internal coefficients of friction for both the single disc and clustered disc particles, stills of these are presented in Appendix A and animations on the CD (attached at the back of the thesis). The data is presented in two formats, 1. the deformation of initially horizontal horizons and 2. the magnitude of maximum relative neighbour displacement, which highlights localised faulting. The plots coloured by relative displacement shows the asymmetry in thrusting during the development of anticlines, steep back-thrusts and shallower thrusts. Reactivation of structures is often seen, best illustrated in the animations. The surface of single disk experiments is generally smoother as it is easier for the particles to roll and slump to fill troughs in the surface.

Animation 3.2 directly compares the evolution of the high and low basal friction experiments for the single disk particles. A careful examination of the first few time-steps illustrates how the nature of the structure abutting the backstop is dependent upon basal friction. High basal friction restricts early deformation to the locale of the backstop, and material is pushed up the boundary so that virtually the entire backstop is abutting the deepest derived material. In contrast, the early stages of evolution for the weaker base were characterised by the propagation of a thrust cored anticline just off the backstop. This style of evolution persisted through the entire growth of the wedge, preserving roughly uniform depths of each horizon abutting the backstop. The mechanism for this behaviour becomes apparent by studying how often large relative displacement is observed along the lower boundary. This occurs frequently for high basal friction as material is thrust under the wedge in a narrow shear band, as can be clearly seen in the evolution of the vertical shading contrast marker.

The evolution of the wedge angles for all runs is plotted in Figure 3.23(a) for single disc particles and (b) for cluster disc particles. All runs demonstrate the tendency for the wedge angle to tend to some constant value dependent on internal and basal friction parameters. The Black lines are for $\mu_e = 0.3$ and the grey for $\mu_e = 0.2$. For both packings, lower μ_b produces

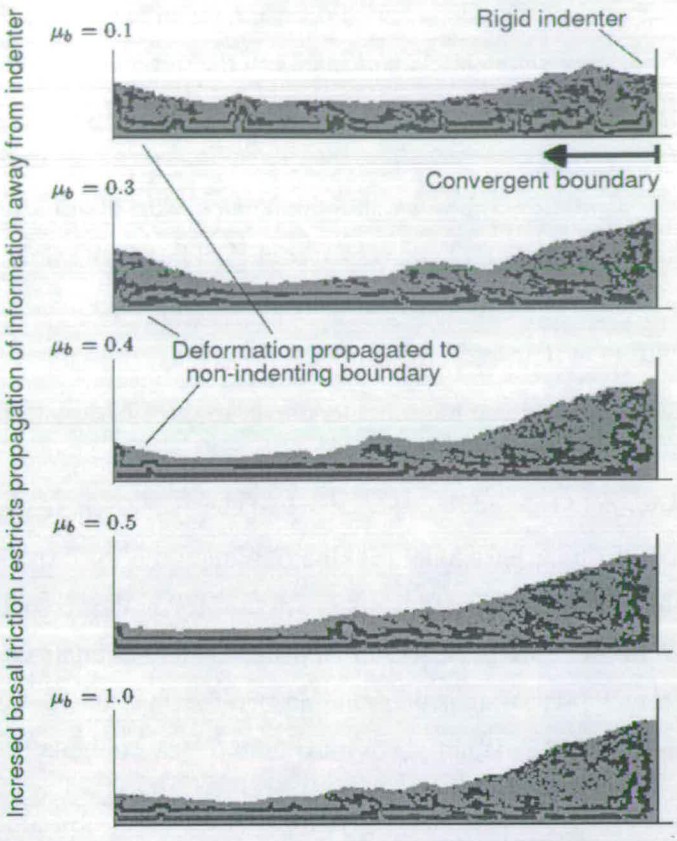

Figure 3.19: Results presented by Burbidge and Braun (2002) with constant internal coefficient of friction ($\mu_e = 0.2$) but varying the basal friction for the same amount of shortening. Note that if deformation propagates to the far boundary, the infinite slab approximation breaks down.

shallower taper. For a given basal friction, higher internal friction generates a shallower taper wedge, in agreement with critical wedge theory. Cluster disk particles produce slightly shallower taper angles than the single disk particles for the same parametrisation, again reflecting that cluster disk particles generate a stronger emergent bulk friction than single disks.

The main difference between the single disc and clustered disc particle wedges becomes apparent by comparing the profiles with those of sandbox experiments (Figure 3.24). Many sandbox analogues (Koyi, 1995; Lohrmann et al., 2003) have an internal-accumulation zone (IAZ) abutting the backstop, which is flatter than the wedge taper angle and relatively inactive. A similar zone only forms in the experiments with the clustered disc particles. The single disc particle experiments have a uniform taper along the whole of the wedge. Importantly, an analogous feature is observed in real accretionary wedges, such as the Sunda margin (Figure 3.25) where Kopp and Kukowski (2003) identified a relatively inactive fossil accretionary prism. This figure highlights conjugate pairs of fore- and backthusts, which compare well in form with those highlighted in the maximum relative displacement plots.

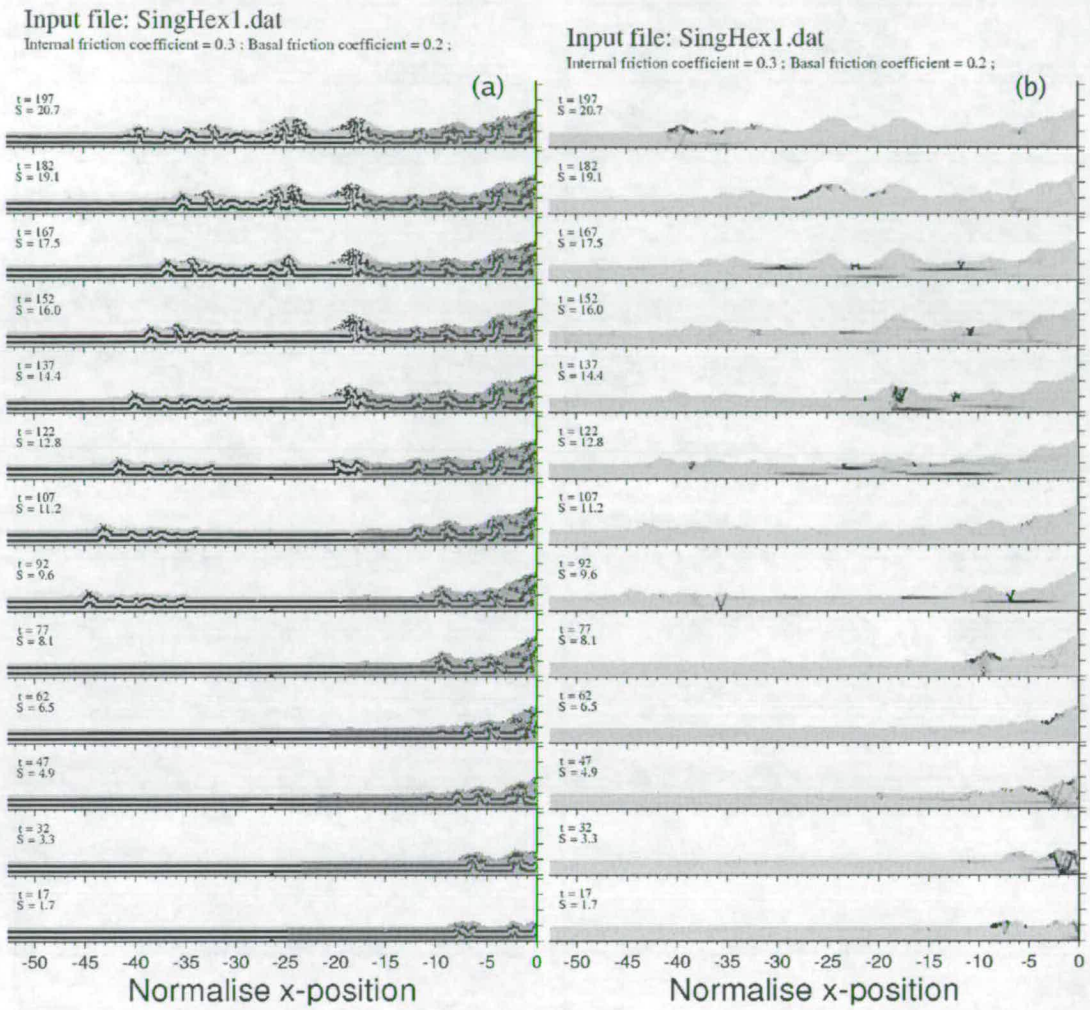

Figure 3.20: Singly-vergent wedge evolution using a regular hexagonal packing (a) shows deformation of horizons and (b) the localisation of relative displacement. The y-axis is parallel to gravity and time increases from bottom to top. Linear chains of particles parallel to the base and at 60^o angles provide an efficient mechanism to transmit strain. Wedges on the same order of magnitude as the principle wedge (that at the backstop) form at distances greater than the wedge width away from the backstop.

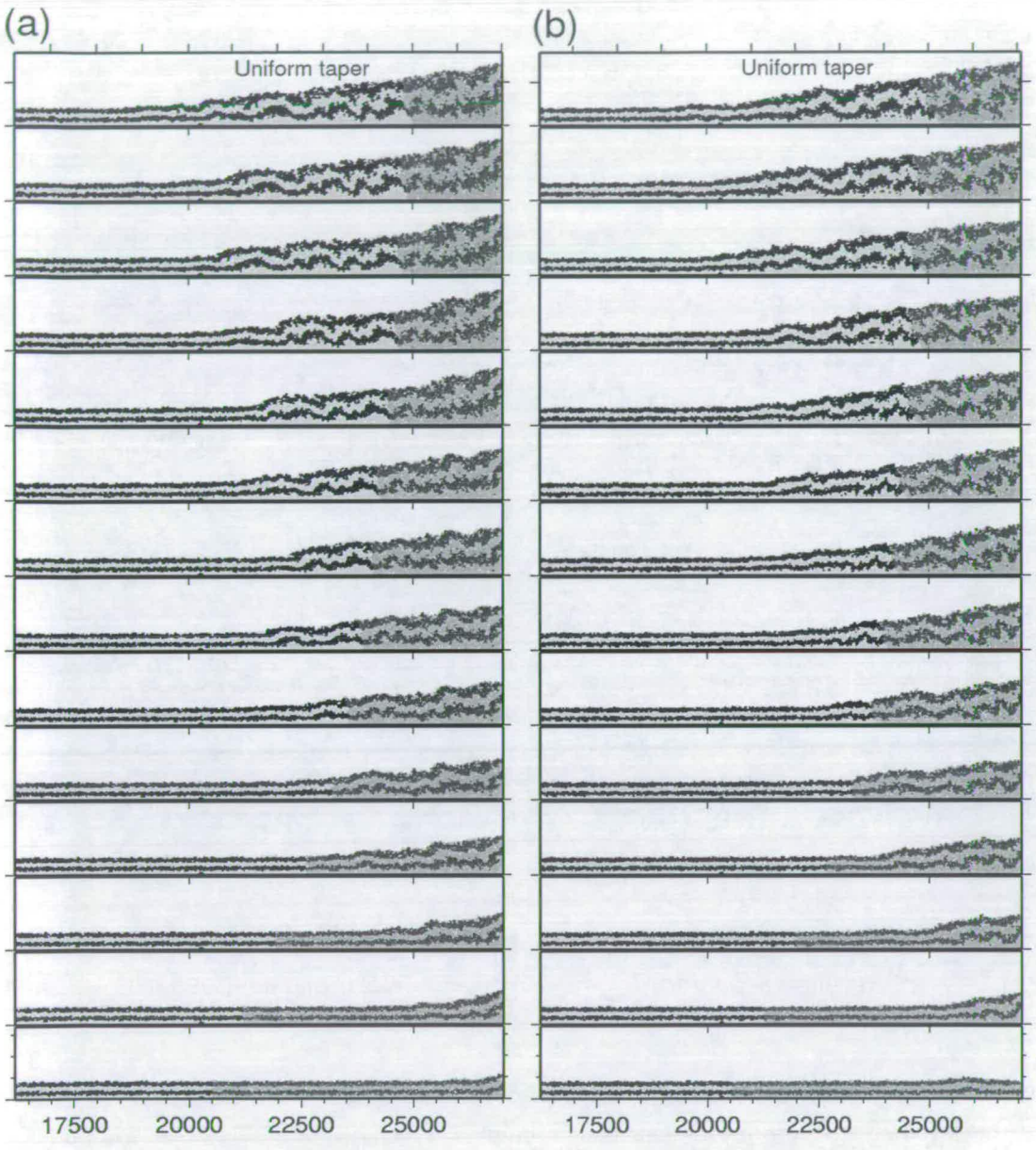

Figure 3.21: Two examples of singly-vergent wedge evolution using a random single disc packing. Deformation is localised to the principle wedge that abuts the backstop which has a uniform and constant taper angle. (a) and (b) are results using the same boundary conditions but different randomly seeded packings.

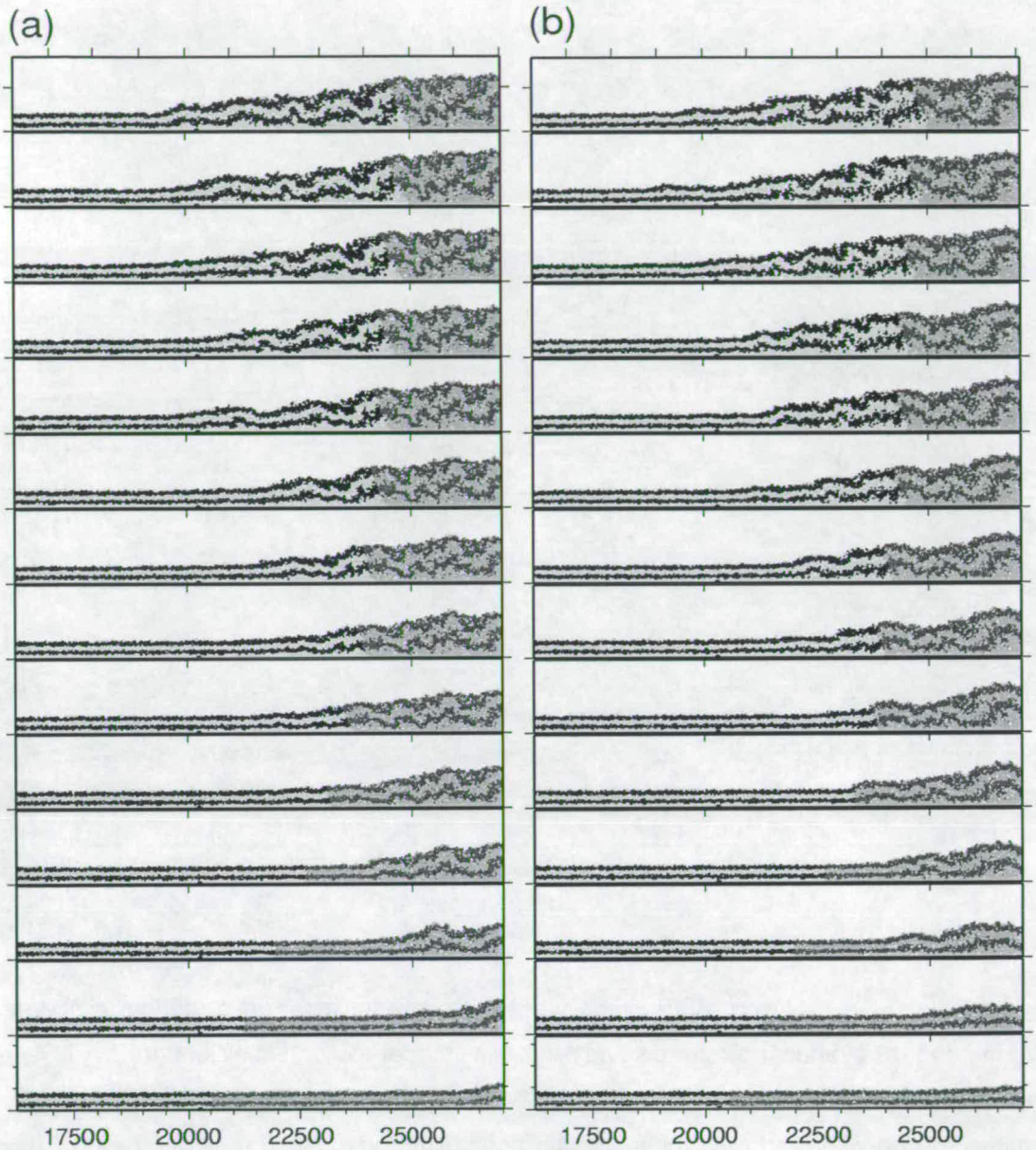

Figure 3.22: Two examples of singly-vergent wedge evolution using a random 3 disc cluster packing. Deformation is localised to the principle wedge abutting the backstop. The wedge appears to consist of two different tapered sections, steeper at the front and shallower at the backstop. (a) and (b) are results using the same boundary conditions but different randomly seeded packings.

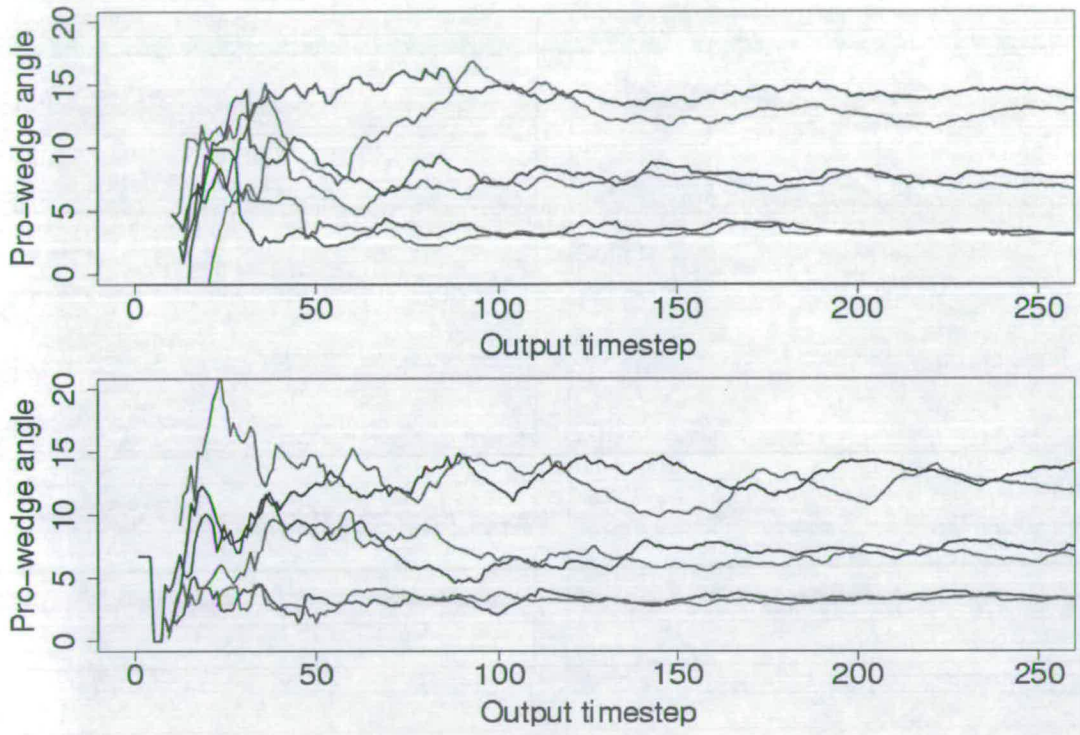

Figure 3.23: Time evolution of the singly-vergent wedge angle for (a) a random single disk packing and (b) a random cluster disk packing. An internal friction coefficient of $\mu_e = 0.3$ was applied for the black lines and $\mu_e = 0.2$ for the grey lines. The angle of friction is most sensitive to basal friction with the lowest basal friction generating the shallowest tapered pairs. From bottom to top, basal friction (μ_b) was given the values $0.1, 0.2$ and 0.3.

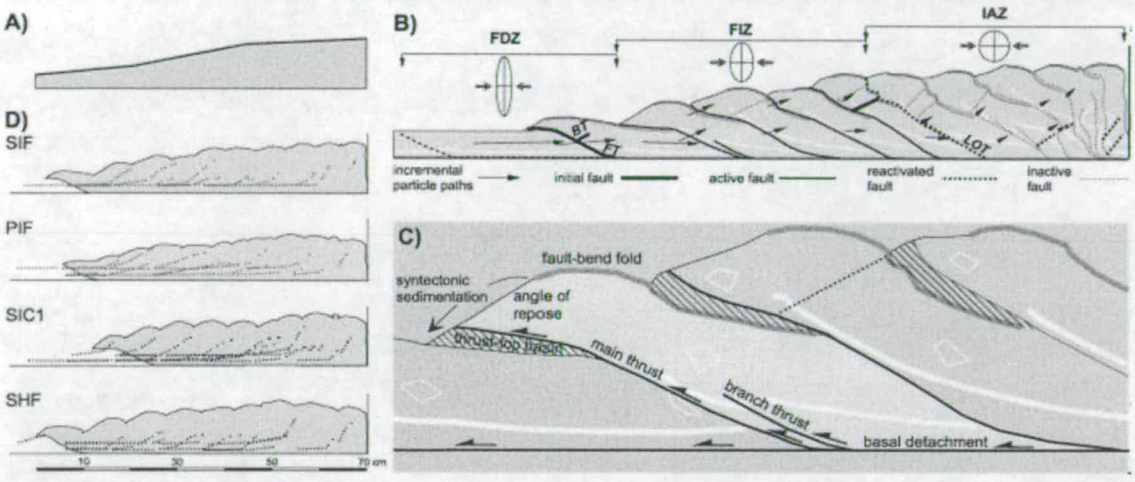

Figure 3.24: *Common features of the convergent sand wedges consisting of different sands. (A) The overall wedge geometry is characterised by three domains with different surface slopes. (B) The kinematic segments (FDZ frontal-deformation zone; FIZ frontal-imbrication zone; IAZ internal-accumulation zone) show typical internal kinematics, horizontal shortening rates and incremental particle paths (FT forethrust; BT backthrust; LOT leading out-of sequence thrust). (C) Internal kinematics of an individual thrust slice with formation of a subsequently overthrust 'thrust-top-basin'. (D) Total displacement fields in the sand wedges do not show any substantial difference.* (Figure and Caption taken from Lohrmann et al., 2003)

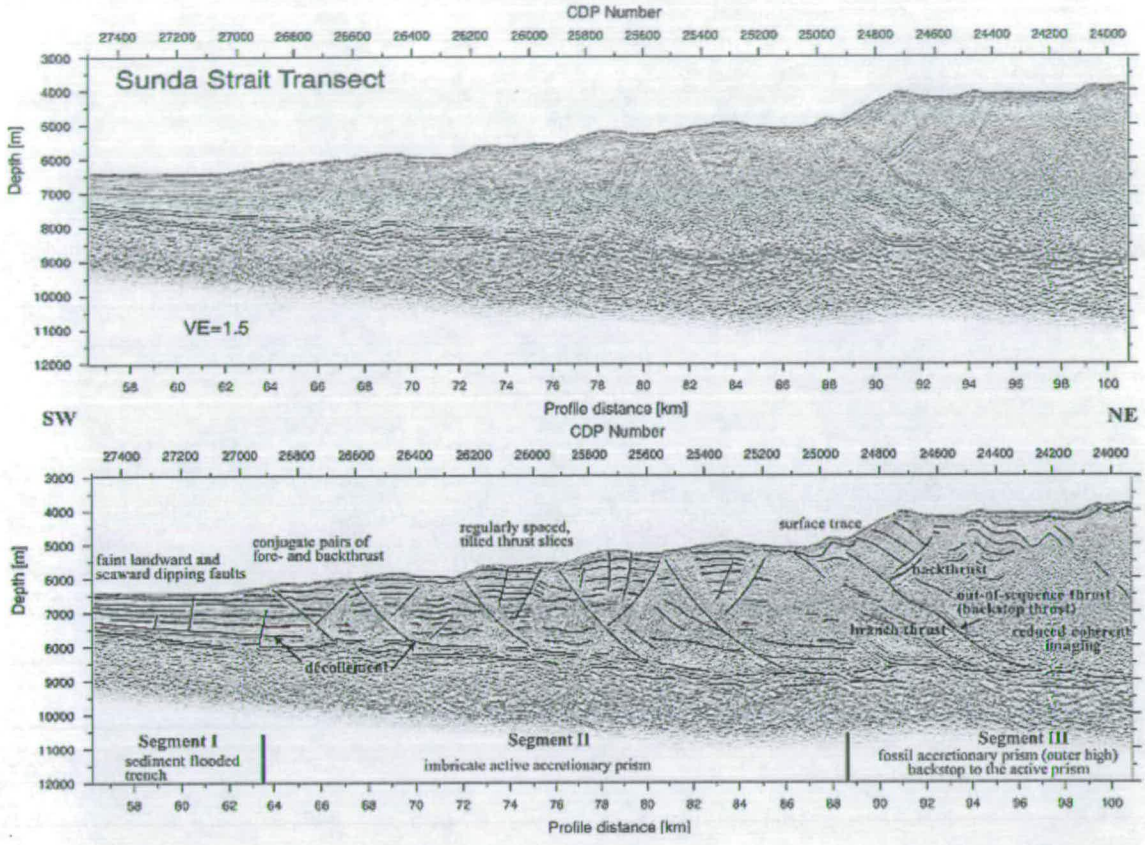

Figure 3.25: Prestack depth-migrated section of the multichannel profile off the Sunda Strait. An arcward increase in material strength results in a segmentation of the margin. Faint seaward and landward dipping faults cut the trench fill in the proto-thrust zone of Segment I, indicating the first stages of faulting. The deformation front marks the onset of faulting in conjugate pairs of forethrusts and backthrusts. The frontal active accretionary prism (Segment II) is composed of tilted thrust slices separated by regularly spaced thrust faults. The transition to the fossil accretionary prism of the outer high is marked by a prominent out-of-sequence thrust. Segment III forms the backstop to the frontally accreted material and displays much reduced tectonic activity mainly manifested in the occasional reactivation of previous thrusts which helps adjust the taper. (Taken from Kopp and Kukowski (2003))

3.2.4 Discussion

The DEM outlined in Chapter 2 is good at simulating granular materials as many of the important phenomena associated with many body problems are emergent from the model. It has been shown that singly-vergent wedges can be modelled using the DEM approach. The next chapter extends the modelling to doubly-vergent wedges by investigation of appropriate boundary conditions.

The results of experiments performed using the hexagonal packing demonstrate a strong coupling with the packing structure for both the angle of repose and critical wedge experiments. Burbidge and Braun (2002) chose this packing because strain weakening effects via dilatancy are most significant and suggested that the closely spaced horizontal layers are analogous to the layered structures of many sedimentary settings. However, the results of the singly-vergent critical wedge experiments do not compare favourably with real accretionary prisms or orogens as the simulations localise features at distances greater than the order of magnitude of the width of the wedge at the indenter.

The use of a random packing structure immediately produces results more comparable with sandbox analogues, FEM simulations and reality. The system we wish to investigate is one where the system evolves in response to changes in the mechanical stress distribution. Single disc particles smooth out the upper surface as they roll more freely. In most cases, this behaviour is probably undesirable as it is uncontrollable and reflects a property specific to non-angular grains. The clustered disc particles produce wedge geometries most consistent with observed analogue and real wedges as they generate a fossil accretionary prism.

The doubly-vergent wedge DEM models will be compared to doubly-vergent sandbox analogue models in the next chapter, so clustered particles, which best reproduce the sandbox results, are the most appropriate in these simulations.

Chapter 4

Doubly-vergent boundary conditions

This chapter has largely been revised from my first paper (Naylor *et al.*, in press). This paper justifies appropriate boundary conditions by comparing and contrasting DEM results with previous doubly-vergent analogue and computational modelling. An investigation of two different lower boundary conditions is presented, which generate different styles of internal deformation, and compare well with the differences observed between the various sand box analogues. This comparison is used to expand our understanding of the analogue modelling and justify the boundary conditions to be used in the rest of this thesis. Animations of the results presented in this chapter are contained on the CD.

4.1 Development of lower boundary conditions

Two examples of real doubly-vergent collisional systems are illustrated in Figures 4.1 A and B. The cartoon suggests that the wedges are fed by a constant flux of material from the pro-side. In the doubly-vergent wedge, the velocity discontinuity is introduced at some point along the base rather than at one of the boundaries, as was the case for the singly-vergent experiments. Sandbox experiments generate traction along the lower boundary by drawing a sheet (e.g. mylar sheet or sandpaper) along the bottom of the box and removing it from the base through a slot in the base, or through some variation on this experimental arrangement (Wang and Davis, 1996; Storti et al., 2000; Persson, 2001). The velocity discontinuity drives the formation of a doubly-vergent wedge. Willett et al. (1993) developed an FEM based on a two-dimensional plane strain deformation of a laterally uniform rigid-plastic layer to investigate doubly-vergent wedges (Figure 4.1 C). The S-point marks the velocity discontinuity and the lower boundary condition is applied to material touching the lower boundary. The imposed velocity regime is such that material to the left of the S-point is advected towards the boundary at some constant velocity, material to the right of the boundary is stationary with respect to the S-point. For plastic materials obeying a Coulomb yield criterion, Levy-Mises plastic theory leads to a strain-

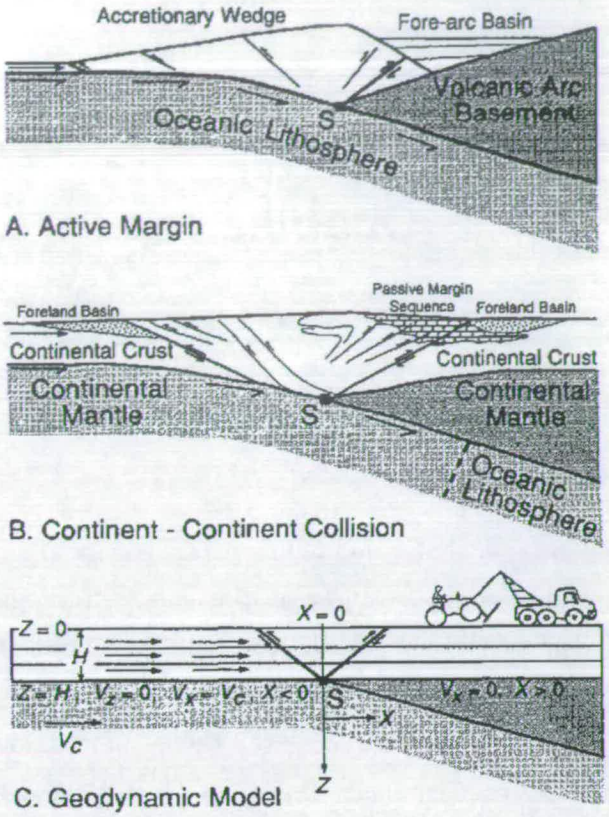

Figure 4.1: Illustration of active margin (A) and continent-continent collision (B). Crustal deformation is focused above S-point, where mantle left of plate detaches and is underthrust. (C) shows typical FEM geodynamic model boundary conditions, in which uniform crust, extending from surface depth H, is deformed under basal velocity boundary conditions. Underlying domain (grey regions) is not modelled. (Taken from Willett et al. (1993))

rate dependent definition of the viscosity (Willett, 1999). The strength of the basal surface is thus defined by specifying a low viscosity in the lowermost cells.

4.2 DEM reduced list trick

During these experiments, deformation is localised in the vicinity of the S-point, however, the amount of convergence imposed in the model requires a supply of a long undeformed slab. A reduced list has been applied so that only particles in the deforming region (near the S-point) are considered in the force comparison list, whilst particles in the undeformed slab are forced to move towards the deforming region at some constant convergence rate, v_x (Figure 4.2). Linking these regions is a narrow zone (the width of a couple of particles) where particles can apply forces of particles within the deforming zone but are themselves forced at constant velocity. The style of particle behaviour is dictated purely by which zone it lies in at that particular time,

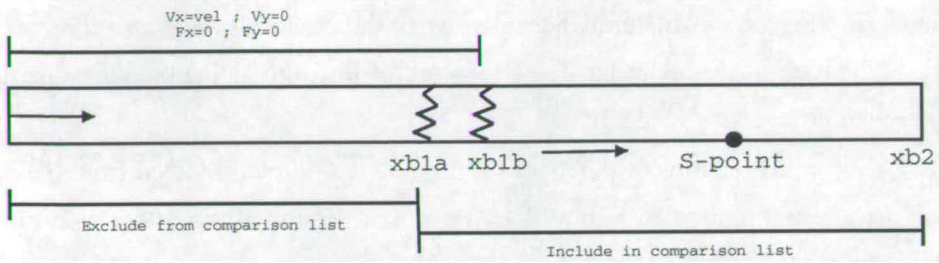

Figure 4.2: Reduced list geometry for doubly-vergent wedge problem. Only particles in the vicinity of the wedge are evaluated. Those not near the wedge are moved towards the wedge at the constant convergence rate, v_x. A transition zone, in the range x_{b1a} to x_{b1b}, where particles exert forces but don't react to them, is used to ensure stability.

and slows down as more particles enter the deforming region. It is important to ensure that the evaluation window is far enough away from the deformation front that its presence does not affect the model output. In order to simplify the introduction of new particles, the disc array reference is sorted by x-position so that it is easy to decide when a particle has transferred to a different zone without searching the entire list. The model runtime is now controlled by the number of particles required to simulate the deforming region rather than the total number used.

4.3 Constant velocity lower boundary condition

The desired model configuration where the pro-side and retro-side basal friction, μ_{bp} and μ_{br} respectively, are definable is illustrated in Figure 4.3(a). As a first pass at generating doubly-vergent boundary conditions, we imposed a constant velocity upon all particles in contact with the lower boundary to one side of the S-point. As a result of this, these particles cannot slip on the base beneath as their velocities are constant and failure only occurs in the material above with an emergent friction value, μ_{bc} that is a function of particle shape, the degrees of freedom of the particles involved and the inter-particle friction coefficient, thus basal friction cannot be defined and must be used as a reference. In order to investigate the response of a wedge to variations in pro-side basal friction, μ_{bp} we need to be able to define it. To achieve this we applied a constant velocity condition to the retro-side and moved the S-point with the same constant velocity and used a rough, rigid base on the pro-side during the model run (Figure 4.3(b)). In post processing, the convergence velocity is subtracted to regain a frame of reference in which the S-point is stationary, shown in Figure 4.3(c). This process is purely

a change in the frame of reference to simplify the coding and does not change the physics of the problem. The emergent basal friction on the constant velocity boundary is higher than the emergent friction of the material because it has the same physical parametrisation and angularity as the bulk material but has fewer degrees of freedom as the boundary particles are not free to rotate or translate vertically.

Some of the typical features of the mature experimental output obtained from these boundary conditions are highlighted in Figure 4.4. Two main wedges form either side of an axial zone. The retro-wedge is steep and is formed by the flux of material through the wedge and the slumping of material down the surface at some angle of repose, β whilst the pro-wedge has a shallower taper, α reflecting its accretionary growth mechanism. A strong retro-vergent thrust is rooted at the singularity (grey line) and tends to the retro-side surface at the tip of the retro-wedge. This retro-vergent thrust effectively decouples the pro- and retro-sides and pins retro-side material at the S-point. Pop-up structures can sometimes be seen to develop beyond the tip of the pro-wedge before being incorporated.

4.3.1 Experiment 1 - Variation in pro-side basal friction, μ_{bp}

Keeping the internal angle of friction constant and relatively high, we varied the pro-side basal coefficient of friction, μ_{bp} relative to the retro-side. The asymmetry in the basal friction is reflected in the asymmetry of the resulting gross morphology and strain history (Figure 4.5; Animation 4.1). Lower values of basal friction cause the pro-side deformation front to propagate out quicker, further into the undeformed pro-side slab. Higher values made the pro-wedge narrower, and made the gross form more symmetric about a vertical plane approximately above the S-point. To sustain this symmetry for successive accretion on the pro-side, motion is required on the retro-verging thrust. Thus the evolution of the retro-wedge is dependent on the basal friction on the pro-side.

The rate of growth of a wedge decreases with convergence, and thus time assuming a constant convergence rate, (Figure 4.6(a)) due to a constant flux of material being added to an ever larger wedge. Higher basal frictions produce steeper-sided wedges, thus to accommodate the same total convergence the wedge must be higher. The lateral deviation of the highest peak (x(Highest peak) $-$ x(S-point)), fluctuates rapidly around the S-point. (Figure 4.6(b)), but a general trend of advection of the highest peak towards the retro-side is also observed; a similar result is seen in FEM experiments. It appears that lower basal angles of friction produce less deviation of the highest point from the S-point.

Initially, for all model runs the angle of all the pro-wedges, α follow the same trend, increasing linearly to a similar value for a normalised convergence of $S \approx 3$ (Figure 4.7(a)). This is *Stage 1* growth where the material fails internally rather than on the weaker base, and is thus independent of basal friction. After this initial peak, the angles diverge to some value

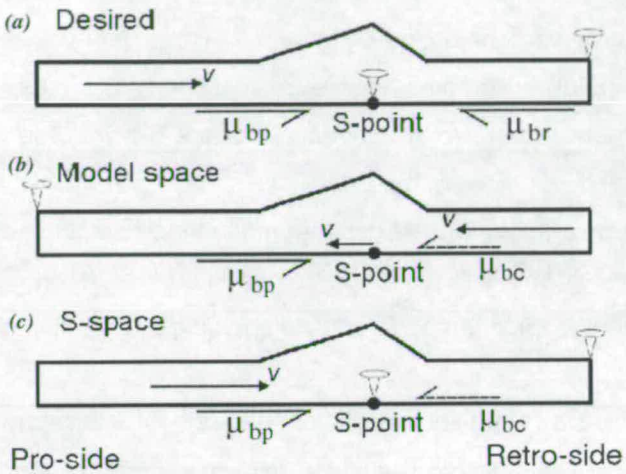

Figure 4.3: Constant velocity boundary constant arrangement which compares with the results of the Malavieille (1984) and Storti et al. (2000) sand box experiments. Pins indicate part of the system that are stationary in each sub-figures frame of reference, v the direction of convergence in each frame and basal friction, μ_b is indicated by half arrows. If the material fails on the base the arrow is below the base; if it fails within the material it is drawn as a dashed line above the base. The desired configuration (a) where both pro-side, μ_{bp} and retro-side, μ_{br} basal friction are parametrised cannot be generated directly as the constant velocity boundary condition does not allow slip on the base, one of the bases must fail within the material with at friction coefficient that is a function of particle shape and particle friction, μ_{bc}. To approximate this ideal we applied a Coulomb failure criteria to the pro-side and a constant velocity condition to the retro-side (b). As the retro-side must be stationary with respect to the S-point, we move the S-point with the same velocity in Model Space. (c) To return to the frame of reference where the S-point is stationary, we subtract this velocity from the results so that the pro-side converges towards the stationary S-point. This post-processing change in frame is purely to aid comparison and does not alter the results.

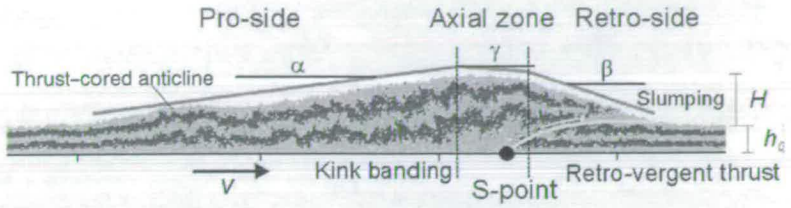

Figure 4.4: Typical doubly-vergent wedge DEM output for constant velocity boundary condition arrangement (Figure 4.3(c)), with some key features labelled. The basal velocity discontinuity (the change in convergence from v to 0) is introduced at the S-point. The angles of the pro- and retro wedges are α and β respectively, the axial zone is the region over which the taper changes from α to β. h_0 is the mean undeformed depth of material to be accreted to the wedge and H is the height of the wedge above the mean undeformed surface. Kink banding, as defined by Malavieille (1984), refers to the internal deformation, folding and faulting of the initial horizons.

dependent upon the pro-side basal friction (*Stage 2*), with lower basal friction producing shallower tapers. The retro-wedge angle, β tends to the same angle for all investigated values of pro-side basal friction. The retro-wedge angle is steeper than the angle of the pro-wedge as it is not formed by an accretionary mechanism. The material in the wedge is fluxed through to the retro-side and the angle of the retro-wedge is limited by some angle of repose of the system. Evidence for this is the presence of slumped material at the base of the retro-wedge. It is important to note that retro-wedge accretion, and hence the development of *Stage 3*, is not achieved in these experiments.

Figures 4.5(c) and (d) show the maximum displacement of neighbouring particles. The initial block uplift bound by two shear zones is evident at $S = 1.3$ for both series. Lower basal frictions produced more discrete structures. This is especially evident when you compare the pro-sides that have undergone greater convergence. The retro-vergent thrust is resolved in both experiments, but again it is clearer in the case of low basal friction. The slumped material on the retro-side is also highlighted, indicating that this process is on the same order of magnitude as the motion along structures.

4.3.2 Experiment 2 - Variation in the internal coefficient of friction, μ_e

Experiment 1 was repeated for the case with a low basal friction ($\mu_{bp} = 0.2$), this time reducing the internal friction of the DEM material (Figure 4.8). A comparison of the evolution of the system is presented in the graphs of Figure 4.9 and Animation 4.2. The pro- and retro-wedge angles are both shallower with the weaker material; thus for the same amount of total convergence, the height of the wedge is less. Also, for the same basal friction and relative shortening, the deformation has propagated further to the pro-side. The increased proportion of slumping

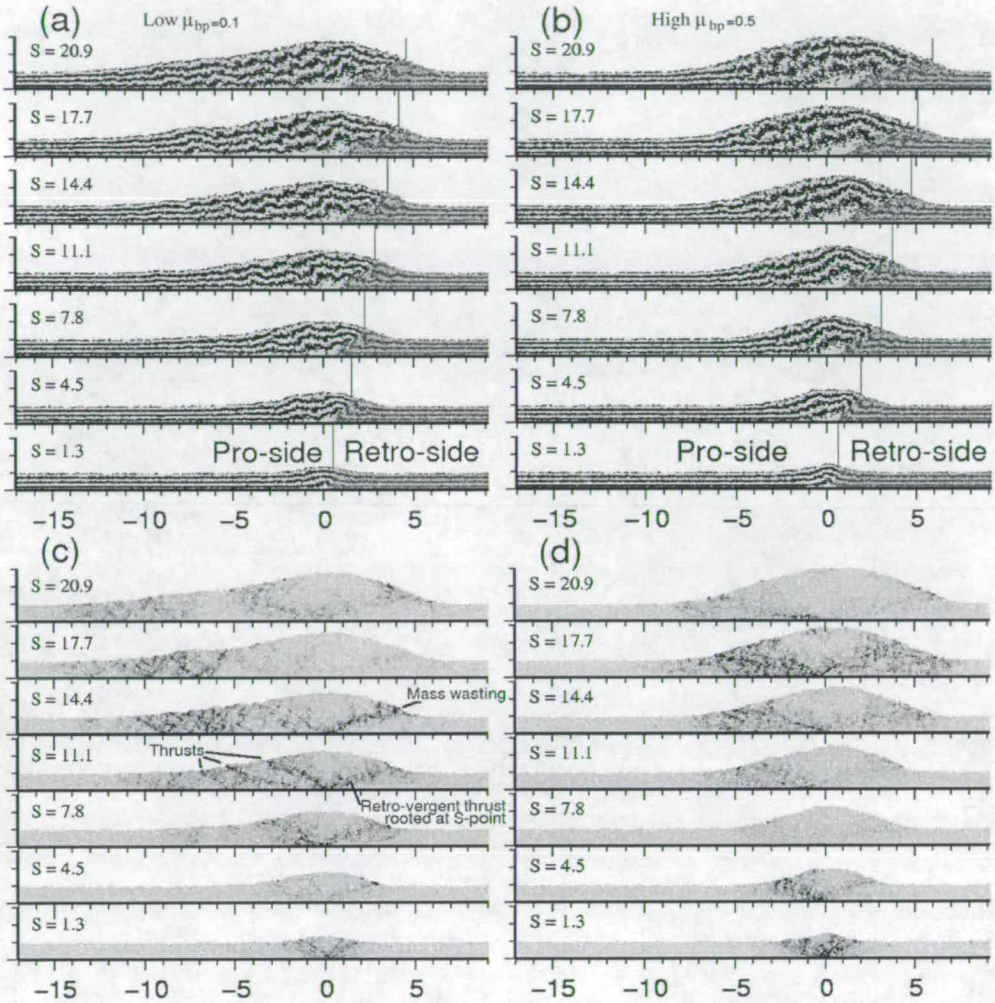

Figure 4.5: Doubly vergent wedge simulation results generated using the constant velocity boundary condition. (a) and (b) compare the deformation of initially horizontal horizons. The higher basal friction ($\mu_{bp} = 0.5$) supports a steeper pro-side wedge. The darker shaded retro-side material is pinned at the S-point. Figs (c),(d) show the maximum relative displacement of adjacent particles, scaled to the maximum value over each interval, for the constant velocity experimental boundary condition. The lower basal friction ($\mu_{bp} = 0.1$) allows the deformation to propagate further into the pro-side. A strongly localised retro-vergent structure is localised, also pinned at the S-point.

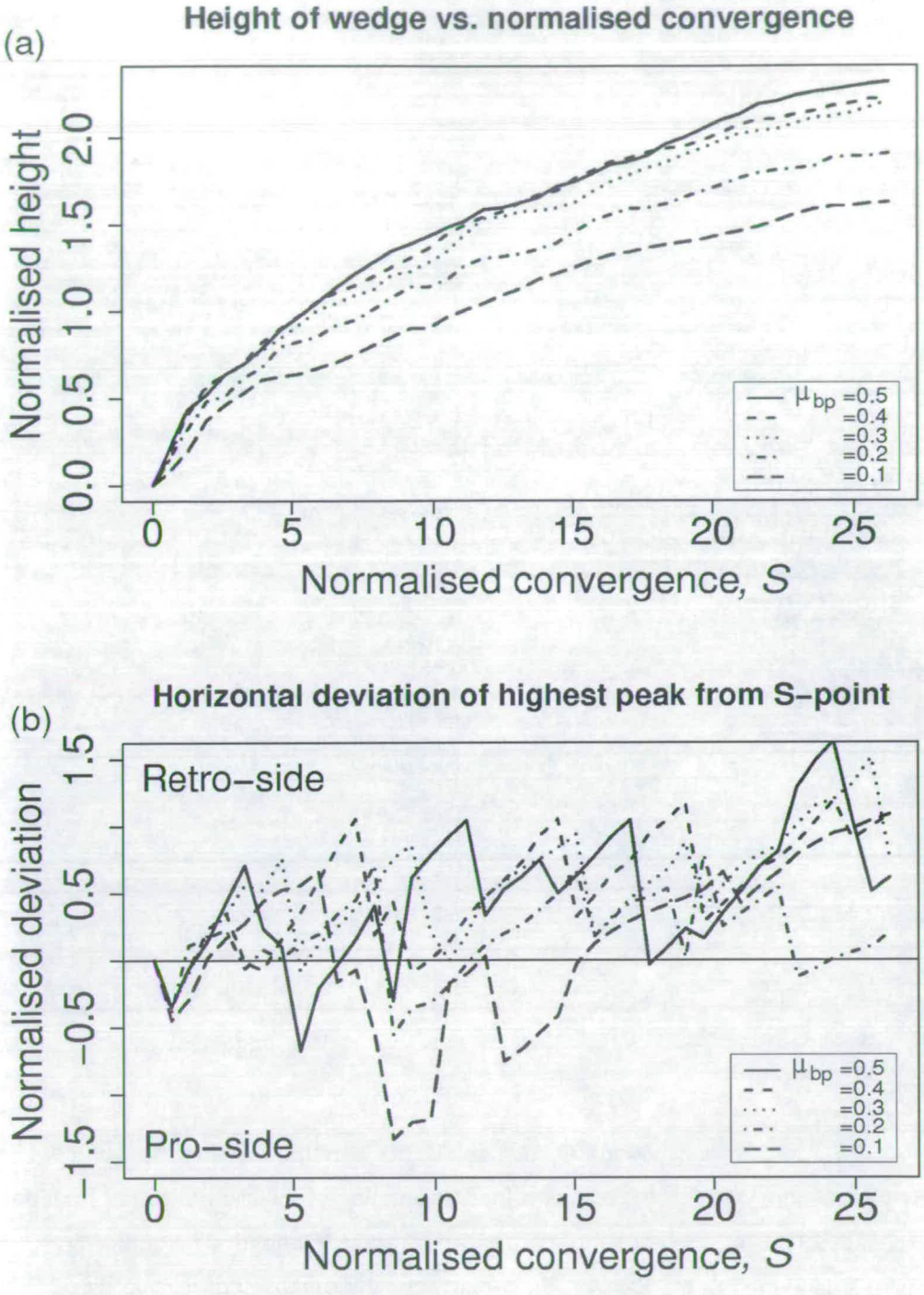

Figure 4.6: Maximum height (a) and deviation of highest point from S-point (b) versus normalised convergence, S per unit model depth for Experiment 1 with a range of pro-side basal friction values, $\mu_{bp} = 0.1 - 0.5$. All length scales are normalise by the mean thickness of accreted material. The height of the wedges increases approximately with $S^{\frac{1}{2}}$, in a relatively smooth curve. The position of the highest peak oscillates rapidly around some point near the S-point, and advects slowly to the retro-side.

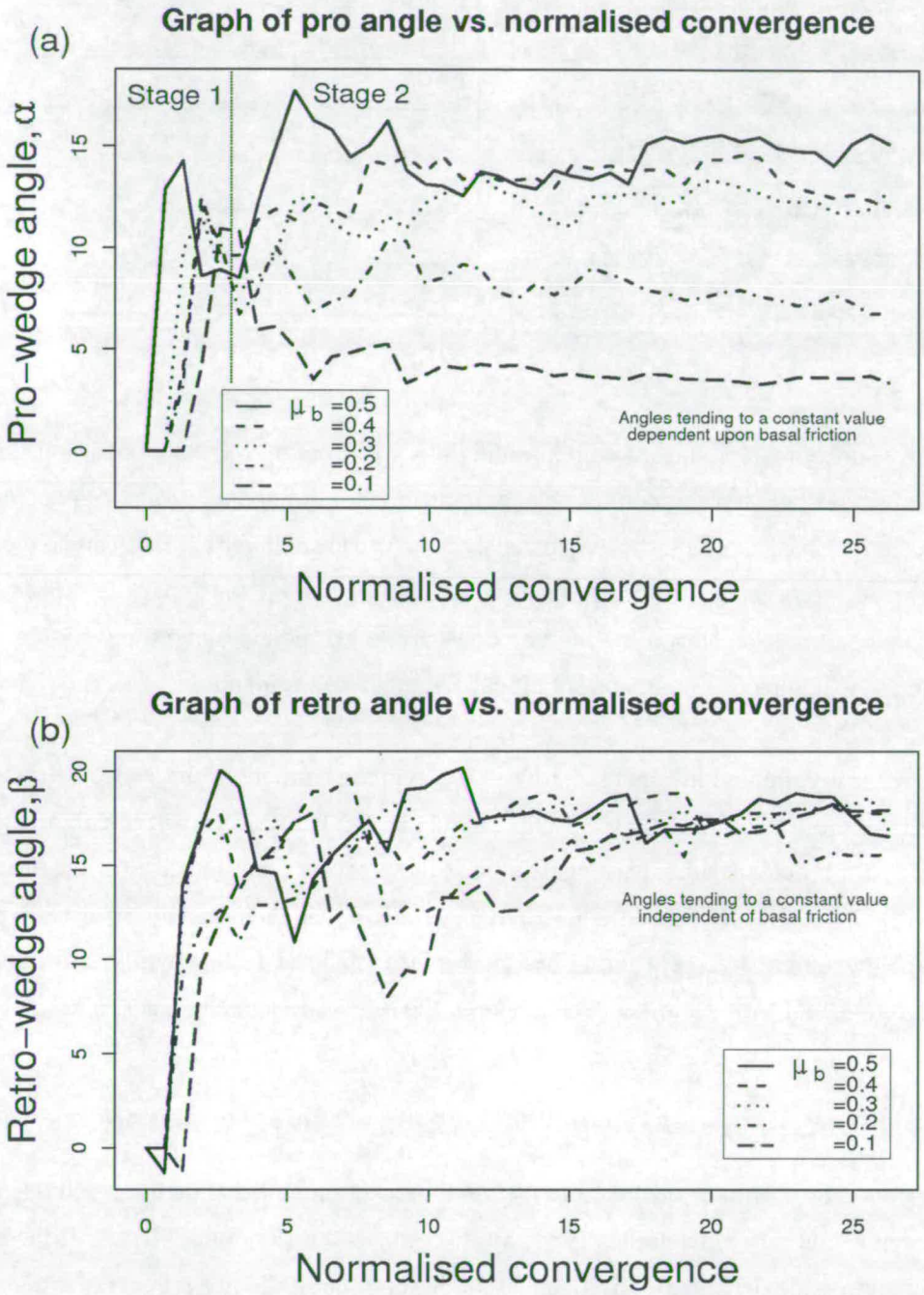

Figure 4.7: Angles of the pro- (a) and retro- (b) wedges versus total convergence per unit depth for Experiment 1 with a range of pro-side basal friction values, $\mu_{bp} = 0.1 - 0.5$. After an initial period of similar growth where the wedges fail internally, the angles of the pro-wedge tend to some limit dependent upon the pro-side basal friction. In contrast, the retro-wedge angles all tend to the same limit.

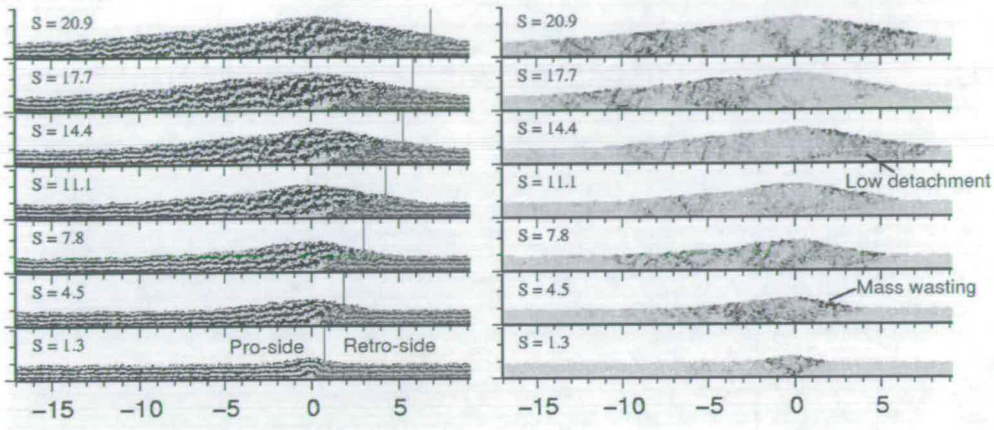

Figure 4.8: Subfigures (a) and (b) compare the deformation of initially horizontal horizons and the maximum relative displacement of adjacent particles for the constant velocity experimental boundary condition with low internal and basal friction. The lower internal friction angle produces wedge angles more similar to those in orogens. The higher angles in Figure 4.5 are more akin to sandbox models. Notice the high amount of relative motion along the wedge surfaces suggesting that slumping is an important process in these experiments.

on the retro- is highlighted in Figure 4.8(b) and seen in the animation, this reflects the fact that the material is too weak internally to sustain a higher taper. The deviation of the highest peak is very similar for both experiments, suggesting that the processes that localise the greatest uplift are relatively independent of the internal coefficient of friction. Interestingly, whilst still pinned at the S-point, the retro-vergent thrust becomes a less localised feature whilst still remaining clearly discrete, and forms a lower detachment in the retro-side at later stages in its evolution.

4.3.3 Summary of results of constant velocity boundary condition

These results show a similar evolution to the sandbox experiments that do not reach the *Stage 3* retro-wedge accretion (Malavieille, 1984; Storti et al., 2000; Persson, 2001). All the experiments saw retro-side deformation initiated at the S-point, but it did not propagate further along the strong base. The retro-vergent thrust is pinned at the S-point and it partitions the deformation. A significant amount of material is seen to slump down the retro-wedge, giving this surface a uniform taper. Higher pro-side basal frictions inhibit stable sliding on the pro-side base, the shortening is accommodated through diffuse internal deformation within the pro-wedge. Lower pro-side basal frictions allow the deformation to be accommodated on more discrete structures at greater distances from the S-point. For all experimental runs, the axial zone remains relatively undeformed and grows in size as deformation shifts further to the pro- and retro-sides.

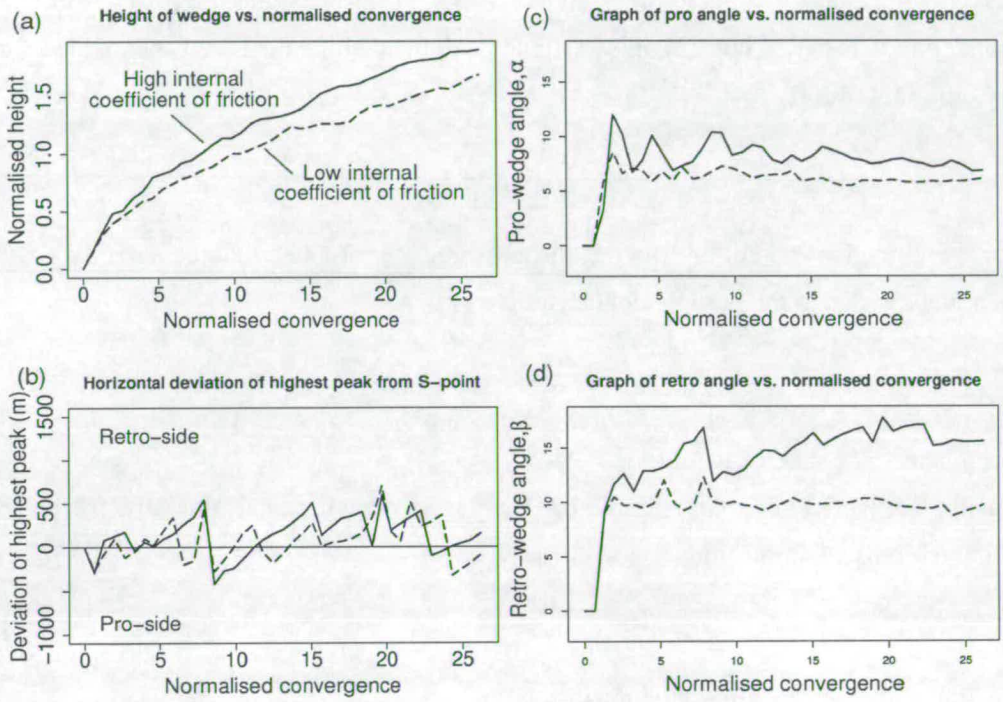

Figure 4.9: Graphs showing the evolution of (a) wedge height, (b) deviation of highest peak from the S-point along the horizontal axis, (c) pro-wedge angle, α and (d) retro-wedge angle, β for Experiment 2 with high and low internal friction (Solid and dashed lines respectively). Wedge angles, and thus wedge height, are all smaller for the case with lower internal friction, for a given amount of convergence. However, the deviation of the highest peak is comparable for both runs.

4.4 Traction force boundary condition arrangement

Willett et al. (1993) suggested that a doubly-vergent system where slip can occur on both bases either side of the S-point, would be the most appropriate boundary condition. The constant velocity boundary condition presented above was not sufficient to achieve this as deformation remained localised at the S-point, never permitting the system to enter Stage 3. To address this issue we developed an alternative approach for the lower boundary condition where both bases were allowed slip through Coulomb failure, but the pro-side also has an extra force term which applies a traction force parallel to the boundary, (4.1). This force tends the particle velocities to the subduction velocity, v' but still allows slip to be defined along the base beneath the elements using Coulomb failure.

$$F_{traction} = \gamma(v - v') \tag{4.1}$$

For this boundary condition to work the convergence rate must induce a displacement, δ_e less than the overlap at the particle contacts, δ_n.

$$\delta_e < \delta_n \tag{4.2}$$

For a constant convergence rate $v' = \frac{\delta e}{dt}$.

The typical particle overlap is found by equating the gravitational force of a particle mass, m, with the repulsive spring force with stiffness, k_s:

$$\delta_n = -\frac{mg}{k_n}$$

Therefore from Equation 4.2, v' must satisfy:

$$\begin{aligned} v' &< \frac{mg}{k_n\, dt} \\ &< \frac{\pi R^2 \rho g}{k_n\, dt} \end{aligned} \tag{4.3}$$

4.4.1 Experiment 3 - Investigating the role of retro-side basal friction

The retro-side basal friction was increased by different factors relative to the pro-side basal friction (Animations DVBC-2a and DVBC-2b). Deformation now propagates into the retro-side and the whole wedge is able to slide stably on both the pro- and retro-bases. This is demonstrated by the advection of all retro-side material (the material shaded darker) away from the S-point (Figure 4.10). Thus the retro-vergent thrust is no longer pinned at the S-point. The angle of the steep retro-wedge is relatively insensitive to the retro-side basal friction as this angle is some angle of repose, primarily limited by the internal strength of the material (Figure 4.12(b)). Less slumping occurs down this surface now as there is a second mechanism

to accommodate shortening on the retro-side. As the whole wedge slides stably, a shallower accretionary wedge forms beyond the toe of the steep retro-wedge. The extent of this wedge is limited by retro-side basal friction (c.f. Figs 4.10(c) and 4.10(d)). The pro and retro-wedge angles shown in Figs 4.12(a) and (b) are averages over the whole pro and retro-wedge and do not highlight the breaks in slope due to pop-ups at the toe of the pro-wedge and accretion of retro-side material into the retro-wedge. As might be expected, higher values of μ_{br} encourage accretion purely on the pro-side toe with the retro wedge preserved at a steep taper. Lower values allow deformation to propagate into the retro-side basin, with a shallow wedge accreting onto the tip of the steep retro-wedge. For the range of retro-side basal frictions investigated, all the wedges grow vertically with similar rates. We now see spikes in both the pro- and retro-wedges as they reach their thresholds upon which they require support on the base (Figures 4.12(a) and (b)). The retro-wedge reaches this threshold later than the pro-wedge.

The highest peak is seen to advect gradually towards the retro-side before suddenly switching to a newly formed peak on the pro-side (Figure 4.11(b)), oscillating approximately two mean thickness's, h_0 either side of the S-point; this has important implications for the advection of topography and drainage capture across the drainage divide of mountain belts (e.g. the Landsborough River, S.Alps, N.Z. Koons, 1994). This behaviour is less erratic and more periodic than for the constant velocity boundary conditions as the system is now free to slide on the retro-wedge whereas before, deformation was forced to localise purely on the pro-side, even when it would have preferred to slide on the retro-side base. The time evolution of the height of the wedge is also more periodic, reflecting periodicity in the deviation of the highest peak. This suggests that the deformation remains more localised over a given period of time, rather than constantly adjusting.

4.5 Time and deformation evolution of the doubly-vergent system

The experiments presented confirm that the doubly-vergent wedge systems evolve through a three stage scheme (Willett et al., 1993) defined by the modes of deformation utilised to accommodate shortening. The boundary conditions applied to some sandbox experiments are such that the system never progresses to *Stage 3* deformation; that is the accretion of retro-side material. We discuss the nature of deformation exhibited in each stage and possible controls on the system which allow the system to enter the next *Stage*.

The key point is that there are thresholds within the system that must be attained before a new mode of deformation is required. Deformation across the wedge is distributed depending upon the extent of sliding along the base which in turn is controlled by friction parameters.

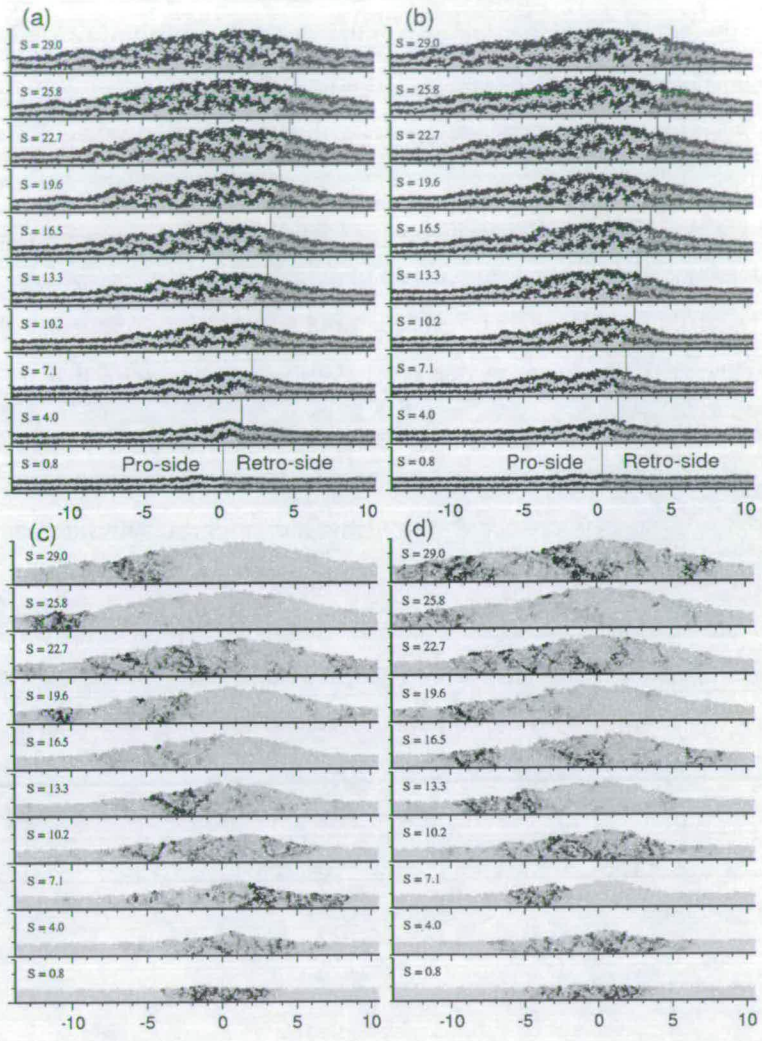

Figure 4.10: Figs (a),(b) compare the deformation of initially horizontal horizons and Figs (c),(d) the maximum relative displacement of adjacent particles for the second experimental boundary condition for high and low retro-side basal friction. Note how the retro-side material, shaded darker, is no longer pinned to the S-point and slides to the retro-side (c.f. Figure 4.5). A second, shallower wedge developed beyond the steep retro-wedge as material is accreted at the toe, the magnitude of retro-side basal friction regulates the amount of material accreted this way. Deformation in the retro-side is not pinned to the S-point.

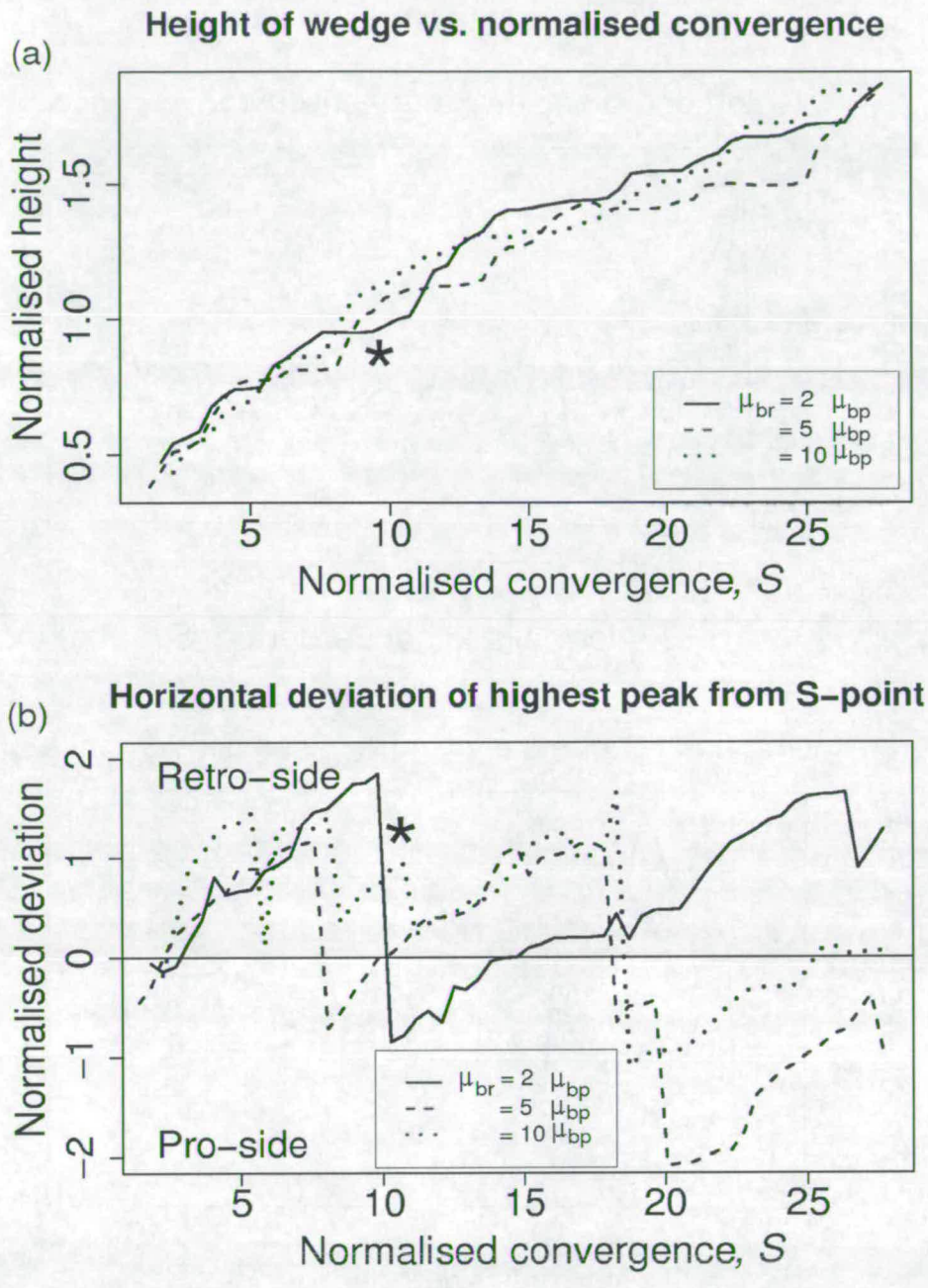

Figure 4.11: Maximum height (a) and deviation of highest point from S-point (b) versus total convergence per unit model depth for Experiment 3 with different ratios of pro- to retro- basal friction, where $\mu_{br} = 2, 5, 10\mu_{bp}$. All length scales are normalised by the mean thickness of accreted material. The increase in height of the wedge and oscillation in highest point is clearly episodic, with a longer time period. Deformation now remains localised in one region as compared with the constant velocity boundary condition arrangements. There is a clear, gradual advection of the highest peak to the retro-side before a rapid switch to a pro-side peak.

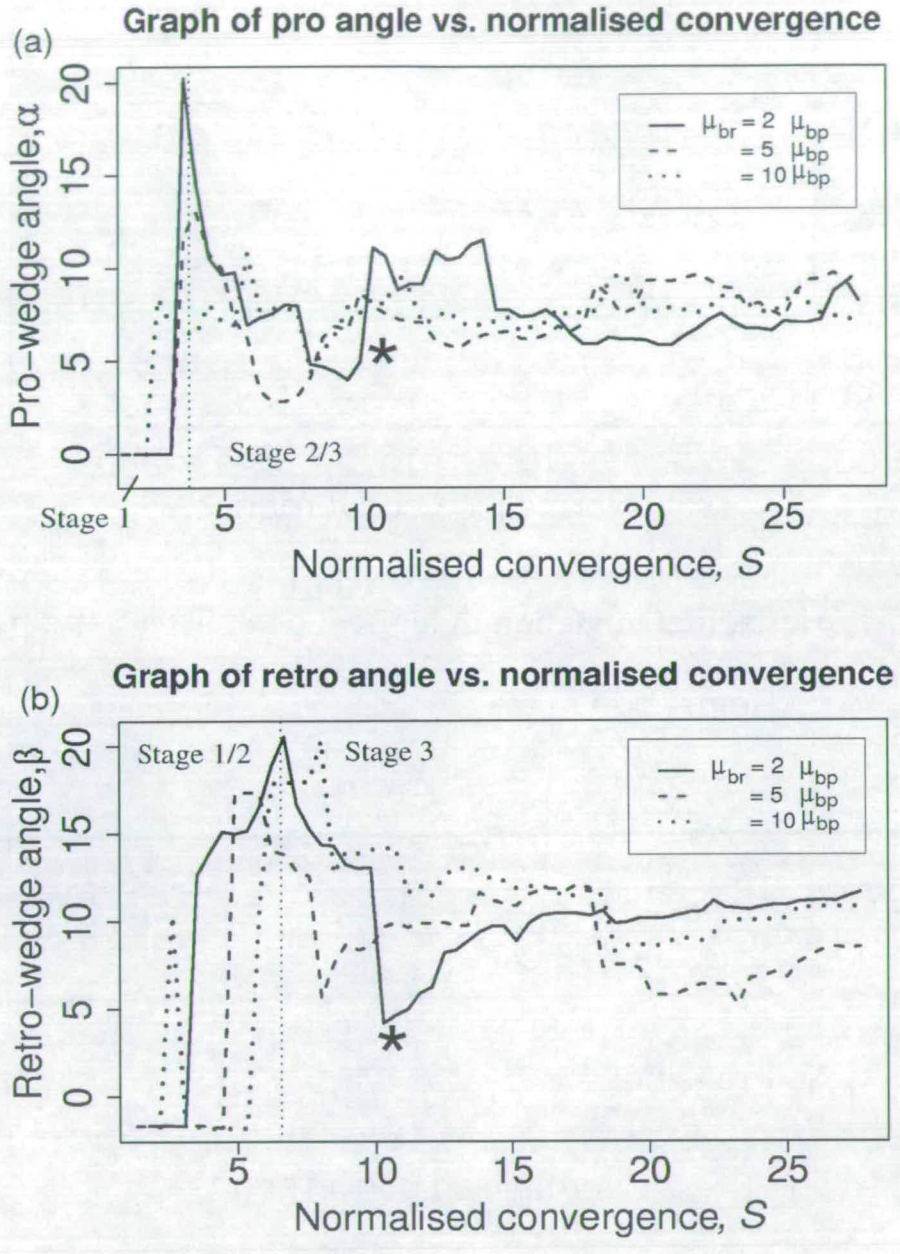

Figure 4.12: Angles of the pro- (a) and retro- (b) wedges versus total convergence per unit model depth for Experiment 3 with different ratios of pro- to retro- basal friction, where $\mu_{br} = 2, 5, 10\mu_{bp}$. There is now a spike in both the pro- and retro-wedge angles. These occur as the respective wedges start to fail on the lower boundary rather than internally. The pro-wedge angle is the first to deviate and subsequently, the retro-side starts to accrete material.

4.5.1 *Stage 1*

Initially, two shear zones rooted at the S-point initiate a V-shape block uplift by translating the plug to the retro-side along the retro-verging shear zone. The angle of these shear zones is strongly dependent upon the global strength of the material. It is this shear zone which develops into the dominant retro-vergent thrust. This can be seen most clearly in Figure 4.5(c) and (d) at $S = 1.3$, although it does occur in all the experiments run.

The duration of *Stage 1* is clearly highlighted in Figure 4.7(a) for a normalised convergence of less than 3, which shows that the angle of the pro-wedge is initially insensitive to pro-side basal friction until the wedge has reached a critical size beyond which the wedge requires support on the base.

All of the doubly-vergent sandbox experiments described in Section 1.5.2.1 formed the retro-vergent thrust at an early stage. This suggests that the formation of the retro-vergent thrust is a result of the kinematic boundary conditions present in both experiments, rather than the presence of a rigid indenter. The kinematic boundary condition provides the primary control on the system. The retro-vergent thrust is a first order structure that is observed in many settings, examples of which include the North Pyrenean Fault (Fischer, 1984), Insubric Line in the European Alps (Pfiffner et al., 1997) and the Longitudinal Valley Fault of eastern Taiwan (Hickman et al., 2002). It is also well resolved in finite element models as regions of highly localised strain.

4.5.2 *Stage 2*

Deformation now propagates to the pro-side of the singularity as the wedge begins to slide stably on the pro-side base. The angle of the pro-wedge is now dependent upon the pro-side basal friction and departs from the initial trend (Figure 4.7(a) for normalised convergence, $S > 3$) and is formed through frontal accretion of foreland material. Once the initial transient response has died down, the angle remains relatively constant. The steeper retro-wedge is formed by material fluxing through the wedge and its angle reflects some angle of repose of the system. Examples of the consequent topographic asymmetry include central Taiwan (Deffontaines et al., 1994) and the Olympic Mountains of Washington State (Pazzaglia and Brandon, 2001).

A low basal friction can only support a shallow pro-side wedge and new thrust sheets are seen to initiate beyond the toe of the wedge. A high basal friction localises deformation nearer the S-point as information cannot travel as far along the base.

4.5.3 *Stage 3*

Sliding on the retro-base is initiated and the deformation front propagates into the undeformed layer beyond the tip of the retro-wedge and initiates the formation of a lower taper wedge. The initiation of sliding can be seen in Figure 4.12(b) where the initial spike in basal friction drops to some lower value once retro-side accretion has been initiated. This second retro-wedge is formed by material accreted onto the toe of the steeper retro-wedge, its angle is lower as it is formed in an accretionary manner, not by a large flux of material as in the case of the steeper wedge.

The experiments run under the first boundary condition do not permit sliding on the retro-side base and this third stage is never reached. However the formation of the deeper detachment in Figure 4.8(b) at $S = 7.8$ does suggest that if the experiments were to run long enough, the models may accrete at the toe. The second boundary arrangement rapidly moved into *Stage 3* very soon after *Stage 2* had been reached. There is a large tolerance for the thresholds that control this transition.

4.6 Comparison with singly-vergent wedge experiments

We compare the pro-wedge of the doubly-vergent wedge experiments presented in this chapter with the singly-vergent wedge experiment of Chapter 3. The main physical difference is that accommodation of deformation within and beyond the axial-zone is permitted when a rigid, vertical backstop is not present. The singly-vergent wedge does not have a mechanism equivalent to Stage 3 deformation where the whole wedge slides stably with respect to the discontinuity, the nearest equivalent is sliding on the base with corner flow up and parallel to the indenter. Whenever singly-vergent wedges are used in either analogue or numerical experiments, the region close to the vertical backstop should be ignored, unless its presence is geologically motivated. Wedge angles are comparable. The doubly-vergent wedge allows extra modes for the accommodation of shortening, and thus the episodicity within them is different.

4.7 Conclusions

The two model boundary conditions presented in this chapter compare well with previous sandbox and FEM approaches. The first formulation has a relatively passive retro-side with the root of deformation pinned at the S-point, over-riding the retro-side. The pro- and retro-sides are relatively decoupled and weaker materials see deformation propagate deeper into the retro-side. The second formulation sees deformation propagate along the retro-side base and retro-side material is accreted to form a second shallower wedge.

Experiments run using variable boundary condition have allowed us to compare and con-

trast previous modelling approaches. Similar model outputs can be obtained for both a system with or without a rigid indenter (as used in some sand-box models), and therefore the primary control on the system is the kinematic boundary conditions not rheological discontinuities.

There are thresholds in geometry and size that regulate the location, duration and mode of deformation (e.g. pro-wedge frontal accretion, underplating, retro-wedge frontal accretion). In all experiments there is significant advection of pro-side material into the retro-wedge.

The main retro-wedge angle is steeper than the pro-wedge angle as it is not formed by accretionary processes. Material in the main retro-wedge is fluxed through the wedge to the retro-side, this is confirmed by the presence of slumped material at the base of the retro-wedge which shows that the angle is near some angle of repose of the material.

Higher values of pro-side basal friction make the wedge more symmetric about the highest peak as the pro-side angle tends towards a similar angle of repose as the retro-side.

The topographic ridge is seen to oscillate approximately around a point above the singularity. The experiments show a gradual advection of the topographic ridge to the retro-side, followed by a rapid switch in location to the pro-side as the deformation was localised internally in order to sustain constant taper angles. This has important implications for drainage capture across the drainage divide, a more complete discussion of this will be given in Chapter 7.

Chapter 5

Investigating the Normal Variability and trends of a doubly-vergent wedge

5.1 Introduction to concept of Normal Variability

The case for describing the Normal Variability of geological systems arises from Occam's Razor, which states that the simplest solution is most likely to be true. Until further facts present themselves this remains the preferable theory. Applying Occam's Razor to orogenic settings, features common to some generic setting are a result of common boundary conditions and do not need to call on special conditions. The envelope of expected behaviour defines the Natural Variability of the system. Perturbations from this normal behaviour require a more complicated explanation. In many studies, this distinction is not always transparent. Special forcings (e.g. climatic, tectonic, lithological) are often called upon to explain specific features observed in geological systems, but how necessary are they?

In this chapter we present four runs where the boundary conditions are identical, but the initial random packing has a different seed. We see rigorous trends and relationships in the output, but a degree of variability in localisation and duration is superimposed upon this. The random packings elucidate the Natural Variability in nature. DEM model results will be compared with the Pyrenees to provide insight into how aspects of the mechanical development could be interpreted.

Any model that hopes to successfully reproduce and investigate behaviour observed in orogenic environments must aspire to generate phenomena common to mountain belts without pre-defining it. For example, all mountain belts experience the accretion of thrust sheets, something they do regardless of inheritance. Inherited structures will modify the detail of the thrust sheets, but do not pre-define their occurrence. If a model intends to make predictions on the scale of individual thrust sheets, then thrust sheets must be an emergent property of the model that does not require pre-definition. Features common to all mountain belts are defined

to be first order and the perturbations of these effects to be second order. Inheritance becomes of primary importance when it produces an effect that is unexpected in a mountain system.

Beaumont et al. (2000b) tried to reproduce key structures of the Pyrenean orogen using a finite element model. They reproduce thrust sheets by including a pre-defined weaknesses along a detachment horizon, which they attribute to inheritance. We argue that any model which tries to reconstruct an orogenic cross-section must be capable of generating elements common to all collisional orogens, without having to prescribe their occurrence by inheritance. Similarly, shallow salt layers localise thrust sheet formation near the surface, however we observe thrust sheet emplacement in similar settings which don't involve such evaporites, e.g. Taiwan. The presence of the salt is a second order control which will perturb the thickness, lateral extent, width and dip of the sheets.

In the field we look for information that is observable, measurable and preserved, to try to build up a picture of how a system evolved at some time in the past. It is easy to over emphasise the importance of information because of its accessibility. Our aim must be to explain behaviour using the simplest system possible, introducing a special feature only when absolutely necessary. Absolute necessity means that we have no way to explain it without introducing a new process.

5.2 Geometric growth of a doubly-vergent critical wedge

Here I outline a simple geometric model to make predictions about the evolution of a doubly-vergent wedge which provides insight into the Natural Variability of the system.

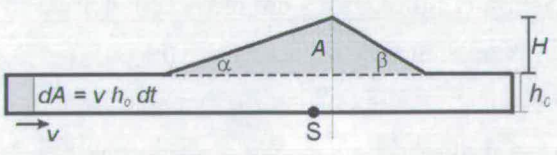

Figure 5.1: Simple analytic model of doubly-vergent wedge growth

Let the surface topography of the doubly-vergent wedge consist of two wedges of constant taper, α and β sloping in opposite directions from some common maximum height, H (Fig. 5.1). An amount of material, dA is added to the system each time-step and the height adjusts to the new total area maintaining the taper angles.

The area under the wedges is given geometrically by,

$$A = \frac{H^2}{2\tan\alpha} + \frac{H^2}{2\tan\beta} \tag{5.1}$$

The total area accreted to the wedge is given by the integrated depth of material accreted

over the regional convergence history. Taking S to be the amount of convergence accommodated and $h(S)$ to be the thickness of material accreted at some total convergence S:

$$A = \int_0^S h(S)\,dS \tag{5.2}$$

For constant depth of accreted material $h(S) = h_0$,

$$A = Sh_0 \tag{5.3}$$

Substituting (5.3) in (5.1) and rearranging for the dimensionless height gives the maximum height attainable for a wedge with critical angles α and β for a given amount of total convergence.

$$\begin{aligned} \frac{H}{h_0} &= \sqrt{\frac{2\tan\alpha\tan\beta}{\tan\alpha+\tan\beta}S} \\ &= C(\alpha,\beta)S^{\frac{1}{2}} \end{aligned} \tag{5.4}$$

In practice the measured heights are lower than this ideal due to the formation of an axial zone, the smoothing of topography through slumping and the accommodation of shortening through the formation of a shallow second retro-wedge. Assuming a constant convergence rate, v the total amount of convergence and time are directly proportional, $S = vt$. Thus, if a constant depth of material is accreted per unit time, geometrically one expects the rate of topographic uplift of an accretionary wedge or prism to decrease with the square root of time.

$$\frac{\partial H}{\partial S} = \frac{1}{2}C(\alpha,\beta)S^{-\frac{1}{2}} \tag{5.5}$$

And as $S \longrightarrow \infty$, $\frac{\partial H}{\partial S} \longrightarrow 0$. This provides a mechanism for the rates of uplift and erosion to converge after an initial period of rapid uplift.

5.3 Model boundary conditions and the scaling of model results to real wedges

The traction force boundary condition arrangement, as outlined and justified in Chapter 4, has been used. Four runs for the same parametrisation, but different random packing seed were performed to determine which features of the model were robust and which were sensitive to the initial packing. Model output to be presented demonstrates good correlation between runs. These runs shall be referred to as N(I), N(II), N(III) and N(IV).

By non-dimensionalising model parameters and results, it is possible to compare the model results with systems on different scales. Assuming some geologically motivated convergence

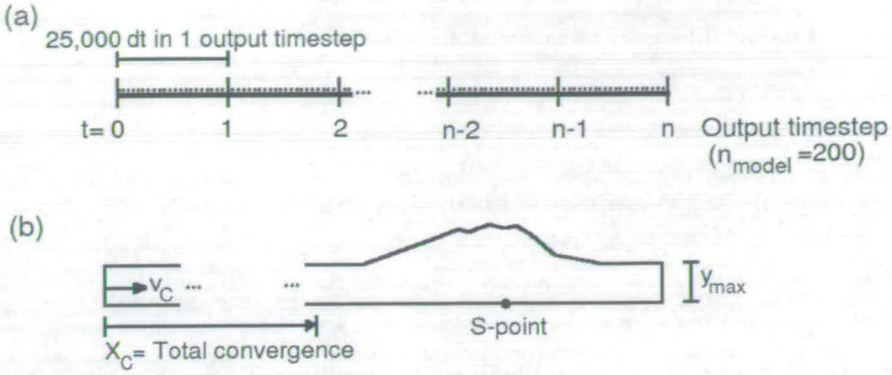

Figure 5.2: Scaling relations in doubly-vergent DEM wedges. (a) Relation between model time-steps and output time-steps. (b) Illustration of key scaling variables to convert between normalised convergence and a real setting.

rate, we can convert this total convergence to some geological time-scale.

$$(Geological\ time) = \frac{(Total\ convergence)}{(Convergence\ rate)}$$

Figure 5.2 shows us the basic geometry with which we can construct the non-dimensional problem and scale it. The total amount of convergence, X_C and the undeformed model depth, y_{max} are known. The ratio of these gives the total non-dimensional convergence per unit model depth. In runs N(I) to N(IV):

$$N_C = \frac{X_C}{y_{max}} \approx 21$$

Slight discrepancies in the total convergence arise from slightly different values in the mean undeformed depth calculation due to differences in the settled packing arrangement. N_C can now be used to scale the system to a particular setting using the actual depth of that system. For example, using $y_{system} \approx 10km$) and assuming some convergence velocity ($v_C \approx 10\text{km Myr}^{-1}$) we can determine the total duration of the model run in geological time.

$$Duration = \frac{N_C y_{system}}{v_C} \approx 21\text{Myr}$$

This total duration is spread across $n = 200$ output time-steps, thus each output time-step corresponds to $\approx$ 105kyr for this scaling.

5.4 Results and behaviour of non-erosive system

Several graphical representations of the four runs have been generated and are presented here. Their evolution is recorded in output time-steps (t), which correspond to the data dumps from

the model every 25,000 model time-steps and using total convergence normalised by the undeformed thickness of material accreted to the system (S). All of the results presented are shown in a frame of reference stationary with respect to the S-point. Animations of the four runs can be found on the CD.

5.4.1 Deformation of horizon plots

Figures 5.3 to 5.6 show the deformation of horizons at various output time-steps, coloured by the initial undeformed depth. Initially, the S-point marks the transition between the subducting and over-riding plates, geologically this often defines the suture zone. Material either side of this boundary has been shaded slightly differently so we can track the evolution of the material derived from this region, as it is advected into the retro-wedge and preserved. The pro-wedge angle is shallower, experiences the most deformation and extends laterally when thrust sheets propagate beyond its tip. Stage 3 accretion in the retro-wedge is also observed. The dip of structures in the pro-wedge changes as they rotate and become incorporated into the axial zone and retro-wedge. N(II) provides the best example of the highest peak advecting towards the retro-side before switching to a more pro-ward highest peak due to a change in the localisation of deformation.

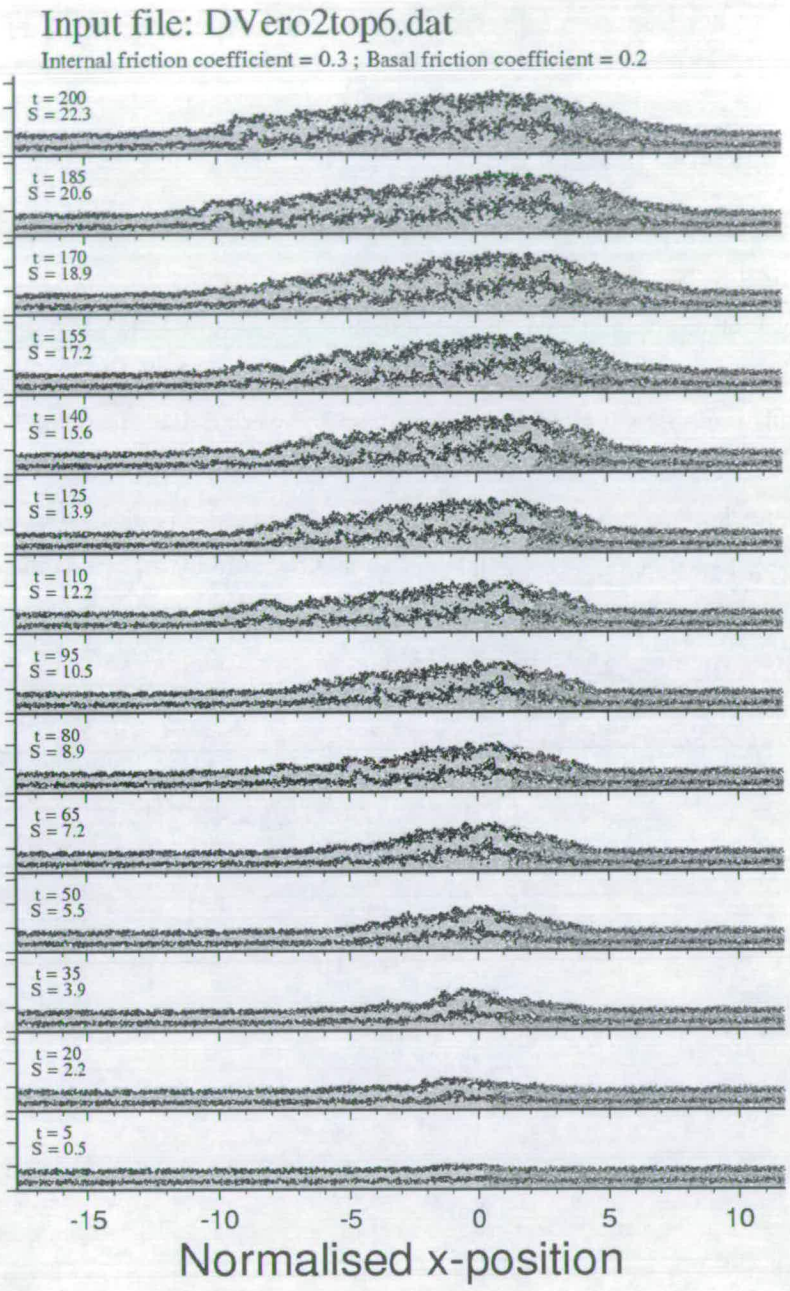

Figure 5.3: Still frame output from the doubly-vergent experiment N(I) using the traction force boundary condition, coloured by undeformed depth horizons. The lower axis is the x-position relative to the S-point, in units of the mean undeformed thickness of accreted material, h_0. The evolution of the model is recorded in the total normalised convergence that has been accommodated (S) and in the number of model timesteps elapsed (t).

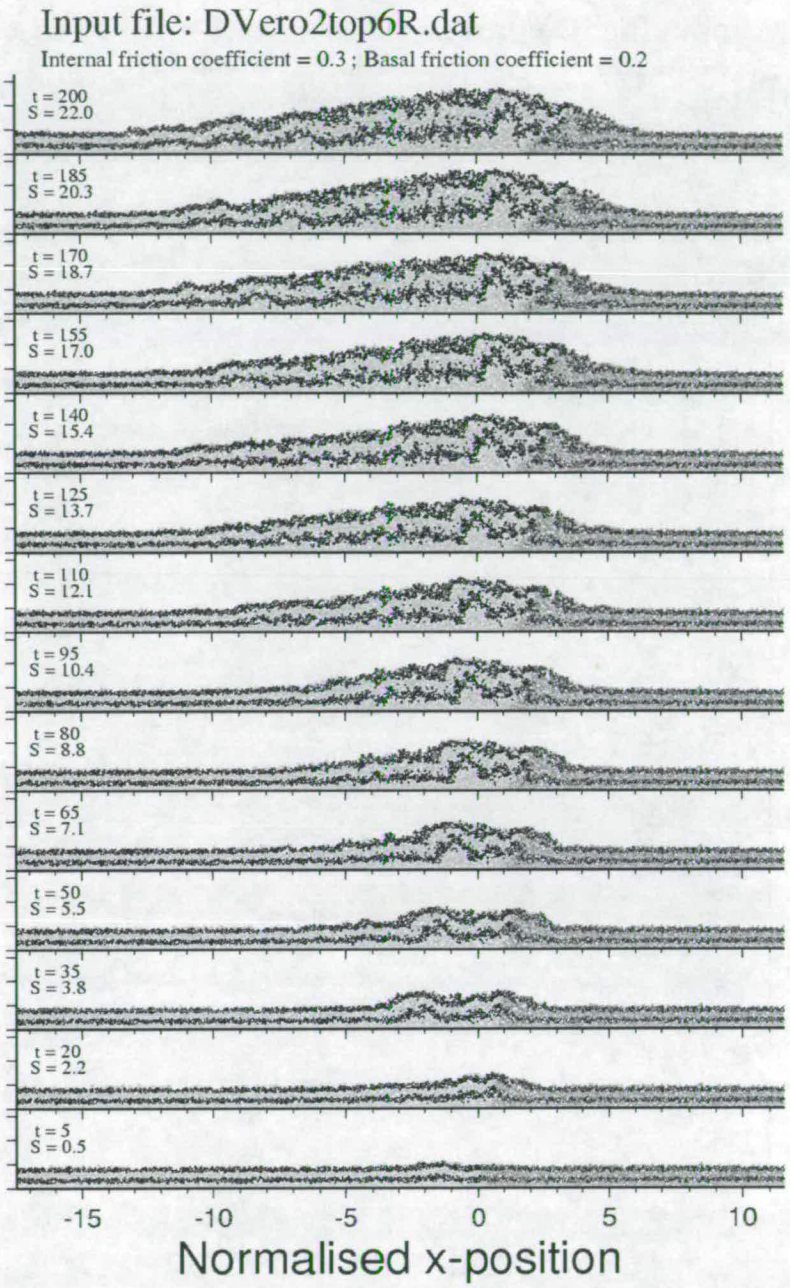

Figure 5.4: Still frame output from the doubly-vergent experiment N(II) using the traction force boundary condition, coloured by undeformed depth horizons. The lower axis is the x-position relative to the S-point, in units of the mean undeformed thickness of accreted material, h_0. The evolution of the model is recorded in the total normalised convergence that has been accommodated (S) and in the number of model timesteps elapsed (t).

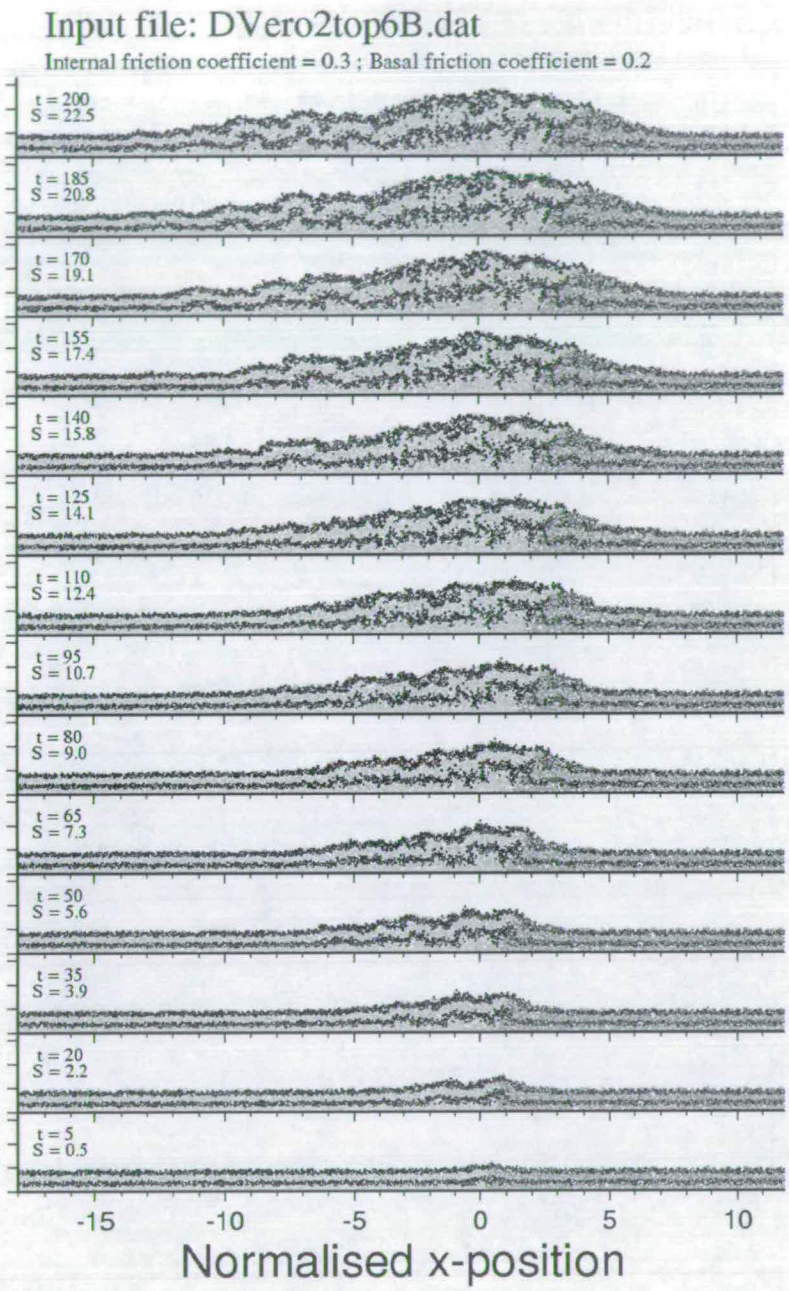

Figure 5.5: Still frame output from the doubly-vergent experiment N(III) using the traction force boundary condition, coloured by undeformed depth horizons. The lower axis is the x-position relative to the S-point, in units of the mean undeformed thickness of accreted material, h_0. The evolution of the model is recorded in the total normalised convergence that has been accommodated (S) and in the number of model timesteps elapsed (t).

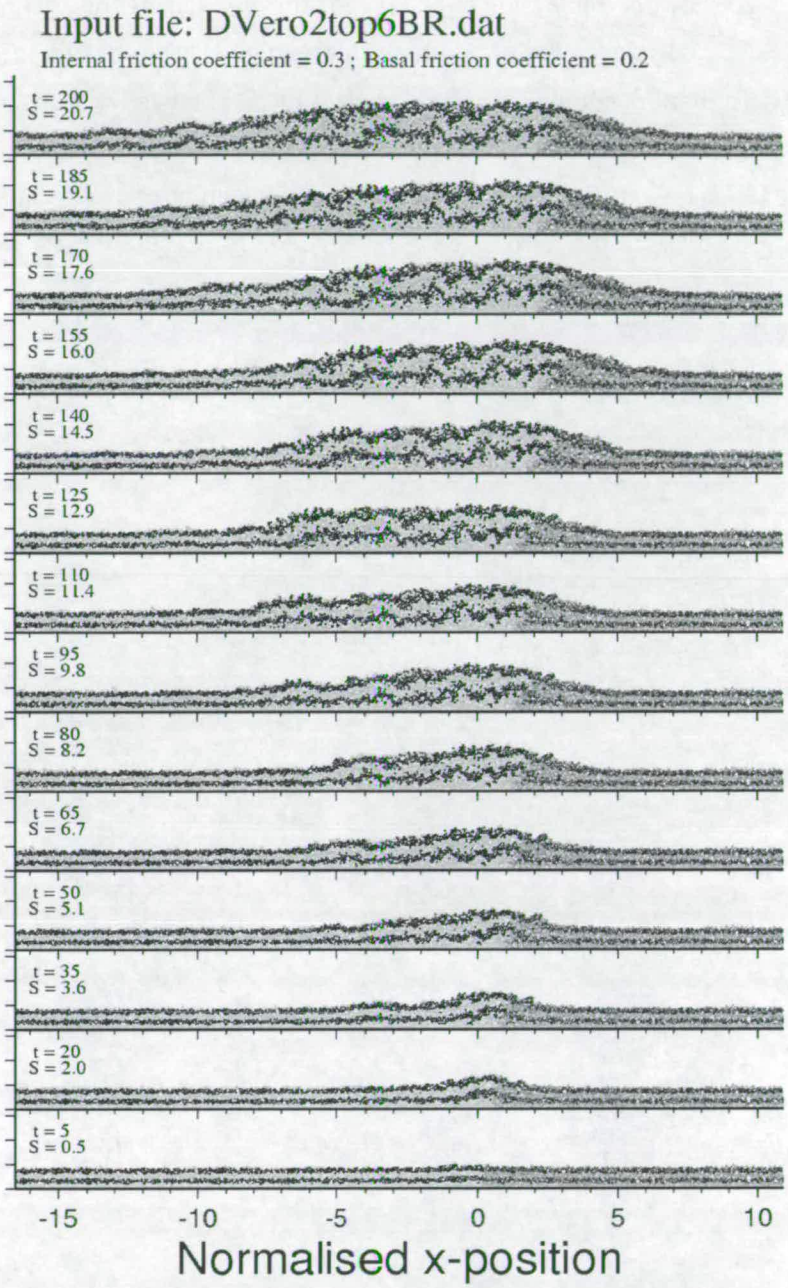

Figure 5.6: Still frame output from the doubly-vergent experiment N(IV) using the traction force boundary condition, coloured by undeformed depth horizons. The lower axis is the x-position relative to the S-point, in units of the mean undeformed thickness of accreted material, h_0. The evolution of the model is recorded in the total normalised convergence that has been accommodated (S) and in the number of model timesteps elapsed (t).

5.4.2 Maximum relative displacement plots

Figures 5.7 to 5.10 show the same time slices as the previous four figures, but are coloured by the maximum relative displacement of neighbouring particles since the previous output time-step. Initially, deformation is highly localised around the S-point as the wedge starts to form. As the wedge grows the localisation of deformation fluctuates within the wedge, the pro-wedge being the most active region. Retro-side deformation is a much rarer event and accommodated by sliding along the base to the retro-side of the S-point. Retro-side thrusts regularly tip out near the base of the retro-wedge.

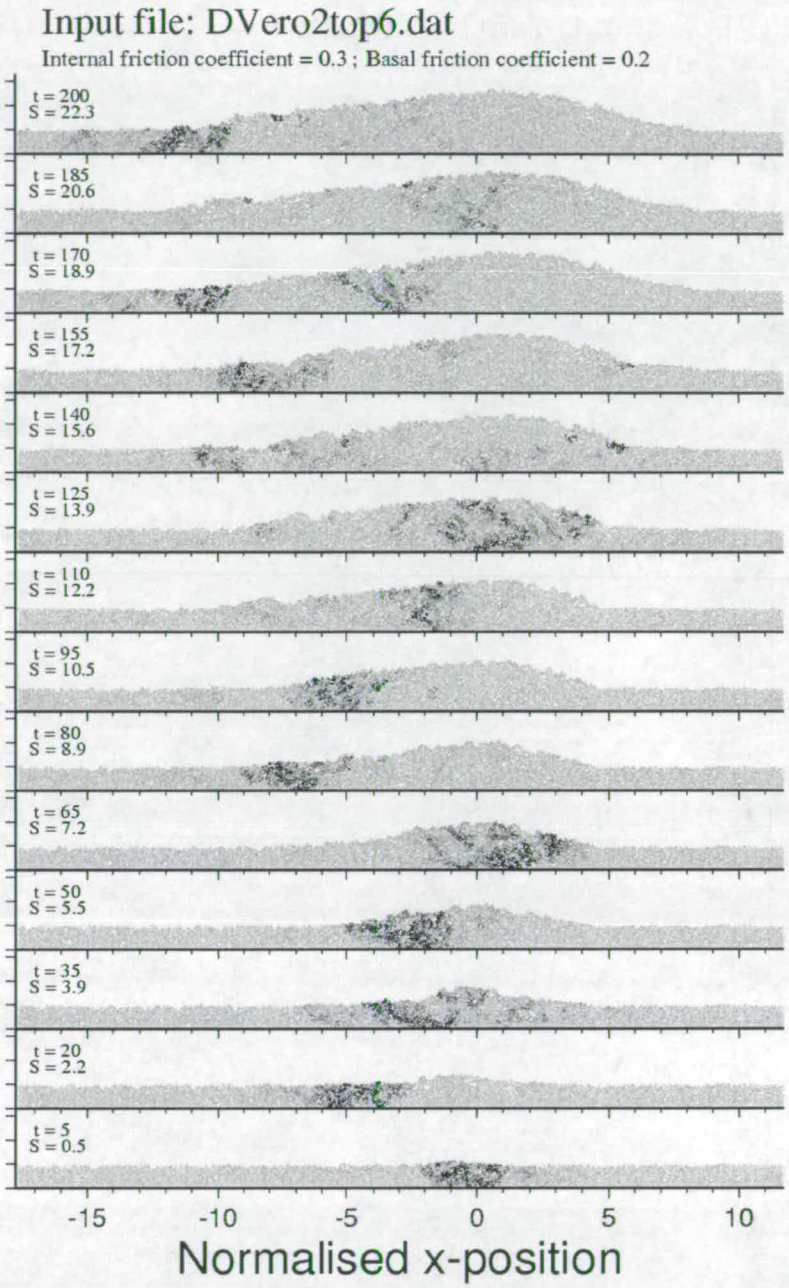

Figure 5.7: Still frame output from the doubly-vergent experiment N(I) using the traction force boundary condition, coloured by the maximum relative displacement of adjacent particles. The lower axis is the x-position relative to the S-point, in units of the mean undeformed thickness of accreted material, h_0. The evolution of the model is recorded in the total normalised convergence that has been accommodated (S) and in the number of model timesteps elapsed (t).

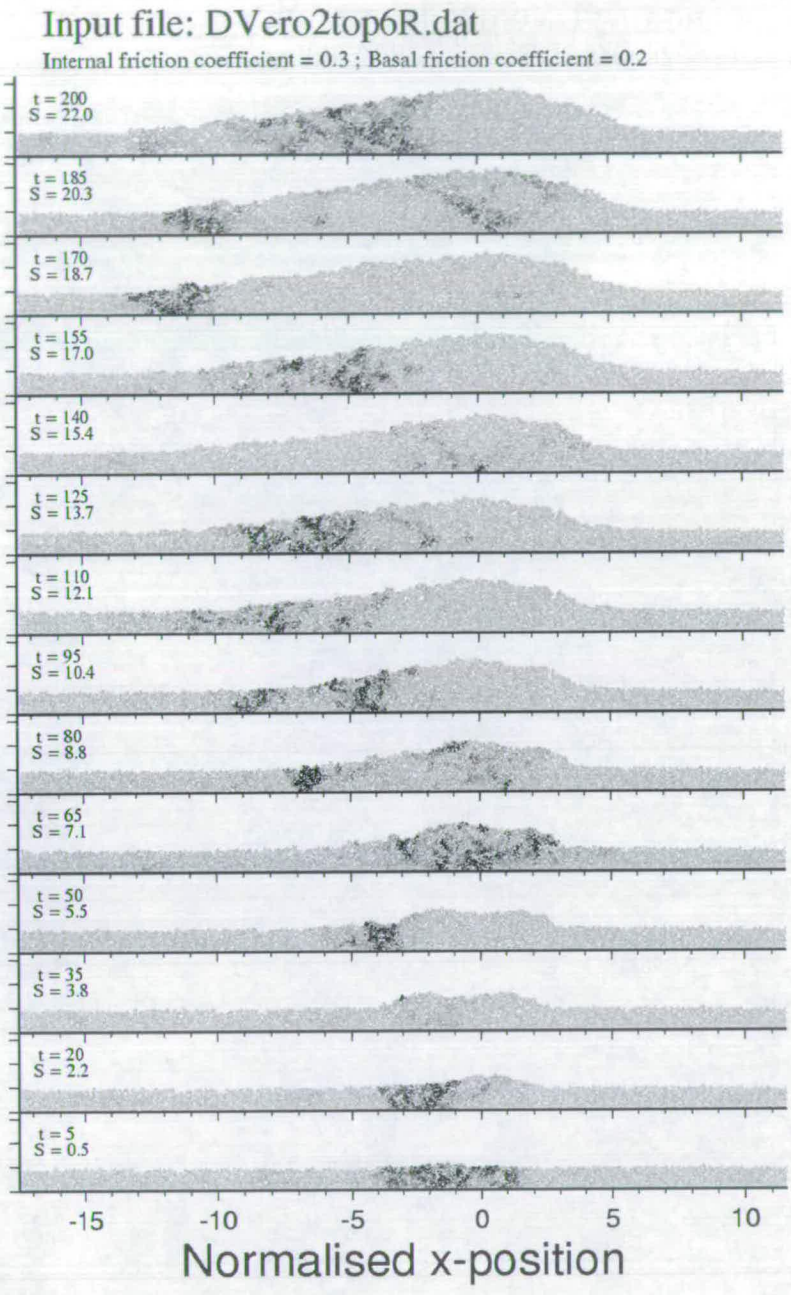

Figure 5.8: Still frame output from the doubly-vergent experiment N(II) using the traction force boundary condition, coloured by the maximum relative displacement of adjacent particles. The lower axis is the x-position relative to the S-point, in units of the mean undeformed thickness of accreted material, h_0. The evolution of the model is recorded in the total normalised convergence that has been accommodated (S) and in the number of model timesteps elapsed (t).

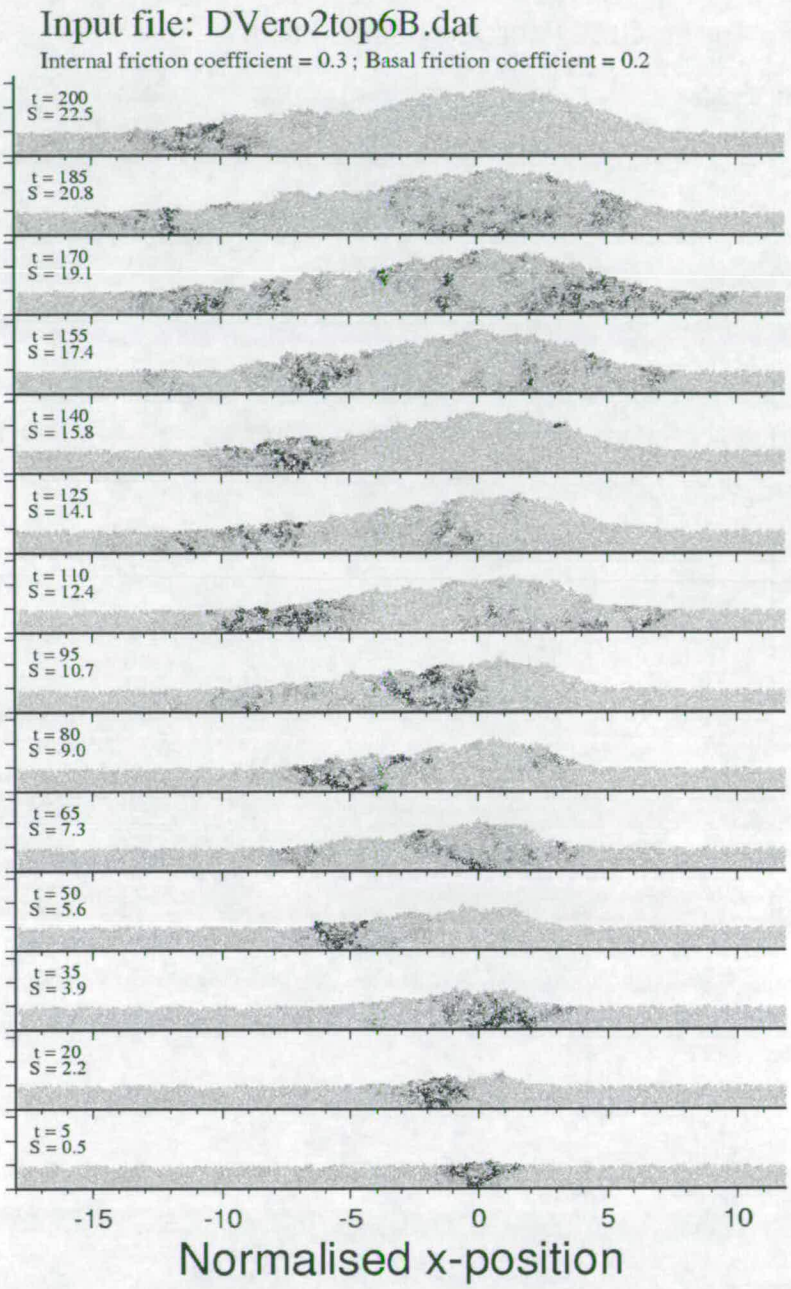

Figure 5.9: Still frame output from the doubly-vergent experiment N(III) using the traction force boundary condition, coloured by the maximum relative displacement of adjacent particles. The lower axis is the x-position relative to the S-point, in units of the mean undeformed thickness of accreted material, h_0. The evolution of the model is recorded in the total normalised convergence that has been accommodated (S) and in the number of model timesteps elapsed (t).

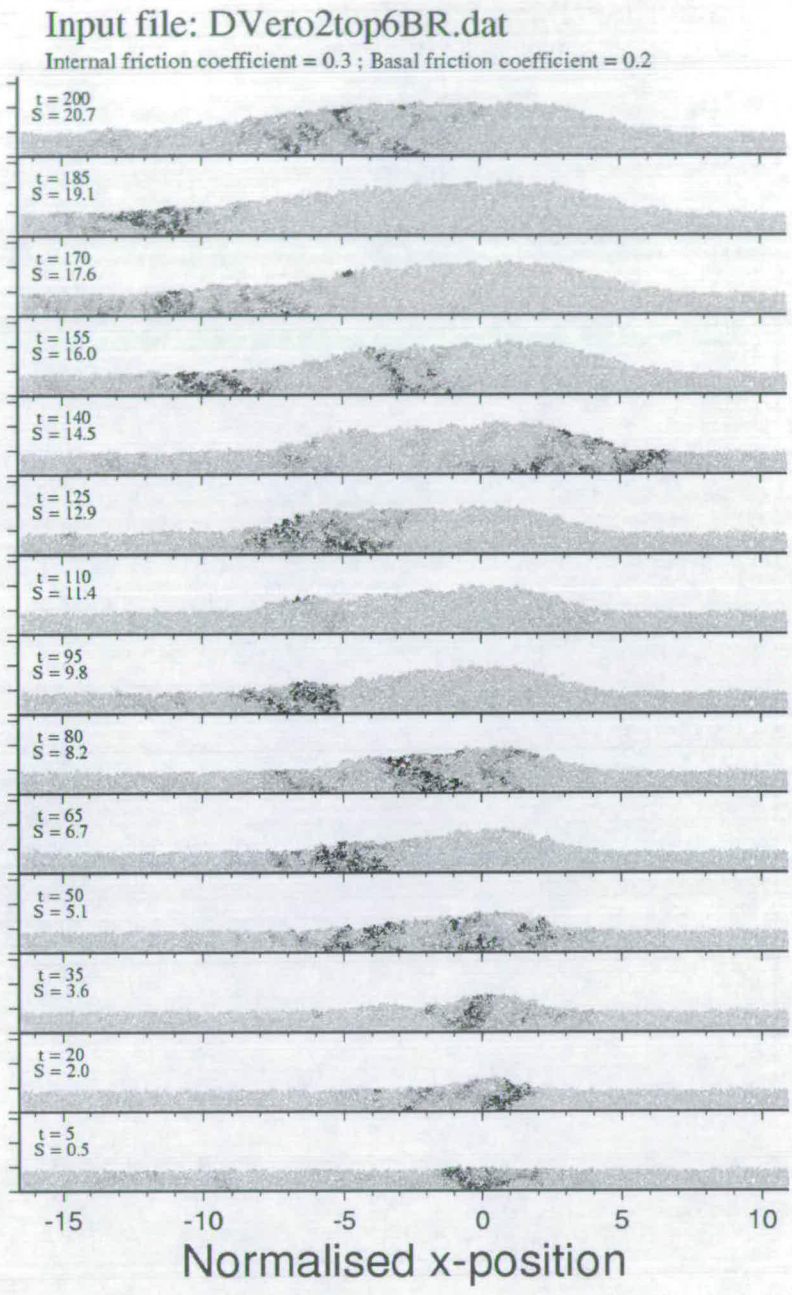

Figure 5.10: Still frame output from the doubly-vergent experiment N(IV) using the traction force boundary condition, coloured by the maximum relative displacement of adjacent particles. The lower axis is the x-position relative to the S-point, in units of the mean undeformed thickness of accreted material, h_0. The evolution of the model is recorded in the total normalised convergence that has been accommodated (S) and in the number of model timesteps elapsed (t).

5.4.3 Deformation vector plots

Figures 5.11 and 5.12 show the time evolution of vector plots of particle motion between the previous three output time-steps relative to the S-point. Areas that have experienced a large translation appear dark relative to those that have not moved far. Shortening is accommodated across clear deformation boundaries that are localised within the wedge, as is indicated by the abrupt change between region of similar velocity vector style. The focus for this localisation varies through time. It is clear from these plots which portion of the wedge is evolving at any given time. Despite internal detail varying between runs, the resulting wedge geometry remains consistent. The question of where deformation localises is equivalent to asking how far the convergence on the pro-side penetrates into the wedge. Thus displacement is always a maximum on the pro-side and a minimum to the retro-side. The overlying geometry affects the angle and localisation of structures within the system. These plots indicate the localisation of retro-vergent structures, as it is across these that the largest displacements occur, they are not so good at highlighting pro-vergent structures, such as at the tip of new thrust sheets.

5.4.4 Upper surface evolution

The time evolution of the upper surface for the four runs is shown in Figure 5.13. Superimposed on these figures is the position of the deformation front (in grey) and vectors showing localisation recent uplift. There is significantly more activity around the pro-deformation front than the retro-deformation front which sees periods of very low activity and the occasional step out.

5.4.5 Interpretation of deformation front plots

We describe the evolution of the wedge using the position of various fronts that move in x, parallel to the model base, as the wedge grows (Figure 5.14(a)). The pro- and retro-deformation fronts are labelled Dp and Dr, the pro- and retro-marker fronts Mp and Mr and the highest peak T, as illustrated in Figure 5.14(a).

- The *deformation fronts* are taken to be the particle with the most extreme values of the wedge, $x(p)$ where:

$$y(p) > y_{max} + (Maximum\ disc\ diameter)$$

- The *marker fronts* represent the most extreme $x(p)$ values where:

$$y(p) > y_{marker}$$

The height of this line is arbitrarily chosen depending upon the range information we wish to investigate, in this case $y_{marker} = 1.5\, y_{max}$.

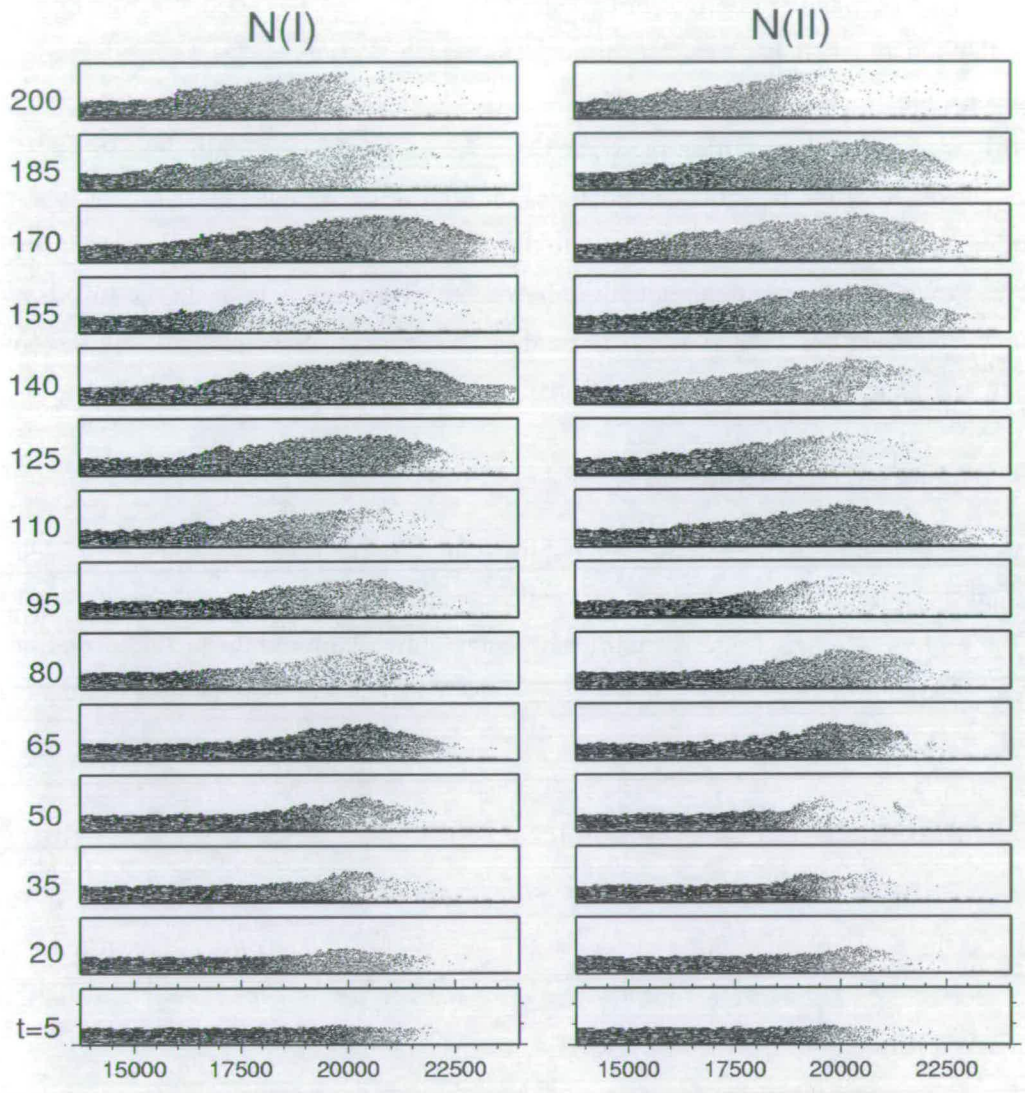

Figure 5.11: Plots of vector motion of particles in system over last three time increments. Discrete structures are clearly highlighted.

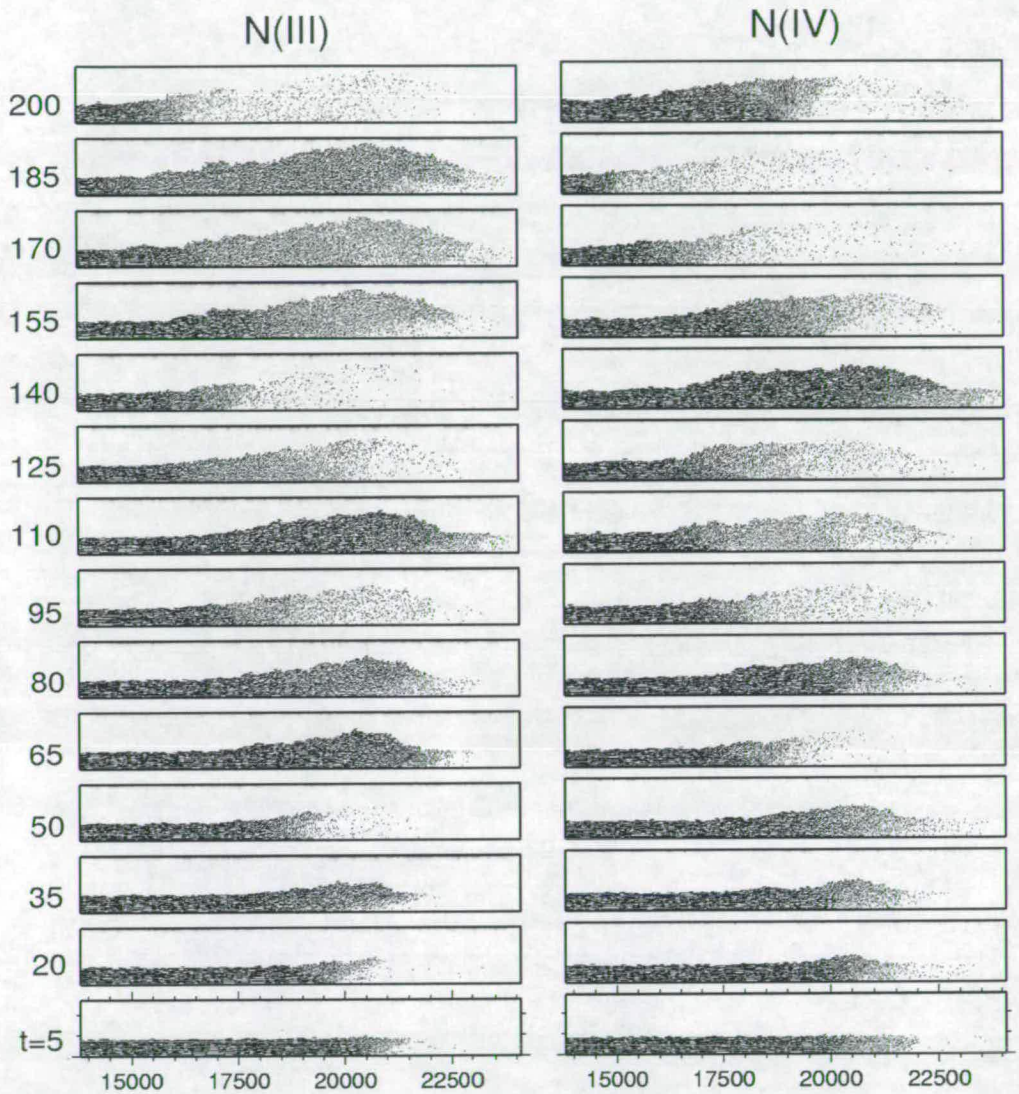

Figure 5.12: Plots of vector motion of particles in system over last three time increments. Discrete structures are clearly highlighted.

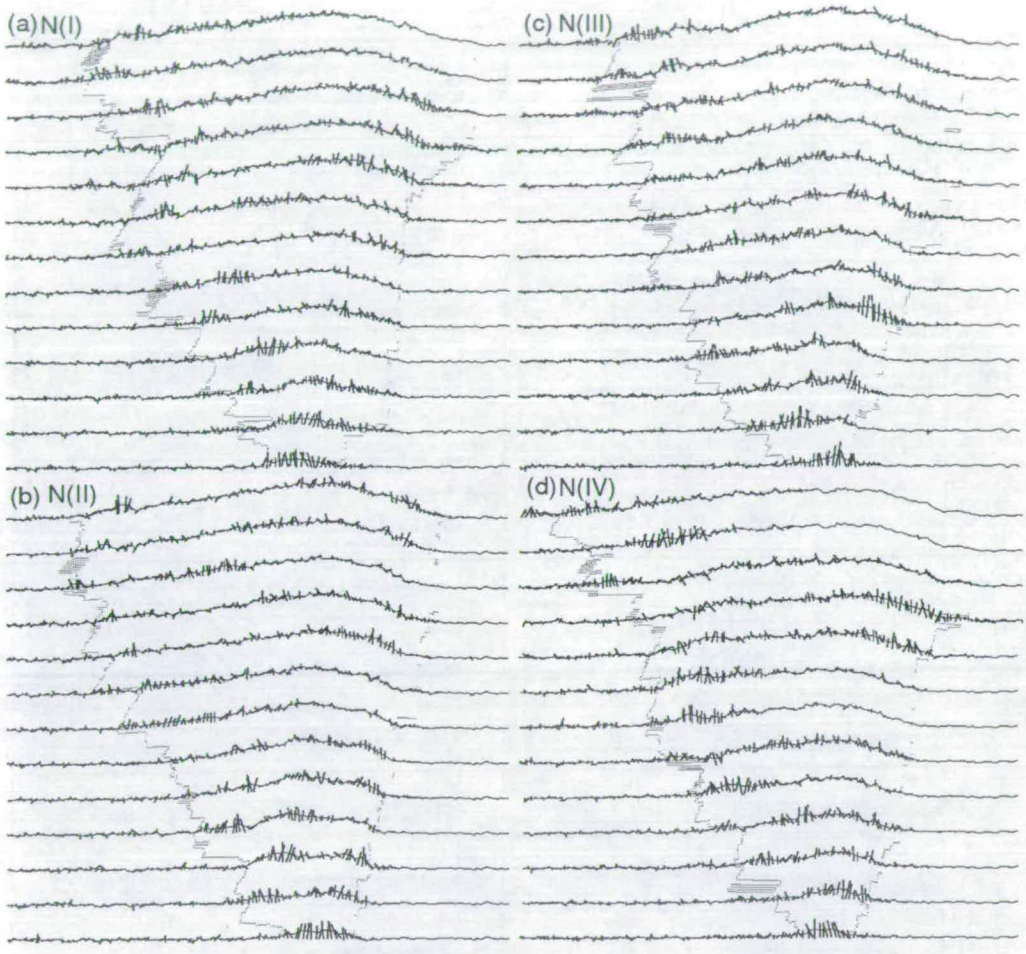

Figure 5.13: Time evolution of the topography with deformation front activity marked. (a), (b), (c) and (d) show the four different runs (N(I), N(II), N(III), N(IV)), with identical boundary conditions but whose random packings have a different seed. Uplift vectors along the upper surface show the localisation of deformation

- The *highest peak front* is $x(p)$ for the particle with the maximum $y(p)$.

The time evolution of these fronts for the four runs is shown in Figure 5.14(b)-(e), which indicate the couplings in the evolution of the pro- and retro-wedges. Superimposed on the pro-deformation fronts is an envelope that illustrates the Natural Variability we might expect around the background trend. This shall later be rigorously defined.

The relative motion of the deformation front and its corresponding marker give insight into the deformation of the part of the wedge between them. If the marker and the deformation front are becoming closer, deformation is occurring in the region between them, and this part of the wedge is steepening. If their positions are diverging, material is being accreted into this part of the system and the wedge is becoming shallower. If they are remaining at some constant separation, this part of the wedge is stable and neither accretion nor deformation has occurred.

The absolute position of these fronts describes the growth and deformation of the whole wedge. If the pro-deformation front is moving towards the interior of the wedge, the wedge is either shortening (Stage 2 deformation) or material is being accreted to the retro-wedge (Stage 3 accretion). If the pro-wedge deformation front is stepping out, a new thrust sheet is being accreted to the pro-wedge (Stage 2 accretion).

The pro-side deformation front propagates out more rapidly than the retro-side and maintains a shallower angle. As successive thrust sheets are accreted the pro-wedge grows quickly; followed by a period of shortening as they become incorporated into the more internal parts of the wedge, before the next accretion is propagated. There is no convergent force beyond the retro-wedge to drive the retro-deformation front back towards the interior of the wedge, thus the retro-deformation front only steps out as the wedge evolves. Convergence on the pro-side drives the internal deformation and shortening of the pro-wedge, producing the periodic accretion of successive thrust sheets.

As an example, we look more closely at inter-relationships between the deformation fronts and markers in Figure 5.15 for run N(I). Colour bars depicting whether the pro- and retro-wedges are widening and shallowing (dark grey), narrowing and steepening (light grey) or maintaining some constant width (pale grey) are added, these states are determined by the sign of the difference between $X_{Dp}(t)$ and $X_{Mp}(t)$ on the pro-side and $X_{Dr}(t)$ and $X_{Mr}(t)$ on the retro-side at some time t. Two horizontal black lines indicate the timings of the two major pro-side thrust sheet propagation events. Three key relationships are noted as (1), (2) and (3) in Figure 5.15.

1. The propagation of a new thrust sheet on the pro-side is preceded by a period of narrowing of the pro-wedge. This shortening over-steepens the wedge, requiring accretion beyond the pro-wedge toe to shallow it.

2. Similarly, we see that a large magnitude Stage 3 shallow retro-wedge accretionary event

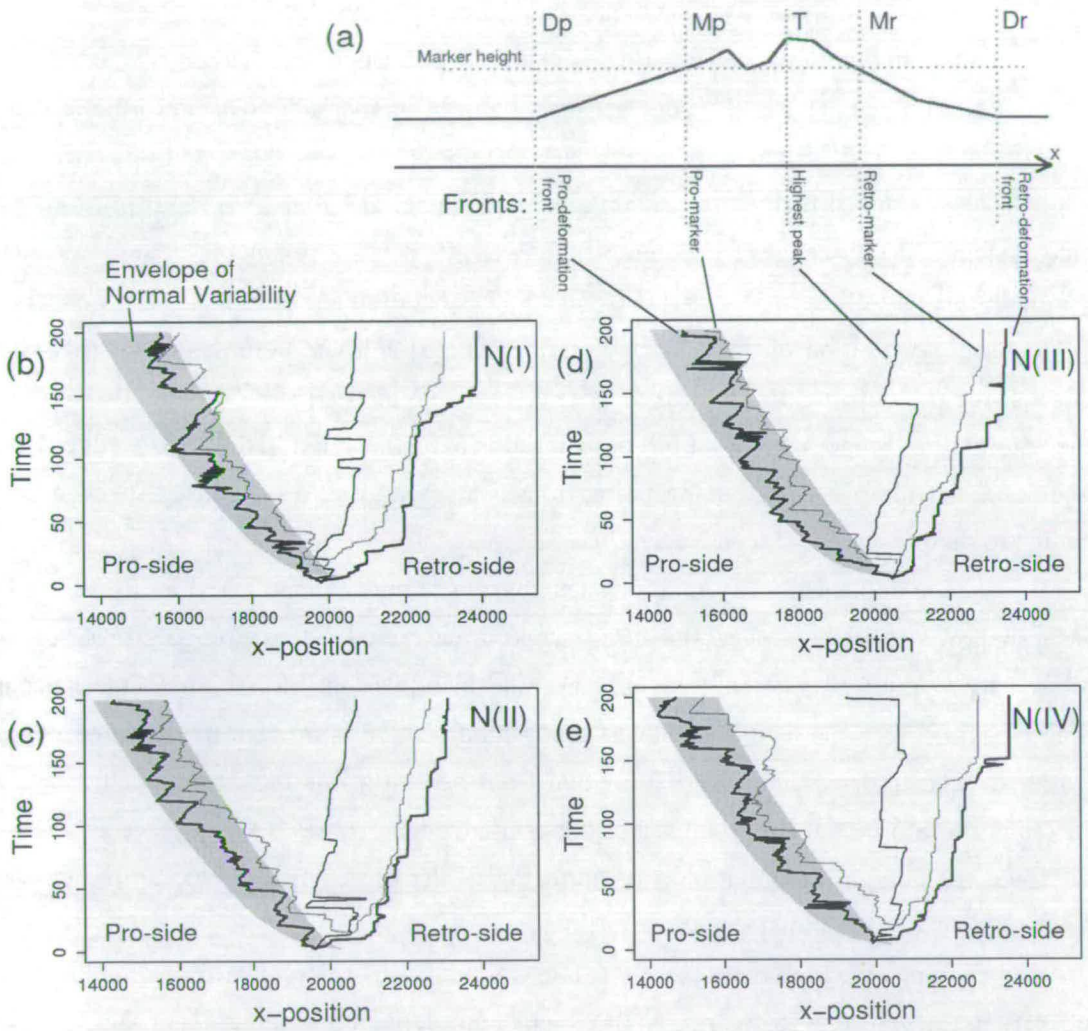

Figure 5.14: Time evolution of the x-position of points of constant elevation along the wedge surface. (a) shows the basic geometry of the data presented, the elevation of the marker height is $1.5\,y_{max}$. (b), (c), (d) and (e) show the time evolution of these markers for the same boundary conditions, but different random packing seeds. The envelope shows the expected Natural Variability within the pro-wedge deformation front.

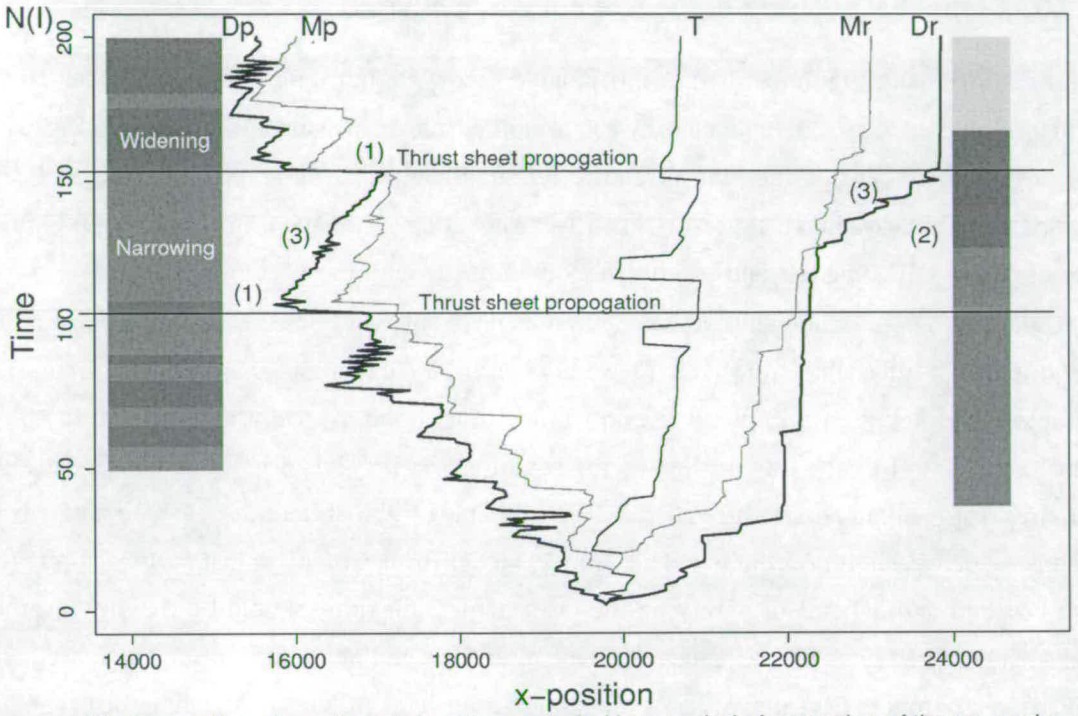

(1) Propogation of new thrust sheet is preceeded by a period of narrowing of the pro-wedge
(2) Retro-wedge accretion is preceeded by a narrowing of the retro-wedge
(3) Large retro accretion event is contemporary with pro-wedge advection towards axial zone

Figure 5.15: A closer examination of the evolution of N(I) from Figure 5.14(b) with some key events and relationships marked. Colour bars depicting whether the pro- and retro-wedges are widening (dark grey), narrowing (light grey) or maintaining some constant width (pale grey) are added.

requires the retro-wedge to over-steepen.

3. This large retro-wedge accretion event requires stable sliding of the whole wedge to transfer deformation beyond the tip of the retro-wedge, thus the pro-wedge deformation and marker fronts advect rapidly towards the retro-side. A weaker signal of the same event is also seen in the migration of the highest peak to the retro-side at this time.

5.4.6 Statistical analysis of the Normal Variability

All of the fronts in Figure 5.14(b), (c), (d) and (e) show similar long term trends when superimposed on each other, as indicated by the sketch envelope of Normal Variability. However, the deviations about this long term trend differ significantly. This rest of this chapter investigates how this variability expresses itself by conducting a statistical analysis of the Normal Variability in DEM models and by comparison with real settings (Section 5.5).

In order to better understand the evolution of the fronts we find some average background trend to use as a baseline from which we can measure the deviation of a particular front. The Simple Model (Section 5.2) predicts a power law fit with the exponent proportional to $t^{0.5}$. It can be tricky to fit such a trend line as the equation $y = ax^b$ has no y-intercept, it therefore requires that the data passes through $y_{x=0} = a'$. We must try to correct the x-position data back to this, which is slightly arbitrary. The Simple Model further predicts that factor $a = exp(a')$ is a constant and dependent purely on the taper angles, thus this should be roughly invariant between the fitted lines for the same boundary conditions and parametrisation. The noise in the highest peak front is the same order of magnitude as its background trend, using this technique on it produces a poor fit.

The steps taken to determine the background trends and Natural Variability can be summarised as:

1. Spatially average x-position of the deformation and marker fronts of Figure 5.14.

2. These trends are roughly extrapolated back to $t = 0$ to determine the offset of the power law function. This offset must be subtracted from the data before we can fit a power law (Figure 5.16).

3. Fit a linear regression to a log-log plot of the time evolution of the averaged trend lines once initial transients have subsided and errors are relatively small, for $t > 50$ output time-steps (Figures 5.17 and 5.18).

4. Define the Normal Variability to be within 2 standard errors of this trend line and plot results (Figures 5.19, 5.20, 5.21 and 5.22)

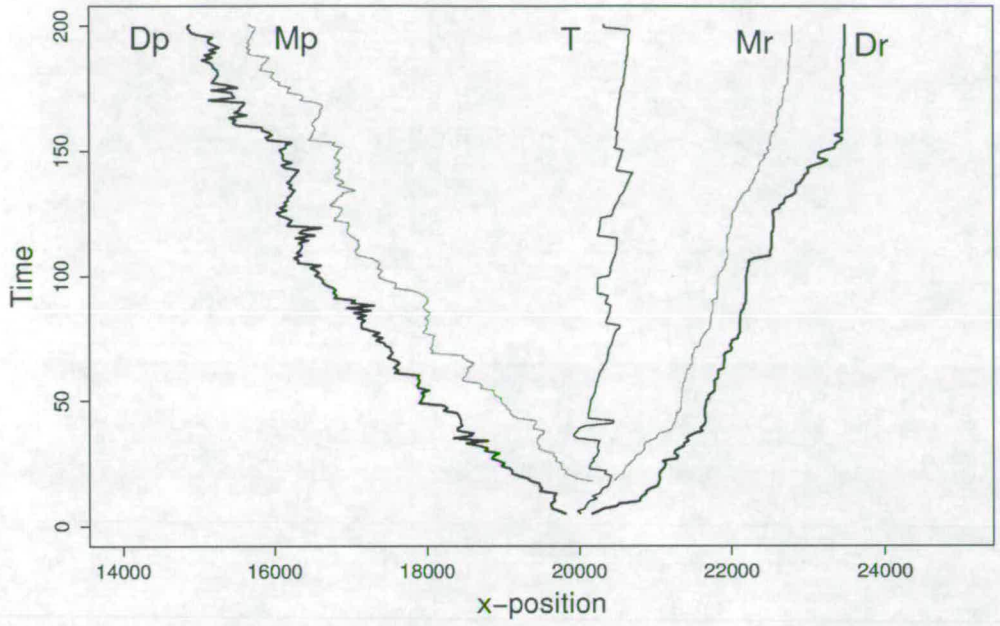

Figure 5.16: The evolution of the deformation fronts, marker lines and highest peak of Figure 5.14 are spatially averaged to show the background trends.

Deformation trend	Offset removed	exp(a')	st.err. a'	b	st. err. b	R^2	Residual st. err.
Dp	21000	6.06	0.0380	0.498	0.00792	0.964	0.0351
Mp	22000	6.13	0.0370	0.492	0.00772	0.965	0.0342
Dr	19500	5.60	0.0451	0.516	0.00942	0.953	0.0417
Mr	19500	5.56	0.0275	0.483	0.00575	0.980	0.0254

Table 5.1: Statistics on fitting of power law to spatially averaged deformation trends.

The coefficients and errors on the fitted lines are given in Table 5.1. Good agreement with the trends predicted by the Simple Model is achieved with the exponent for the growth of all fronts being approximately proportional to $t^{0.5}$ and a roughly constant value for the coefficient a. The offset introduced in order to fit the trend has been given, the choice was motivated by extrapolating the averaged fronts in Figure 5.16 back to $t = 0$.

From the Simple Model (Section 5.2), one would expect the coefficients $a = \sqrt{\frac{\tan\alpha \tan\beta}{2(\tan\alpha+\tan\beta)}}$. For reasonable wedge angles, one would predict $a \sim 0.1$. The predicted value is an order of magnitude less than the fitted values. There are a number of sources of error here, the main ones being the artificial offset and the fact that the wedge is not precisely two back to back triangles as assumed in the Simple Model. The exponent b is the more relevant and interesting parameter from the statistical analysis.

For clarity, the individual fronts and their corresponding Natural Variability trends have

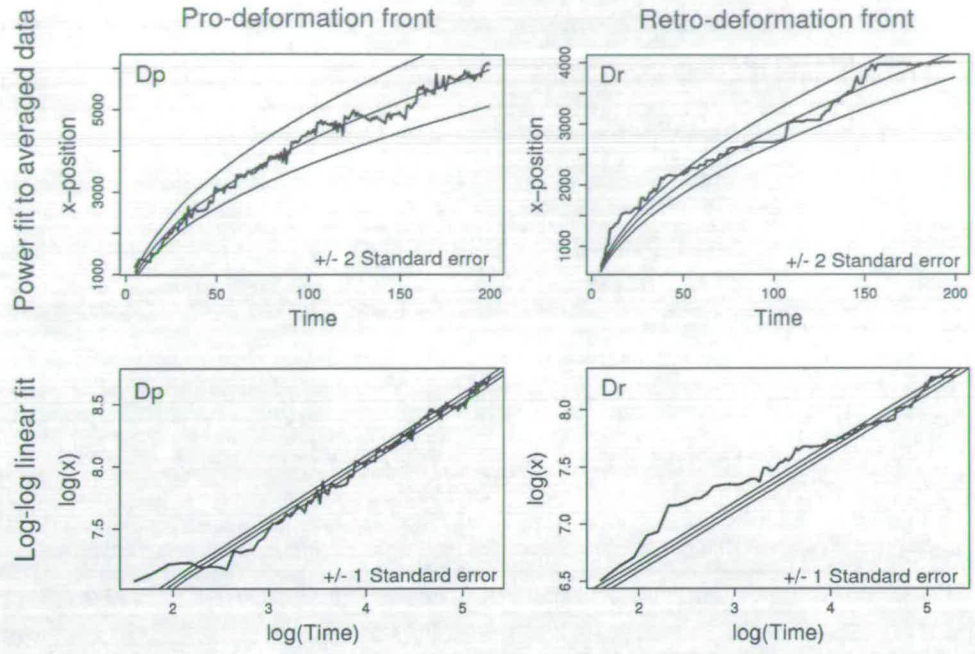

Figure 5.17: Trend lines fitted to the average pro- and retro- deformation front evolution of N(I), N(II), N(III) and N(IV). The fit is expected to be a power law. Coefficients and errors are presented in Table 5.1.

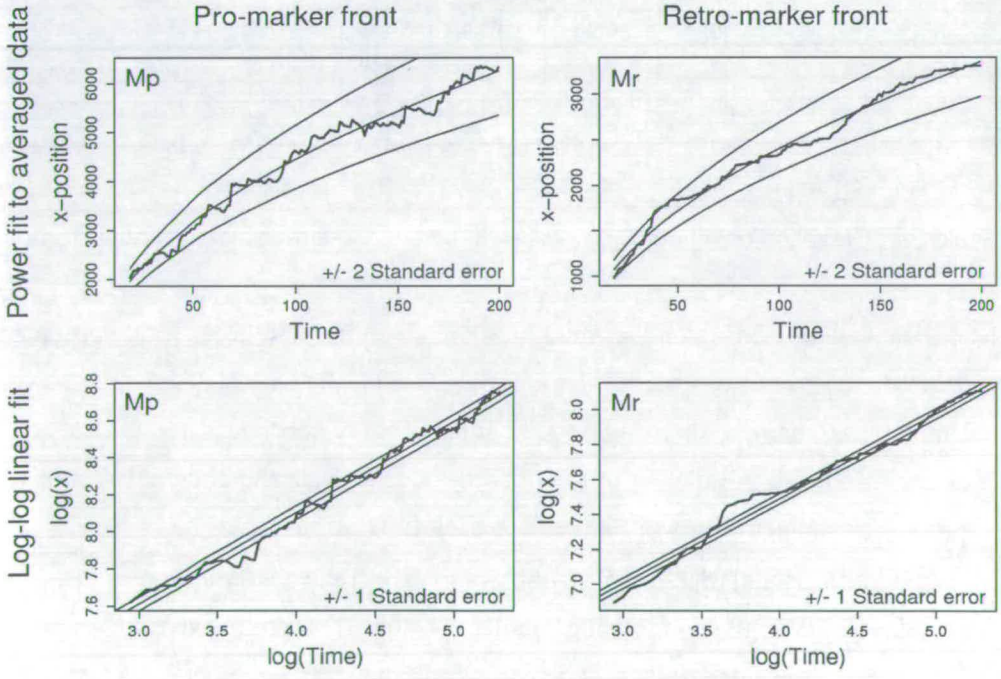

Figure 5.18: Trend lines fitted to the average pro- and retro- deformation front evolution of N(I), N(II), N(III) and N(IV). The fit is expected to be a power law and I only try to fit the data once the system appears steady (for $t > 50$). Coefficients and errors are presented in Table 5.1.

been plotted individually in Figures 5.19, 5.20, 5.21 and 5.22. These plots can be used in a number of ways to better interpret the evolution of the systems. The trend lines and envelopes of Normal Variability provide a framework in which we can describe whether the fronts deviate further out or in than the averaged expected behaviour. They allow us to correlate whether events between different fronts are linked.

Cartoon illustrations of possible correlations in front movement are presented in Figures 5.23 and 5.24. These depict the evolution of specific features. However, the model is only sampled every 25,000 model time-steps which will act to time average the data. Thus the model front evolution plots may not be as distinct.

If accretion of a new thrust sheet accommodates all of the convergence over some period, the wedge would experience no internal deformation. Thus the pro-deformation front would step out whilst all other fronts would remain stationary in space. For example: N(I) $t = 80$; N(II) $t = 198$; N(III) $t = 150$. The signal becomes less obvious if the accretion of the thrust sheet is contemporary with some internal deformation which will see the pro-deformation front step out more than the pro-marker. For example: N(I) $t = 105$. A lag between thrust sheet accretion causing a step out in the pro-deformation front and the pro-marker front is highlighted for N(IV) in the shaded blocks. A simple explanation for skewness in the propagation-advection cycle is illustrated in the cartoon Figure 5.23, where it becomes clear that the amount of convergence required to accrete a new thrust sheet of a given wavelength is significantly smaller than the convergence required to shorten the wedge by the same amount.

An illustration of front evolution for the N(I) Stage 3 retro-side accretion event, between $130 < t < 160$ in Figure 5.19, has been exploded in Figure 5.24. In order to achieve retro-side accretion, we require stable sliding of the whole wedge. This being the case, one would expect all of the fronts to move retro-ward, with the greatest movement to be localised on the retro-deformation front where the proportion of convergence being accommodated per unit total depth of wedge is at its greatest, i.e. to accommodate a convergence of area A the undeformed retro-surface must go up by a total area A which is more noticeable here than in the interior of the wedge where the material added would be insignificant compared with the total amount of material already present.

Figure 5.20 shows how different wedges can lie within the Natural Variability. Generally, the pro-wedge and retro-wedge are shifted further pro-ward than the trend-lines. This maintains the taper angles and just shifts the whole wedge within the acceptable limits.

5.4.7 Discussion

Convergence must be accommodated, if it is not accommodated in the pro-wedge, it must be accommodated through internal thickening or retro-side accretion. In describing the evolution of the deformation fronts and markers in Figure 5.13 we must try to extract the processes and

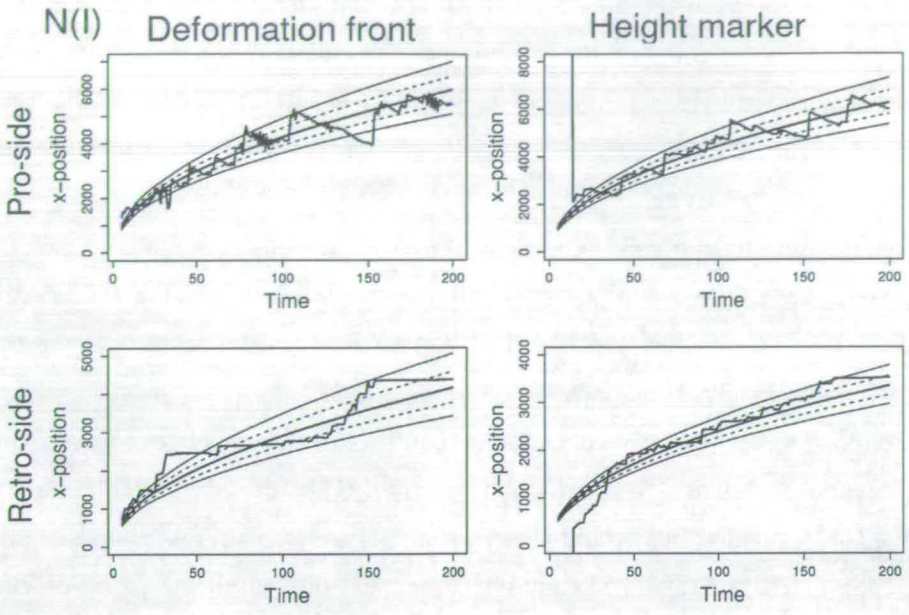

Figure 5.19: Graphs of the time evolution of the pro- and retro- deformation and height marker fronts for the run N(I). Trendlines averaged over the four runs have been added to indicate the background Normal Variability. The dashed lines are with +/- 1 standard error and the outer solid lines +/- 2 standard error.

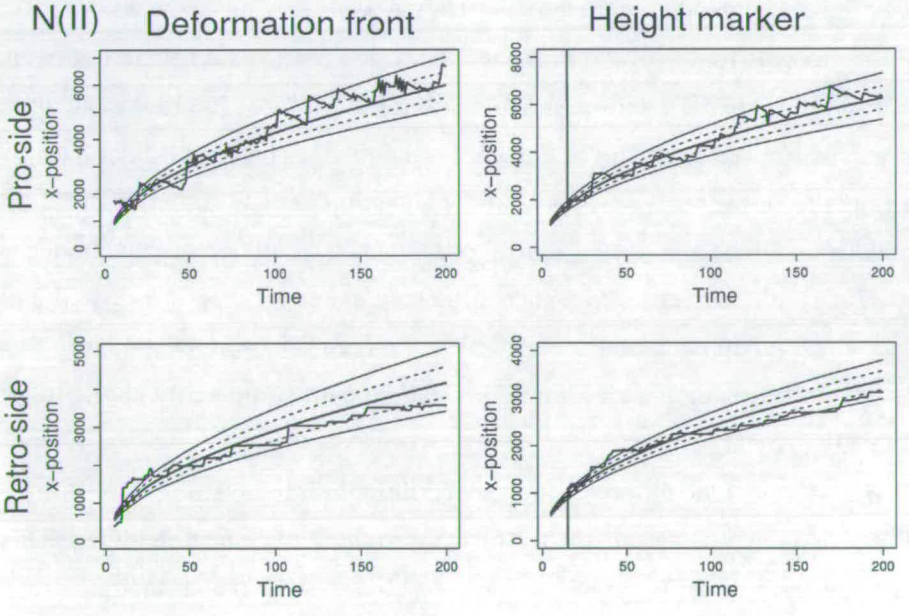

Figure 5.20: Graphs of the time evolution of the pro- and retro- deformation and height marker fronts for the run N(II). Trendlines averaged over the four runs have been added to indicate the background Normal Variability. The dashed lines are with +/- 1 standard error and the outer solid lines +/- 2 standard error.

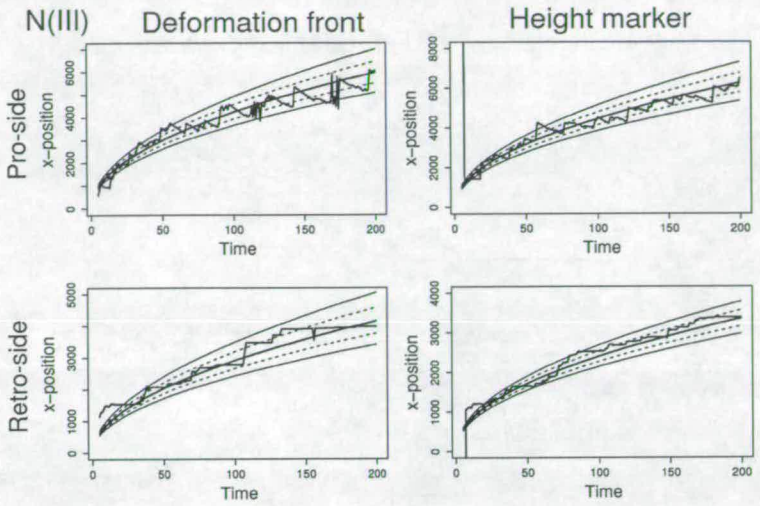

Figure 5.21: Graphs of the time evolution of the pro- and retro- deformation and height marker fronts for the run N(III). Trendlines averaged over the four runs have been added to indicate the background Normal Variability. The dashed lines are with +/- 1 standard error and the outer solid lines +/- 2 standard error.

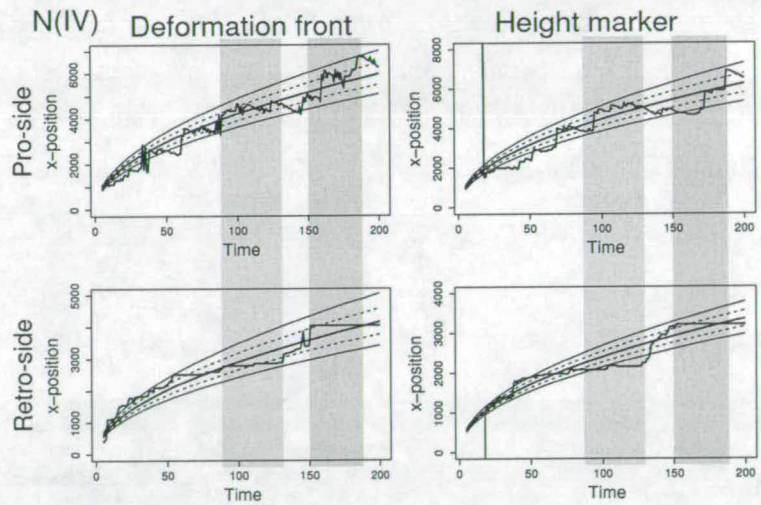

Figure 5.22: Graphs of the time evolution of the pro- and retro- deformation and height marker fronts for the run N(IV). Trendlines averaged over the four runs have been added to indicate the background Normal Variability. The dashed lines are with +/- 1 standard error and the outer solid lines +/- 2 standard error. The grey bars correlate periods of inactivity in the retro-wedge with periods of activity in the pro-wedge deformation front. The retro-wedge deformation front and marker front are much more closely correlated than the pro-side pair.

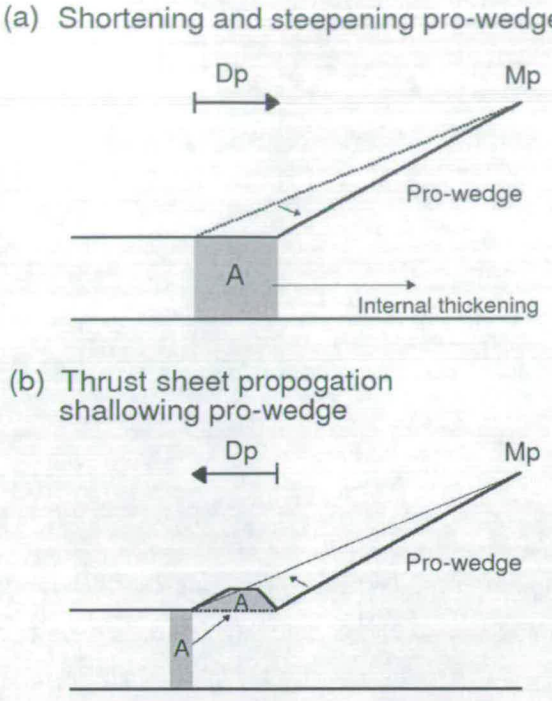

Figure 5.23: Illustration to indicate the amount of convergence required to (a) propagate and (b) completely incorporate a new thrust of a given length. Dp and Mp indicate the position of the pro-side deformation and marker fronts. Significantly less convergence is required to propagate the thrust sheet which accounts for the saw tooth pattern superimposed of the power law background trend in Figures 5.19 to 5.22.

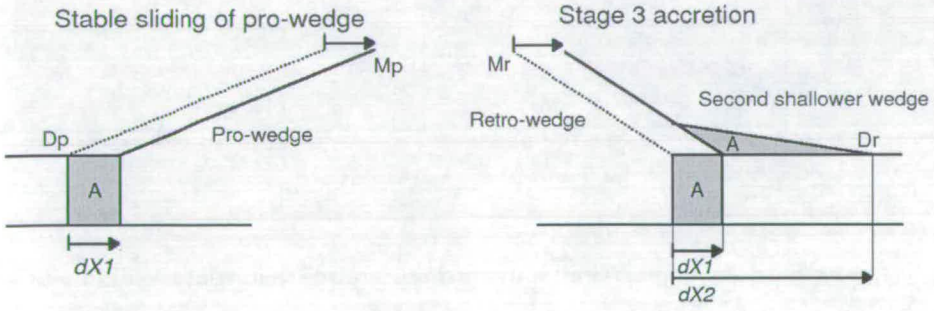

Figure 5.24: Illustration of the evolution of the fronts during the Stage 3 accretionary event in N(I) $130 < t < 160$. Stable sliding of the whole wedge results in a large step out in the retro-deformation front, accreting a second shallower wedge.

relationships governing the evolution. The first order trend of the deformation fronts is for them to diverge as the wedge accretes more material. This accretion produces a background trend proportional to $\approx t^{0.5}$. Removing this trend, on the pro-side we see periodic saw tooth deformation. It rapidly steps out before gradually advecting back towards the interior of the wedge. This cycle is the propagation and incorporation of successive thrust sheets.

Fluctuations in the localisation of uplift within the wedges were highlighted in Figure 5.13. We observe localisation of deformation across well defined structures. The modelling demonstrates that high erosion rates are not required to localise deformation, regular fluctuations in deformation are an emergent phenomenon.

The amount of convergence required to propagate a new thrust sheet of a given wavelength (Figure 5.23(b)) is significantly less than the convergence required to shorten the wedge by the same wavelength (Figure 5.23(a)). Thus, thrust sheet propagation is a much more rapid event than wedge shortening.

Pro- and retro-deformation is coupled for the case of a non-erosive wedge. On the most basic level, this is implied by the necessity to maintain some critical form. When we examine the timings of deformation in the pro- and retro-wedges, we see that the coupling is stronger. The best example is shown in Figure 5.15 where growth of the retro-wedge between $125 < t < 150$ requires stable sliding of the whole wedge to propagate the front (Figure 5.23). This retro-deformation front step out is the largest magnitude of the four shown. The event is so large because it was preceded by the retro-deformation front lying at the minimum end of the Normal Variability envelope; it required a large jump to maintain Normal Variability.

5.5 Comparison with Pyrenees - 1D Natural Variability

The Pyrenees provides a good example with which to compare both the geometry and processes described above for the Normal Variability of doubly-vergent wedges. In this case we examine a 1D cross section in the central Pyrenees running from south (pro-side) to the north (retro-side) (Figure 5.26).

5.5.1 Geological setting - Background on Pyrenean orogenesis

Around 84 Ma the Iberian continent collided with the over-riding Eurasian continent, partially closing the Bay of Biscay (Boillot and Capdevila, 1977) and initiating the growth of the Pyrenees that lasted from late Cretaceous to early Miocene times (Roest and Srivastava, 1991). The North Pyrenean Fault forms the suture and is believed to have developed during sinistral displacement of Iberia. At least 165 km of shortening is recorded in the restored cross section of Munoz (1992). The subduction of the Iberian plate to the north has been inferred from the ECORS deep seismic reflection profile (Choukroune and Team, 1989) and other geophysical

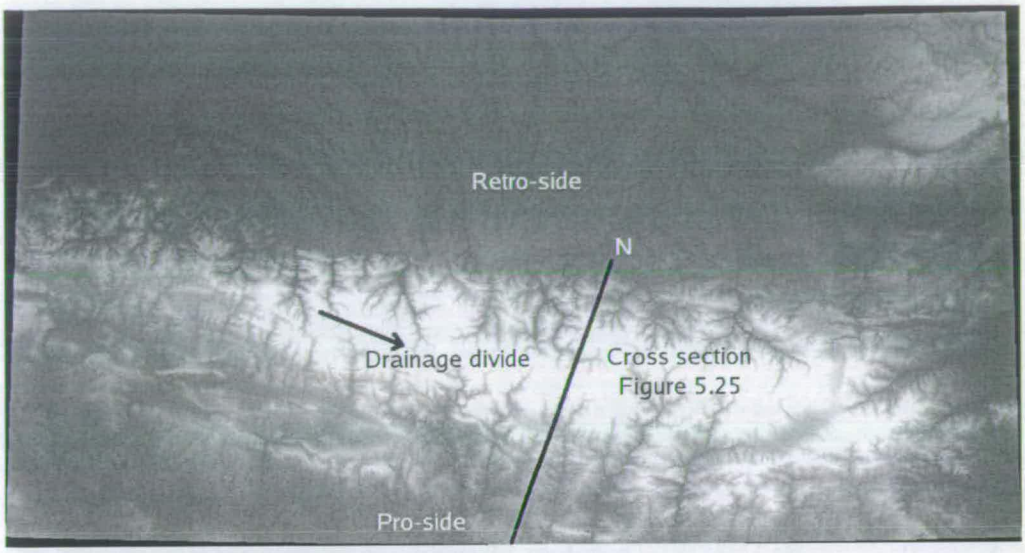

Figure 5.25: Digital elevation model of the Pyrenees

evidence (Pous et al., 1995). The modern orogen is approximately 150 km wide, with the Axial Zone (believed to be a major antiformal stack) dominated by Hercynian basement flanked by thin-skinned fold-and-thrust belts (South Pyrenean Fold and Thrust Belt to the south and the Sub-Pyrenees to the north) and associated foreland basins (Ebro Basin to the south and the Aquitaine Basin to the north). The southern exposure of the Nogueres Zone is the tip of the uppermost thrust sheet in the antiformal stack and forms a narrow region of Carboniferous to Triassic sediments that separate the South Pyrenean Fold and Thrust Belt from the Axial Zone (Séguret, 1972; Munoz et al., 1986).

During late Eocene and Oligocene times, the south Pyrenees were draped with up to 2 km thick sequences of sediments and conglomerates, with an associated base-level rise in the Ebro Basin. It is known that the Axial Zone was exposed at this time, as granitic and metamorphic clasts are found in the conglomerate.

5.5.2 Modern-day geometry

The geometry we see today is the result of erosion acting on the Pyrenees for 20 Myr since convergence ceased. I define the pro-wedge, axial-zone and retro-wedge with respect to the modern day geometry, but acknowledge that these may well not delimit the paleo-geometry. The modern-day drainage divide may be different to the paleo-divide when the orogen was last active, however we know that the paleo-drainage divide must have been located within the present-day Axial Zone based on the provenance of pebbles from Oligocene and Miocene sediments in the Ebro and Aquitaine Basins (Vergés et al., 1995; Mellere, 1993). The analysis of accretion will focus on the South Pyrenean Fold and Thrust Belt and the Sub Pyrenees.

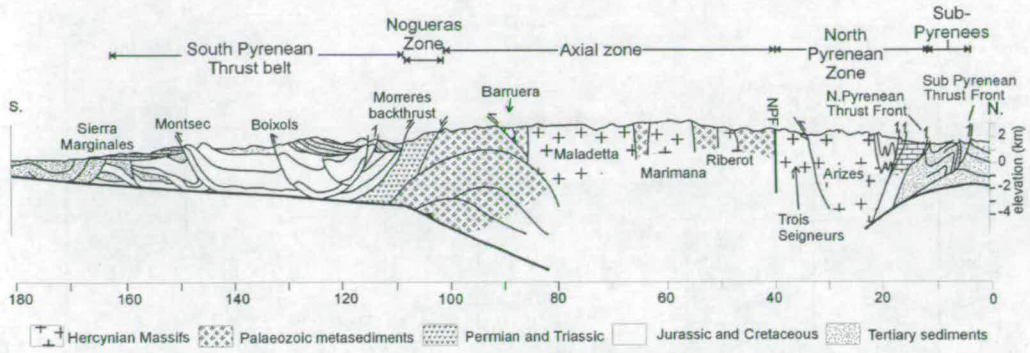

Figure 5.26: Modern day geological cross section through the Pyrenees (Modified from Sinclair et al., submitted)

Much of the evolution described here is summarised in the chronostratigraphic figure modified from Sinclair *et al.* (submitted, Figure 5.27).

5.5.2.1 Modern pro-wedge

The pro-wedge in the central Pyrenees, defined to be the South Pyrenean Fold and Thrust Belt, was formed by the successive accretion of the Boixols (60Ma), Montsec (50Ma) and Sierra Marginales (36-30Ma) thrust sheets, (Séguret, 1972; Meigs et al., 1996; Meigs, 1997) as the thrust front propagated south into the Ebro Basin. These detached along Triassic evaporites and contain thick sequences of Mesozoic carbonates and Palaeogene siliciclastic rocks in their hanging walls. They bound the Pobla, Ager and Tremp basins which contain syn-tectonic Tertiary sediments that have been used for documenting the history of thrust activity (using thinning strata, onlap, intraformational unconformities, growth strata and similar stratal relationships) (e.g. Mutti and Sgavetti, 1987; Deramond et al., 1993; Mellere, 1993; Beamud et al., 2003). The Boixols thrust sheet is the thickest at 5 km. A minimum displacement of 10 km on the 2 km thick Monsec thrust is well constrained by Comiols oil well data and from cut-off points in the hanging wall (Munoz, 1992). The Sierra Marginales thrust sheet is interpreted to have had slid stably for approximately 30 km from 37.0 to 29.5 Ma (Meigs, 1997). There has only been approximately 1.2 km of shortening to the south of the Sierra Marginales thrust sheet since 30 Ma (Meigs, 1997), on relatively minor structures that locate the pro-side deformation front. During Oligocene to early Miocene times the entire flank of the orogen was draped with up to 2 km thick conglomerates, some of which are still preserved in extensive formations (such as the Pobla de Segur or Sis Conglomerates) and high terraces give some indication of the complex erosional history of the range.

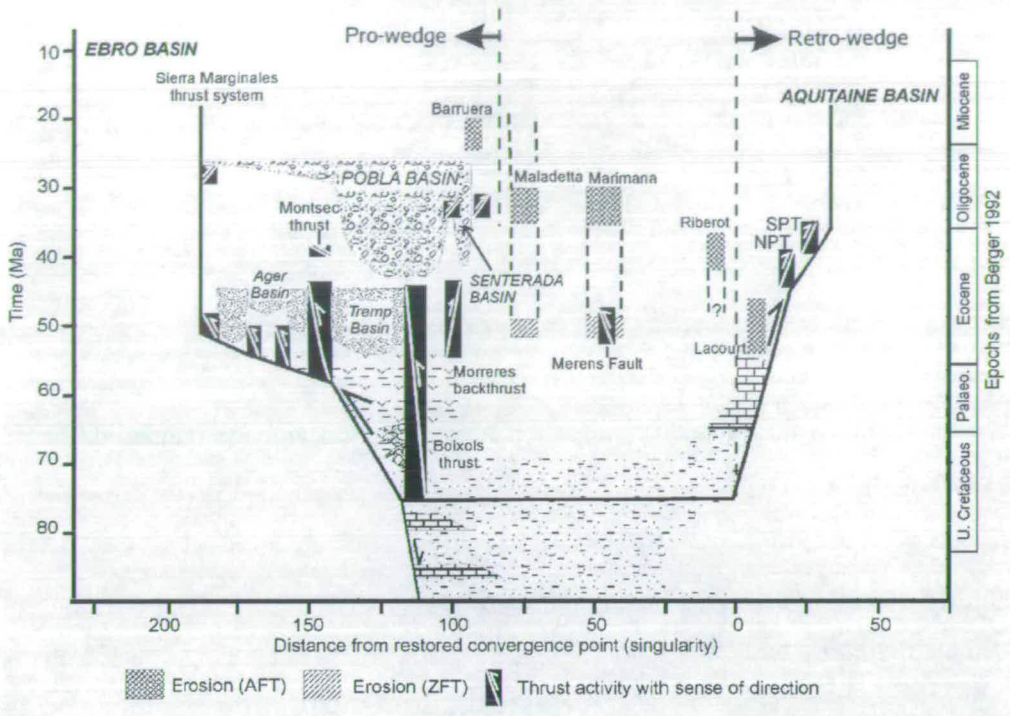

Figure 5.27: Chronostatigraphic evolution of the Pyrenees. (Modified from Sinclair *et al.* Submitted)

5.5.2.2 Modern axial zone

The Axial Zone is bound to the south by the Nogueres Zone and to the north by the North Pyrenean Fault, which is interpreted as the suture between the European craton and the Iberian craton (Fischer, 1984). It comprises numerous upper-mid crustal igneous and high-grade crystalline basements, ideal for thermochronometry, and forms a south vergent antiformal stack (Munoz, 1992), the main thrust sheets being the Rialp, Orri and Nogueres (from lower to upper). The geometry of the antiformal stack is defined through the arrangement of back rotated thrusts and faults. Currently exposed are a series of granitic massifs (e.g. Maladeta, Marimaña and Riberot), as they are more resistant to erosion they currently form the highest peaks and are a strong control on the modern watershed.

5.5.2.3 Modern retro-wedge

To the north of the Axial Zone lies the North Pyrenean Zone, where elevation drops quickly to the North Pyrenean Thrust front, which thrusts over the Sub-Pyrenees. The Sub-Pyrenees are a shallow, narrow strip of thin-skinned accretion of Tertiary foreland basin strata, bound to the north by the Sub-Pyrenean thrust front (Deramond et al., 1993). Within the North Pyrenean Zone lies the Arizes massif, that forms a pop-up structure overthrusting at both sides.

5.5.3 Comparison and interpretation

Many of the features documented in the Pyrenees compare well with the DEM modelling (Table 5.2).

I take the model pro-wedge region to be that part of uniform taper overlying the subducting plate. The model deformation front evolution plots (Figure 5.13) show how the thrust front propagates out in a series of episodic events to shallow the taper, separated by periods of pro-wedge shortening. This is analogous to the evolution of the Boixols, Montsec and Sierra Marginales thrust sheets which propagated at approximately 10 Myr intervals. The modelling suggests that their propagation was likely to have been a relatively rapid event compared to the internal thickening that followed.

The model axial zone is the central portion of the wedge over which the wedge taper changes between pro-vergent to retro-vergent. What we define to be the axial zone determined geometrically does not coincide with the lithologically defined Axial Zone of the Pyrenees. Placing an axial zone into the Pyrenees, as defined geometrically, would position the northern extreme near, but not much further north, than the Marimaña massif. This places the North Pyrenean Fault suture well within the retro-wedge for the modern system, and as there is no evidence for the drainage divide to have been significantly further northward at the end of the orogenic event (20 Ma), within the retro-wedge for the paleo system as well. The divide between the initial pro- and retro-material in the model was illustrated by a change in shading in Figures 5.3 and 5.6. This modelling agrees with the modern analogue as the transition is advected into the model retro-wedge. Within the model axial zone, thrust sheets have undergone significant thinning and rotation as the wedge developed, similar to the formation of the antiformal stack within the Pyrenees. The main difference between the modelling and the Pyrenees is the nature of how the sheets were incorporated, in the Pyrenees this was by underplating of the Orri and Rialp thrust sheets resulting in a more vertically stacked pattern, rather than by frontal accretion assumed in the modelling, which generates more horizontal stacking.

Mean elevation drops off rapidly between northern most limit of the geometrically defined axial zone and the North Pyrenean Thrust Front and experiences relatively little deformation. This is in agreement with the model retro wedge which shows much steeper angles than the pro-wedge and much less deformation than the pro-wedge. The Sub-Pyrenees are much shallower and represent a later accretionary event, in a similar manner to the Stage 3 second shallow retro-wedge accretion, during a period of inactivity on the pro-wedge.

A comparison of the evolution of model deformation fronts from Figures 5.13 and 5.14 with the chronostratigraphic evolution of the Pyrenees (Figure 5.27) highlights problems with how the chronostratigraphic plots illustrate the evolution of the pro- and retro-deformation fronts. It is important to understand the frames of reference used in constructing the chronostratigraphic figure (Figure 5.27). The positions of the pro- and retro-deformation fronts are

Stage	Model feature	Pyrenean analogue
Stage 1	Steep retro-wedge	N. Pyrenean Zone
	Retro-vergent thrust	N. Pyrenean Thrust Front
	Pro-retro material suture in retro-side	N. Pyrenean Fault
Stage 1-2	Transition between pro-retro wedges	Axial zone
Stage 2	Pro-wedge fold and thrust belt	S. Pyrenean Thrust Belt
Stage 3	Second shallower retro wedge	Sub-Pyrenees
	Shallow wedge thrust front	Sub Pyrenean Thrust Front

Table 5.2: Comparison between model features described in Chapter 4 and Pyrenean analogue

measured relative to an observer stood on the pro- or retro-plates respectively. This means that the deformation front can only get nearer to the observer and is always seen to step out. The plot does not give an indication of the time evolution of the true width of the orogen (the distance between the two deformation fronts). Figure 5.14 shows how we might expect the true width of the orogen to vary. The orogen will only grow in size if material is accreted to the pro-side by the propagation of a new thrust sheet or by the accretion of material into the second shallower retro-wedge. Given some constant convergence, the wedge can only remain the same width if the incoming material is completely underthrust and underplated into the interior of the orogen. If material is not being accreted into the wedge, the width of the wedge must be shortening. These conclusions are not evident from Figure 5.27.

To consider the change in the width of an orogen, let $dX_p(t)$ and $dX_r(t)$ be positive numbers equating to the step out in the pro- and retro-deformation fronts and $dX_i(t)$ be a negative number equating to the amount of shortening of the wedge due to internal deformation at some time t (Figure 5.28). X_p steps out periodically in discrete units of $dX_p = \lambda_{thrust}$. As the new thrust sheets are rotated and incorporated into the wedge, it narrows ($dX_r < 0$).

If $dX_r + dX_p + dXi > 0$ then net growth of wedge occurs.

If $dX_r + dX_p + dX_i < 0$ then net shortening of wedge occurs.

If we can constrain the timings of pro-side thrust propagation and retro-side accretion, and we can measure the magnitude and timing of internal deformation in the field, we can constrain periods of widening and narrowing of the wedge.

The restored cross section from Munoz (1992) suggests that the Boxiols and possibly Montsec thrusts were formed at the tip of the Orri and Rialp thrust sheets respectively. These thrust sheets then underthrust the fold and thrust belt and are underplated into the axial core. Thus there is a shallow structure ($\sim$ 10 km) across which motion is poorly coupled, the lower basement driving the fold and thrust belt. There will be times when an observer on the over riding plate will be moving towards the tip of the pro-wedge, with low deformation of the fold

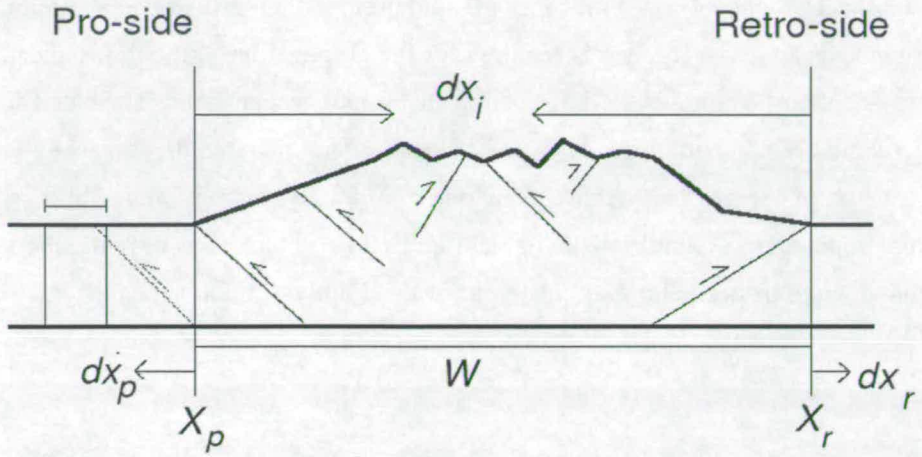

Figure 5.28: Variables contributing to growth and decay of wedge width.

and thrust belt. This being the case, the shortening experienced by the pro-wedge is an underestimate of the total amount of convergence which requires a knowledge of the amount of internal thickening due to underplating, as was attempted by Munoz (1992). This raises important implications regarding the nature of appropriate boundary conditions applied in orogenic modelling.

The next Chapter investigates how erosion perturbs the Normal system, again using the Pyrenees as an onshore analogue.

5.6 Discussion and conclusions

In summary, we introduce the term Natural Variability to describe the range of behaviour that might be expected and is common to a particular system. Departures from this Natural Variability can then be identified. Such information might constitute a range of parameter space within which a system might be expected to lie, but then we make an observation which requires a parametrisation that lies outside that space. Such an observation requires that we either find out whether we have the normal parameter space defined correctly or that we can identify the cause for the departure. I have given a definition and justification of Normal Variability using the Simple Model, a statistical analysis of DEM modelling and by application to field examples. For example, I have shown that the models grow proportional to $t^{0.5}$ as predicted by the Simple Model.

Episodicity in localisation of deformation is part of the natural cycle for the growth and evolution of doubly-vergent wedges, the record of which we should expect to interpret from field studies. Thus, erosion is not a pre-requisite for localised deformation, although it may enhance the signal. I shall explore the role of erosion further in the next chapter.

Thrust sheet propagation is a much more rapid process than pro-wedge shortening over the same distance as less convergence is required for the propagation of the thrust sheet.

There are many examples of deformation in the pro-wedge being attributed to a special case reactivation of some inherited structure. We have demonstrated that this is nothing special and is just part of the normal, cyclic behaviour of a doubly-vergent wedge and as such does not require some special conditions to explain it. Extra complexity is only required to explain events that deviate from the normal behaviour of the doubly-vergent system.

Chapter 6

Investigation into the response of the doubly vergent wedge to erosion

Erosion and deposition are generic terms for the surface processes by which mass is redistributed in a wedge. The changing load at the surface modifies the stress distribution within a wedge, feeding back into the tectonic evolution of the system. In turn, the localised uplift encourages further localisation of erosion. This has been demonstrated computationally (Willett, 1999) and tested in the field with varying degrees of success (Molnar, 2003).

6.1 A brief history of erosion modelling

The relief structure of unglaciated mountain landscapes is mostly set by bedrock channels, which convey signals of tectonic and climatic change through the system (Whipple and Tucker, 1999; Whipple, 2001). The incision rate of bedrock channels controls the landscape denudation rate as it forms the lower boundary condition for all hillslopes. It is generally accepted that bedrock channel incision rate is dependent upon lithology, tectonic setting, climatic conditions and topographic relief (Howard et al., 1994; Tucker and Slingerland, 1996; Tucker and Bras, 1998; Whipple and Tucker, 1999; Tucker and Whipple, 2002). There has long been an emphasis on transport-limited processes (e.g. Mackin, 1948). However, the recent focus on detachment-limited incision forms a significant departure. It is widely recognised that a simple classification of river types into primarily detachment- or transport-limited systems is problematic in the field. For example, bedrock that is covered with a layer of sediment or cobbles may become detachment limited in extreme flood events. The question then becomes, which of these mechanisms is the dominant erosive mechanism? Further, different segments of a river profile may simultaneously be limited by different processes.

Modelling efforts have reflected the evolution in understanding river systems. Early efforts utilised simple diffusion modelling to attain characteristic concave profiles. As theory

developed, models explored more complex transport-limited, detachment-limited and hybrid systems. Modelling of both 1D stream profiles assuming some dependence of catchment area upon down stream distance (Hack's Law) and erosion of 2D evolving topographies has been done (e.g. GOLEM by Tucker and Slingerland, 1994, 1997). True tectonic-erosion coupled models are still limited by computational considerations.

When applying any of these models to real systems it is important to understand the implications of the underlying assumptions of each type of model. Modern testing of different erosion models utilises the response of model systems to transient pulses against real settings, as the endpoints are rarely distinct. One equilibrium concave profile looks much like another. It is how the system got there that is important. This reflects the difference in time-scales that are observable in the modern system versus the long term evolution.

6.2 Simple model extended to erosion

We generalise the simple model presented in Section 5.2 to include an erosive flux. Assuming all eroded material is instantaneously removed from the system, a flux steady state will be attained when the time averaged erosional removal of material balances the flux of material into the wedge due to shortening:

$$v h_0 = \int \dot{e}.dx \tag{6.1}$$

As more material is incorporated into the wedge, the rate of mean surface uplift decreases (proportional to $S^{0.5}$) and the total amount of surface area available to be eroded increases (the x-limits of the integral in Equation 6.1 diverge). This increase in erosion and decrease in uplift allows a time averaged flux steady state to be attained after an initial period of wedge growth.

We can further generalise the model to allow for the recycling of a proportion of eroded material, γ that is deposited in the foreland generalising Equation (6.1) to Equation (6.2). Well documented examples of this process are found in the European Alps, where Cenozoic and Mesozoic sediments of the Po and Molasse basins have been successively reincorporated into the interior of the orogen through the propagation of new thrust sheets into the basins (Sinclair, 1997). A flux steady state now requires that the amount of material removed from the system balances the constant accretionary flux, including the proportion of recycled material:

$$v h_0 = (1-\gamma) \int \dot{e}.dx \tag{6.2}$$

In summary, orographic enhancement of erosion and the reduction in mean rock uplift rate as the wedge becomes large, provides a mechanism for the system to tend to a flux steady state.

6.3 The erosional algorithm

Given that generating a full 3D coupled tectonic-surface process model is beyond the scope of this project, the system will be investigated using a very simple erosional algorithm that removes all particles above some threshold elevation. The threshold will be quoted as a multiple of h_0, the mean height of the undeformed surface. This scheme is an extreme end-member scenario to be compared with non-erosive model runs. The previous chapter demonstrated that localised erosion is not a pre-requisite for localised uplift. However, I show here that erosion will change the locus of that localisation. Plots of the evolution of the normal variability of the deformation fronts deviate from the non-erosive case as a time averaged flux steady state is achieved, but still maintain the same degree of variability.

6.4 Results of DEM simple erosive scheme

The erosive experiments use the same boundary conditions as the non-erosive experiments so a direct comparison between the results can be made. During each model time-step, the erosional algorithm determines the mean elevation of each particle and removes any particles that lie above some threshold elevation. The height of this threshold is varied and repeat runs are done varying the random packing seed to check for consistent results. E(I) and E(II) refer to two repeat runs with the erosive threshold at $1.5h_0$, while E(III) and E(IV) are repeat runs with the erosive threshold at $2.0h_0$. These four runs will be discussed in the first half of this Chapter as an introduction to the behaviour of the longer runs, E(V) and E(VI), which ran for 636 output time-steps with an erosion threshold at $2.0h_0$. This allows a more complete investigation of the time averaged flux steady-state regime to be made.

6.4.1 Deformation of horizon plots

The time evolution of initially undeformed horizons are presented for E(I) and E(II) in Figures 6.1 and 6.2 with an erosive threshold at $1.5h_0$ and for E(III) and E(IV) in Figures 6.3 and 6.4 with the threshold at $2.0h_0$. Until the wedge has reached the erosive threshold, it evolves identically with the non-erosive runs investigated in the previous chapter. Once the erosive threshold is reached and material is removed from the wedge, the background evolution of the system changes. The width of the upper erosive surface rapidly grows laterally tending to some optimal width where the flux of incoming material balances the flux of eroded material. At this point the retro-wedge becomes relatively inactive and deformation becomes localised on the pro-side of the wedge. Specific thrust sheets have been tracked through Figures 6.1 and 6.4 by labelling them with letters.

The horizons highlight the depth from which material exhumed to the surface has orig-

inated. The regular, well nested trend would be for the original surface material to become successively deeper towards the centre of the wedge, and mirrored on both sides. However, run E(IV) at $t = 200$ (marked with a star in Figure 6.4) shows that this trend is not always observed. The preferential erosion of a peak at the top of the pro-wedge has exposed deeper material than the material bounding either side, as is commonly observed in real systems. The figures suggest that the deepest rocks (analogous to the highest grade metamorphic rocks) are skewed to the retro-side of the axial-zone. Eroded material on the pro-side of the axial-zone is replaced by shallow material accreted from the pro-wedge.

6.4.2 Interpretation of deformation front plots

The x-limits of the deformation fronts and the erosive surface are plotted in Figure 6.5. Superimposed on these plots are sketch-envelopes of Normal Variability for the pro-wedge deformation front, which highlight the contrast in evolution between the erosive and non-erosive model wedges. Once the erosive threshold has been reached, the wedge rapidly tends to a flux steady state where the retro-wedge becomes dormant and the pro-wedge fluctuates around some mean value. The pro-wedge fluctuations show a repeating asymmetric cycle of rapid propagation of the deformation front followed by a slow retreat back into the wedge as it shortens. This pulsed influx of material into the wedge is carried through the pro-wedge and removed at the upper surface completing the time averaged flux balance.

The evolution of the pro-wedge fronts for runs E(I) and E(II) are examined in greater detail in Figures 6.6 and 6.7. Once the wedge has attained steady state, the height of the pro-wedge is the difference between the erosion threshold surface and the undeformed surface. Thus the pro-wedge taper angle increases as its width decreases, i.e. the difference between the x-positions of the pro-deformation front and pro-marker front can be used as a proxy for the steepness of the pro-wedge. Both figures show how the pro-wedge angle shallows when the deformation front propagates out. Superimposed on these plots is the cumulative erosion, which shows a strong correlation between periods of low erosion from the axial-zone when new thrust sheets are propagated.

The evolution of deformation fronts for the longer runs, E(V) and E(VI), are presented in Figure 6.8. These systems clearly reach a flux steady state after approximately 120 output timesteps.

6.4.3 Axial zone still frame trajectory plots

A trajectory is the path taken by a particle to reach its position in the current time-step t. The still frame trajectory plots show the trajectories for a subset of particles that are currently at the erosive surface. The trajectories have been plotted against two vertical axes. Figure 6.9(a) plots the absolute height above the lower base (y) against the position along the base (x), Fig-

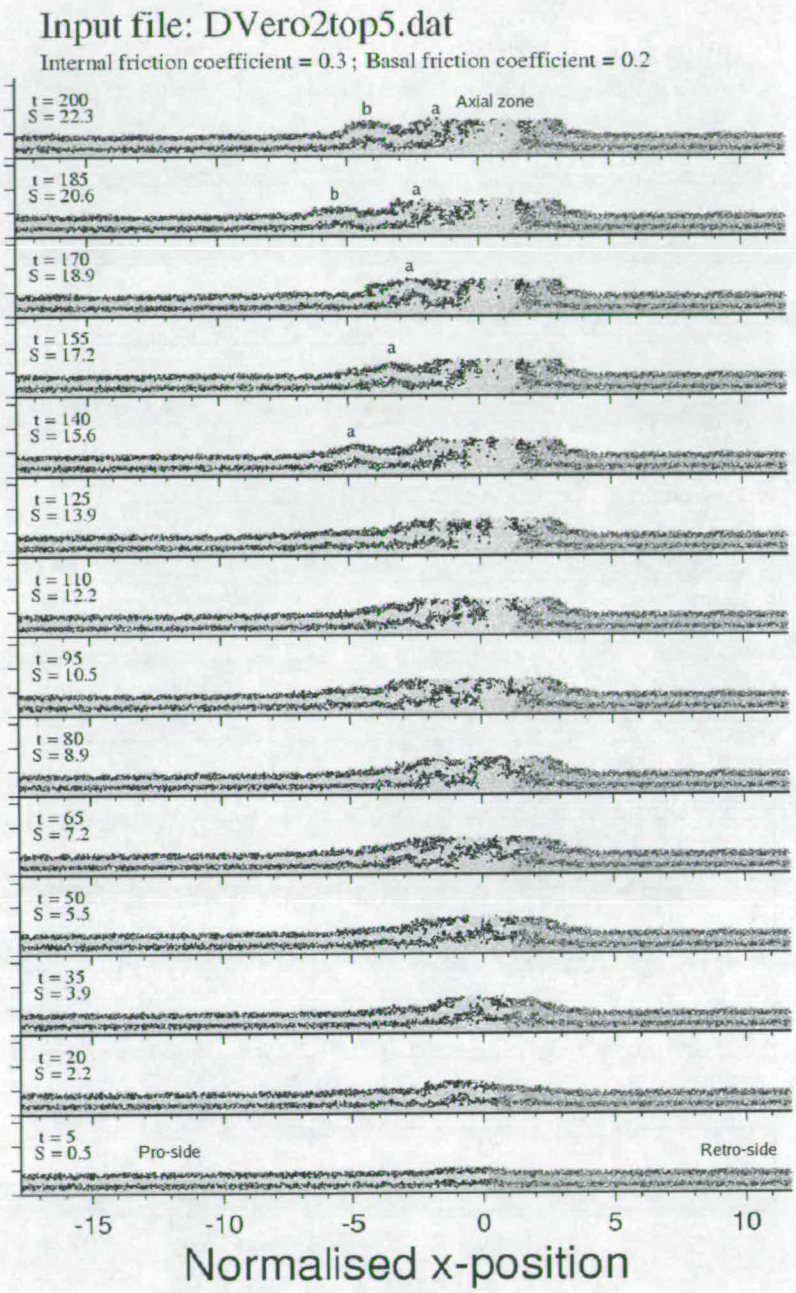

Figure 6.1: Deformation of initially horizontal horizons for run E(I) with an erosion threshold at $1.5h_0$. Time increases from the lower to upper figures. The y-axis tic marks show unit depth of the undeformed layer. Two thrust cored anticlines that are propagated and incorporated on the pro-side are highlighted with letters a and b.

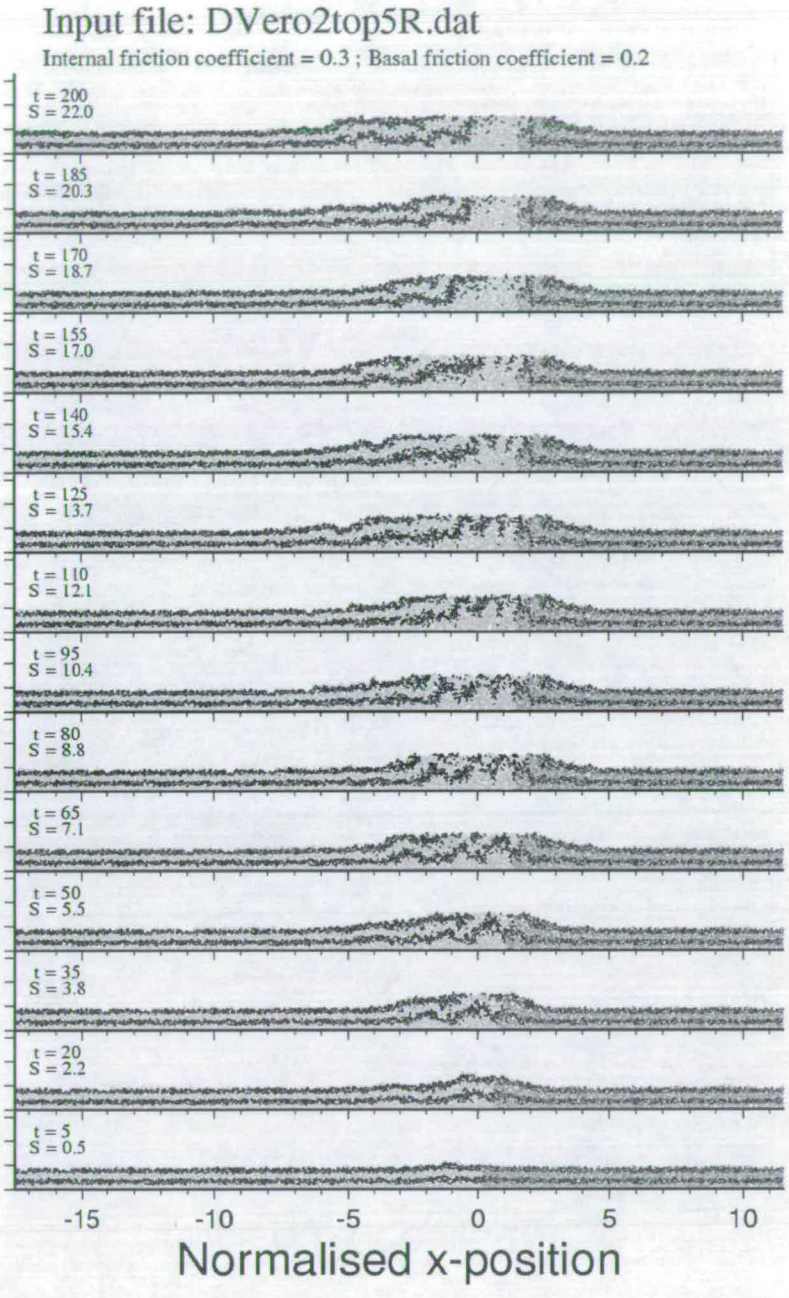

Figure 6.2: Deformation of initially horizontal horizons for run E(II) with an erosion threshold at $1.5h_0$. Time increases from the lower to upper figures. The y-axis tic marks show unit depth of the undeformed layer.

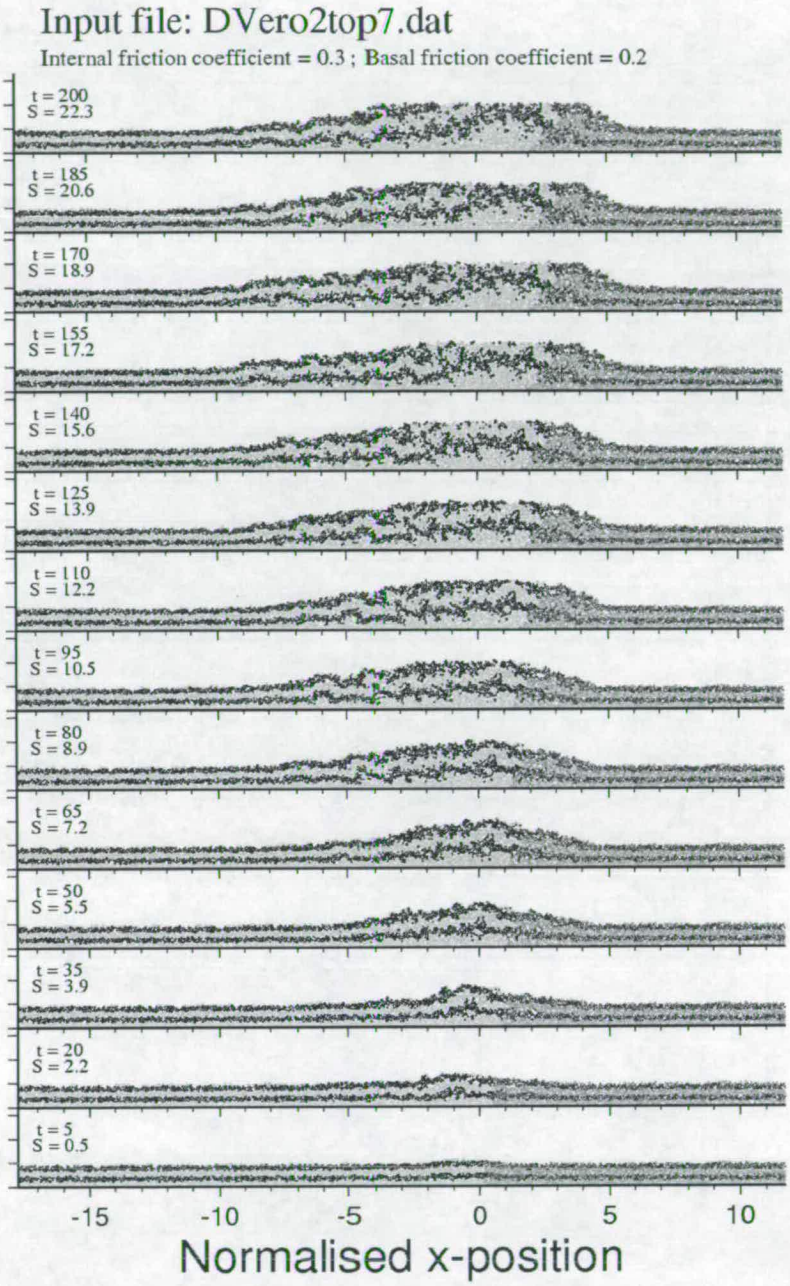

Figure 6.3: Deformation of initially horizontal horizons for run E(III) with an erosion threshold at $2.0h_0$. Time increases from the lower to upper figures. The y-axis tic marks show unit depth of the undeformed layer.

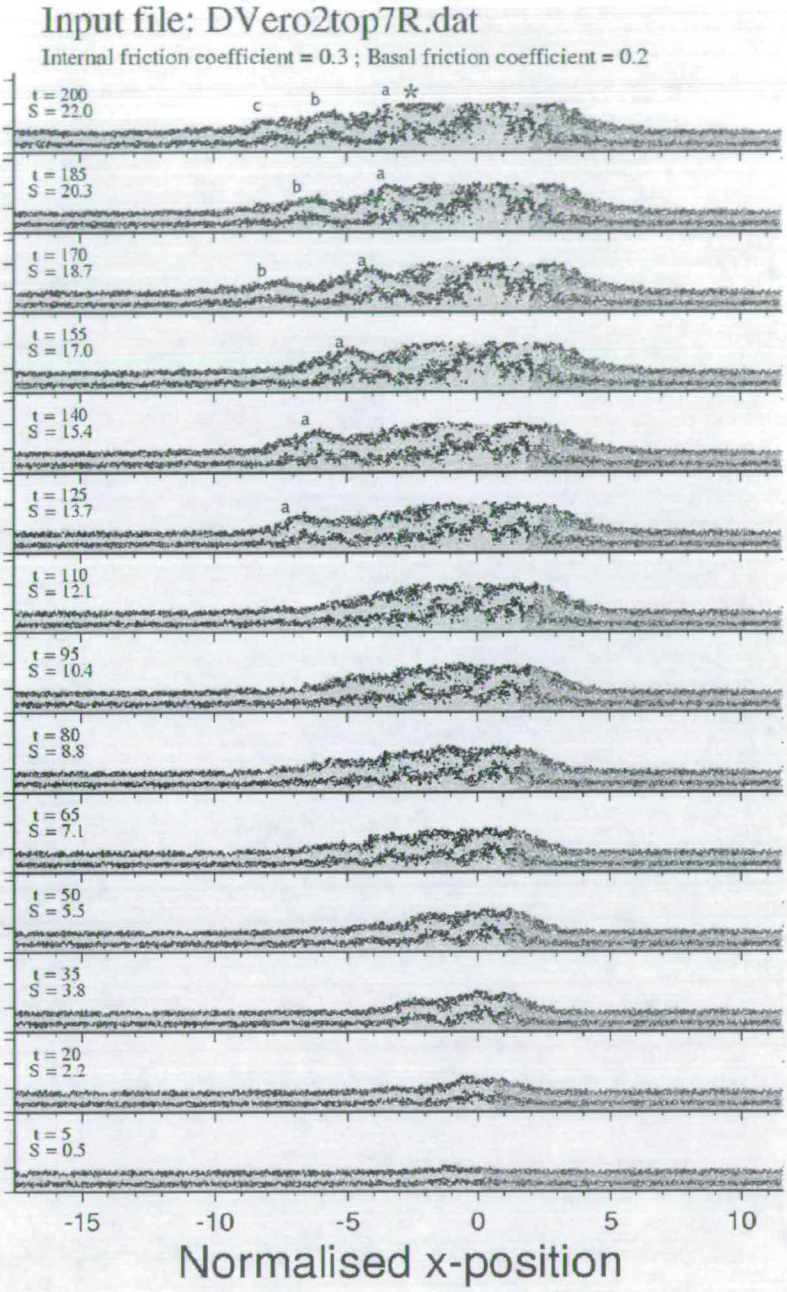

Figure 6.4: Deformation of initially horizontal horizons for run E(IV) with an erosion threshold at $2.0h_0$. Time increases from the lower to upper figures. The y-axis tic marks show unit depth of the undeformed layer. The letters a, b and c track the progress of individual thrust cored anticlines as they are generated and subsequently propagated towards the axial zone of the wedge. The star in the final time slice indicates a region where shallow material is bound by deeper material on either side.

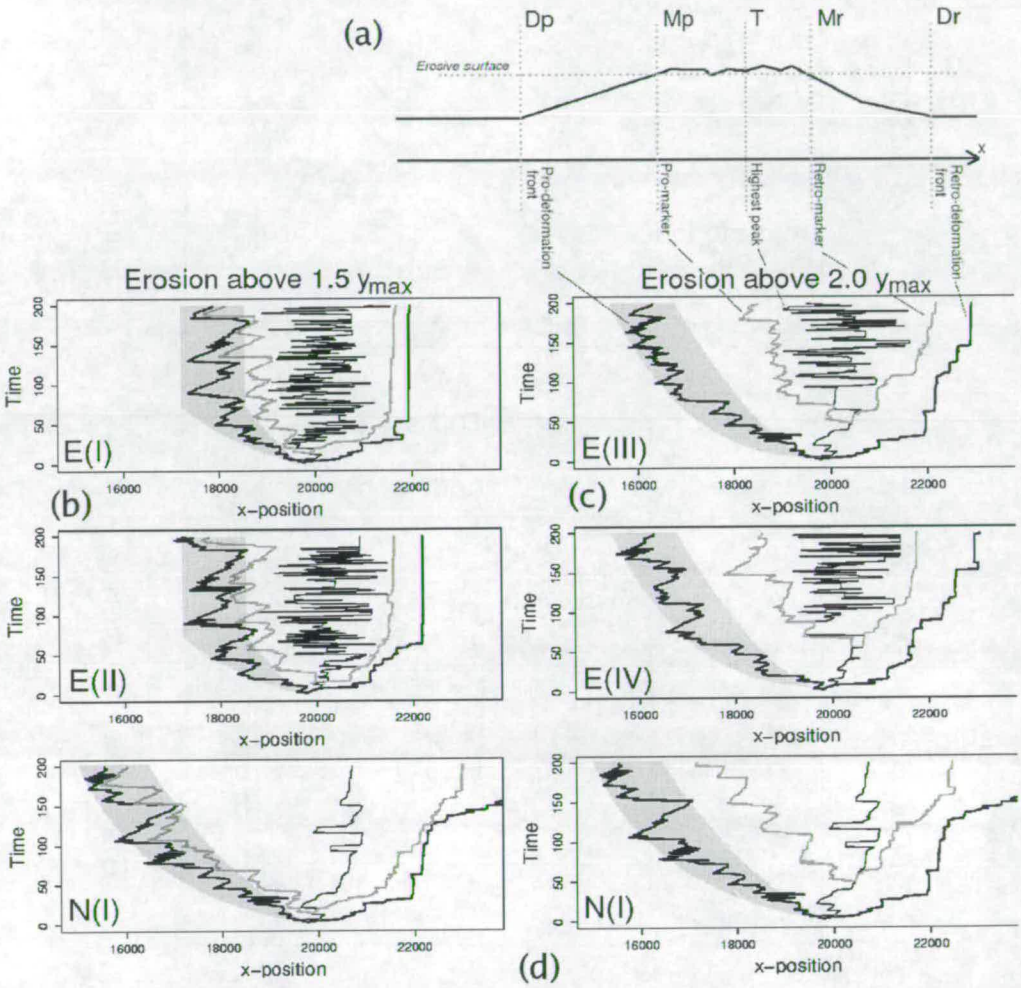

Figure 6.5: Time evolution of the x-position of points of constant elevation along the wedge surface. (a) shows how these markers relate to the wedge geometry. (b) experiences total erosion above $y_{Marker} = 1.5h_0$ and can be compared with (c) which is a Normal run with the same intercept marked. (d) experiences total erosion above $y_{Marker} = 2.0h_0$ and can be compared with (e) which is a Normal run with the same intercept marked.

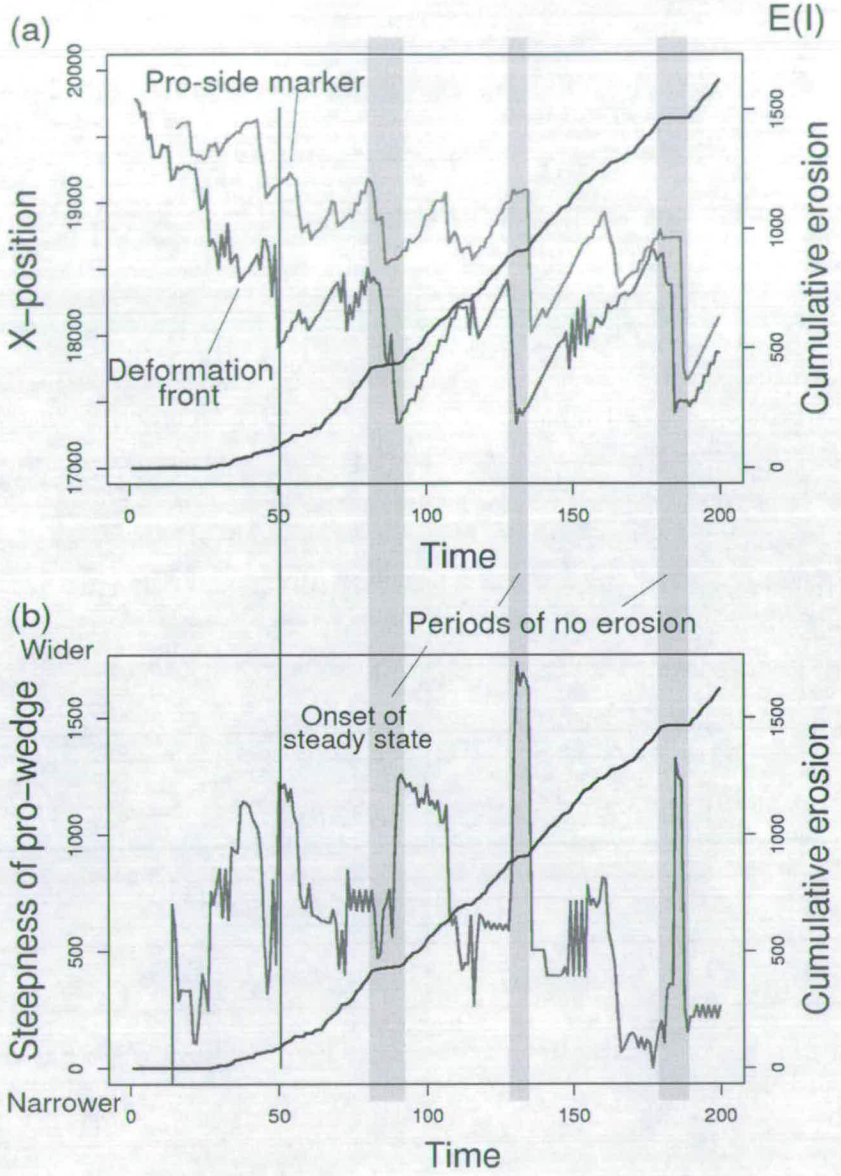

Figure 6.6: Two figures examining the evolution of the pro-wedge and corresponding erosion with time for E(l). (a) shows the evolution of the pro-deformation front and upper surface marker and compares these with cumulative total erosion. Periods of no erosion are marked in grey and coincide with periods of accretion of new thrust sheets. (b) plots the difference between the pro-side deformation front and upper surface marker. The difference between these lines gives a proxy for the steepness of the wedge. Periods of no erosion correspond with sudden shallowing of the pro-wedge angle.

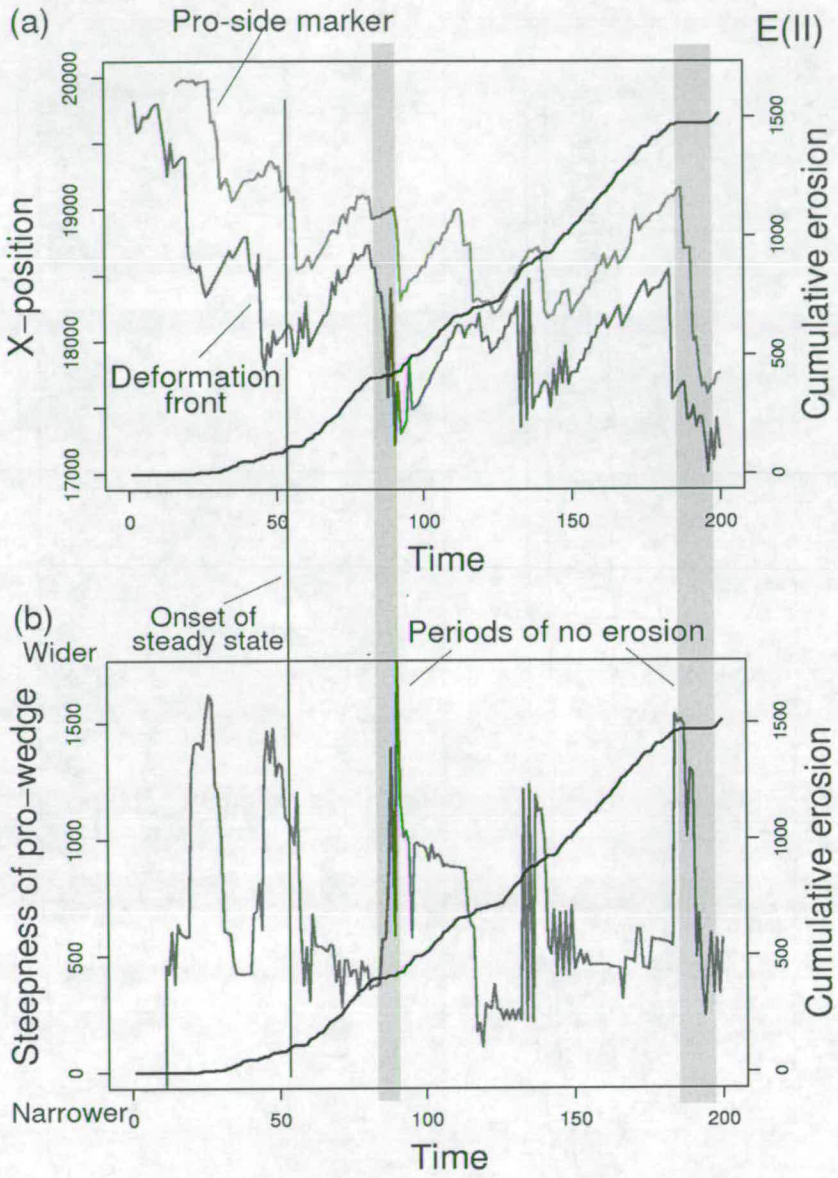

Figure 6.7: Two figures examining the evolution of the pro-wedge and corresponding erosion with time for E(II). (a) shows the evolution of the pro-deformation front and upper surface marker and compares these with cumulative total erosion. Periods of no erosion are marked in grey and coincide with periods of accretion of new thrust sheets. (b) plots the difference between the pro-side deformation front and upper surface marker. The difference between these lines gives a proxy for the steepness of the wedge. Periods of no erosion correspond with sudden shallowing of the pro-wedge angle.

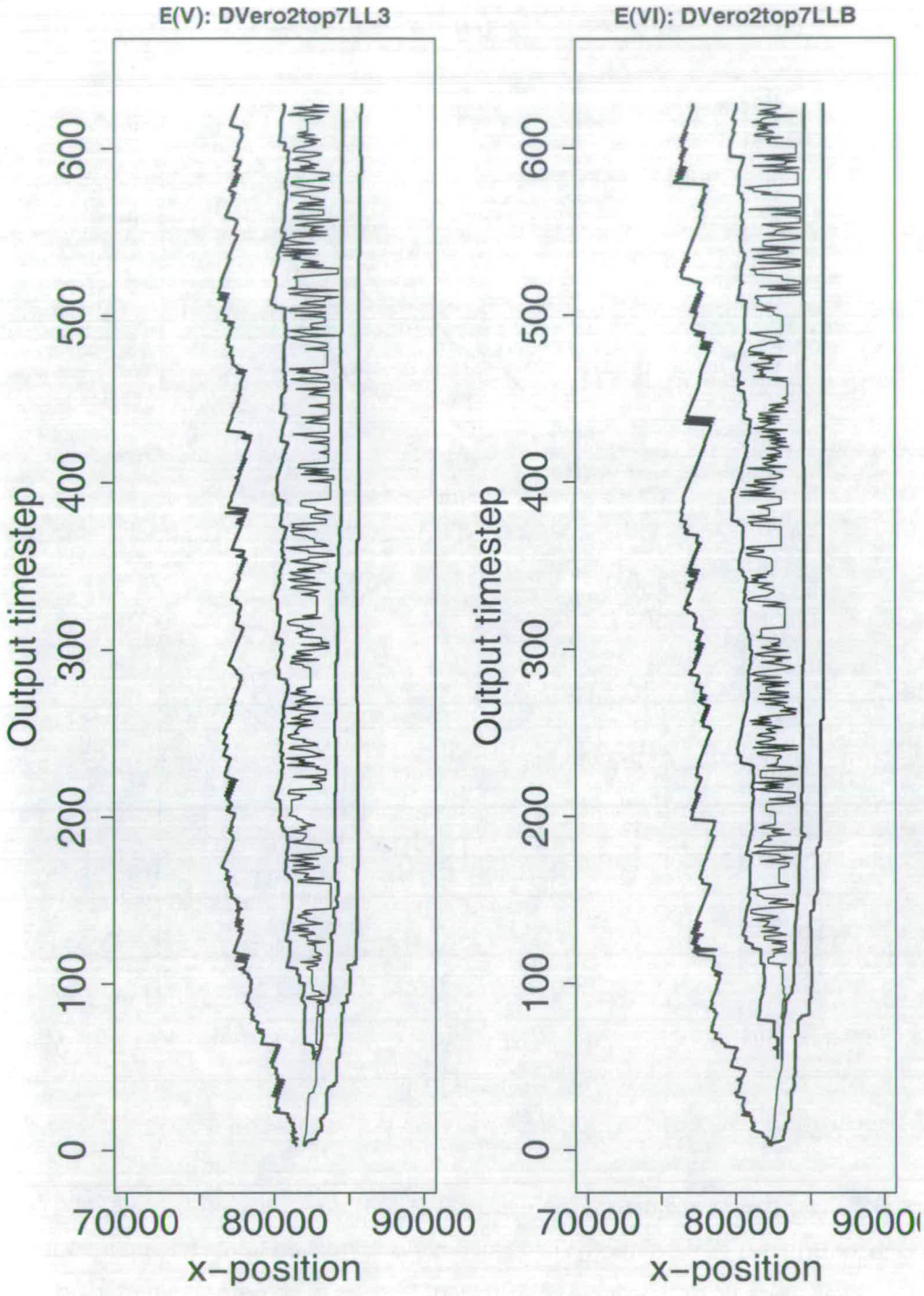

Figure 6.8: Time evolution of the deformation and marker fronts for the long runs E(V) and E(VI). The systems reach a time averaged flux steady state after approximately 120 output timesteps. The pro-wedge fronts record the accretion of successive thrust sheets whilst the retro-wedge remains relatively inactive once steady state has been achieved.

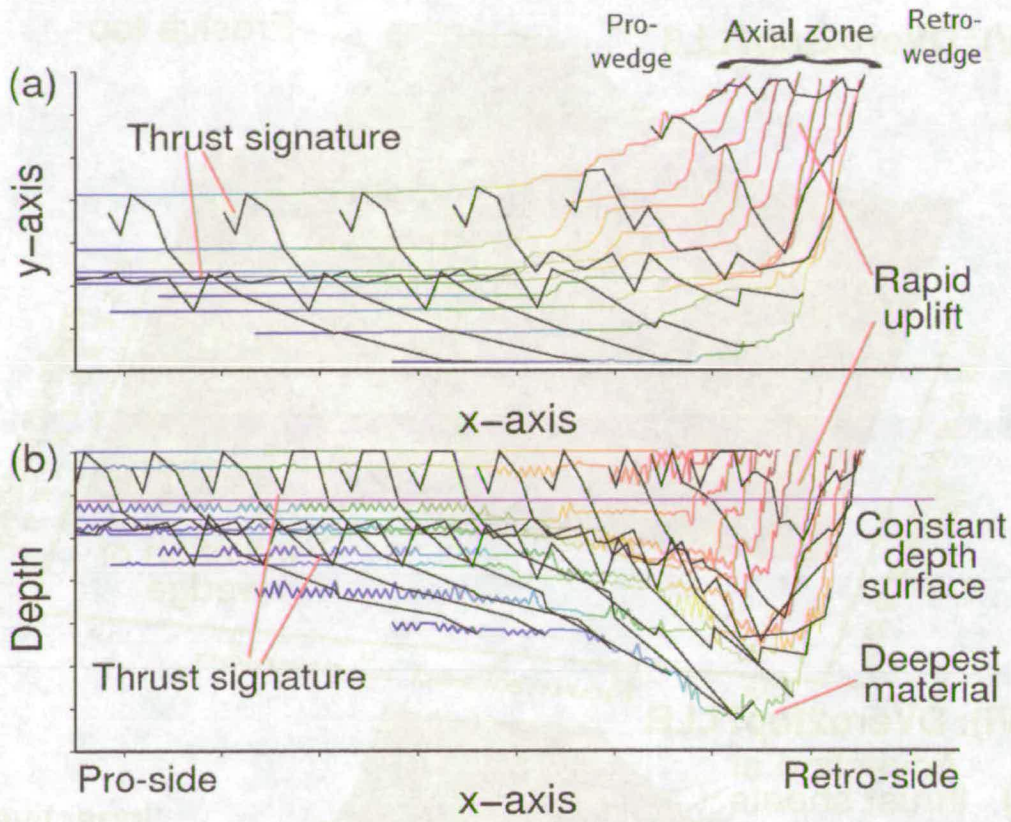

Figure 6.9: Patricle trajectories plotted against (a) absolute height and (b) depth below the surface for particles at the surface of the axial zone coloured by time. Contours of constant time (black lines) have been added. Zig-zags in the time contouring (black lines) indicate regions which have undergone thrusting to flatten out the contour by the final timestep. The very deepest exhumed material is emplaced earlier than the rest of the material.

ure 6.9(b) plots the vertical depth of the particle below the surface, calculated at each time interval, against the position along the base (x). Both have been coloured according to time. Contours of constant time have been added (black lines) such that the contour is flat at the final output timestep. The trajectories are shown for a selection of particles at the erosive surface during the final timestep, thus a different plot could be output every timestep. The variability of these plots between timesteps gives an indication of how steady the flow regime within the wedge is. It would be difficult to present the number of graphs needed to investigate the variability properly, so this section describes the nature of these cross sections, and later sections present summary plots where specific subsets of information are plotted onto 3D topography-time surfaces.

The contours of constant time highlight signatures of thrusted material by restoring surfaces of material at the surface in the final timestep back to their undeformed location. Vertical zig-zags in the contours show where material has been thrusted to attain the final configuration.

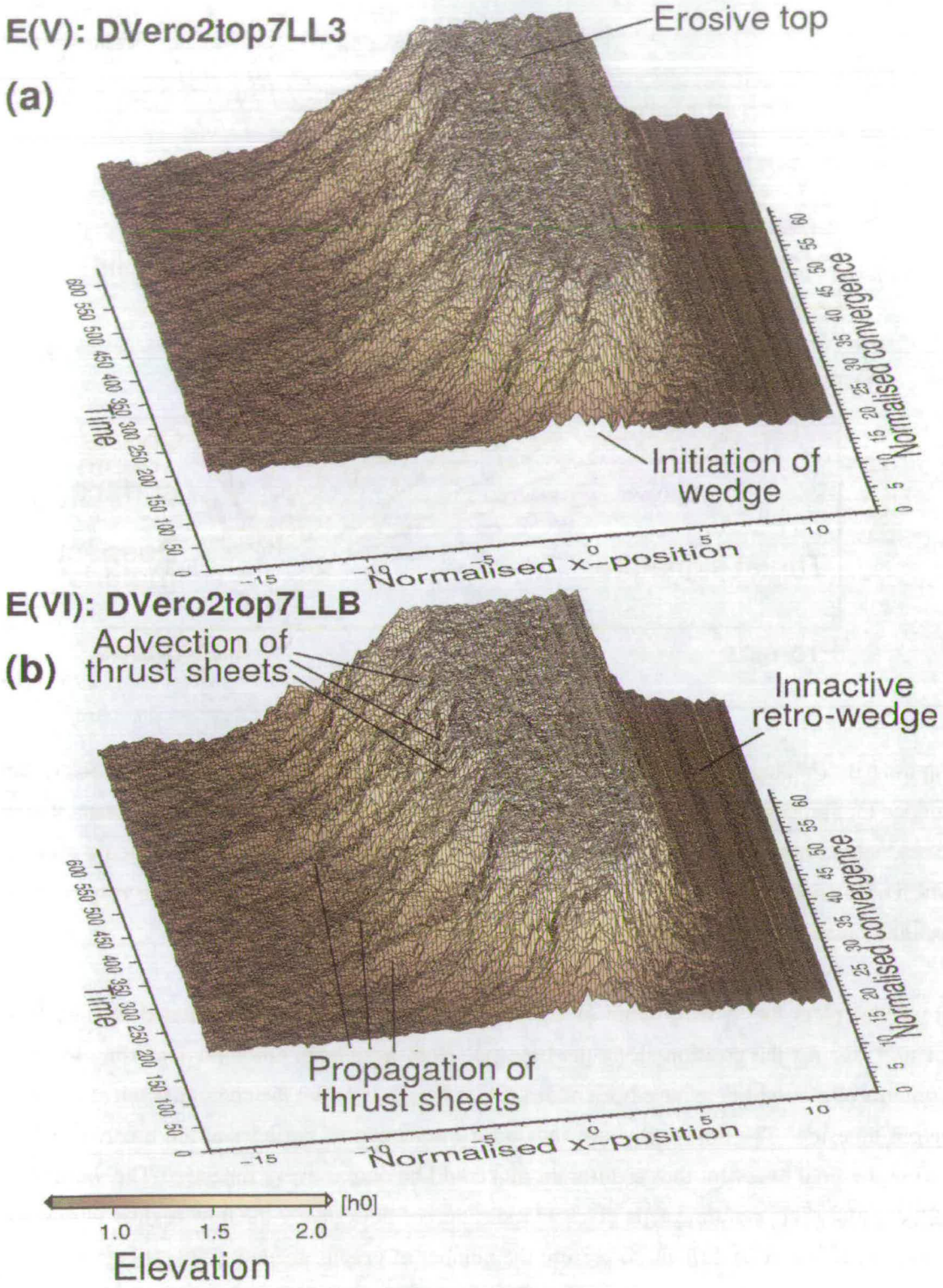

Figure 6.10: Time evolution of upper surface coloured by topography to highlight evolutionary features common to both runs. The horizontal and vertical axes show 2D wedge cross-sections, which evolve with time into the figure. Absolute convergence is normalised using the thickness of the undeformed layer.

Clearly, trajectories are not always well nested as deeper material is thrusted over younger. This is in contrast to the results of continuum finite element models, which predict smooth and steady trajectory paths in mature systems. Material is emplaced in the retro-wedge early on, where as material within the axial zone is fluxed more rapidly. Pro-side material has experienced a much shallower trajectory, thus limiting the opportunity to reset thermochronometers.

6.4.4 3D space-time plots coloured by topography

Using the longer runs (E(V) and E(VI)), 3D tins of the time evolution of the upper surface were constructed. The upper surface has been coloured by the surface particles' elevation, maximum depth of exhumation, cumulative erosion and time since passing through various closure depth surfaces. Depth is defined to be the vertical distance from the upper surface to the position of the particle at some time t.

The plots coloured by topography (Figure 6.10) should be used to understand the space time relations in the system's evolution, allowing a better interpretation of subsequent figures to be made. The gross form of the images shows the initiation of a small wedge rapidly tending to a time averaged flux steady state. The steep retro-wedge (right hand side) and shallow pro-wedge (left hand side) are clearly defined. The persistent ridges on the retro-side demonstrate the lack of deformation on the retro-side (i.e. the time invariance of this surface). The pro-side shows constant activity. The incorporation of successive thrust sheets into the pro-wedge can be clearly seen as the thrust packets are advected back into the mountain belt with some fairly uniform taper in time. The erosive zone constitutes the flat upper section above which material is removed.

This style of figure will be investigated further in the rest of this chapter, so here I define some of the terminology and background to aid interpretation. The particles forming the upper surface were determined by dividing the horizontal axis into cells of constant width $dx = 2.3R$, with low numbers at the pro-side boundary and high numbers at the retro-side boundary. All particles were sorted into a column by their x-position and their heights compared. The highest particle in each column defines the upper surface at each timestep. The variable pertaining to cell number is nx. Graphs will often be used looking along constant nx, to show how the properties of a point fixed in space vary in time, or how trends vary with nx, from the pro-side to the retro-side. Where surface properties are determined from a history, it is done by investigating the history of the highest particle in the column nx.

These plots will often be discussed in terms of time rather than convergence as this is more natural for discussing the age distribution of material at the surface. The two are directly proportional assuming a constant convergence rate.

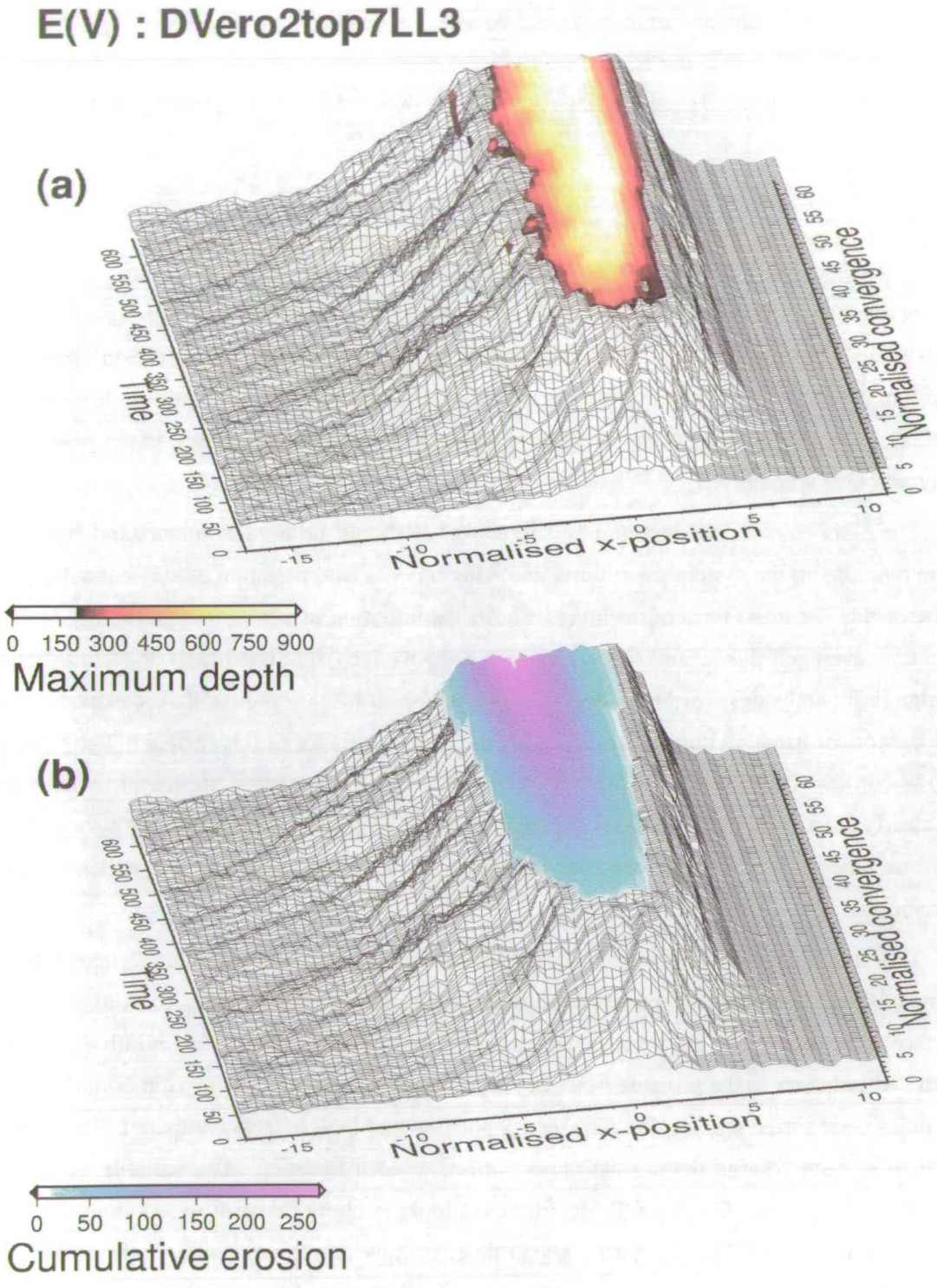

Figure 6.11: Time evolution of upper surface of the long doubly vergent wedge run E(V) coloured by (a) maximum depth of exhumation and (b) cumulative erosion.

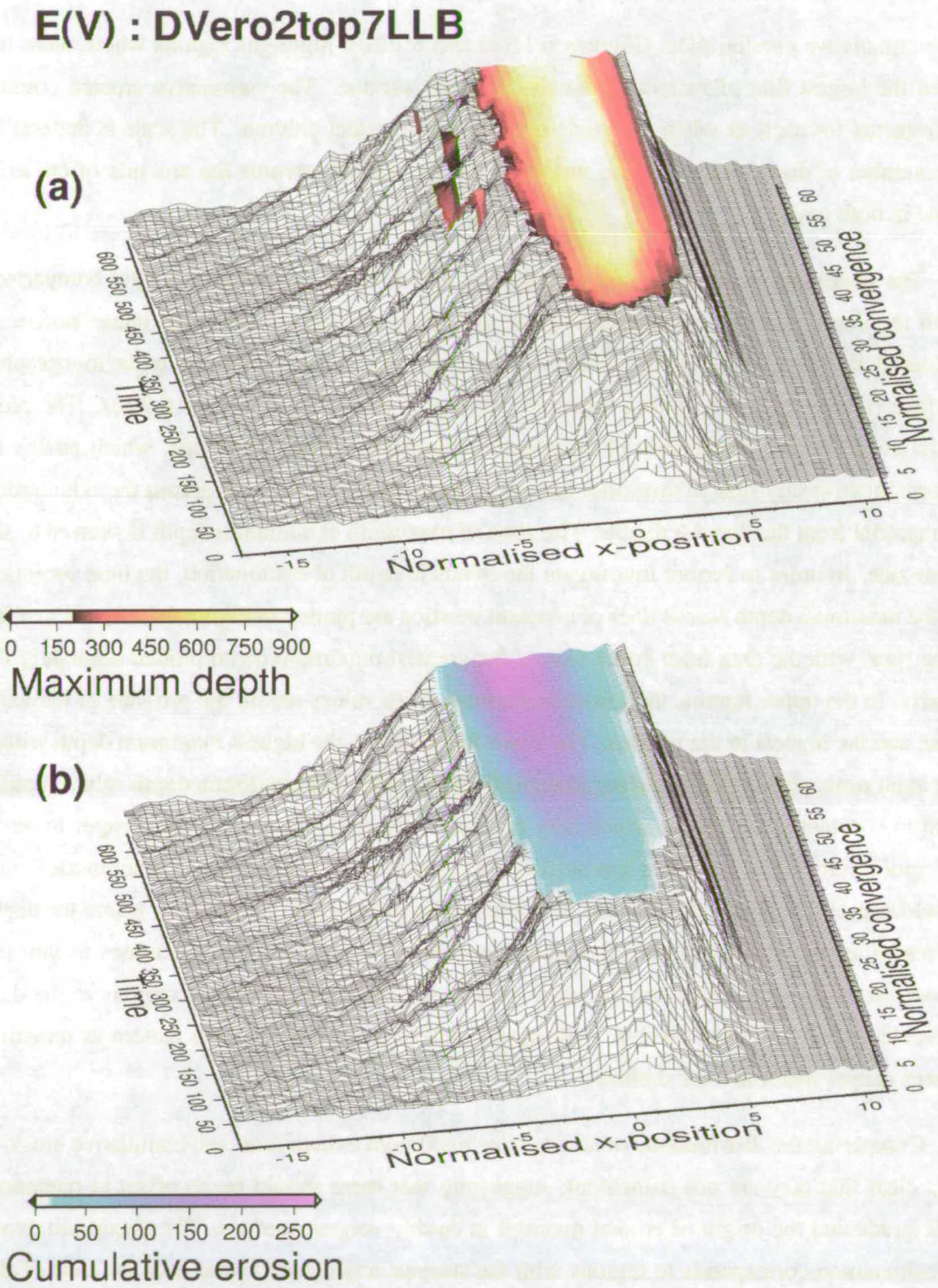

Figure 6.12: Time evolution of upper surface of the long doubly vergent wedge run E(IV) coloured by (a) maximum depth of exhumation and (b) cumulative erosion.

6.4.5 Comparison of cumulative erosion and maximum depth

The cumulative erosion plots (Figures 6.11(b) and 6.12(b)) highlight regions where there has been the largest flux of material through the upper surface. The cumulative erosion counter increments for each *nx* when a particle is removed from that column. The scale is defined by the number of discs removed. The surface is clearly skewed towards the pro-side of the axial zone in both cases.

The maximum depth plots (Figures 6.11(a) and 6.12(a)) are motivated by a comparison with the distribution of metamorphic grade across an eroding wedge. The upper surface is coloured according to the maximum depth the surface particles reach relative to the topographic surface (i.e. the greatest depth a trajectory reaches if plotted as in Figure 6.9(b)). The plots show a well nested distribution of maximum exhumation across the wedge, which attains an approximate steady state in time once enough shortening has occurred to permit the exhumation of material from the deepest depths. The zone of maximum exhumation depth is skewed to the retro-side. In order to further investigate the trends in depth of exhumation, the time evolution of the maximum depth across lines of constant position are plotted in Figure 6.13 for each of the long runs, with the data from either side of the greatest maximum depth plotted separately for clarity. In the upper figures, the lowest maximum depth values are on the pro-side of the axial zone and the highest in the interior. The lower figures show the highest maximum depth within the axial zone, with depths reducing towards the retro-side. The maximum depth values rapidly tend to constant values about which they oscillate. The retro-side values take longer to reach an equilibrium value as there is less activity on the retro-side. From finite element models, one would expect the regular distribution of deepest exhumation to be well nested, where the depth increases as you move into the axial zone from the pro-wedge and then decreases as you the move out of the axial zone into the retro-wedge. It is possible to identify regions in the data presented where the lines overlap, indicating a departure from the regular pattern as thrusting places deeper material over shallow.

Comparing the distributions of steady state maximum exhumation and cumulative erosion, it is clear that they are not coincident, suggesting that there should be an offset in metamorphic grade and the origin of eroded material in doubly vergent wedges. The maximum depth of exhumation corresponds to regions with the steepest trajectories rather than the zone of the highest erosion. If the incoming trajectories are relatively shallow (as is required in a shallow wedge) and there is an effective backstop experiencing little deformation, there must be a transition zone from shallow trajectories experiencing large displacements to steep trajectories with relatively little displacement, to preserve a time averaged smooth and continuous transition in velocity across the wedge. This condition is necessary to ensure the backstop remains inactive.

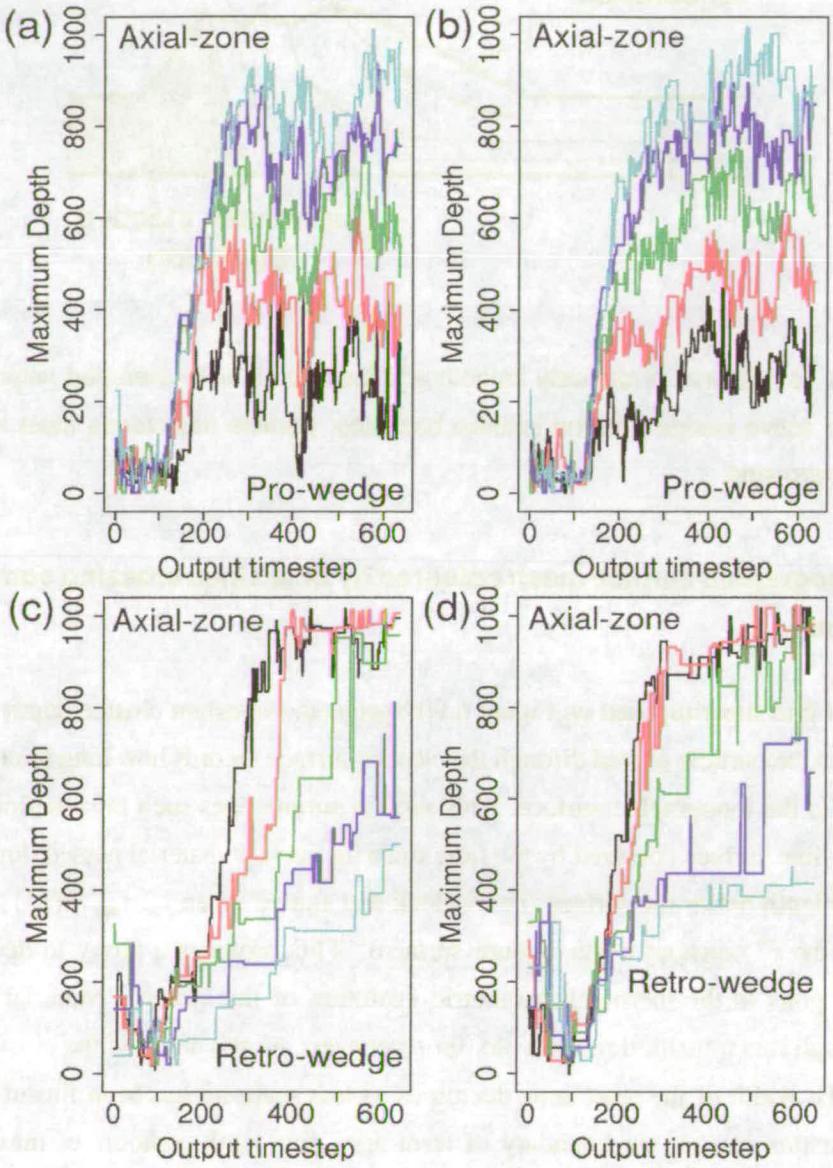

Figure 6.13: Time evolution of the maximum depth attained by surface material for different positions across the axial zone. The left hand figures are for run E(V) and the right E(VI). The upper figures are for the pro-side region where the depth of exhumation increases towards the retro-side, thus the lowest line is the most pro-ward and the highest is nearest the axial zone. The lower figures are plotted for the data where the depth of exhumation is now decreasing as we move further retro-ward, thus the highest lines are in the axial zone and the lowest are in the retro-wedge.

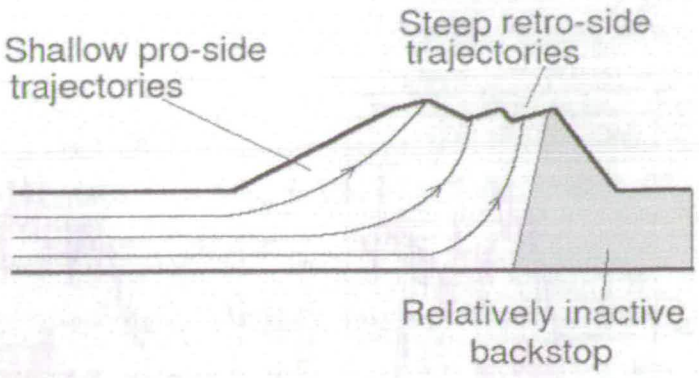

Figure 6.14: To preserve a relatively smooth and continuous time averaged velocity transition between the active wedge and the inactive backstop, particle trajectories must steepen from pro-side to retro-side.

6.4.6 Topographic surface mesh coloured by time since crossing some constant depth

A horizontal line superimposed on Figure 6.9(b) projects a constant closure depth surface. The time at which the particle passed through the closure surface records how long it took to exhume the particle to the topographic surface. This section summarises such information using a 3D topography-time surface coloured by the time since the surface material passed through a specified closure depth below the surface (i.e. A clock that started when $y_{surface}(x(p)) - y(t,p) < h_i$ where h_i is the i^{th} constant depth closure surface). This provides a proxy to describing processes analogous to the thermochronometric evolution of the system. Material that has not passed through this transition records old, un-reset ages. As the depth of the closure surface is increased, the width of the reset zone decreases as less material has been fluxed through that surface. For this reason, the boundary of reset ages goes with contours of maximum depth below the surface in the model (i.e. if the material has not reached a certain depth, it will not be reset). This assumption becomes more complicated in real systems which involve a real thermal regime. For this reason, the zone of reset ages is shifted retro-ward of the zone of maximum exhumation for deep thermochronometers and tends towards the zone of cumulative erosion as the reset depth tends to zero. This trend agrees with the modelling and thermochronometry presented by (Batt et al., 2001).

Figures 6.15 and 6.16 compare the age distribution across the topographic surface for both long runs using closure depths of (a) $h_i = 0.15h_0$ and (b) $h_i = 0.7h_0$. Animation 6.1 presents the same style of figure but with a finer resolution in the closure depth, h_i. These plots show that the system does not reach a steady state distribution of ages for any of the constant depth surfaces investigated. Primarily, this is due to the episodic behaviour of the system. The system

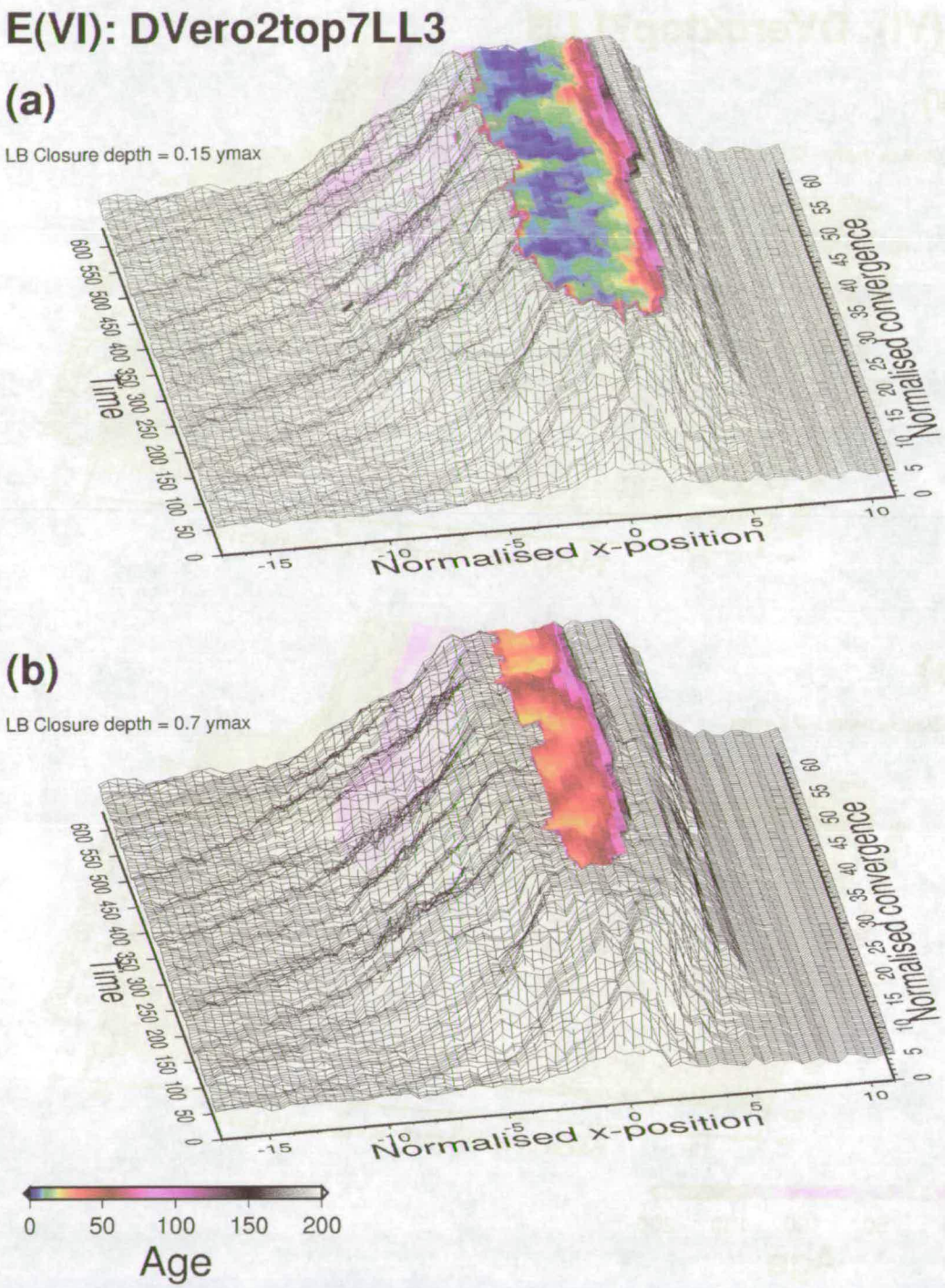

Figure 6.15: Surface age of material since it passed through a closure depth of (a) $h_i = 0.15h_0$ and (b) $h_i = 0.7h_0$ for the run E(V).

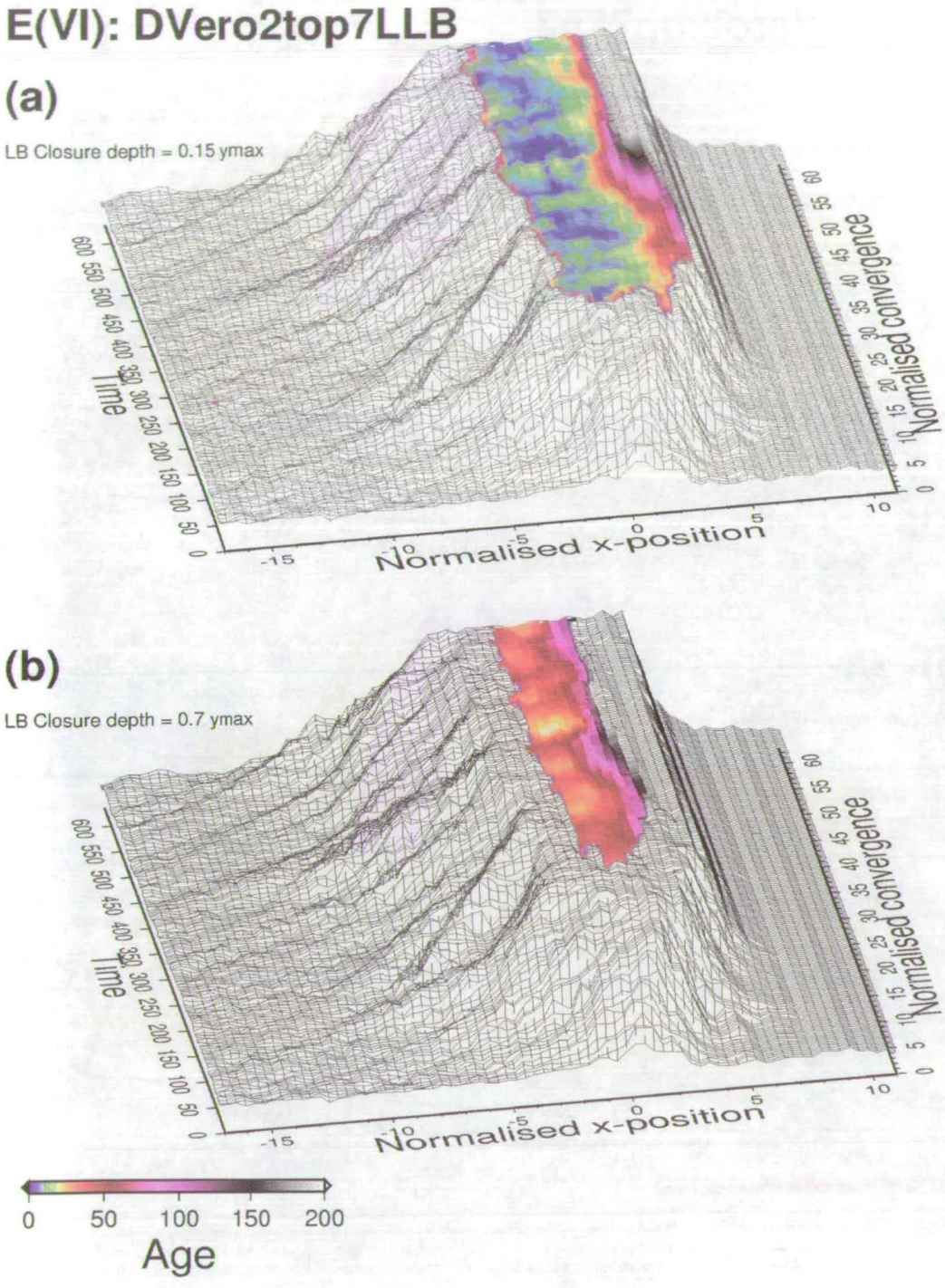

Figure 6.16: Surface age of material since it passed through a closure depth of (a) $h_i = 0.15h_0$ and (b) $h_i = 0.7h_0$ for the run E(VI).

pulses as thrust sheets are propagated, incorporated and eroded. The magnitude of these pulses is comparable and scales with the duration of the thrust sheet life cycle. This is problematic for the interpretation of thermochronometric data in mountain belts as an assumption regarding exhumational steady state is often made.

To provide further insight into the change in age across the axial zone with time, graphs have been plotted showing how the age varies in time for a constant position in space for different closure depths for run E(V) (Figure 6.17). The data presented divides the axial zone into cells of constant width and position and looks at how the ages in each cell vary from the pro-side ($nx = 930$) to the retro-side ($nx = 954$). Initially, all ages increase linearly from zero at some constant rate, this is un-reset material that is simply ageing. Once erosional exhumation of material that has been reset commences (the closure depth has been exhumed) the age of surface material drops significantly and starts to oscillate about some time averaged constant value. It takes longer for retro-side material to reach the surface so this transition occurs later as nx increases and the time average age is higher. Deeper reset depths take longer to exhume as the material must travel a greater distance, which increases the duration of un-reset ages as well as the mean reset age. Visually, it is easy to see that the surface on the pro-side experiences more frequent, lower magnitude replacement of surface material where as the retro-side evolves on a longer time period with bigger events.

Many graphs could be constructed for both runs similar to Figure 6.17 for more closure depths and at a finer resolution across the axial zone. The number of graphs would be very great, so instead a statistical analysis of this larger data-set is presented for E(V) in Figure 6.18 and E(VI) in Figure 6.19. The trends identified for the two runs are consistent. The left hand figures examine properties of the individual ages through time highlighting (a) the maximum age recorded at each nx, (b) the minimum age recorded at each nx and (c) difference between the maximum and minimum ages. These show a general ageing of material towards the retro-wedge. The deepest thermochronometer in run E(VI) for $nx > 955$ shows a zero maximum age (Figure 6.18(b)) and infinite minimum age (Figure 6.18(a)), indicating that this thermochronometer is un-reset in this portion of the wedge.

The right hand graphs investigate the properties in the differences in adjacent ages. A jump is defined to be a rapid younging event which occurs as new material is brought to the surface (indicated on Figure 6.17). The jump sum in sub-figures (c) gives the cumulative magnitude of all jumps across the axial zone. Sub-figures (d) show that the total number of jumps decreases towards the retro-side, thus producing a mean jump (e) which increases towards the retro-side. This suggests that there will be a larger variability of retro-side ages with time as the surface material resides for a long time before being rapidly replaced. Greater activity on the pro-side results in more consistent ages. This also implies the potential for much larger contrasts in age across individual structures on the retro-side.

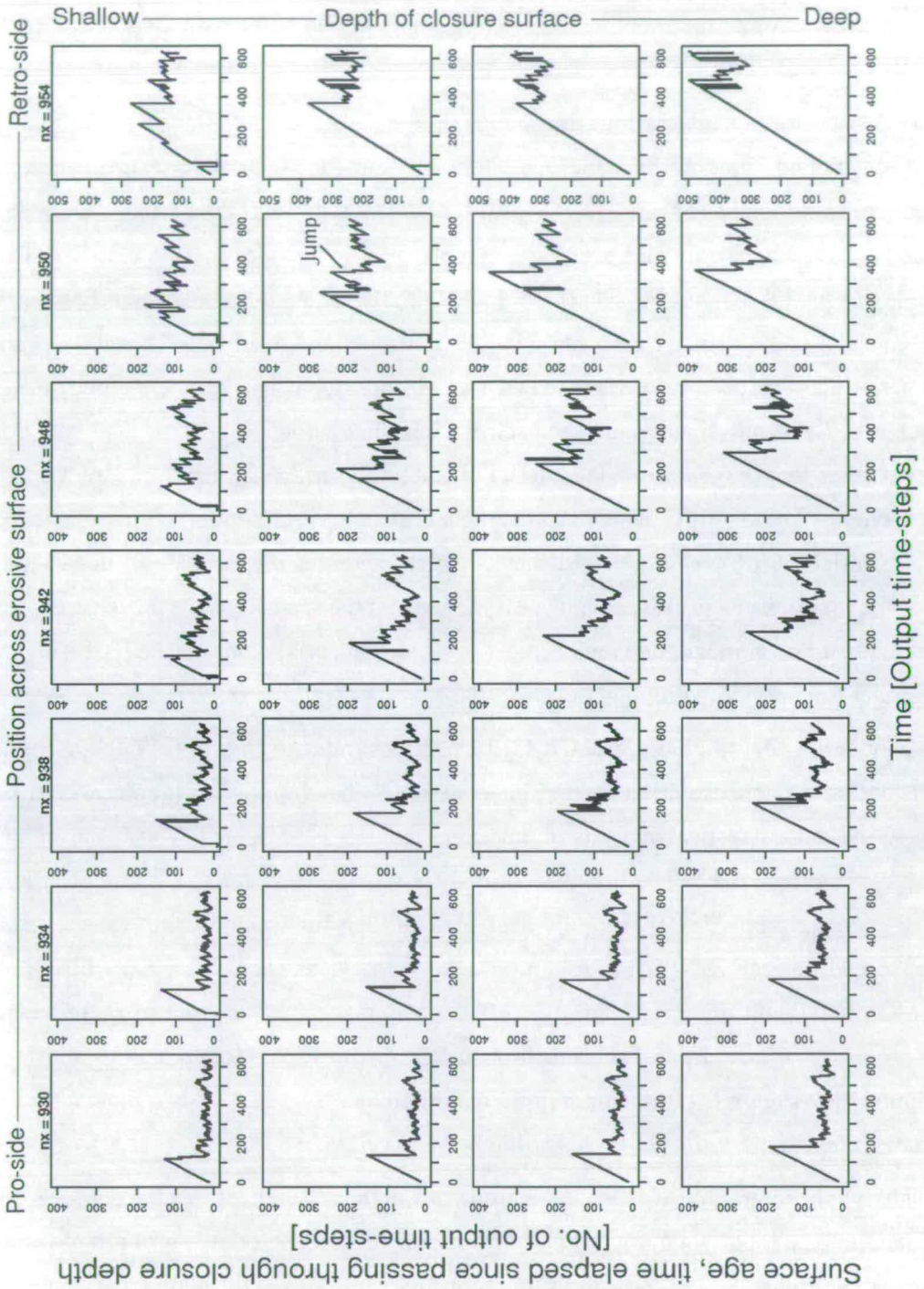

Figure 6.17: Time evolution of surface age at different points along the axial zone from pro-side ($nx = 930$) to the retro-side ($nx = 954$). Depth of closure surfaces = $0.3, 0.5, 0.7$ and $0.9h_0$ below the topographic surface.

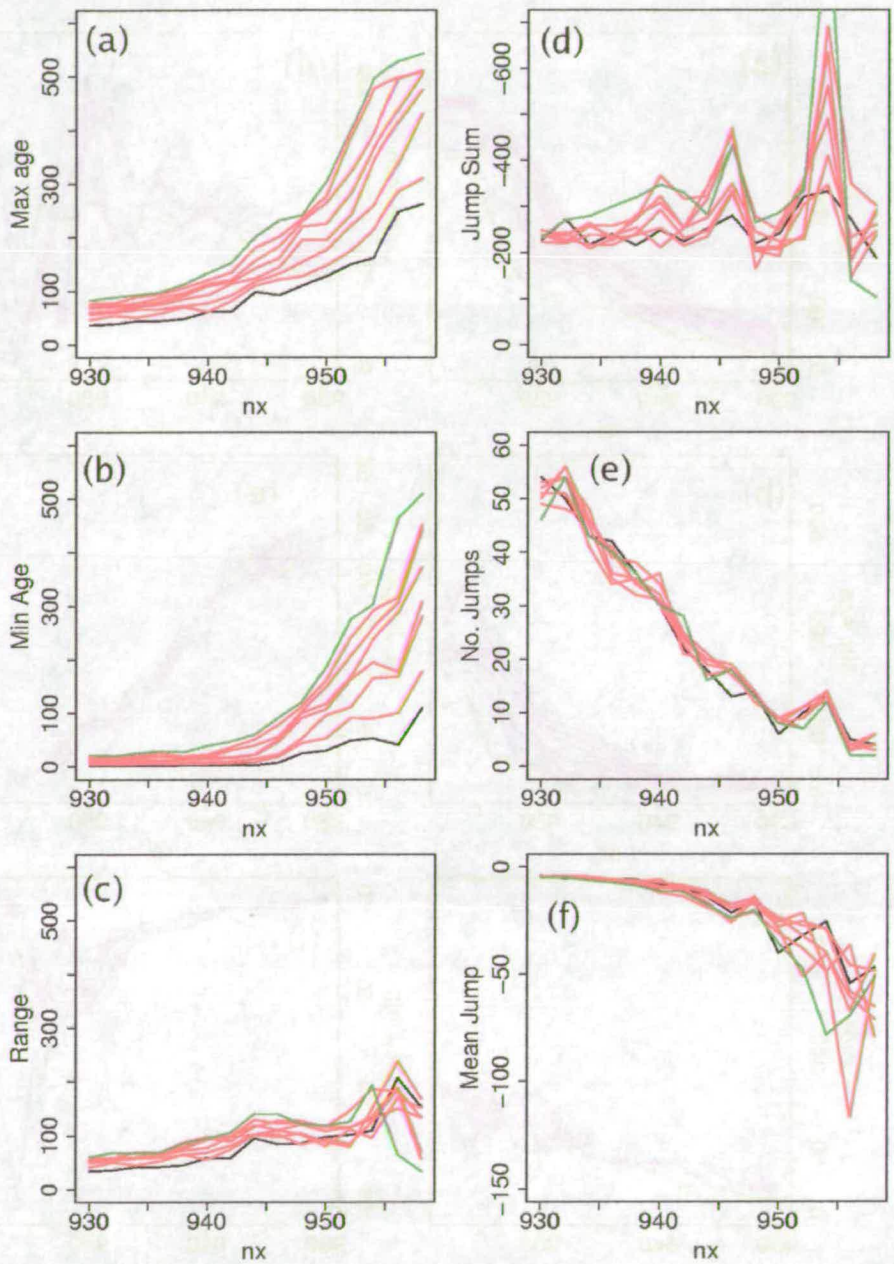

Figure 6.18: Statistical summary of the age position data derived from constant depth surfaces for E(V). The left hand figures focus on the absolute ages and the right hand figures on the changes in ages between successive time steps. A jump is defined to be a sudden younging event at the surface. The black line is the most pro-ward data and the green line the most retro-ward data.

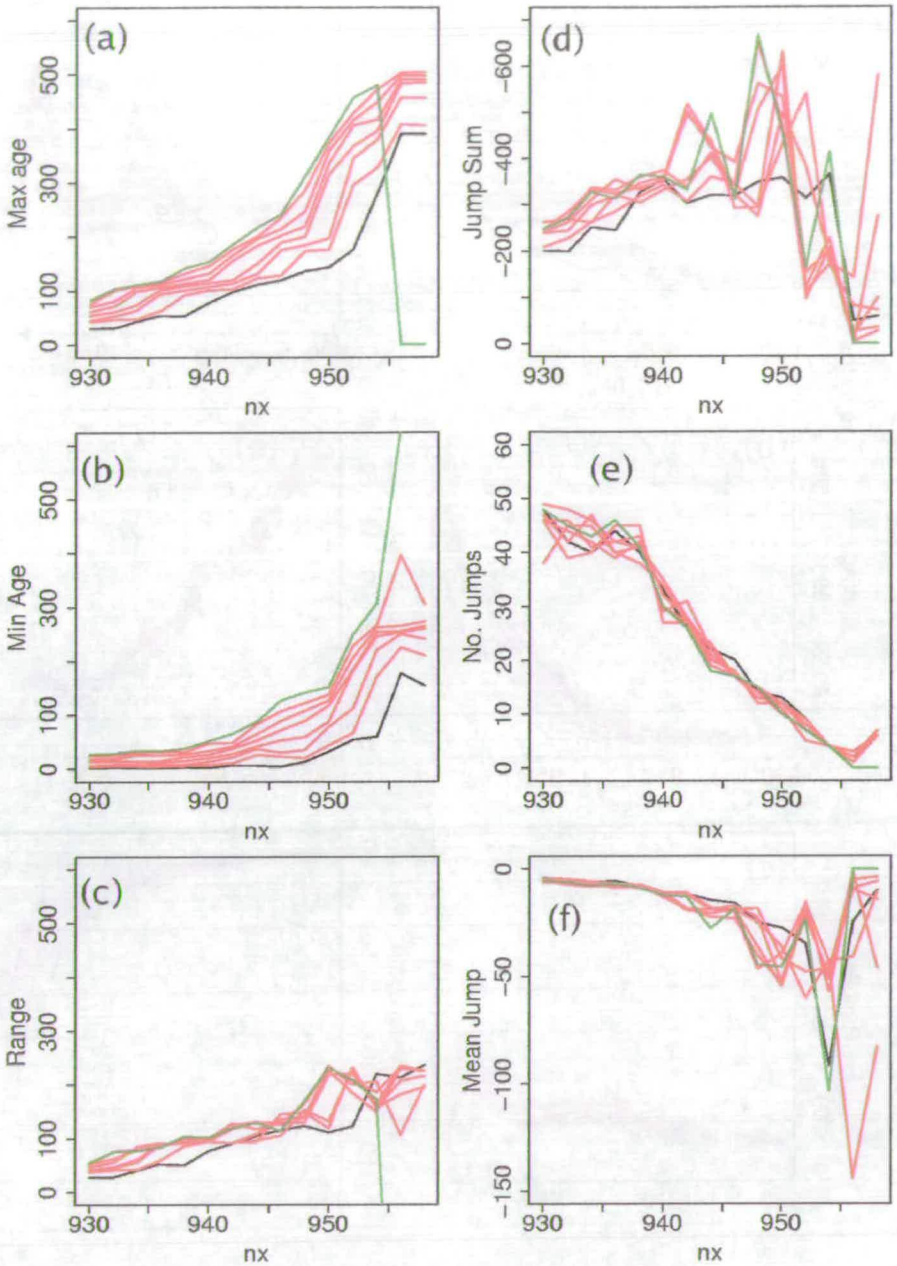

Figure 6.19: Statistical summary of the age position data derived from constant depth surfaces for E(VI). The left hand figures focus on the absolute ages and the right hand figures on the changes in ages between successive time steps. A jump is defined to be a sudden younging event at the surface.

This approximation to some isothermal surface is crude. However it does provide insight into the time evolution of the ages across the axial zone. This work highlights the difficulties in achieving exhumational steady state in real systems, as the wedge responds on time-scales comparable with those resolvable with thermochronometry. Introducing further complexity through a more complicated erosion algorithm is unlikely to resolve the problems in producing an exhumational steady state.

6.5 Discussion regarding the calculation of erosion rates from thermochronometry

Animation 6.2 shows how the distribution of ages from different closure depth surfaces changes with the depth of the surface, colouring a cumulative erosion surface mesh. Two of the snapshots for closure depths of $0.15h_0$ and $0.7h_0$ are presented for E(V) in Figure 6.20 and E(VI) in Figure 6.21. These are the same closure depths that were plotted onto the surface topography in Figures 6.15 and 6.16. The shallow closure depth produces a broad reset age distribution where the entire region of positive curvature is covered. However, as cumulative erosion tends to zero, a difference in the pro- and retro- age distributions is seen. The transition of reset ages is abrupt on the pro-side with no old ages. Derived from the shallow flux, the lowest parts of the pro-side cumulative erosion surface mesh are not reset. In contrast, due to the slow exhumation on the retro-side, the lowest parts of the cumulative erosion surface mesh gradually age until a time averaged steady state distribution is attained, where enough shortening has occured to replace all surface material in the eroding zone with material from below the relevant closure depth. Certain assumptions are made in order to use the modelling presented here to elucidate thermochronometric systems. This simplifies the system so that underlying behaviour can be identified and then discussed in a geological context. Using a more complex erosional algorithm would only add further complexity when applying the model to real systems.

6.5.1 Simplifying model assumptions

1. The i^{th} thermochronometer has a thin closure surface at a depth h_i below the topographic surface
2. The i^{th} closure surface is always at a constant depth h_i below the topographic surface, thus all closure surfaces are parallel to the topographic surface
3. When material moves below the i^{th} closure surface, the i^{th} thermochronometric age (A_i) is completely reset and remains at zero until the depth of the particle becomes less than h_i
4. The age of material that is above the i^{th} closure surface (A_i) increments with model time

5. The closure surface is assumed to be thin, thus there is no equivalent to a partial retention zone or partial annealing zone. This is excluded on the basis that it only adds further complexity and varies between thermochronometers

6. Material that has never been deeper than h_i is termed *un-reset* for the i^{th} thermochronometer

6.5.2 Interpretation of model results

This discussion will primarily focus on three sources of information from the models.

The maximum depth plots (Figures 6.11(b) and 6.12(b)) which indicate the maximum depth attained by particles at the surface. For the i^{th} thermochronometer to be reset, it must have been deeper than h_i. Thus the contour corresponding to h_i in the maximum depth plot bounds the zone of reset ages. We have already seen that maximum depth contours of the deepest material are offset to the retro-side of the cumulative erosion maxima, thus the use of deep thermochronometers in the determination of spatially extensive erosion rates must be questioned. The most retro-ward material is derived from deep within the wedge and thus the surface distribution of reset ages varies little with the h_i. The ages are persistently older than the rest of the wedge. In contrast, ages within the central to pro-side region of the erosion zone vary significantly on time scales related to thrust sheet propagation, incorporation and erosion. Material in the pro-wedge is frequently sourced from shallow material that is fluxed through a shallow surface layer. Inevitably, there will always be a flux of shallow material eroded off the pro-side that is not reset at the pro-side minima of cumulative erosion. For shallow thermochronometers (Figures 6.20(a) and 6.21(a)), bounding the pro-side reset to un-reset transition is a narrow band of ages that are relatively old as compared with the majority of pro-side ages. This reflects the critical transition between un-reset to reset material that has experienced a long, oblique trajectory since passing through the shallow closure surface and is observed in thermochronometric studies, such as the Olympic Mountains, Washington State (Batt et al., 2001). This transition zone is less obvious for the age distribution of deeper thermochronometers which experience steeper exhumation trajectories. The pro-side old ages are not as old as the retro-side old ages as these are exhumed at much slower rates. The origin of material eroded on the pro-side varies depending upon whether the mechanism to accommodate shortening is frontal accretion or internal thickening. Oscillations in the amount of un-reset material distributed across the cumulative erosion envelope can be related to the evolution of pro-side thrust sheets. When an anticline is being eroded deeper material, and thus more reset material, is exposed. Inbetween the erosion of anticlines, material with shallower trajectories is removed, which is composed of less reset material. Thus, the erosion of anticlines is coincident with the rapid younging of pro-side material.

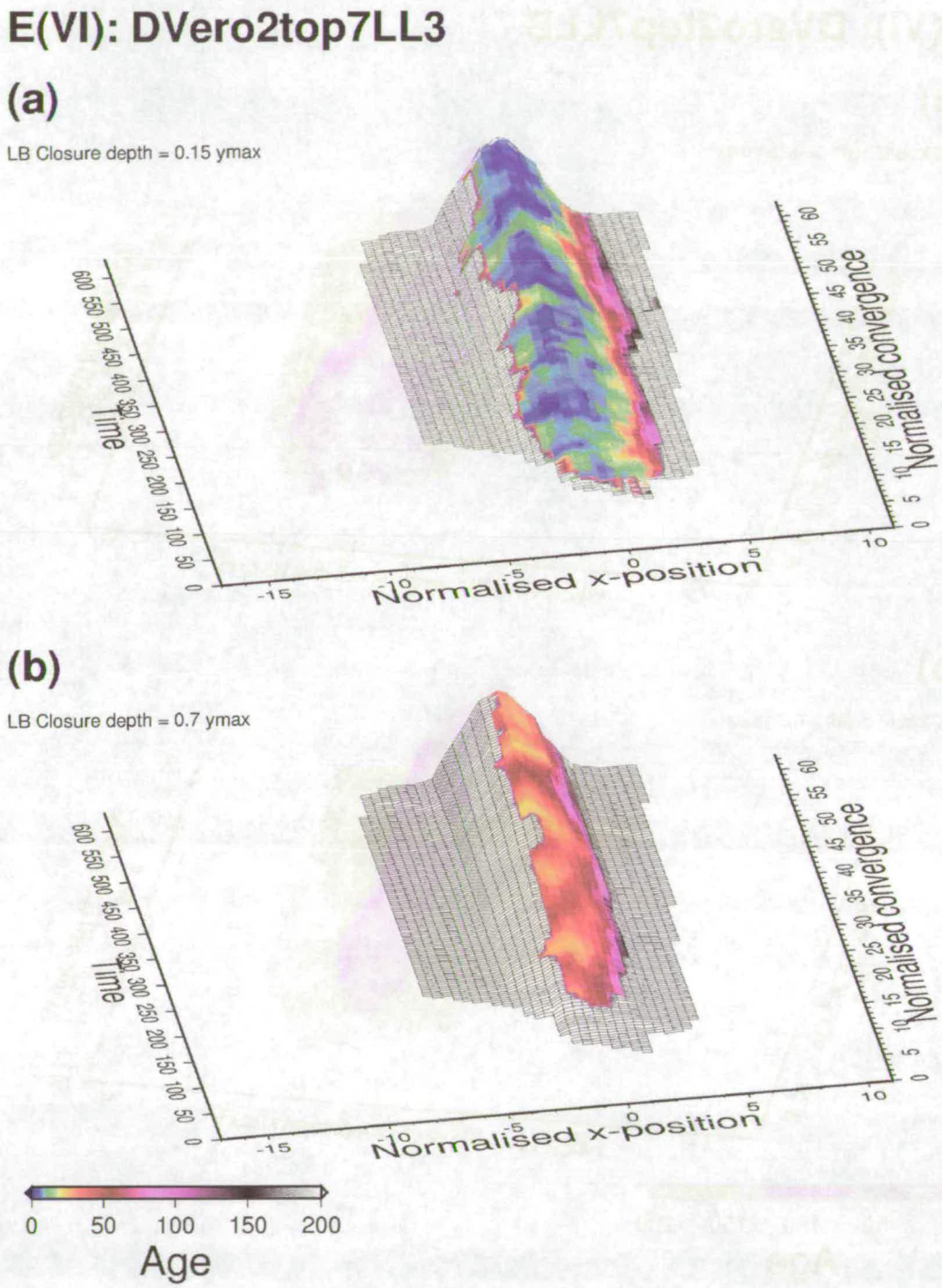

Figure 6.20: Age of surface material derived from closure depths of $0.15h_0$ and $0.7h_0$ mapped onto a surface mesh of cumulative erosion to compare the localisation of these two processes for run E(V).

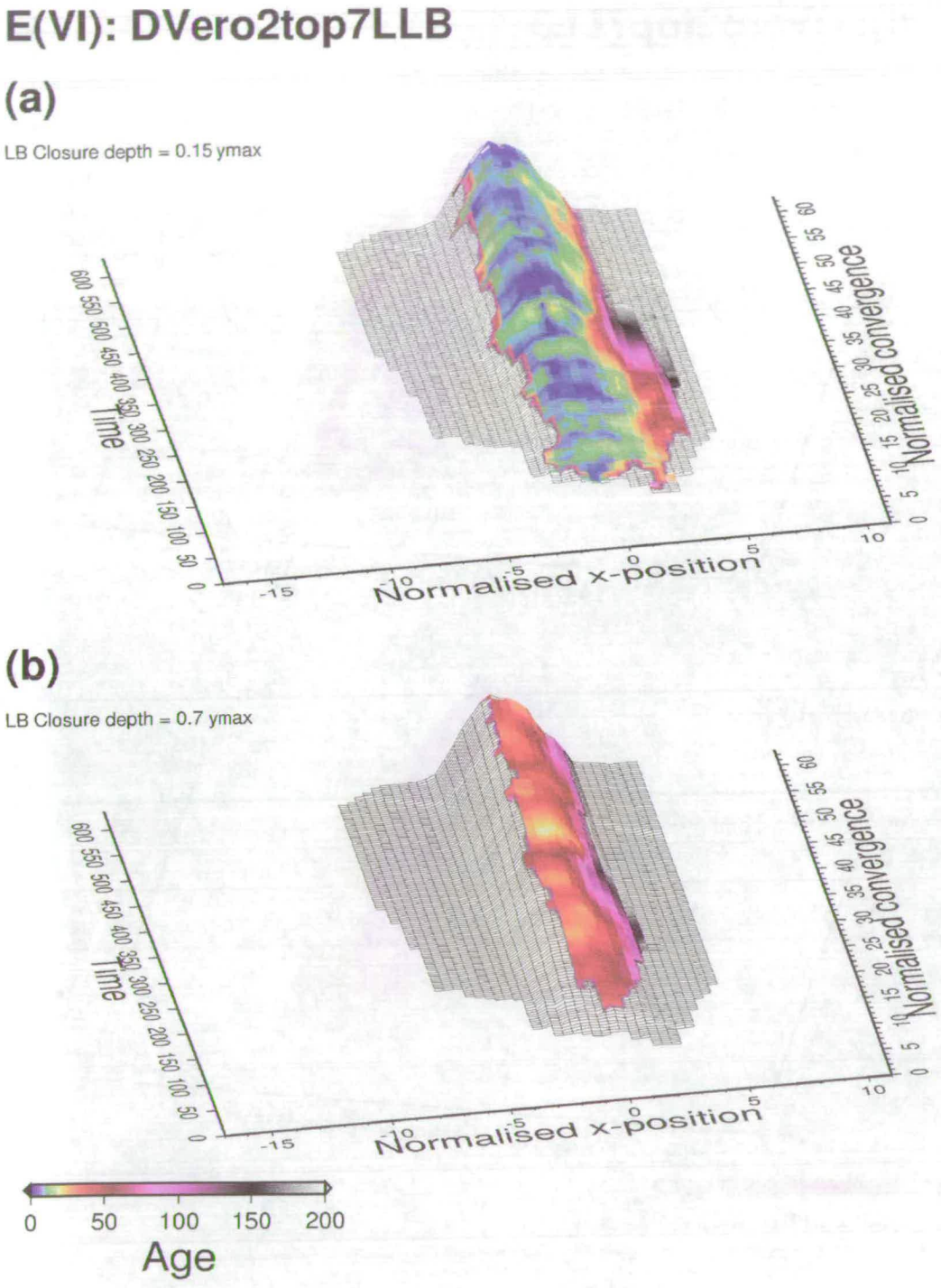

Figure 6.21: Age of surface material derived from closure depths of $0.15h_0$ and $0.7h_0$ mapped onto a surface mesh of cumulative erosion to compare the localisation of these two processes for run E(VI).

Shallow thermochronometers record more of the spatial distribution of erosion than deep thermochronometers. Both experience a variability in age within the central to pro-side region of a factor of 2, and the ages are not steady in time. This suggests large uncertainties with the use of thermochronometers in the derivation of erosion rates.

Many workers assume that thermochronometric ages can be used to describe erosion rates. The modelling presented demonstrates that the mapping from thermochronometry to erosion is not trivial, suggesting that erosion rates on the pro-side are likely to be underestimated by shallow thermochronometers beyond the transition between reset to un-reset ages. The narrow strip of old ages at the pro-retro transition describes the oblique nature of pro-side trajectories rather than cumulative erosion. Thermochronometry only records erosion when trajectories are vertical. The thermochronometric record is a product of a combination of wedge kinematics and the closure zones.

6.5.3 Discussion of assumptions

The assumption that closure surfaces are parallel to topographic surfaces does not hold for deep thermochronometers. The topographic influence decreases with depth and isotherms flatten in real systems (Stuwe et al., 1994). Less material would therefore be reset as the i^{th} isotherm is now generally deeper within the wedge, further accentuating the trend of smaller distributions of ages for deeper thermochronometers.

The erosional algorithm applied is crude, however the majority of material eroded from orogens is generally derived from the highest peaks. The 2D DEM approximates some spatially averaged system rather than a topographic regime, so this assumption may not be too bad. The regions of greatest error will probably be at the abrupt transition from erosion to no-erosion. This would produce a wider range of very old values on the retro-side and broaden the band of old values of the pro-side.

6.6 Comparison with real studies

Using sediment stratigraphy we can document periods of low and high denudation integrated over a catchment. For the Pyrenees, this information has been summarised by Sinclair et al. (Submitted) in a chronostratigraphic diagram (Figure 6.22). Assuming low temperature thermochronometry can be used to derive erosion rates, Sinclair et al. (Submitted) went on to illustrate envelopes of cumulative erosion over the Pyrenees, shown in Figure 6.23. Initially, the Pyrenean record suggests that surface uplift and erosion is fairly symmetric for the small wedge, but as the wedge grows, deformation migrates towards the pro-side. This asymmetry compares well with cumulative erosion plots generated by the modelling (Figures 6.11(b) and 6.12(b)). The metamorphic grade across the Pyrenees does not follow the same trend as the low

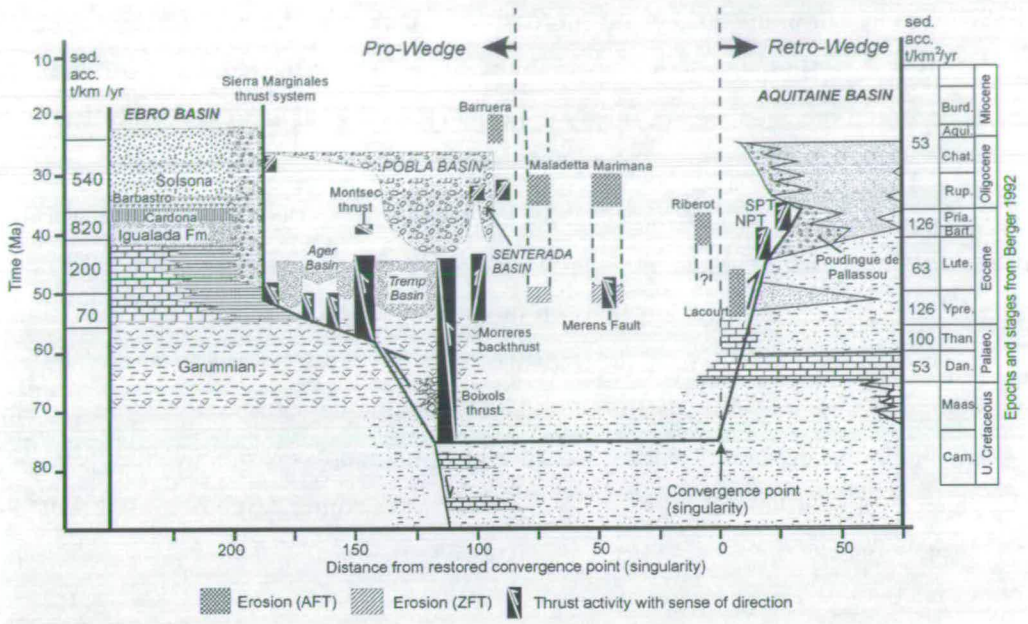

Figure 6.22: Chronostatigraphic evolution of the Pyrenees, including syntectonic sedimentary flux information (Modified from Sinclair *et al.*, Submitted)

temperature thermochronometry. The metamorphic grade is skewed to the retro-side which is also consistent with the model predictions. However, this study shows that this technique of deriving cumulative erosion from thermochronometry may under-estimate erosion rates on the pro-side where trajectories may be oblique.

The Southern Alps, New Zealand, exhumes the highest grade metamorphics on the retro-side of the orogen. However, in this case the youngest thermochronometric ages are also skewed retro-ward. This is not inconsistent with our findings once asymmetric erosion is taken into account. One would expect that increased denudation towards the retro-side would continue exhuming deep rocks, and push the envelope of erosion, and thus younger ages, retro-ward.

Molnar (2003) presented a review of four papers which provided contradictory interpretation of the significance of the erosion - tectonic coupling in active mountain belts. All of the studies used thermochronometry to estimate erosion rates. In Taiwan, Dadson et al. (2003) showed that apatite fission track ages are not reset in the pro-wedge whilst the highest grade is skewed to retro-side. However, the spatial distribution of erosion does not compare well with the scheme employed in this study. In Taiwan, erosion is primarily controlled by supply and that supply is controlled by earthquaking and slip on the steepest slopes, which tend to be on the retro-side; not jointly governed by precipitation and relief. This would enhance the exhumation of particularly deep material.

The Cascades, Washington State, were investigated by as part of the review by Reiners

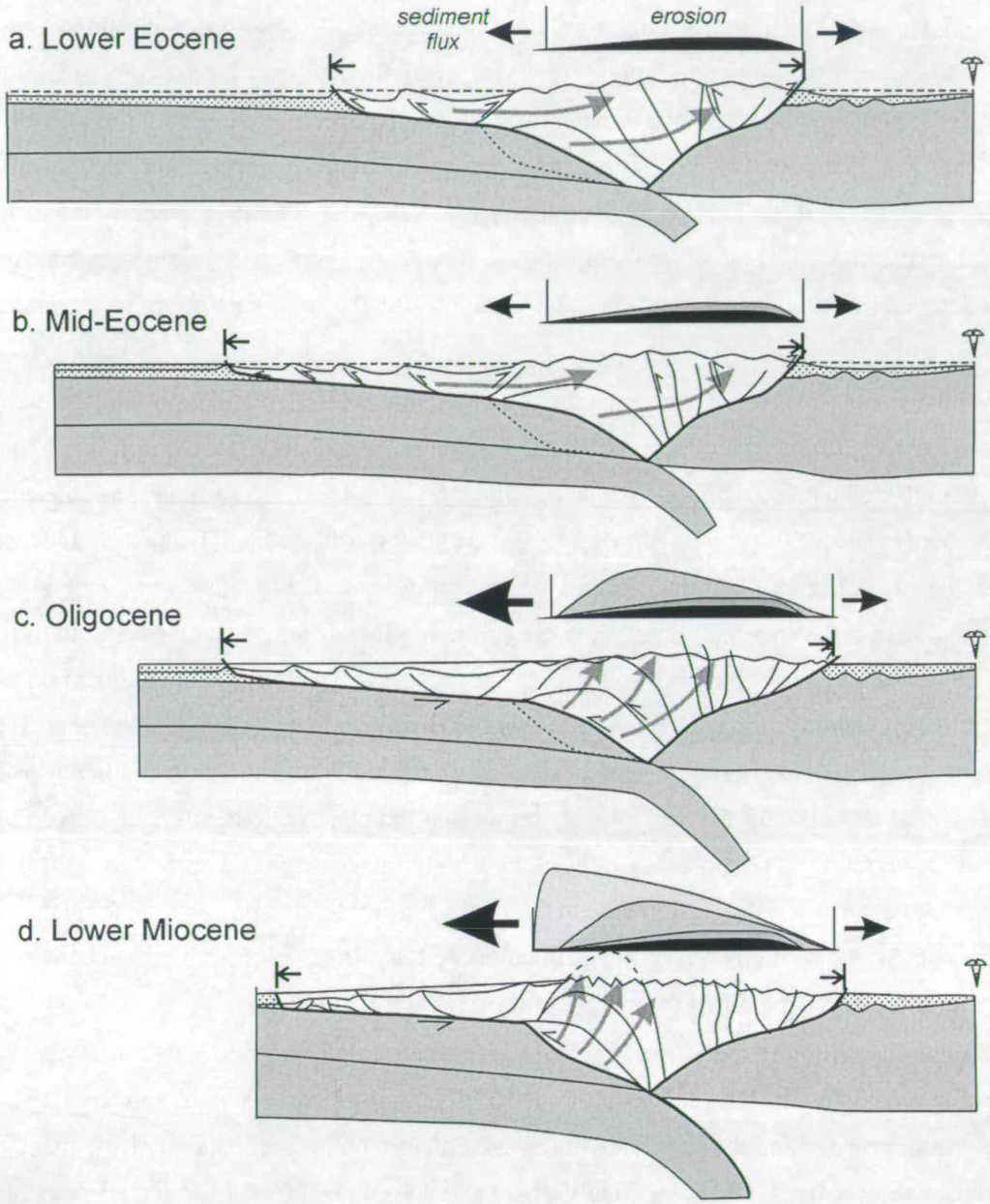

Figure 6.23: Structural reconstruction of the Pyrenees showing the corresponding sediment fluxes and cumulative erosional envelopes. Sediment flux arrows are directly proportional the sediment accumulation rates of 6.22. The erosive envelopes are implied from denudation rates using low temperature thermochronometry.

et al. (2003). High exhumation rates, derived from low (U-Th)/He ages, lie within the pro-wedge and coincide with the highest precipitation. As there are no obvious structures and the orogen is assumed to have been emplaced isostatically due to the absence of any tectonic process. They demonstrate a strong correlation between high erosion rates and the maxima in modern day mean annual precipitation. However, the extrapolation of modern day precipitation rates to the geological past has large errors. An alternative interpretation could be that the age distribution is primarily a fossil record of the past kinematic history of the wedge prior to its isostatic exhumation. The old ages on the pro-side are equivalent to the band of ages in the modelling that described the oblique trajectories. The central portion of young ages indicate the most active part of the wedge and the older ages towards the retro-side describe the relatively inactive retro-wedge.

Whilst localised erosion can enhance a signal, this thesis lends support to the work of Burbank et al. (2003), which suggests that precipitation is probably not the dominant control. The natural kinematics of doubly vergent wedges tends to localise uplift for periods across a large extent of the wedge with the most frequent events towards the tip of the pro-wedge tending to less frequent, higher magnitude events further retro-ward. If the episodic kinematic model presented here holds in real systems, it is not surprising that different studies come to different conclusions about the degree of coupling between erosion and tectonics, depending upon which part of the cycle the system is in. For the case of the Himalaya, paleomagnetic data make it clear that a large amount of shortening has been accommodated across the entire Himalayan front (Dewey et al., 1989), and that the total shortening on the plate scale is insensitive to orders of magnitude variation in precipitation rates along the Himalayan front (Wobus et al., 2003). This shortening has driven deformation across the Himalaya front. This prompts a consideration of the ways in which spatially varying precipitation perturbs the way this system accommodates shortening, in comparison to a case with uniform precipitation.

Submarine settings experience very low erosion rates compared with subarial systems. The threshold erosion algorithm predicts that once a submarine wedge becomes subaerial, the axial zone should broaden and the retro-side of the accretionary prism becomes relatively inactive. A second, shallower retro-side accretionary prism should only be present for accretionary prisms greater than some threshold size.

6.7 Conclusions

This chapter has demonstrated the relationships between erosion, exhumation and kinematics of a simple erosional doubly vergent wedge system. It suggests that whilst metamorphic grade and cumulative erosional flux can reach steady distributions, the time takeen for material to travel from some specified depth to the surface is highly variable depending upon the state of

the wedge (i.e. whether the wedge is thickening internally or accreting frontally). This prompts a review of current applications of thermochronometry in mountain belt systems. This might help resolve some of the differences in interpretation revealed in recent studies (Molnar, 2003) as to the significance of erosional - thermochronometric coupling in real data sets.

The erosional algorithm applied in the model is relatively crude, but it does provide a good end member scenario when compared with the non-erosive case.

Chapter 7

Discussion

This thesis focuses on elucidating processes within doubly-vergent systems rather than simulating specific real wedges. Much of what is discussed can be applied to real settings to aid understanding of their evolution. Section 7.1 discusses issues pertaining to the development of the DEM and how they relate to the the modelling results. Section 7.2 focuses on the use of modelling to illuminate the evolution of real settings.

7.1 DEM model formulation

7.1.1 General structure of the DEM

In designing the DEM, compromises had to be made regarding the resolution of the model to ensure a realistic run time was maintained. A run time of less than a week on a desktop machine, running at 2.4GHz, was chosen as appropriate for the scope of this study. Future implementations of the model on faster machines would use more particles to improve structural resolution, and be generalised to 3D, incorporating along strike effects. Due to the discrete calculation of the inter-particle force increments, the code would parallelise well, providing that the 3D model can be divided into tessellating units with a low surface area to volume ratio, each containing a large number of particles.

7.1.2 The DEM material

The strength of the material is a function of the packing structure, particle geometry and the inter-particle force laws. The use of a regular packing arrangement, as proposed by Burbidge (2000), introduces strain weakening into regions where the packing has been disturbed. However, using this technique the degree of strain weakening in a given packing cannot be prescribed as it is an emergent phenomena. It is better to develop a parametrised strain weakening term in the contact force algorithm.

There is potential to develop the singly-vergent critical wedge work further. The emergent formation of the passive, shallower backstop with the clustered packing is interesting as it is a feature observed in sandbox experiments (Lohrmann et al., 2003) and real accretionary wedges (Kopp and Kukowski, 2003). Understanding why the single disc particle packing does not form this feature may elucidate the processes involved in turning off activity in this backstop region. The regular hexagonal packing did not form singly-vergent critical wedges, but this does not mean that the processes it simulates are not found in nature. The Jura mountains in the European Alps are a possible analogue for the behaviour exhibited by the singly-vergent hexagonal packing experiments. In this setting, deformation is propagated a long distance from the main orogen (the Alps) along laterally continuous, competent limestone beds, beneath a Siliciclastic foreland sedimentary cover detached on weak Triassic evaporites. The resulting structures form the thrust cored anticlines which comprise the Jura (Laubscher and Bernoulli, 1982).

A lower inter-element coefficient of friction would produce more realistic wedge taper angles, but the values chosen for this study had to ensure that a reasonable amount of convergence could be accommodated without deformation localising at the model boundaries. The angles generated in this study are more consistent with those observed in sandbox models. The generalisation to 3D introduces two extra degrees of freedom, one translational and one rotational, that will affect the material properties, making it easier for particles to pass at high densities.

7.1.3 Boundary conditions

The first order difference between the DEM constant velocity and traction force boundary conditions are comparable with the differences observed in different sand box and computational doubly-vergent wedge simulations. Identifying the key mechanism in producing this difference (i.e. the nature of the basal discontinuity and basal friction) allows us to start discussing the relative merits of different boundary conditions as applied to real systems. This is important as it sets up a framework in which we can compare previous work objectively.

The use of a traction force is an important development that facilitated the study of doubly-vergent DEMs. Generally, other studies use particles, angular surfaces or normal motion of a perpendicular boundary to force motion parallel to a boundary. The limitations of these approaches in producing a velocity singularity at some point along a boundary have been made clear in this thesis and Naylor *et al.* (In press).

The sensitivity of the model results (analogue, FEM and DEM) to the boundary conditions employed demonstrates the need to use boundary conditions appropriate to the setting one wishes to investigate. Hopefully, the fact that resulting deformation patterns are non-unique will provide an opportunity to probe the geological reality in the future. As a first step to achieving this, it is important to understand the reason behind differences in model results.

7.1.4 Erosional algorithm

The erosional algorithm employed was crude, but provided insight into how the internal mechanics of a doubly-vergent system may be perturbed. This is one of the main areas where the model should be developed. However, it is non-trivial as the gradual removal of mass (in units less than the particle size) from the system is difficult.

The mapping of a real 2D erosional environment onto a 1D cross section raises difficult conceptual issues about the averaging assumptions used in 1D models. For example, is the topography in the 1D cross section best represented by the minimum, mean or maximum elevation of a swath through a real orogen? Given that the profiles are not concave, we can rule out the minimum topography. The topography probably represents some mean elevation, so a down stream catchment averaged erosion law is probably the most appropriate to use in such scenarios. However, this may be the wrong approach to take as our ultimate aim is to develop a full 3D coupled model. Starting work on this now and waiting for computational power to catch up would make a significantly greater advance than improving a fundamentally problematic 2D system.

7.2 Further tectonic implications

There are a number of issues where the modelling stimulates a discussion of our understanding and interpretation of geological processes. The interaction of different elements of the system have to work together and be consistent with the evidence available if a proposed model holds. Some of these ideas are critically discussed below.

7.2.1 The S-point, underplating and isostacy

The term S-point was introduced to describe the velocity discontinuity on the lower boundary of computational models (Willett et al., 1993). Conceptually, this relates to the transition between the subducting and over riding plates. In order to understand the limitations of its role within the FEM and DEM modelling, a consideration of real orogenic wedge systems is required. In plan view, wedges form where collision between two distinct plates occurs. The wedge grows as material from the plates, primarily the subducting plate, is incorporated. An understanding of the vertical depth of the S-point is more complicated. One definition of the depth of the S-point is the point below which all material is subducted, thus bisecting the incoming plate into two portions: the upper part is accreted into the wedge, while the lower part is subducted. Following on from this model arises a definition of *underplating* as an event where material is incorporated into the wedge from a depth that would have previously been subducted. Such an event could represent an irreversible drop in the lowest detachment, initiating an increase in the flux of material into the wedge. This is a distinctly different process to

frontal accretion or internal thickening of material derived from above the lowest detachment, which is termed here *basal accretion*. The modelling presented in this thesis, as with much of the FEM modelling, only incorporates the frontal accretion and internal thickening mechanisms as they assume a constant thickness of incoming material. This may be appropriate for submarine accretionary prisms that accrete a thin sedimentary cover (Bigi et al., 2003), but is unlikely to characterize the entire history of large wedges. This assumption is also made in this project as the interactions governing the change in regime are beyond its scope.

This has been recognised by Beaumont et al. (1999), who has developed an alternative FEM coupled model in which the proportion of incoming material that is subducted and incorporated varies. The variation in the depth of material accreted is likely to be a complicated function of the size of the wedge, the structure of the incoming material and the nature of the subduction.

Such discussion prompts another look at the lateral position of the S-point and its relation of other features in the wedge. Figures 7.1 and 7.2 show how the evolution of the coupled tectonic-erosion FEM models vary for different degrees of asymmetric erosional forcing. The erosion number, N_e is defined to be the ratio of the rates of erosion and tectonic uplift. In the asymmetric models presented here erosion is applied to only one side of the topographic divide. The amount of material eroded is given by the projection of the Lagrangian mesh above the ground surface. The ground surface is given by the bold line at the top of the Eulerian mesh. Consider the localisation of the S-point, the topographic divide and the bottom of the isostatic root in these figures. The topographic divide is always approximately above the isostatic root. However, the position of the S-point varies significantly with the erosion number. For low values of the erosion number ($N_e = 2$ in Figure 7.1) the S-point is always to the pro-side of the isostatic root. However, for high values of retro-side erosion number ($N_e = 10$ in Figure 7.2(a)) the S-point becomes localised to the retro-side of the isostatic root. This appears unphysical. In private correspondence, Willett suggested that in mature systems, the S-point is not too problematic because as the lower crust gets weak, it effectively detaches upper crustal deformation from mantle motion, so that is does not matter whether the S-point is a perfect discontinuity or whether the same convergence is distributed. However, an examination of Figures 7.1 and 7.2 shows that the regions of highest strain rate are approximately symmetrically distributed about the S-point. FEM models with low values of erosion number may be valid, but if Figure 7.2(a) is not physical, the transition between the physical and unphysical regimes needs to be defined.

7.2.2 Implications of varying the depth of incoming material via underplating

In certain settings, it should be possible to detect underplating as defined here. For example, the first time an accretionary prism comprised of sediment cover incorporates underlying crustal material using seismic, well data or gravity measurements.

The Simple Model (Section 5.2) assumed a constant thickness of accreted material in the

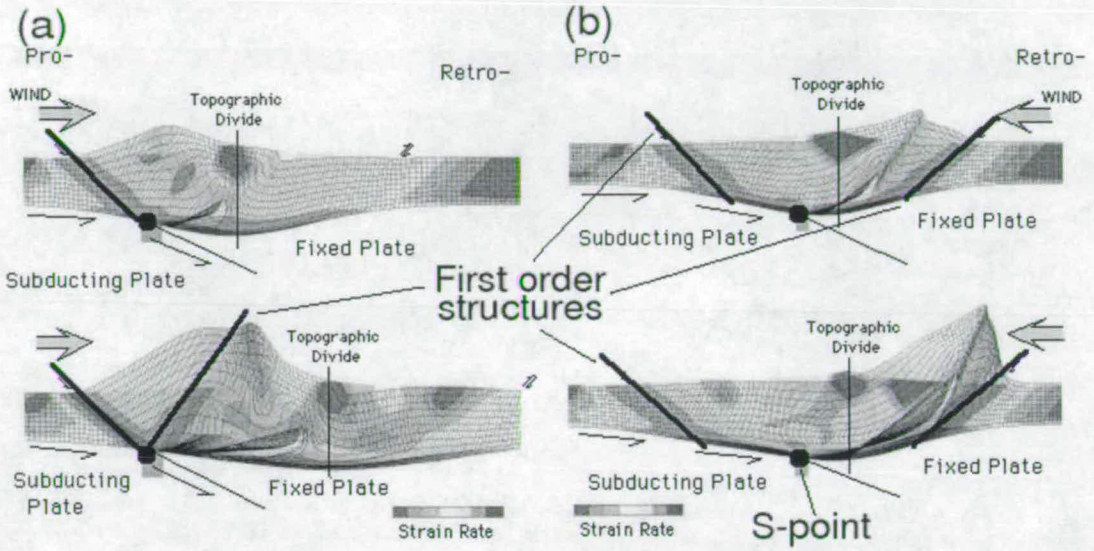

Figure 7.1: Erosion-tectonic coupled FEM models with low asymmetric erosion ($N_e = 2$) taken from Willett (1999). The orographic effect in these systems is such that there is no erosion on the leeward side of the mountains. In the left hand figures, precipitation and erosion are focussed on the orogenic wedge above the subducting plate (the pro-wedge). Note progressive focussing of deformation into pro-wedge to the left and highest exhumation in the orogen interior. In the right hand figures, precipitation and erosion are focussed on the orogenic wedge above the overriding plate (the retro-wedge). In contrast to model above, deformation remains focussed on each edge of orogen. Highest exhumation occurs at low elevation at the retro-wedge deformation front. Top to bottom shows model results with increasing time. (Taken from Willett, 1999).

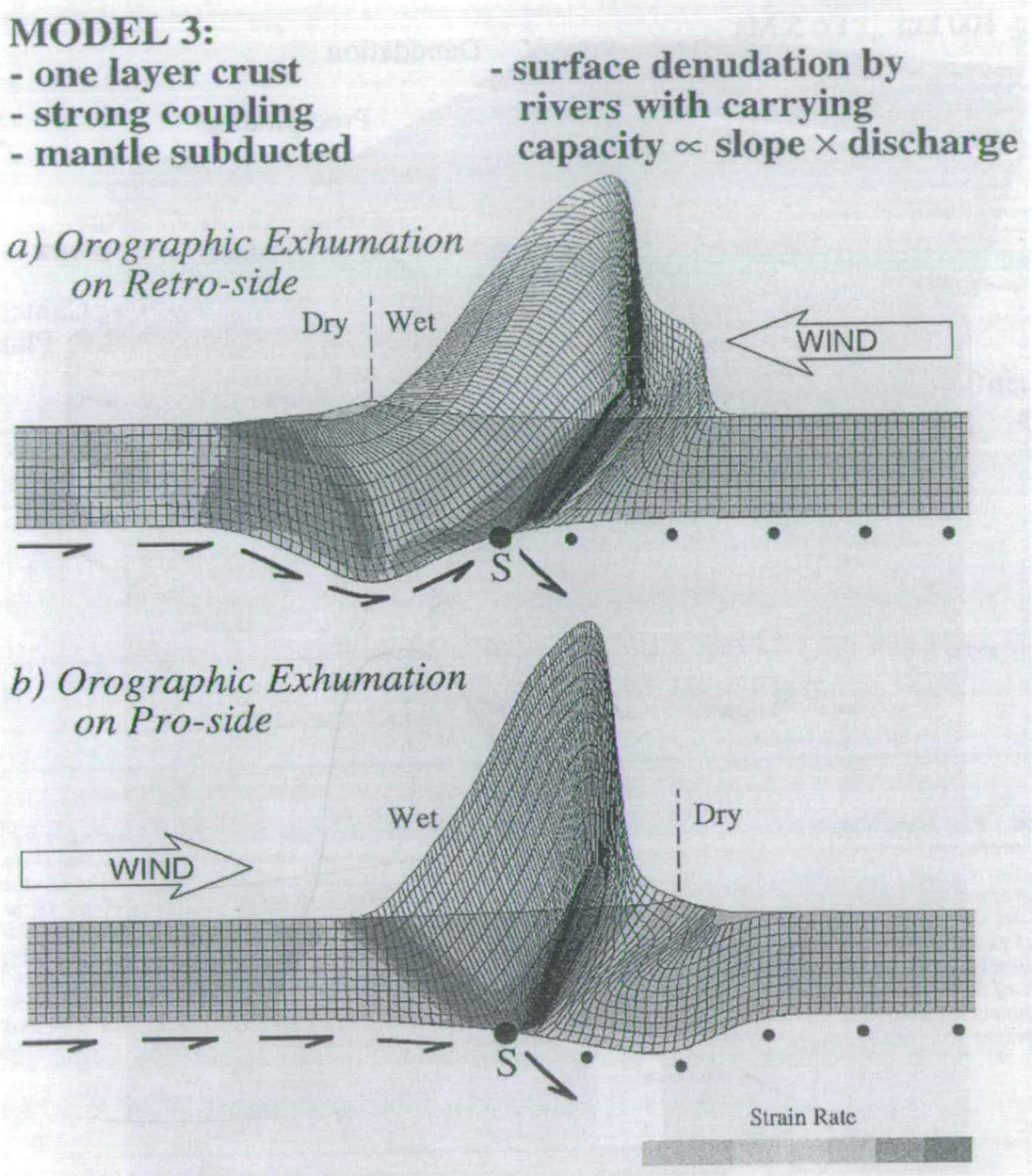

Figure 7.2: Erosion-tectonic coupled FEM models with high asymmetric erosion taken from Beaumont et al. (2000a), $N_e = 10$ on erosive side and $N_e = 0$ on non-erosive side. The localisation of the S-point with respect to the topographic divide switches side with the localisation of erosion as a product of the high erosion rates.

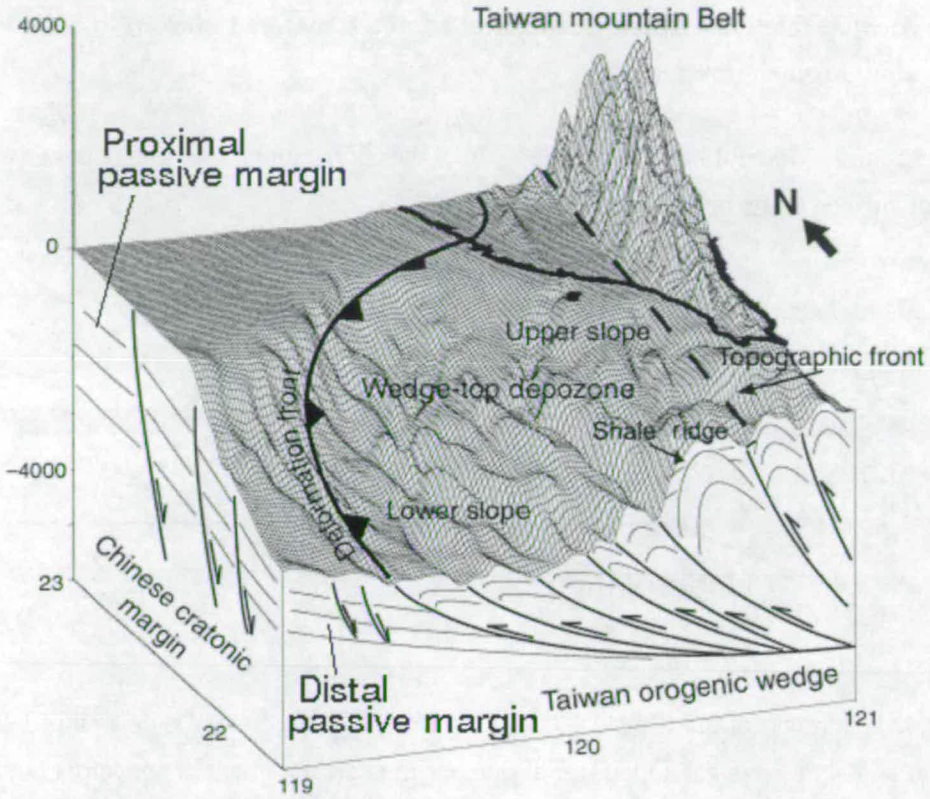

Figure 7.3: *The overall structural styles of a series of west-verging imbricated thrusts and folds and shale ridges in the wedge-top depozone confined by the topographic front proximal to the Taiwan Orogen and by the distal submarine deformation front transition to the passive Chinese margin (modified from Wu, 1993; Liu et al., 1997; Chiang, 1998).* Figure and Caption taken from Chiang et al. (2004).

derivation of a decreasing surface uplift rate. The accretion of an increasing thickness of material would result in more rapid wedge growth. An example of this process occurs when the thickness of the accreted cover increases (Chiang et al., 2004). In Taiwan, in the north the entire passive margin is accreted, whereas in the south only the tip of the passive margin is accreted. The length of the island is limited by the coincidence of the oblique subduction zone with the passive margin (Figure 7.3), as the uplift rate is low where the sediment cover accreted is thin. In this region, the deformation front and thrusts appear to parallel topographic contours as this is probably most efficient way to deform the sediments given the stage of strain within the wedge due to internal body forces.

7.2.2.1 At what rate would the thickness of accreted material thicken to sustain a constant surface uplift rate?

Using the Simple Model, I briefly investigate how the accreted material must thicken to sustain a constant surface uplift rate, illustrated in Figure 7.4.

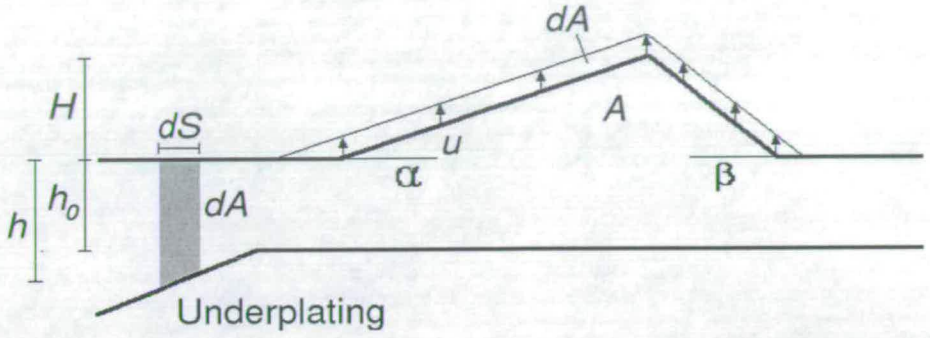

Figure 7.4: Illustration of the Simple Model extended to incorporate a drop in the detachment level, h, to sustain a constant surface uplift rate, u. dS is an increment of convergence that adds an area dA of material into the cross-sectional area of the wedge. $alpha$ and $beta$ are constant pro- and retro-taper angles.

A surface uplift rate that increases linearly with shortening can be expressed:

$$\frac{\partial H}{\partial S} = u \tag{7.1}$$

when convergence commences, $S = 0$ and $H = 0$ therefore,

$$H = uS \tag{7.2}$$

Using the incremental material added to the wedge for a depth of material $h(S)$,

$$\partial A = \partial S h(S) \tag{7.3}$$

and the change in height by adding an amount of material ∂A,

$$\partial A = \partial H H \left(\frac{\tan\alpha + \tan\beta}{\tan\alpha \tan\beta} \right) \tag{7.4}$$

$$\begin{aligned}
\frac{\partial H}{\partial S} &= \frac{\partial H}{\partial A}\frac{\partial A}{\partial S} \\
u &= \frac{h(S)}{H}\left(\frac{\tan\alpha\tan\beta}{\tan\alpha+\tan\beta}\right) \\
h(S) &= uH\left(\frac{\tan\alpha+\tan\beta}{\tan\alpha\tan\beta}\right) \\
&= u^2 S\left(\frac{\tan\alpha+\tan\beta}{\tan\alpha\tan\beta}\right)
\end{aligned} \tag{7.5}$$

Thus the rate at which the incoming material must thicken to sustain a constant uplift rate is,

$$\Rightarrow \frac{\partial h}{\partial S} = u^2\frac{\tan\alpha+\tan\beta}{\tan\alpha\tan\beta} \tag{7.6}$$

So for this simple model, $h \propto S$ to sustain a constant average surface uplift rate, maintaining a doubly-vergent wedge with constant tapers α and β. Taking $\frac{\tan\alpha+\tan\beta}{\tan\alpha\tan\beta} \sim 1$ the key parameter is u^2. If the deepest detachment of incoming material cannot drop at rate comparable to u^2, that rate of surface uplift wedge will decrease with time. We get the same relation with time for a constant convergence rate, $v = dS/dt$.

7.2.3 Thrust sheet accretion

In the southern Pyrenees, the restoration of accreted thrust sheets demonstrates that they thin towards the deformation front (Figure 5.26) as they detach along successively shallower ramps (Vergés, 1999). This implies a scheme that is different to that investigated by most sandbox, FEM and DEM models in which new thrust sheets are propagated into a constant thickness, undeformed material. This is a fundamental difference, as the southern Pyrenean fold and thrust belt is pre-defined along a dipping horizon. This is also observed in Taiwan (Chiang et al., 2004) where the oblique nature of the collision allows the foreland basin to be observed at different stages of its evolution. Figure 7.5(d) shows that in the early stages, the thrust sheets are defined by a shallowly dipping horizon. In the mature system (Figure 7.5(c)), these thrust sheets are incorporated by back rotation and internal thickening. What was the tip in the immature system is now replaced by a foreland basin, recycling a proportion of the material eroded from the sub-aerial part of the wedge.

The important scale in the DEM models presented was the total convergence per unit depth of material accreted. Thrust sheets were propagated roughly every 5 unit depths of convergence. For a given amount of convergence, shallow wedges would comprise of more thrust sheets.

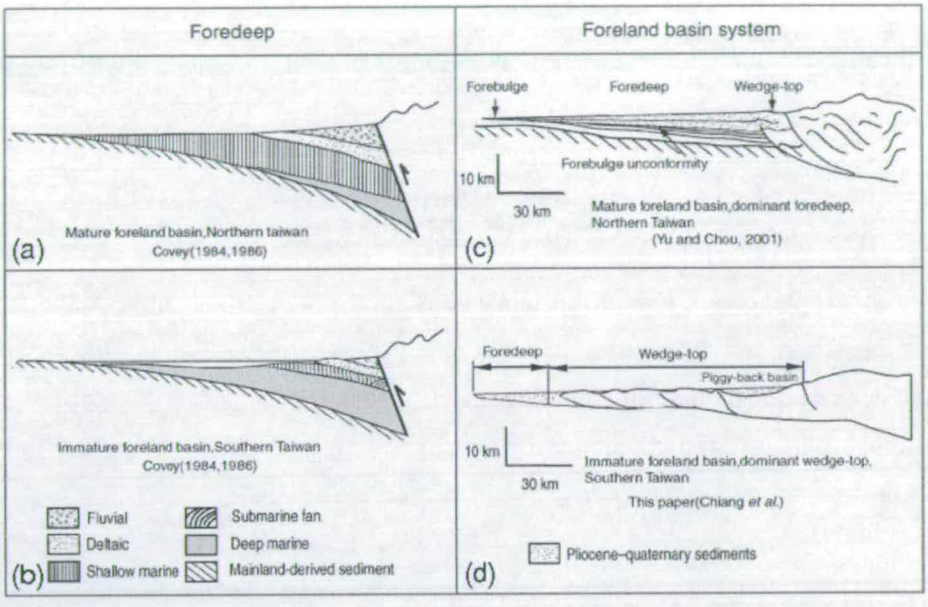

Figure 7.5: *The western Taiwan foreland basin can be divided into a mature basin in the northern Taiwan and an immature one in the southern Taiwan. In terms of lithofacies, the mature basin consists mainly of shallow marine and fluvial sediment and the immature one is dominated by deep marine fine-grained sediment (left column). Using the foreland basin system nomenclature of DeCelles & Giles (1996), the mature basin consists of distinguished features from east to west: a wedge-top depozone, a dominant foredeep depozone and a forebulge. The immature one is characterized by a dominant wedge-top depozone and an incipient foredeep (right column).* Figure and Caption taken from Chiang et al. (2004).

7.2.4 Catchment capture

Strong evidence for coupling between the topographic evolution and the internal kinematics in the modelled data occurs for the traction force boundary condition with the lowest relative retro-side friction, and is marked with a star in Figures 4.11 and 4.12. Figure 4.11(b) shows that this event corresponds to a change in position of highest peak from the retro-side to the pro-side. This process may be compared with catchment capture events in real systems such as has been suggested for the Landsborough River in the Southern Alps, New Zealand (Tippett and Hovius, 2000). In moving the highest peak to the pro-side, we see a corresponding rapid steepening of the pro-wedge and a shallowing of the retro-wedge in Figures 4.12(a) and (b) immediately followed by a gradual correction back towards the mean taper angles. This demonstrates a coupling between topography and internal kinematics resulting in localised deformation with relatively slow rates of migration of the drainage divide away from the pro-side, related to the incorporation of successive thrust sheets. In contrast, migration of the drainage divide towards the pro-wedge occurs in relatively instantaneous events generated by localised uplift to the pro-side of the drainage divide; once the shift in position has taken place, the maximum height of the wedge starts to increase again, localised on the new drainage divide (Figure 4.11(a)).

7.3 Summary

This chapter provides insight into the further implications of the thesis, in a wider context. The computational, material, boundary condition and erosional limitations of the current DEM are acknowledged, prompting future work. It highlights problems in our conceptual understanding of the S-point, boundary conditions and mechanisms of accretion in real subduction zones. The effects of increasing the magnitude of the flux of material into the system are significant, so the use of a constant depth of accreted material is problematic. The geometry of the material comprising the pro-side fold-and-thrust belt in real systems is often pre-defined along shallowly dipping detachments rather than a homogeneous, undeformed section. The internal wedge kinematics have the potential to modify the drainage as the system evolves.

Chapter 8

Conclusions

The conclusions of thesis thesis are:

Advances in discrete element modelling of material phenomena. Regular packing structures introduce an extra length-scale into discrete element systems. This results in length-scale dependent phenomena not observed using random packing structures. This is demonstrated by the slump angle of repose experiments where the random material produced uniforms surface taper, but regular hexagonal packed materials exhibit concave equilibrium profiles. The global friction of the DEM material is an emergent property that is dependent on particle angularity, packing structure and inter-particle interaction coefficients.

Understanding the mechanisms of wedges using a discrete element model approach. Discrete element models using randomly packed materials successfully simulate much of the behaviour observed in singly- and doubly-vergent wedges. In singly-vergent wedges, random single disc materials produce uniform taper wedges. The random clustered disc material produces results most consistent with many sandbox analogue and real accretionary wedges due to the emergence of a shallowly tapering, inactive region adjacent to the backstop boundary. However, the regular hexagonal packing does not produce critically tapered wedges. In this case, long linear chains of adjoining particles allow strain to be transmitted for very long distances away from the primary wedge.

In generalising singly-vergent simulations to doubly-vergent problems, the nature of the lower boundary conditions had to be re-visited to introduce the velocity discontinuity at some point along the base rather than at the vertical side boundary. Lower boundaries that consist of particles present a problem as the frictional interaction of these boundary particles with those particles overlying the boundary is emergent. Further, this emergent friction is greater than the internal friction due to the reduced number of degrees of freedom in their motion. The traction force presented is a significant development as it allows the Coulomb failure limit to be specified. Discrete element simulations of doubly-vergent systems demonstrate how sandbox analogues which show partitioning of deformation across a single retro-vergent structure rooted

at the S-point versus those which exhibit Stage 3 retro-side accretion are the same problem but with very high or low retro-side basal friction respectively. Further, the partitioning in the high basal friction experiments also encompasses analogue experiments which intruded a shallowly dipping, rigid indenter.

New insights into orogenesis.

1. Assuming a constant convergence rate, v, the accretion of thrust sheets of constant length, l, into a wedge introduces a time-scale given by the time it takes to incorporate successive thrust sheets into the wedge such that $t \sim l/v$.

2. The width of an orogen fluctuates around a background trend as thrust sheets are propagated and incorporated. The propagation of a new thrust sheet is a rapid process as the additional cross-sectional area above the undeformed surface is small, requiring only a small amount of convergence. In contrast, the total incorporation of the new thrust sheet requires a large amount of convergence, slightly less than l, and thus takes longer. Thus, it is predicted that a signal relating to t is seen in the evolution of real deformation fronts.

3. Further, as the deformation is episodic, one would expect to see a signal in erosive pulses and thermochronometric records. If present, this should be measurable in real wedges as t is comparable or greater than the structural, sedimentological and thermochronometric resolution available in many systems.

4. In contrast to finite element modelling of erosive systems, DEM models predict signatures of thrusting in thermochronometric ages and metamorphic grade.

5. The significance of the oblique nature of trajectories in accretionary systems is highlighted by the deepest exhumed material being skewed to the retro-side of the cumulative erosion envelope.

6. Thermochronometers are most likely to underestimate erosion on the pro-side of orogens where trajectories are most oblique. The greatest offset in ages across structures are predicted to be in the retro-side of an orogen where deformation occurs infrequently, but with a large magnitude.

Appendix A

Singly-vergent critical wedge experiments

The Singly-vergent wedge results presented in this appendix extend those results presented in Chapter 3. They were all run with identical boundary conditions, only the nature of the packing structure and inter-disc coefficient of friction were varied. For each run, figures showing the deformation of initially horizontal horizons and the localisation of large relative displacement are shown. Where appropriate, the critical taper angle is displayed.

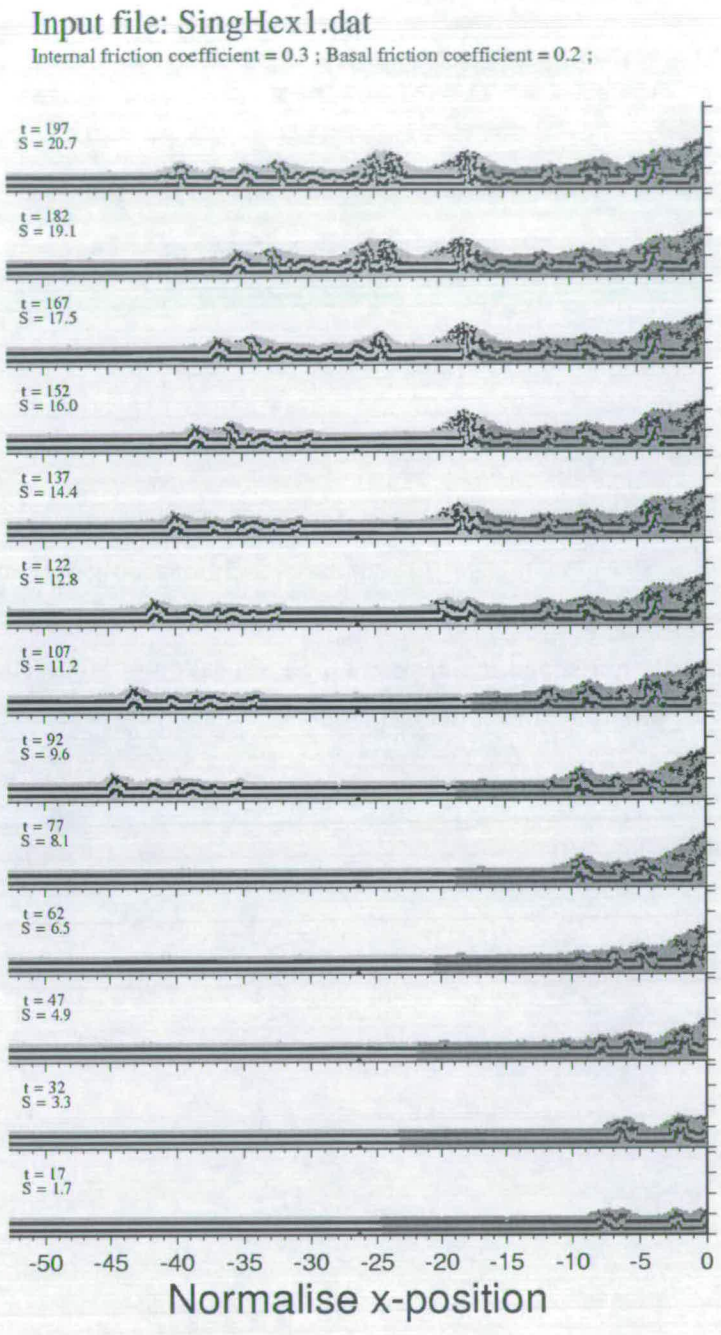

Figure A.1: Horizon deformation plot of Singly-vergent critical wedge boundary conditions applied to the regular hexagonal packing does not produce a critically tapered wedge due to the geometric constraints placed on the system.

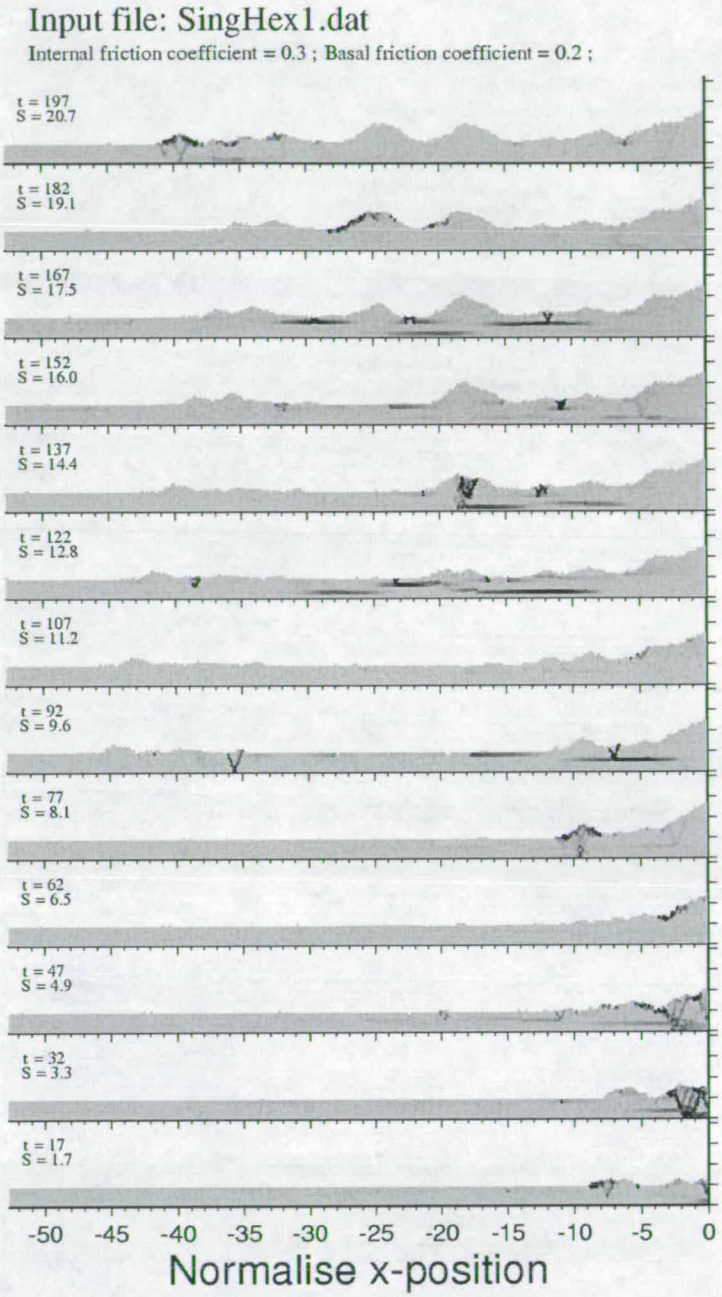

Figure A.2: Relative displacement plot of Singly-vergent critical wedge boundary conditions applied to the regular hexagonal packing does not produce a critically tapered wedge due to the geometric constraints placed on the system. This is highlighted by the large relative displacement chainsalong the horizontal and 60^o planes.

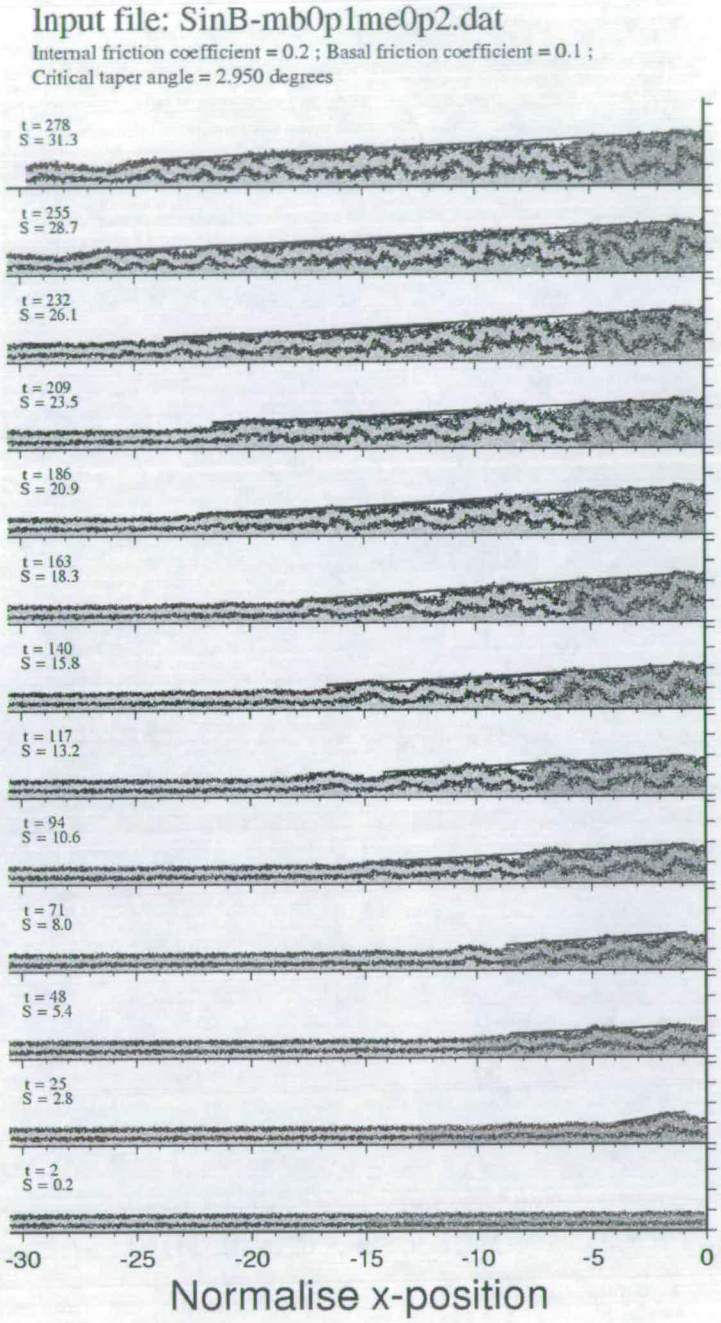

Figure A.3: Singly-vergent horizon deformation plot for the random single disc particle structure with $\mu_b = 0.1$ and $\mu_e = 0.2$.

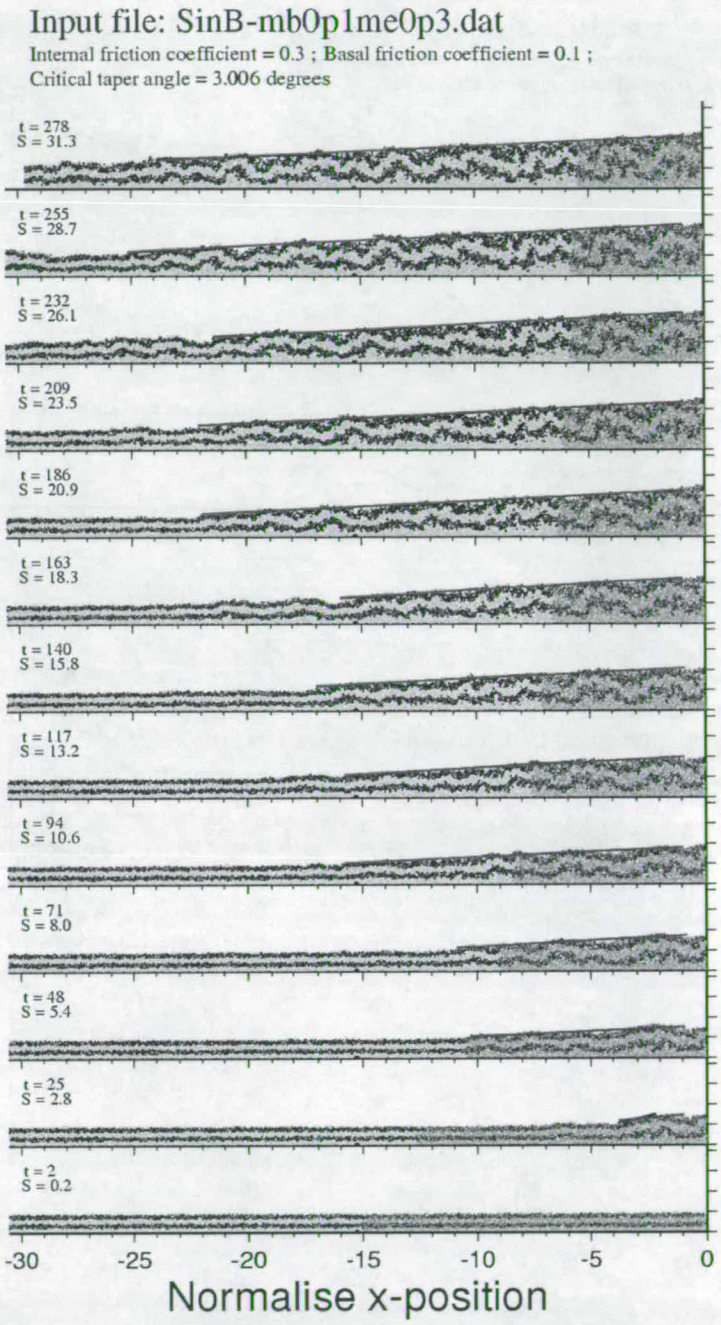

Figure A.4: Singly-vergent horizon deformation plot for the random single disc particle structure with $\mu_b = 0.1$ and $\mu_e = 0.3$.

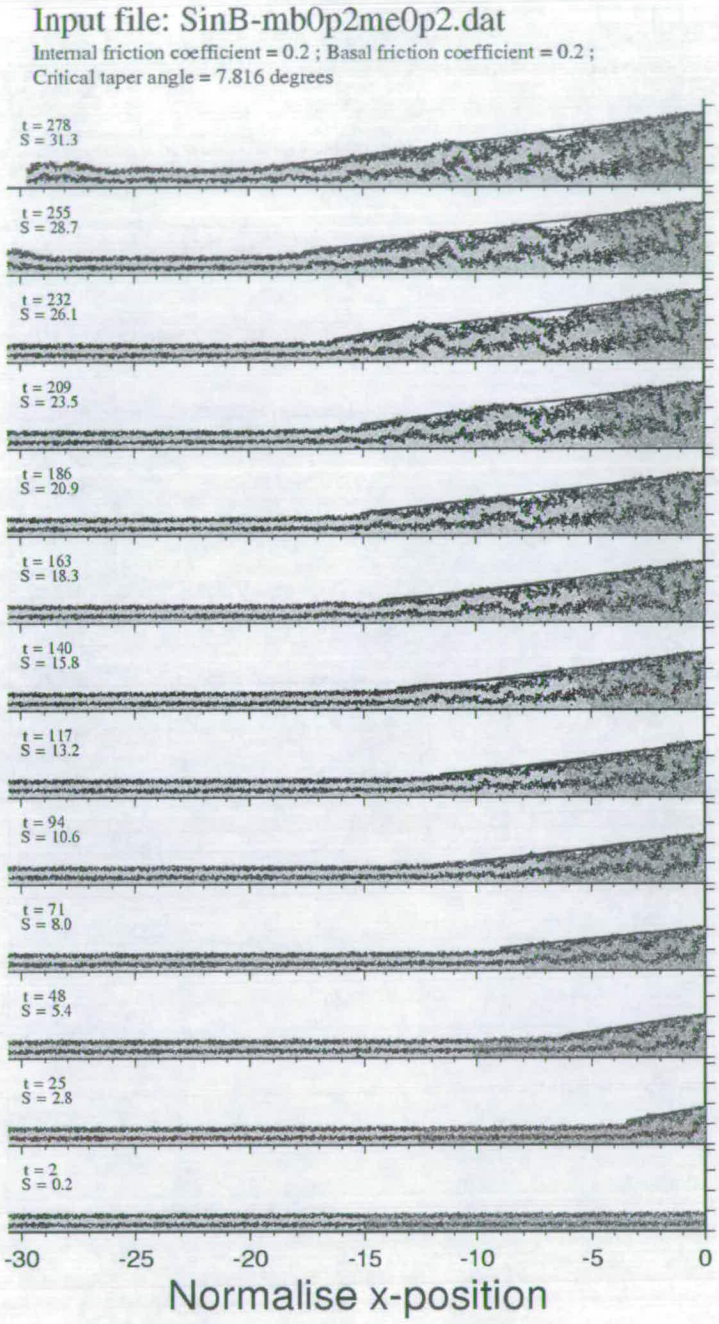

Figure A.5: Singly-vergent horizon deformation plot for the random single disc particle structure with $\mu_b = 0.2$ and $\mu_e = 0.2$.

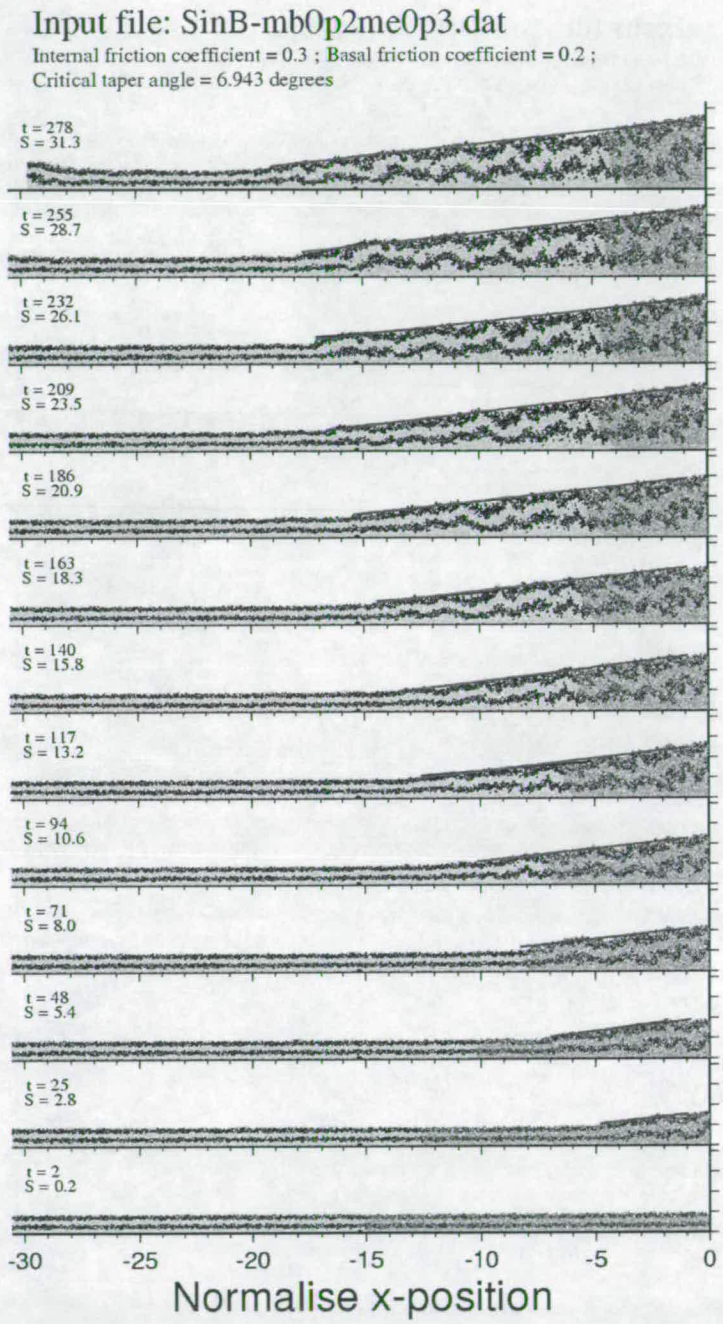

Figure A.6: Singly-vergent horizon deformation plot for the random single disc particle structure with $\mu_b = 0.2$ and $\mu_e = 0.3$.

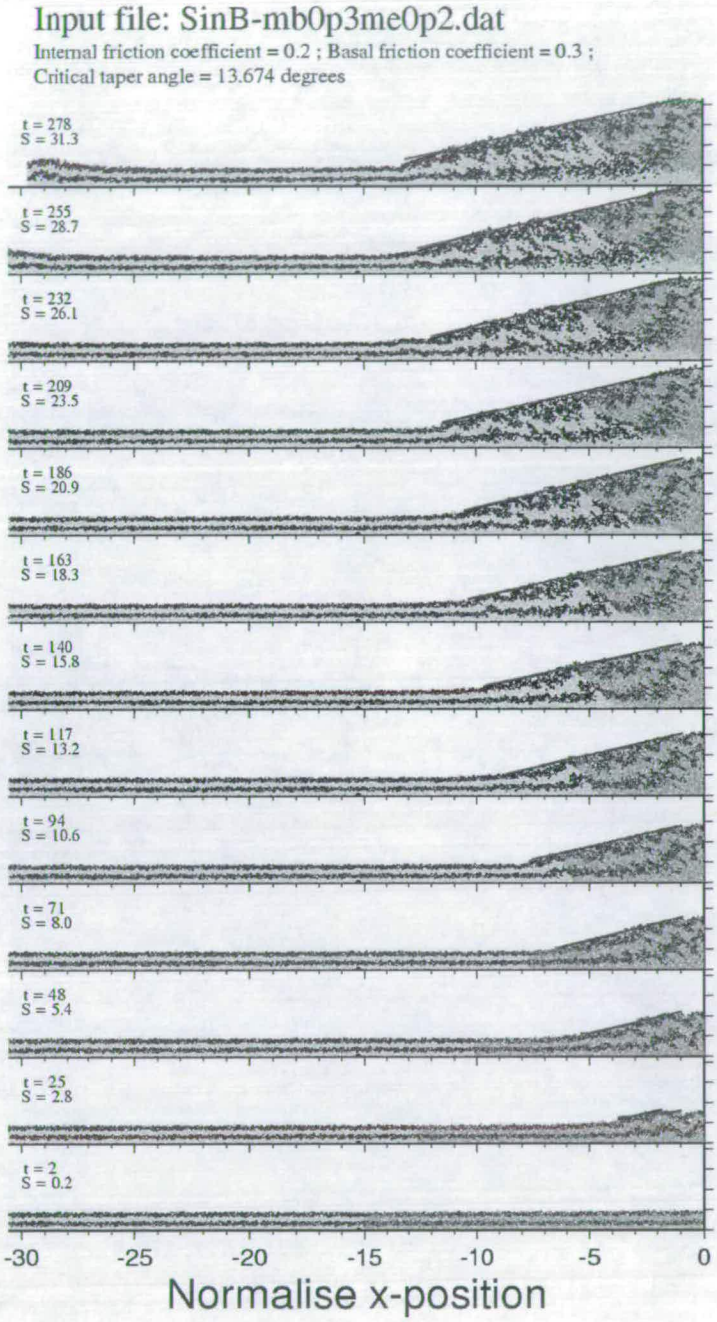

Figure A.7: Singly-vergent horizon deformation plot for the random single disc particle structure with $\mu_b = 0.3$ and $\mu_e = 0.2$.

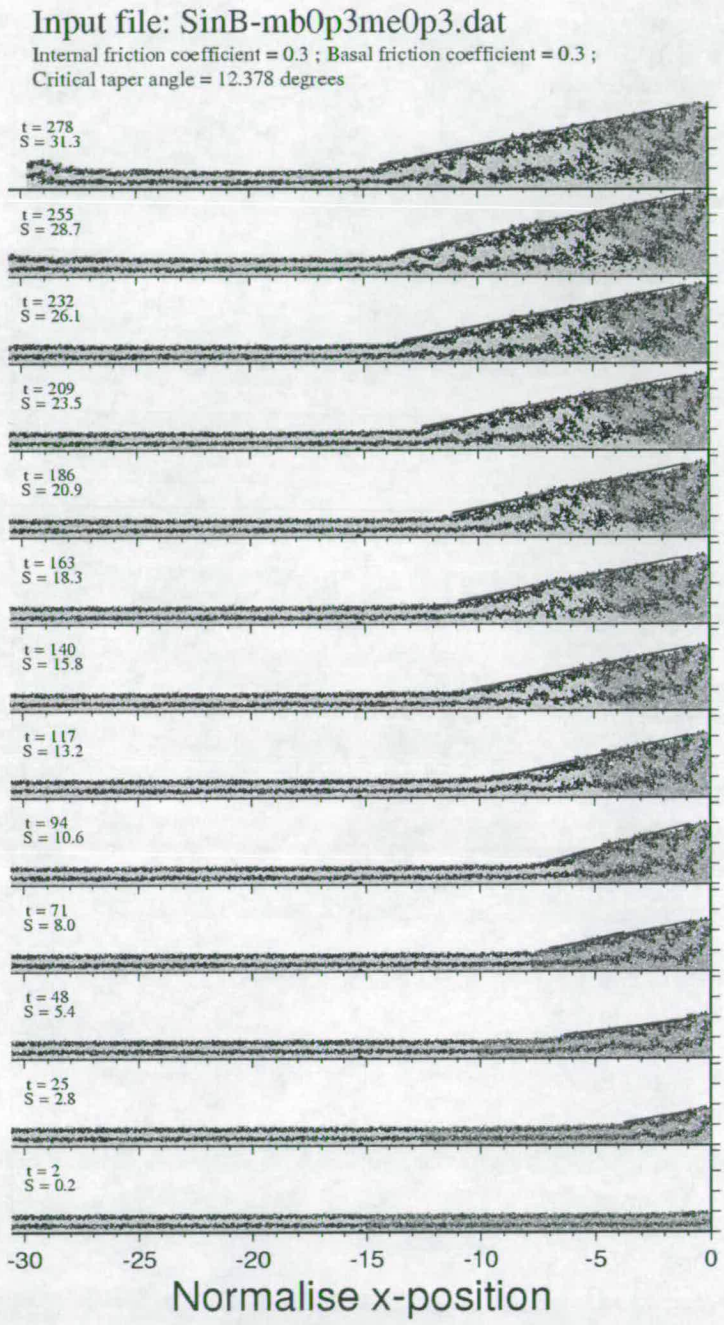

Figure A.8: Singly-vergent horizon deformation plot for the random single disc particle structure with $\mu_b = 0.3$ and $\mu_e = 0.3$.

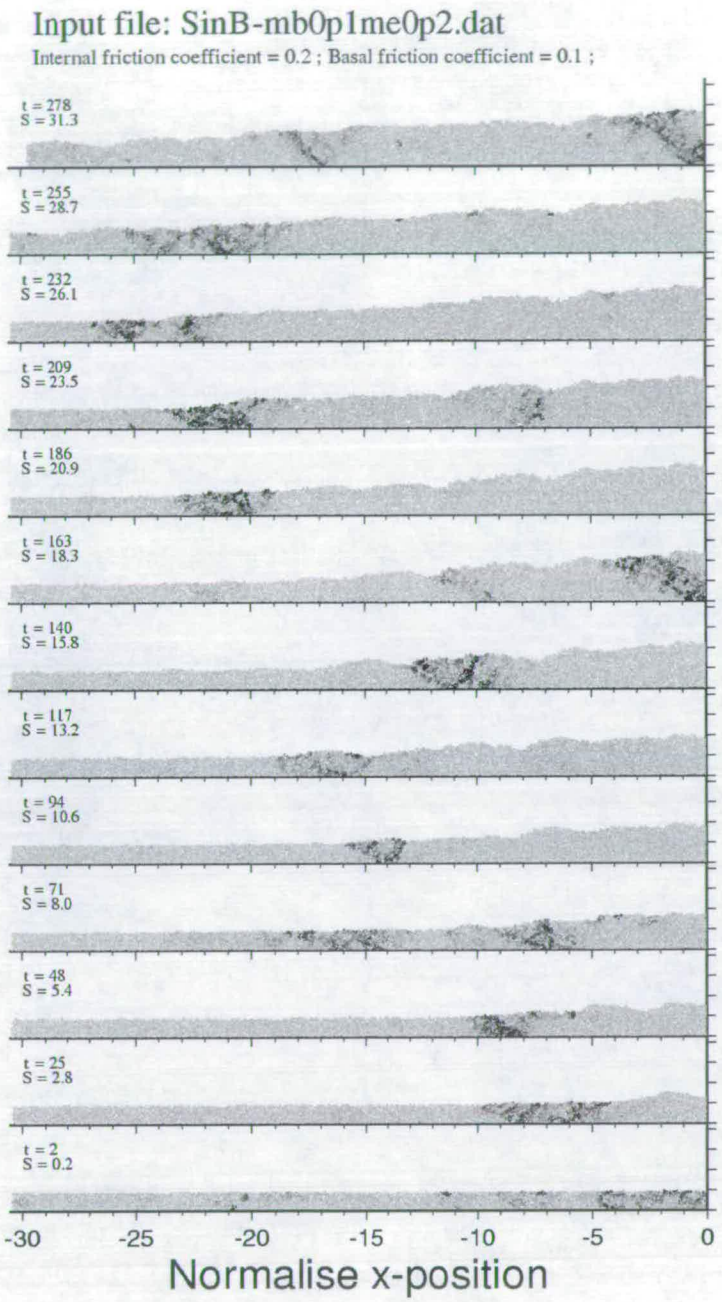

Figure A.9: Singly-vergent relative displacement plot for the random single disc particle structure with $\mu_b = 0.1$ and $\mu_e = 0.2$.

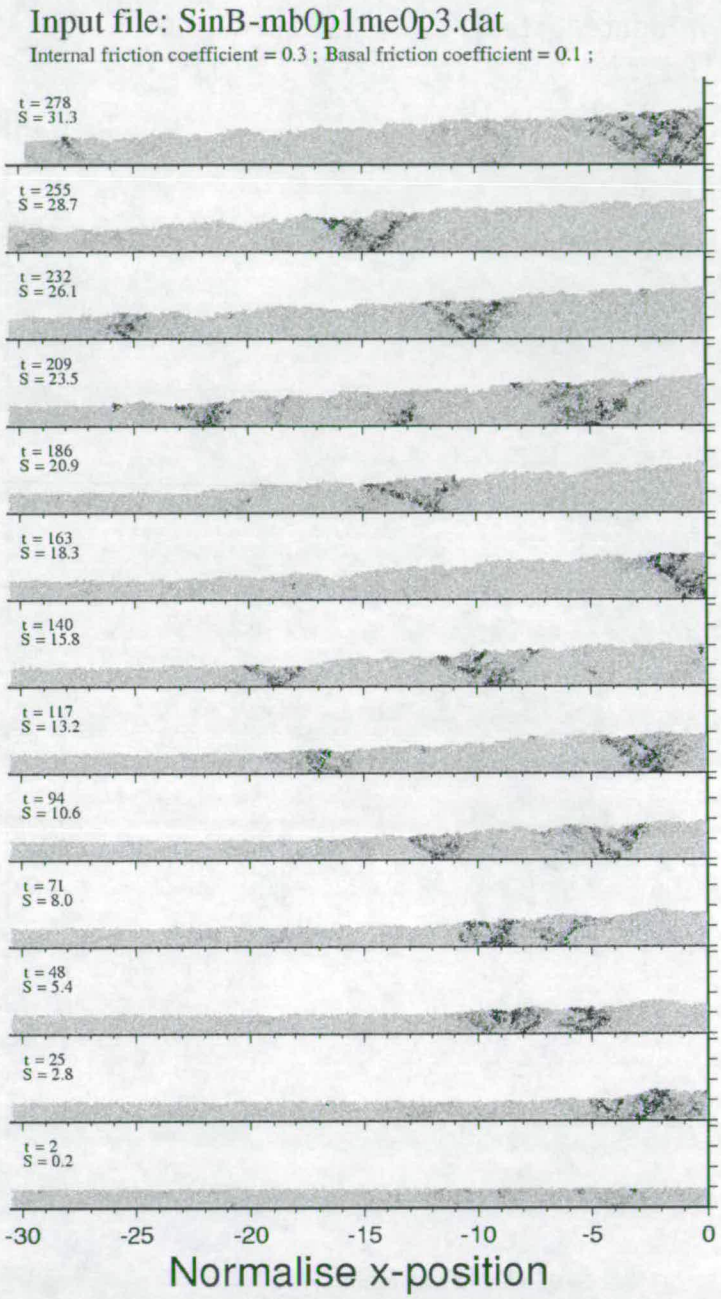

Figure A.10: Singly-vergent relative displacement plot for the random single disc particle structure with $\mu_b = 0.1$ and $\mu_e = 0.3$.

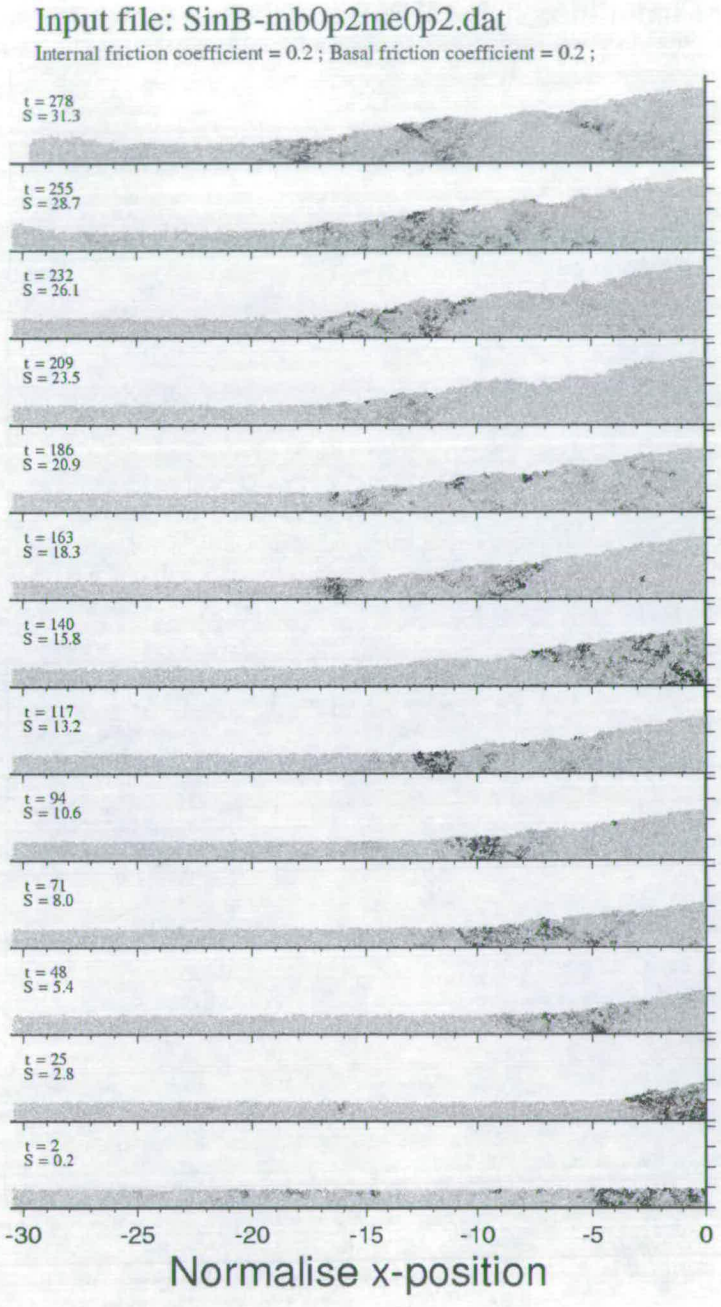

Figure A.11: Singly-vergent relative displacement plot for the random single disc particle structure with $\mu_b = 0.2$ and $\mu_e = 0.2$.

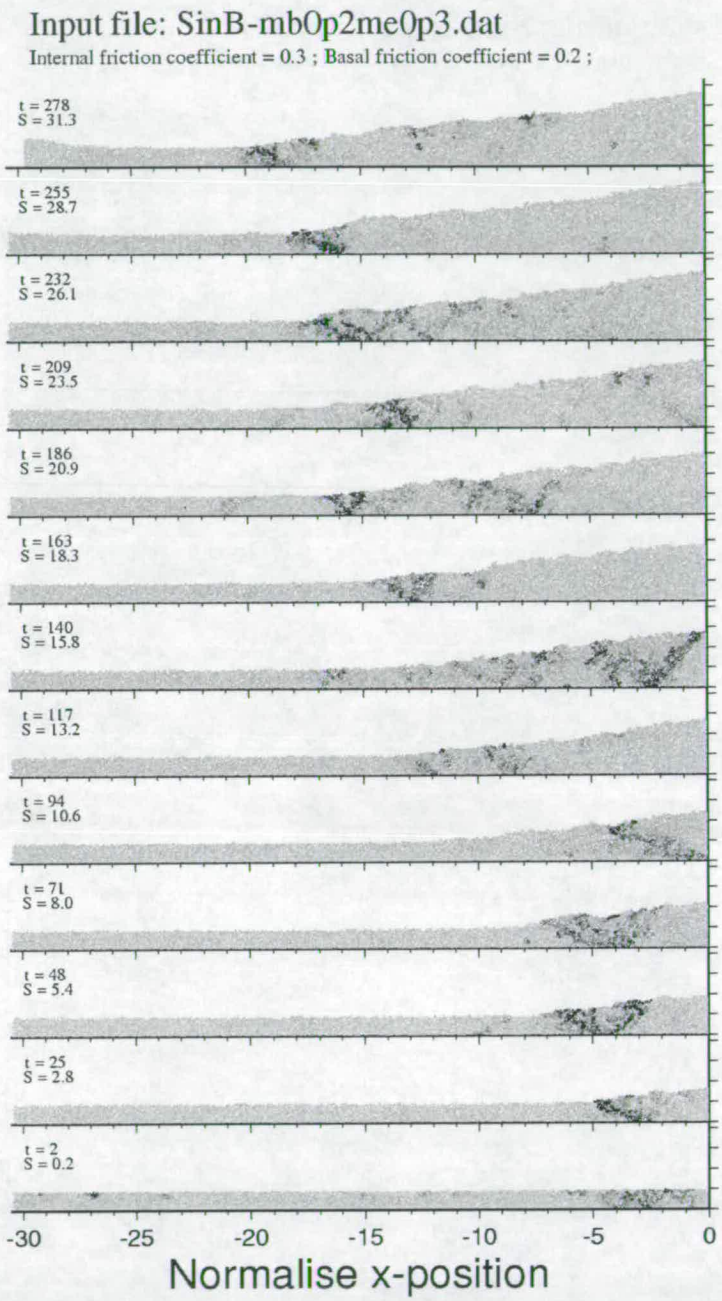

Figure A.12: Singly-vergent relative displacement plot for the random single disc particle structure with $\mu_b = 0.2$ and $\mu_e = 0.3$.

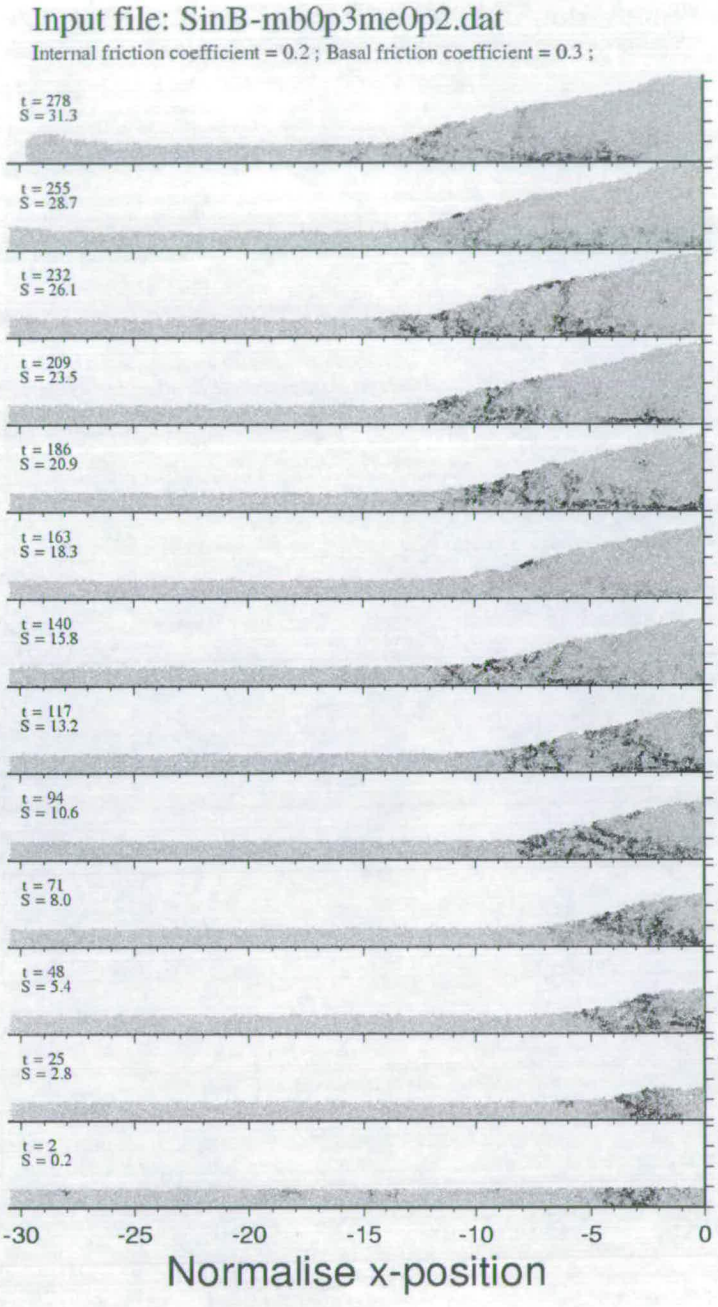

Figure A.13: Singly-vergent relative displacement plot for the random single disc particle structure with $\mu_b = 0.3$ and $\mu_e = 0.2$.

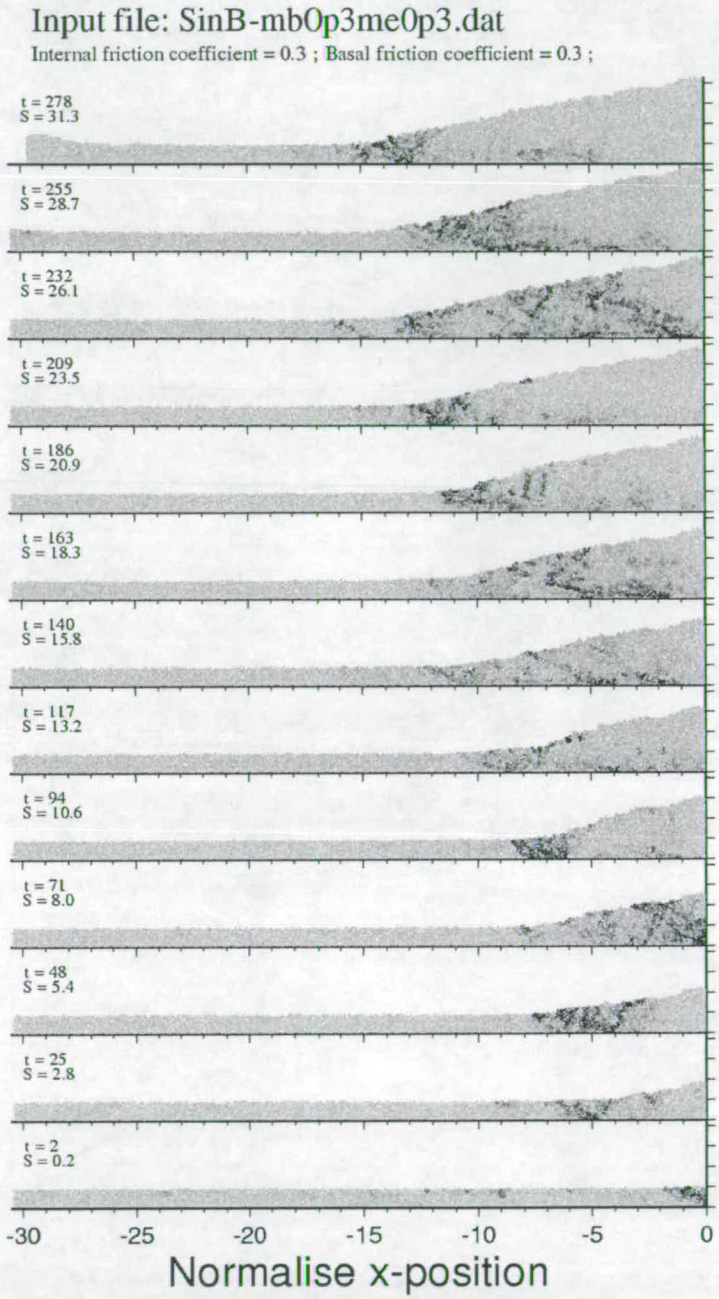

Figure A.14: Singly-vergent relative displacement plot for the random single disc particle structure with $\mu_b = 0.3$ and $\mu_e = 0.3$.

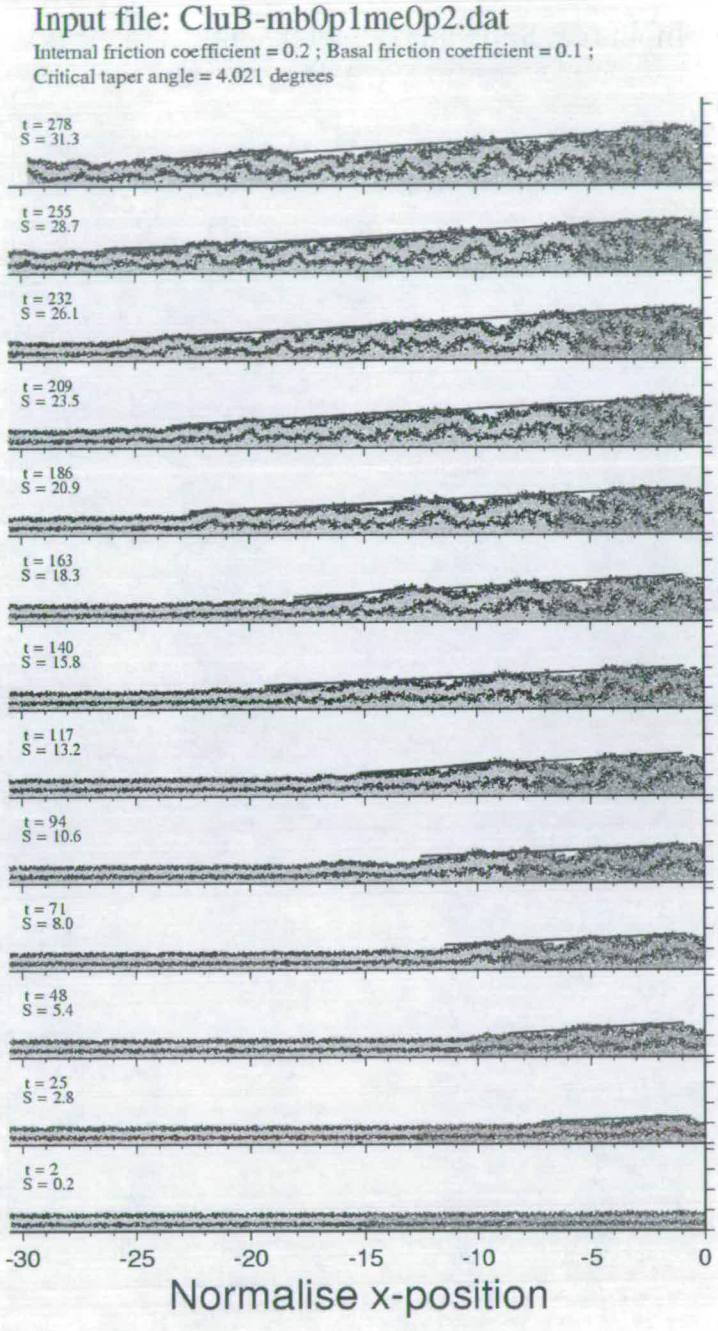

Figure A.15: Douby-vergent horizon deformation plot for the random single disc particle structure with $\mu_b = 0.1$ and $\mu_e = 0.2$.

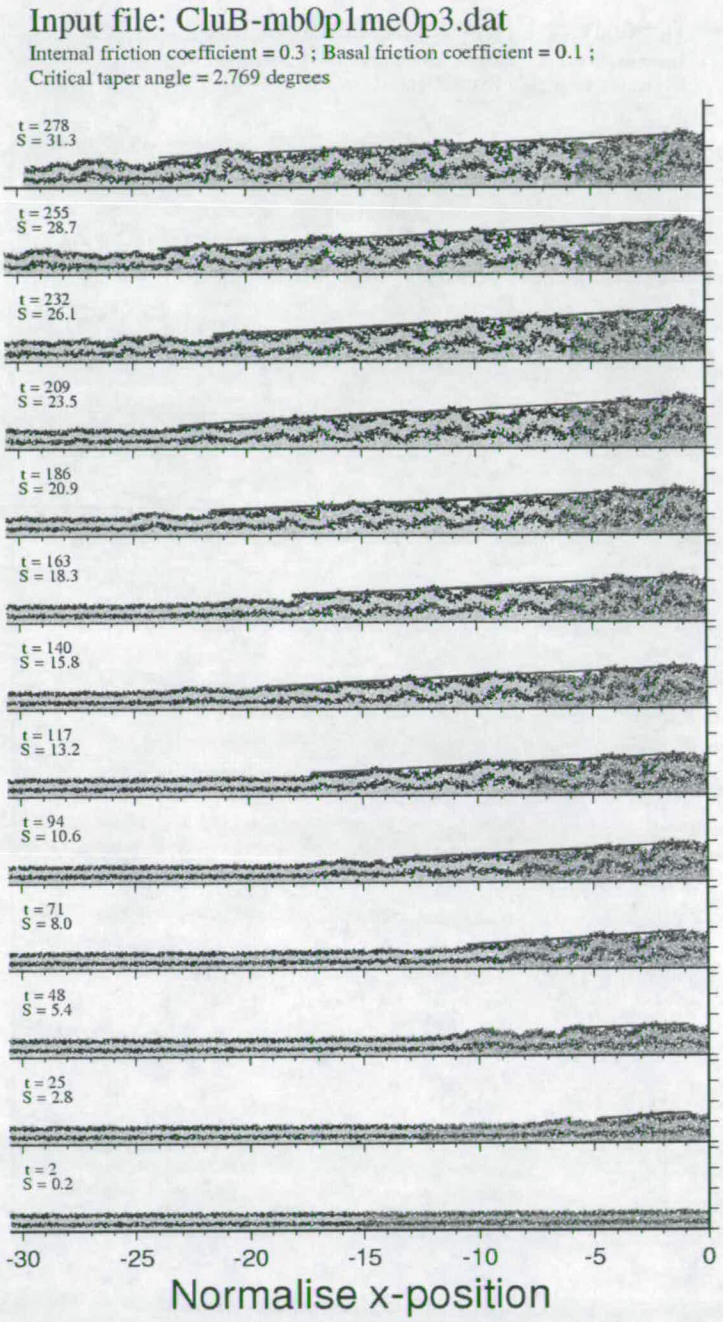

Figure A.16: Douby-vergent horizon deformation plot for the random single disc particle structure with $\mu_b = 0.1$ and $\mu_e = 0.3$.

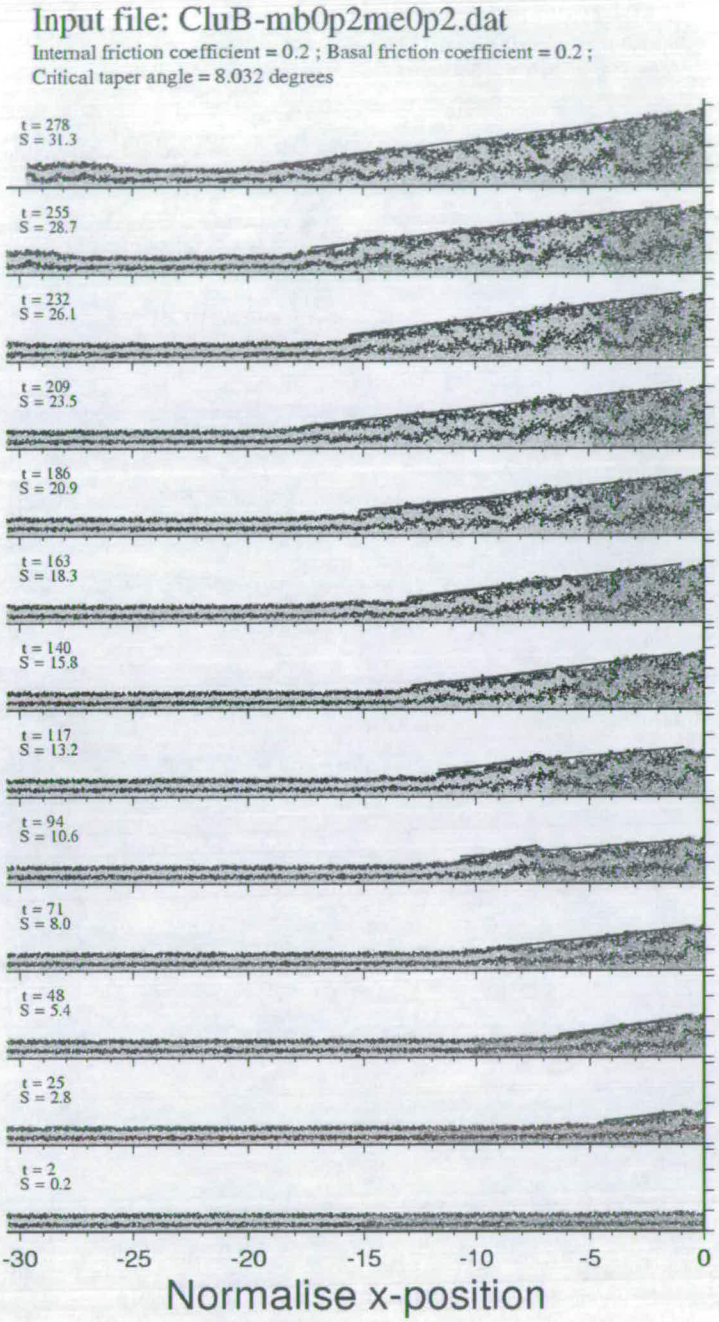

Figure A.17: Douby-vergent horizon deformation plot for the random single disc particle structure with $\mu_b = 0.2$ and $\mu_e = 0.2$.

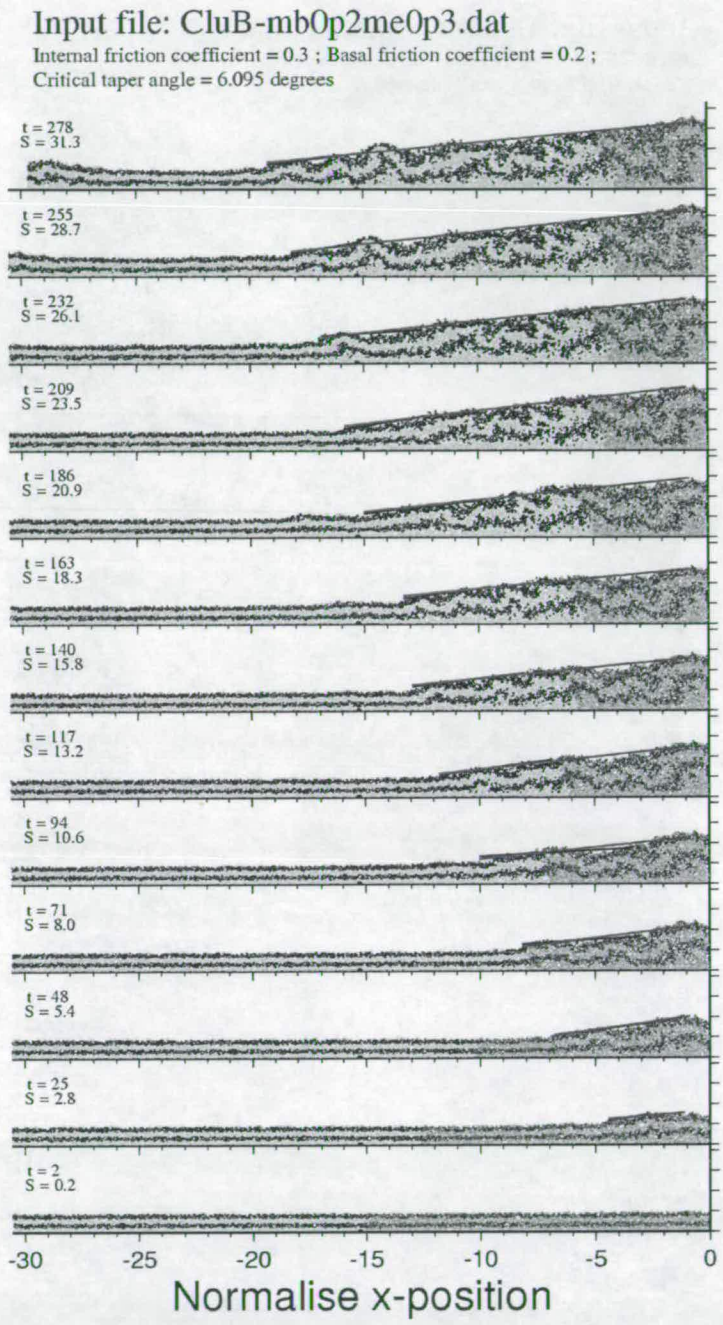

Figure A.18: Douby-vergent horizon deformation plot for the random single disc particle structure with $\mu_b = 0.2$ and $\mu_e = 0.3$.

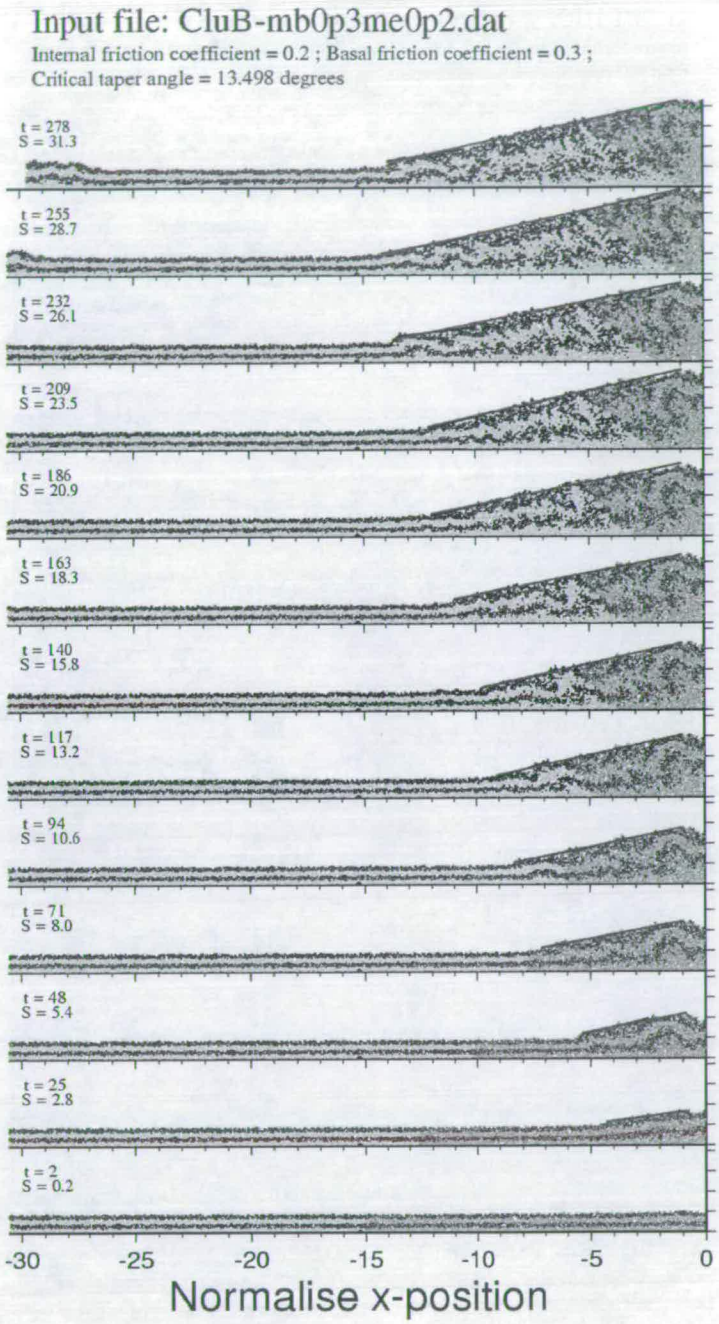

Figure A.19: Douby-vergent horizon deformation plot for the random single disc particle structure with $\mu_b = 0.3$ and $\mu_e = 0.2$.

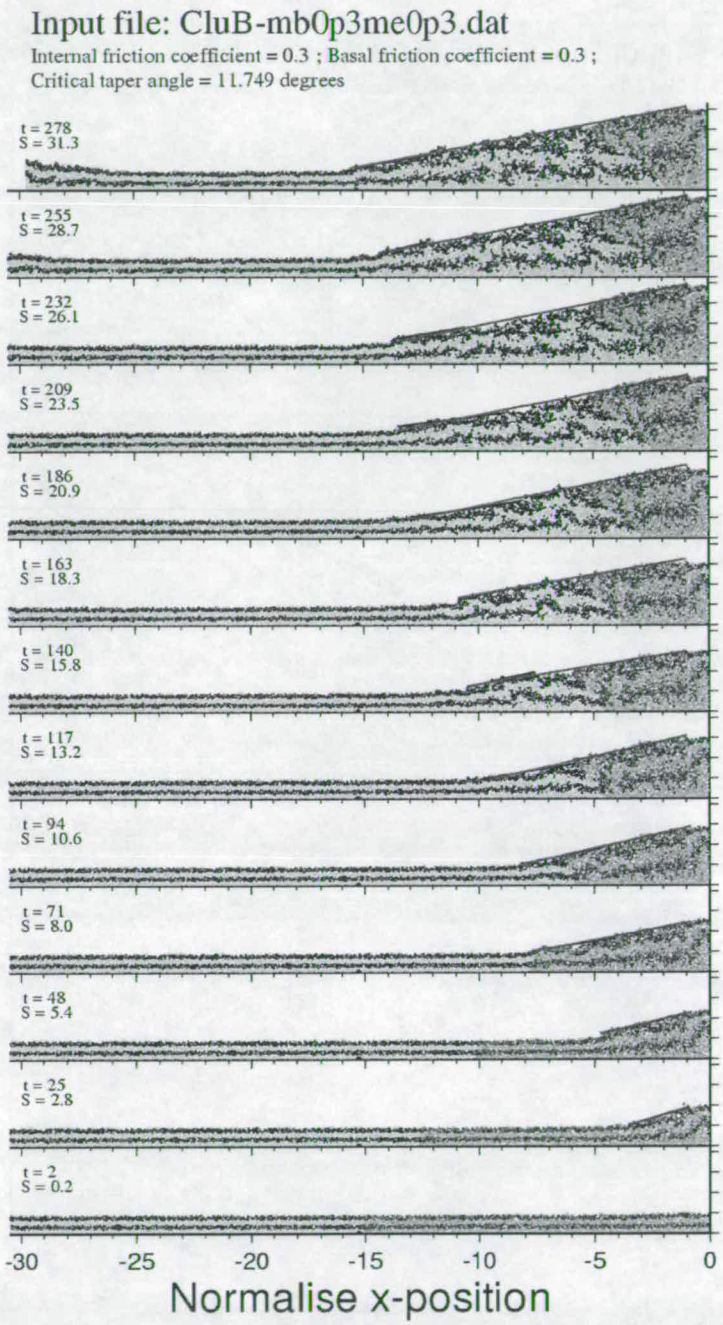

Figure A.20: Douby-vergent horizon deformation plot for the random single disc particle structure with $\mu_b = 0.3$ and $\mu_e = 0.3$.

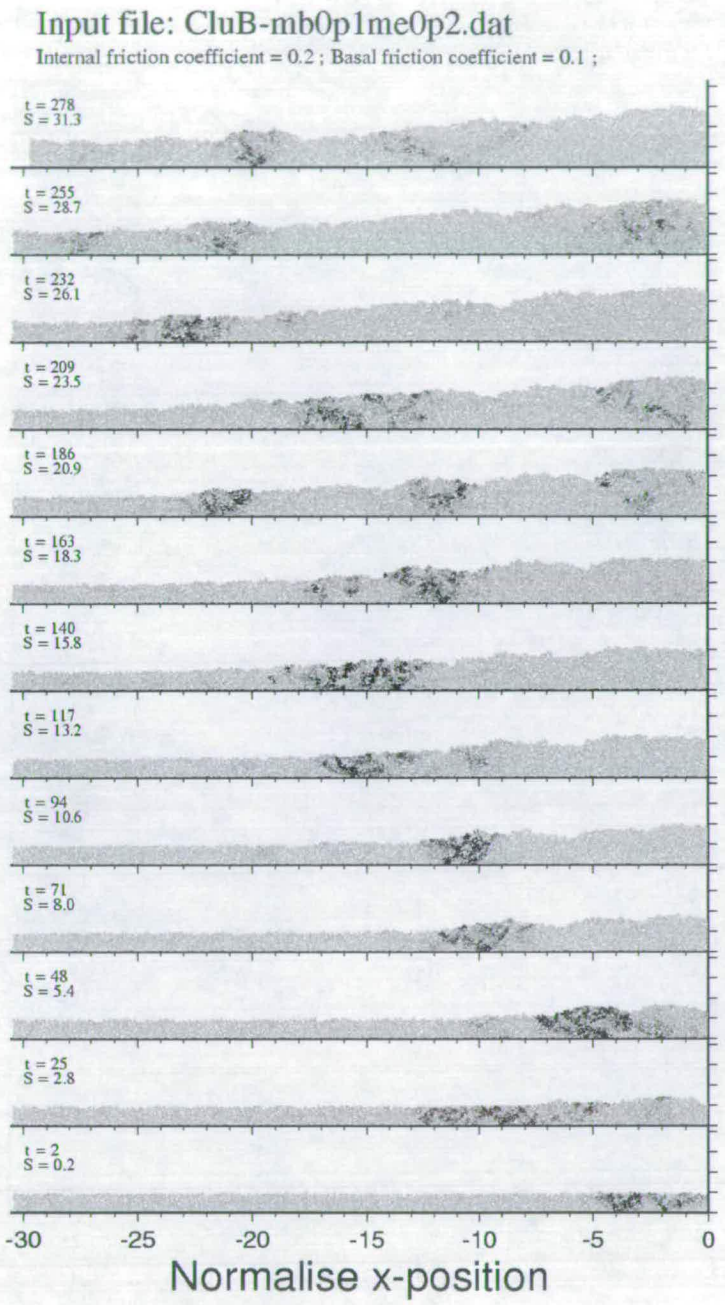

Figure A.21: Doubly-vergent relative displacement plot for the random single disc particle structure with $\mu_b = 0.1$ and $\mu_e = 0.2$.

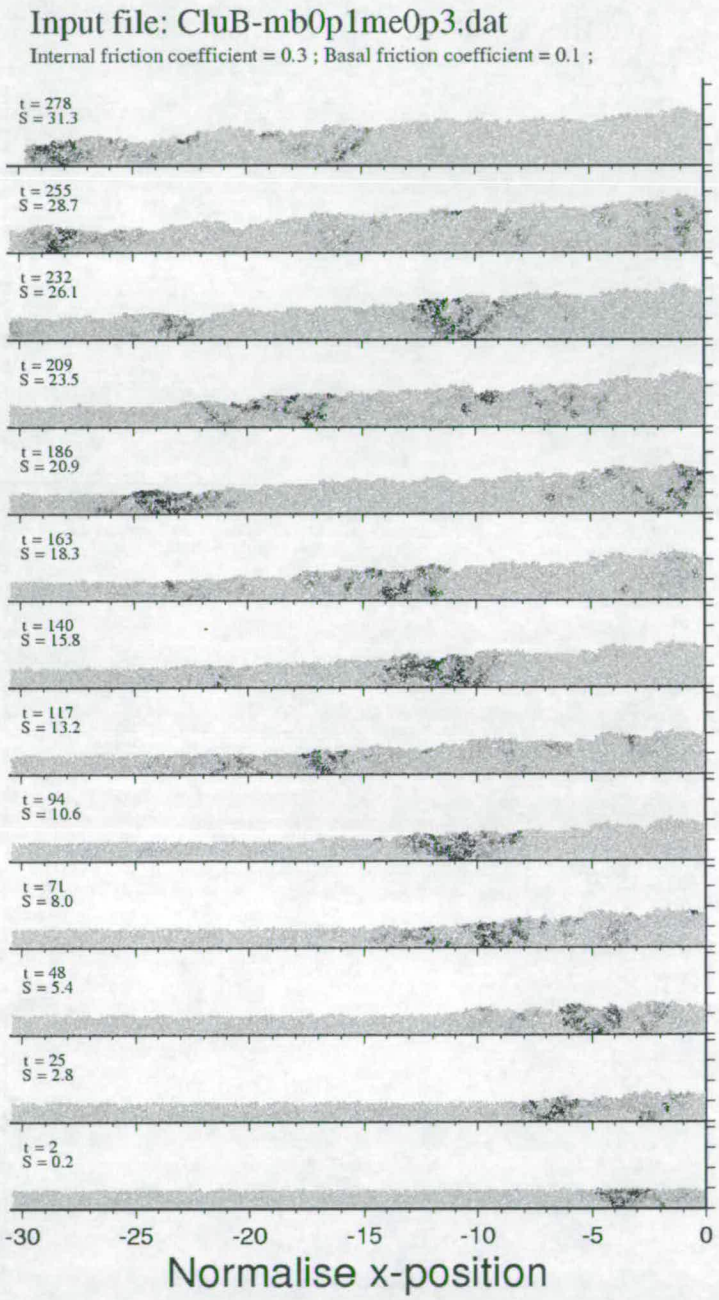

Figure A.22: Doubly-vergent relative displacement plot for the random single disc particle structure with $\mu_b = 0.1$ and $\mu_e = 0.3$.

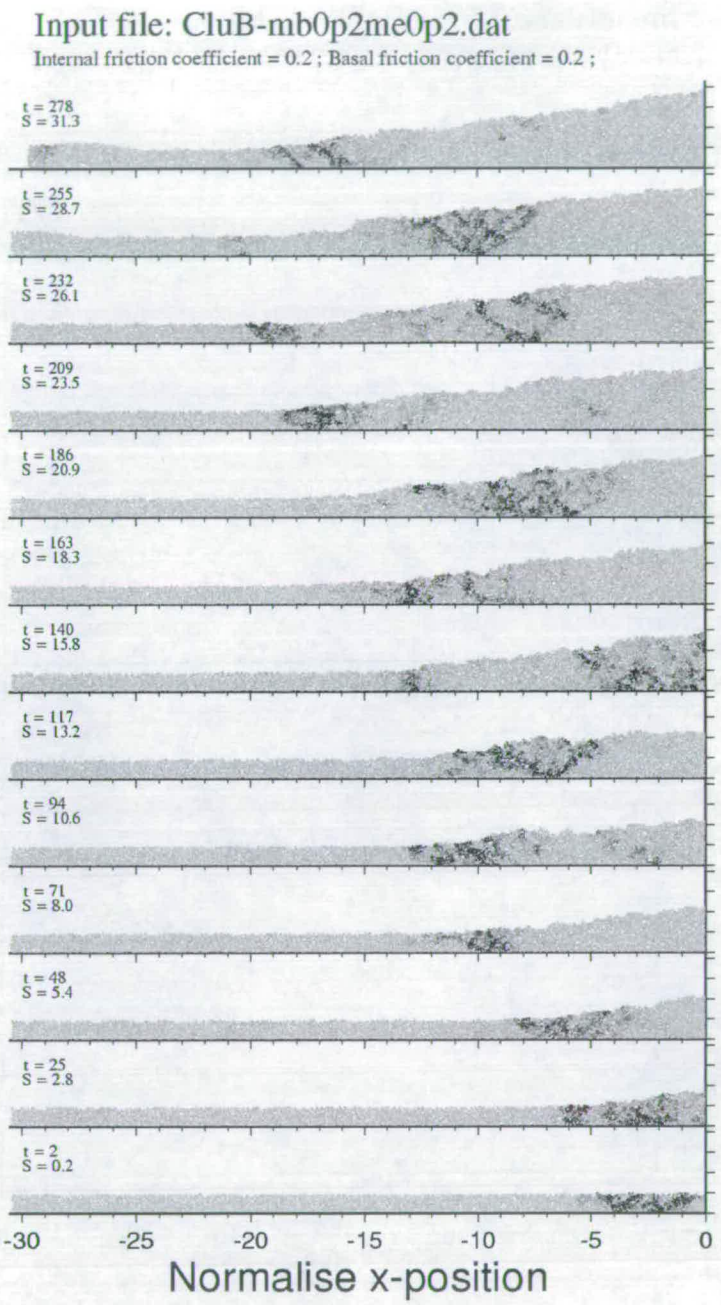

Figure A.23: Doubly-vergent relative displacement plot for the random single disc particle structure with $\mu_b = 0.2$ and $\mu_e = 0.2$.

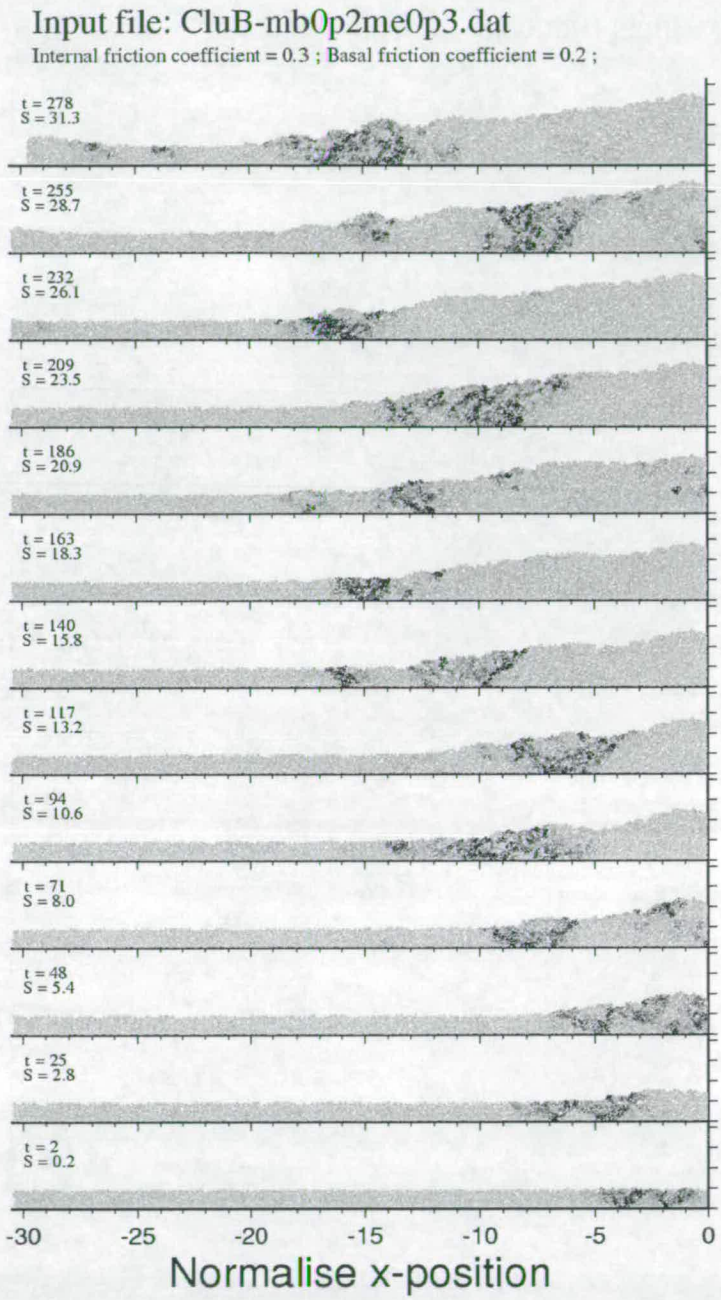

Figure A.24: Doubly-vergent relative displacement plot for the random single disc particle structure with $\mu_b = 0.2$ and $\mu_e = 0.3$.

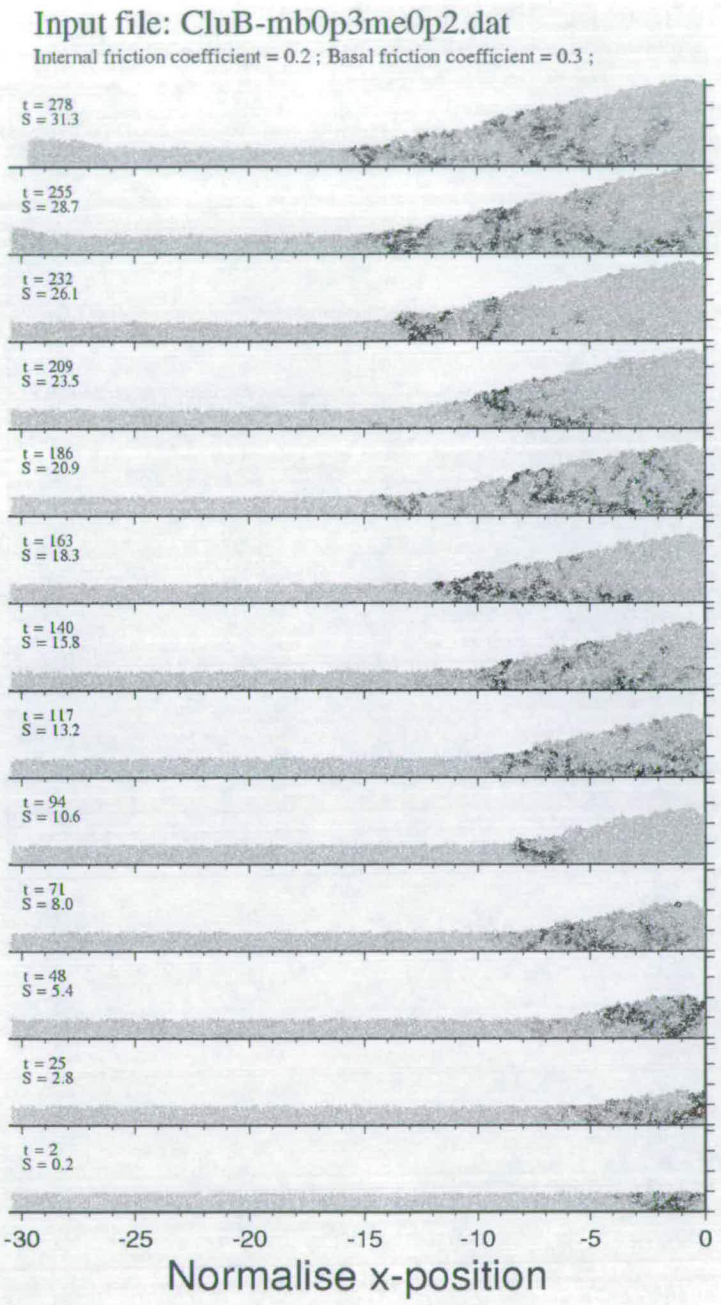

Figure A.25: Doubly-vergent relative displacement plot for the random single disc particle structure with $\mu_b = 0.3$ and $\mu_e = 0.2$.

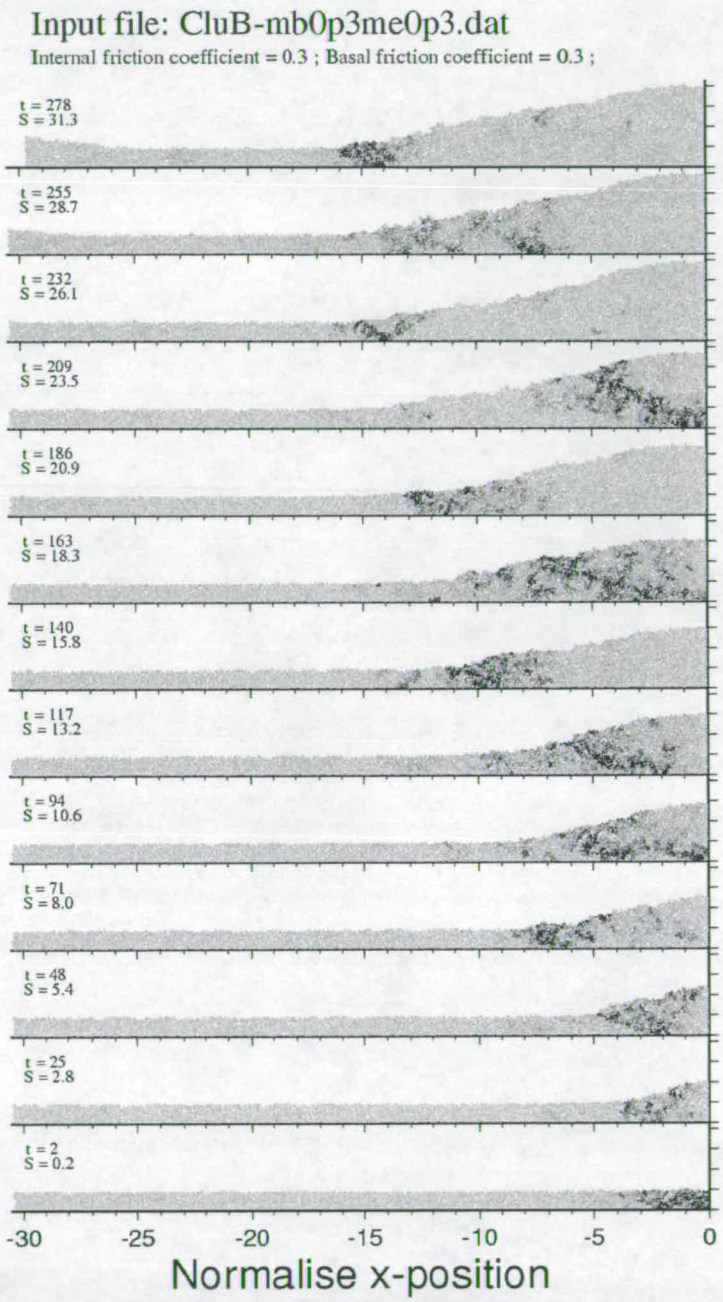

Figure A.26: Doubly-vergent relative displacement plot for the random single disc particle structure with $\mu_b = 0.3$ and $\mu_e = 0.3$.

Bibliography

Allen, M. P. and Tildesley, D. J. (1987). *Computer Simulation of Liquids*. Oxford University Press, Oxford, 2nd edition.

Batt, G. E., Brandon, M. T., Farley, K. A., and Roden-Tice, M. (2001). Tectonic synthesis of the Olympic Mountains segment of the Cascadia wedge, using two-dimensional thermal and kinematic modeling of thermochronometric ages. *J. Geophys. Res.*, 106(B11):26,731–26,746.

Beamud, E., Garces, M., Cabrera, L., Munoz, J. A., and Almar, Y. (2003). A new Middle to Late Eocene continental chronostratigraphy from NE Spain. *Earth and Planetary Science Letters*, 216:501–514.

Beaumont, C., Ellis, S., Hamilton, J., and Fullsack, P. (1996). Mechanical model for subduction-collision tectonics of Alpine-type compressional orogens. *Geology*, 24(8):675–678.

Beaumont, C., Ellis, S., and Pfiffner, A. (1999). Dynamics of sediment subduction-accretion at convergent margins. *J. geophys. Res.*, 104(B8):17573–17601.

Beaumont, C., Kooi, H., and Willett, S. (2000a). Coupled tectonic-surface process models with applications to rifted margins and collisional orogens. In Summerfield, M. A., editor, *Geomorphology and Global Tetconics*, chapter 3, pages 29–55. Wiley.

Beaumont, C., Munoz, J. A., Hamilton, J., and Fullsack, P. (2000b). Factors controlling the Alpine evolution of the central Pyrenees inferred from a comparison of observations and geodynamical models. *J. Geophys. Res.*, 104(B7):8121–8145.

Bigi, S., Lenci, F., Doglioni, C., Moore, J. C., Carminati, E., and Scrocca, D. (2003). Décollement depth versus accretionary prism dimension in the Appenines and the Barbados. *Tectonics*, 22(2).

Boillot, G. and Capdevila, R. (1977). The Pyrenees, subduction and collision? *Earth and Planetary Science Letters*, 35:243–255.

Bombolakis, E. G. (1994). Applicability of critical-wedge theories to foreland belts. *Geology*, 22:535–538.

Brace, W. F. and Byerlee, J. D. (1966). Stick-slip as a mechanism for earthquakes. *Science*, 153:990–992.

Burbank, D. W. and Anderson, R. S. (2001). *Tectonic Geomorphology*. Blackwell Science.

Burbank, D. W., Blythe, A. E., Putkonen, J., Pratt-Sitaula, B., Gabet, E., Oskin, M., Barros, A., and Ojha, T. P. (2003). Decoupling of erosion and precipitation in the Himalayas. *Nature*, 426:652–655.

Burbidge, D. R. (2000). *The Complex Evolution of Accretionary Wedges and Thrust Belts: Results from Numerical Experiments Using the Distinct Element Method.* PhD thesis, Australian National University.

Burbidge, D. R. and Braun, J. (2002). Numerical models of the evolution of accretionary wedges and fold-and-thrust belts using the distinct-element method. *Geophys. J. Int.*, 148:542–561.

Byerlee, J. (1978). Friction of rocks. *Pure and Applied Geophysics*, 116:615–626.

Chapple, W. M. (1978). Mechanics of thin-skinned fold-and-thrust belts. *Geol. Soc. Am. Bull.*, 89:330–345.

Chiang, C. S., Yu, H. S., and Chou, Y. W. (2004). Characteristics of the wedge top depozone of the southern Taiwan foreland basin system. *Basin Research*, 16:65–78.

Choukroune, P. and Team, E. (1989). The ECORS Pyrenean deep seismic profile reflection data and the overall structure of an orogenic belt. *Tectonics*, 8:23–39.

Cundall, P. A. and Strack, O. D. L. (1979). A discrete numerical model for granular assemblies. *Geotechnique*, 29:47–65.

Dadson, S. J., Hovius, N., Chen, H., Dade, W. B., Hsieh, M. L., Willett, S. D., Hu, J. C., Horng, M. J., Chen, M. C., Stark, C. P., Lague, D., and Lin, J. C. (2003). Links between erosion, runoff variability and seismicity in the Taiwan orogen. *Nature*, 426:648–651.

Dahlen, F. A. (1984). Noncohesive critical Coulomb wedges: An exact solution. *J. Geophys. Res.*, 89:10125–10133.

Dahlen, F. A., Suppe, J., and Davies, D. (1984). Mechanics of fold and thrust belts and accretionary wedges: Cohesive Coulomb theory. *J. Geophys. Res.*, 88:10087–10101.

D'Anna, G., Mayor, P., Barrat, A., Loreto, V., and Nori, F. (2003). Observing Brownian motion in vibration-fluidized granular matter. *Nature*, 424:909–912.

Davis, D., Suppe, J., and Dahlen, F. A. (1983). Mechanics of fold and thrust belts and accretionary wedges. *J. Geophys. Res.*, 88:1153–1172.

Deffontaines, B., Lee, J. C., Angelier, J., Carvalho, J., and Rudant, J. P. (1994). New geomorphic data on the active Taiwan orogen: A multisource approach. *J. Geophys. Res.*, 99:20243–20266.

Deramond, J., Souquert, P., Wallez, M. J. F., and Specht, M. (1993). Relationships between thrust tectonics and sequence stratigraphy by surfaces in foredeeps : models and examples from the Pyrenees. In *V71*, pages 193–219. Geological Society Special Publication.

Dewey, J. F. and Bird, J. M. (1970). Mountain belts and the new global tectonics. *J. Geophys. Res.*, 75:2625–2647.

Dewey, J. F., Cande, S., and Pitman, W. C. (1989). Tectonic evolution of the India/Eurasia collision zone. *Eclogae Geol. Helv.*, 82(3):717–734.

Duran, J. (1997). Static and dynamic arching effect in granular materials. In *Physics of Dry Granular Media*, pages 197–216. NATO Advanced Study Unit, Kluwer Academic Publishers.

Dury, C. M. and Ristow, G. H. (1999). Competition of mixing and segregation in rotating cylinders. *Physics of Fluids*, 11(6):1387–1394.

Finch, E., Hardy, S., and Gawthorpe, R. (2003). Discrete element modelling of contractional fault-propogation folding above rigid basement fault block. *J. Struc. Geo.*, 25:515–528.

Fischer, M. W. (1984). Thrust tectonics in the Northern Pyrenees. *Journal of Structural Geology*, 6:721–726.

Fullsack, P. (1995). An arbitrary Lagrangian-Eulerian formulation for creeping flows and its application in tectonic models. *Geophys. J. Int.*, 120:1–23.

Geng, J., Longhi, E., Behringer, R. P., and Howell, D. W. (2001). Memory in two-dimensinoal heap experiments. *Physical Review E*, 64(060301).

Heim, A. (1897). *Untersuchungen uber den mechanisms de Gebirgsbildung im Anschluss an die geologische Monographie der Todi-Windgallen-gruppe*. Schwabe Basel.

Helbing, D. (1997). Similarities between granular and traffic flow. In *Physics of Dry Granular Media*, pages 547–552. NATO Advanced Study Unit, Kluwer Academic Publishers.

Hickman, J. B., Wiltschko, D. V., Hung, J. H., Fang, P., and Bock, Y. (2002). Structure and evolution of the active fold-and-thrust belt of southwestern Taiwan from Global Positioning System analysis. *Geological Society of America*, Special Paper 385:75–92.

Howard, A. D., Dietrich, W. E., and Seidl, M. A. (1994). Modeling fluvial erosion on regional to continental scales. *J. Geophys. Res.*, 99(B7):13971–13986.

Huiqi, L., McClay, K., and Powel, D. (1992). Physical models of thrust wedges. In McClay, K., editor, *Thrust Tectonics*, pages 71–81. Chapman and Hall.

Jaeger, H. M., Nagel, S. R., and Behringer, R. P. (1996). Granular solids , liquids and gases. *Reviews of Modern Physics*, 68(4):1259–1273.

Jensen, P. R., Bosscher, P. J., Plesha, M. E., and Edil, T. B. (1999). DEM simulation of granular media-structure interface: effects of surface roughness and particle shape. *International Journal for Numerical and Analytical Methods in Geomechanics*, 23:531–547.

Karner, G. D. and Watts, A. B. (1983). Gravity anomalies and flexure of the lithosphere at mountain ranges. *J. Geophys. Res.*, 88(B12):10449–10477.

Koons, P. O. (1994). 3-Dimensional critical wedges - tectonics and topography in oblique collisional orogens. *Journal of Geophysical Research*, 99(B6):12301–12315.

Kopp, H. and Kukowski, N. (2003). Backstop geometry and accretionary mechanics of the Sunda margin. *Tectonics*, 22(6):1–16.

Koyi, H. (1995). Mode of internal deformation in sand wedges. *J. Struc. Geo.*, 17(2):293–300.

Krantz, R. W. (1991). Measurements of friction coefficients and cohesion for faulting and fault reactivation in laboratory models using sand and sand mixtures. *Tectonophysics*, 188:203–207.

Lallemand, S. E., Schnurle, P., and Malavieille, J. (1994). Coulomb theory applied to accretionary and nonaccretionary wedges: Possible causes for tectonic erosion and/or frontal accretion. *J. Geophys. Res.*, 99(B6):12033–12055.

Landry, J. W., Grest, G. S., Silbert, L. E., and Plimpton, S. J. (2003). Confined granular packings: Structure, stress, and forces. *Physical Review E*, 67.

Lanier, J. and Jean, M. (2000). Experiments and numerical simulations with 2D disks assembly. *Powder Technology*, 109:206–221.

Laubscher, H. P. and Bernoulli, D. (1982). History and deformation in the alps. In Hsu, K. J., editor, *Mountain Building Processes*, pages 169–180. Academic Press, London.

Lohrmann, J., Kukowski, N., Adam, J., and Oncken, O. (2003). The impact of analogue material properties on the geometry, kinematics and dynamics of convergent sand wedges. *Journal of Structural Geology*, 25:1691–1711.

Mackin, J. H. (1948). Concept of the graded river. *Geol. Soc. Am. Bull.*, 101:1373–1388.

Mair, K., Frye, K. M., and Marone, C. (2001). Influence of grain characteristics on the friction of granular shear zones. *J. Geophys. Res.*

Malavieille, J. (1984). Modelisation experimentale des chevauchements imbriques: application aux chaines de monta. *Bull. Soc. geol. Fr.*, pages 129–138.

McClay, K. R. (1990). Deformation mechanics in analogue models of extensional fault systems. In Knipe, R. J. and Rutter, E. H., editors, *Deformation mechanisms, rheology and tectonics*, pages 445–453. The Geological Society.

McKenzie, D. P. and Morgan, W. J. (1969). Evolution of triple junctions. *Nature*, 224:125–133.

Meigs, A. (1997). Sequential development of selected Pyrenean thrust faults. *Journal of Structural Geology*, 19:481–502.

Meigs, A., Verges, J., and Burbank, D. W. (1996). Ten-million-year history of a thrust sheet. *Geological Society of America Bulletin*, 108:1608–1625.

Mellere, D. (1993). Thrust generated, back-fill stacking of allivial fan sequences, south-central Pyrenees, Spain (La Pobla de Segur Conglomerates). In Frostick, L. E. and Steel, R. J., editors, *Tectonic Controls and Signatures in Sedimentary Successions*, pages 259–276. Special Publication of the International Association of Sedimentologists.

Molnar, P. (1984). Structure and tectonics of the Himalaya. *Annual Review of Earth and Planetary Sciences*, 12:489–518.

Molnar, P. (1988). Continental tectonics in the aftermath of plate tectonics. *Nature*, 335:131–137.

Molnar, P. (2003). Nature, nurture and landscape. *Nature*, 426:612–614.

Molnar, P. and Chen, W. P. (1982). Seismicity and mountain building. In Hsu, K. G., editor, *Mountain Building Processes*, pages 41–57. Academic Press, London.

Montgomery, D. R., Balco, G., and Willett, S. D. (2001). Climate, tectonics, and the morphology of the andes. *Geology*, 27(7):579–582.

Morgan, J. K. and Boettcher, M. S. (1999). Numerical simulations of granular shear zones using the distinct element method: I. shear zone kinematics and micromechanics of localization. *J. Geophys. Res.*, 104(B):2703–2719.

Morgan, J. K. (1999). Numerical simulations of granular shear zones using the distinct element method: II. the effect of particle size distribution and interparticle friction on mechanical behavior. *J. Geophys. Res.*, 104(B):2721–2732.

Munoz, J. A. (1992). Evolution of a continental collision belt: ECORS-Pyrenees crustal balanced cross-section. In McClay, K., editor, *Thrust Tectonics*, pages 235–246. Chapman and Hall.

Munoz, J. A., Martínez, A., and Vergés, J. (1986). Thrust sequences in the eastern Spanish Pyrenees. *Journal of Structural Geology*, 8:399–405.

Mutti, E. and Sgavetti, M. (1987). Sequence stratigraphy of the Upper Cretaceous Aren strata in the Orcau-Aren region, south-central Pyrenees, Spain: distinction between eustatically and tectonically controlled depositional sequences. *Annali del l'Universita di Ferrara*, 1:1–22.

Oger, L., Savage, S. B., Corriveau, D., and Sayed, M. (1998). Yield and deformation of an assembly of disks subjected to a devioric stress loading. *Mechanics of Materials*, 27:189–210.

Orman, J. V., Cochran, J. R., Weissel, J. K., and Jestin, F. (1995). Distribution of shortening between the Indian and Australian plates in the central Indian Ocean. *Earth and Planetary Science Letters*, 133:35–46.

Paterson, M. S. (1978). *Experimental Rock Deformation*. Springer, New York.

Pazzaglia, F. J. and Brandon, M. T. (2001). A fluvial record of long-term steady-state uplift and erosion across the Cascadia forearc high, western Washington State. *American Journal of Science*, 301:385–431.

Persson, K. S. (2001). Effective indenters and the development of doubly vergent orogens: Insights from analogue sand models. In *Tectonic Modelling*, chapter 14, pages 191–206. GSA.

Pfiffner, O. A., Lehner, P., Heitzmann, P., Muller, S., and Steck, A., editors (1997). *Deep Structure of the Swiss Alps: Results of PNR 20*. Birkhauser Verlag AG.

Platt, J. P. (1986). Dynamics of orogenic wedges and the uplift of high-pressure metamorphic rocks. *Geol. Soc. Am. Bull.*, 97:1037–1053.

Pous, J., Munoz, J. A., Ledo, J. J., and Liesa, M. (1995). Partial melting of subducted continental lower crust in the Pyrenees. *Journal of the Geological Society of London*, 150:1065–1094.

Reiners, P. W., Ehlers, T. A., Mitchell, S. G., and Montgomery, D. R. (2003). Coupled spatial variations in precipitation and long-term erosion rates across the Washington Cascades. *Nature*, 426:645–674.

Roest, W. R. and Srivastava, S. P. (1991). Kinematics of the plate boundaries between Eurasia, Iberia and Africa in the North Atlantic from late Cretaceous to the present. *Geology*, 19:613–616.

Roux, J. N. (2000). Geometric origin of mechanical properties of granular materials. *Physical Review E*, 61(6):6802–6836.

Rutter, E. H. (1972). The effects of strain-rate changes on the strength and ductility of Solenhofen limestone at low temperatures and confining pressure. *International Journal of Rock Mechanics and Mining Sciences*, 9:183–189.

Schellart, W. P. (2000). Shear test results for cohesion and friction coefficients for different granular materials; scaling implications for their usage in analogue modelling. *Tectonophysics*, 324(1-2):1–16.

Séguret, M. (1972). *Étude tectonique des nappes et séries décollées de la partie centrale du versant sub des Pyrénées*, volume Geologie Structurale. n. 2. Publications de l'Universite de Sciences et Technique de Languedoc, Montpellier.

Silbert, L. E., Grest, G. S., Plimpton, S. J., and Levine, D. (2002). Boundary effects and self-organisation in dense granular flows. *Physics of Fluids*, 14(8):2637–2646.

Sinclair, H. D. (1997). Tectonic-stratigraphic model for underfilled peripheral basins: An Alpine perspective. *Geological Society of America Bulletin*, 109:324–346.

Sinclair, H. D., Gibson, M., Naylor, M., and Morris, R. G. (Submitted). Pyrenean orogenesis revealed through flux measurement and modelling. *American Journal of Science*.

Staron, L., Vilotte, J. P., and Radjai, F. (2001). Friction and mobilization of contacts in granular numerical avalanches. *Powders and Grains*.

Storti, F., Slavini, F., and McClay, K. (2000). Synchronous and velocity-partitioned thrusting and thrust polarity reversal in experimentally produced and doubly-vergent thrust wedges: Implications for natural orogens. *Tectonics*, 19(2):378–396.

Stuwe, K., White, L., and Brown, R. (1994). The influence of eroding topography on steady-state isotherms: Application to fission track analysis. *Earth Planet. Sci. Lett.*, 124:63–74.

Terzaghi, K. (1943). *Theoretical soil mechanics*. Wiley, New York.

Ting, J. M., Khwaja, M., Meachum, L., and Rowell, J. (1993). An ellipse-based discrete element model for granular materials. *International Journal for Numerical and Anlaytical Methods in Geomechanics*, 17:603–623.

Ting, J. M., Meachum, L. R., and Rowell, J. D. (1995). Effect of particle shape on the strength and deformation mechanisms of ellipse shaped granular assemblages. *Engng. Comput.*, 12:99–108.

Tippett, J. M. and Hovius, N. (2000). Geodynamic processes in the Southern Alps, New Zealand. In Summerfield, M. A., editor, *Geomorphology and Global Tectonics*, chapter 6, pages 109–134. John Wiley & Sons Ltd.

Toomey, A. and Bean, C. J. (2000). Numerical simulation of seismic waves using a discrete particle scheme. *Geophys. J. Int.*, 141:595–604.

Tsuji, Y., Kawaguchi, T., and Tanaka, T. (1992). Discrete particle simulation of two-dimensional fluidized bed. *Powder Technology*, 77:79–87.

Tucker, G. E. and Bras, R. L. (1998). Hill slope processes, drainage density, and landscape morphology. *Water Resour. Res.*, 34:2751–2764.

Tucker, G. E. and Slingerland, R. L. (1994). Erosional dynamics, flexural isostasy, and ling-lived escarpments: A numerical modelling study. *J. Geophys. Res.*, 99(B6):12229–12244.

Tucker, G. E. and Slingerland, R. L. (1996). Predicting sediment flux from fold and thrust belts. *Basin Research*, 8:329–349.

Tucker, G. E. and Slingerland, R. L. (1997). Drainage basin response to climate change. *Water Resour. Res.*, 33:2031–2047.

Tucker, G. E. and Whipple, K. E. (2002). Topographic outcomes predicted by stream erosion models: Sensitivity analysis and intermodel comparison. *J. Geophys. Res.*, 107(B9).

Umbanhowar, P. (2003). Shaken sand - a granular fluid? *Nature*, 424:886–887.

Vergés, J. (1999). Estudi geologic del vessant sud del pirineu oriental i central evolucio cinematica en 3d. In *Col-leccio Monografies técniques*, volume 7, page 194. Institute Cartographic de Catalunya, Barcelona.

Vergés, J., Millàn, H., Roca, E., Munoz, J. A., Marzo, M., Cirés, J., Bezemer, T. D., Zoetemeijer, R., and Cloetingh, S. (1995). Eastern Pyrenees and related foreland basins: pre-, syn- and post-collisional crustal scale cross-sections. *Marine and Petroleum Geology*, 12:893–915.

Wang, W. H. and Davis, D. M. (1996). Sandbox model simulation of forearc evolution and noncritical wedges. *J. Geophys. Res.*, 101(B5):11329–11339.

Whipple, K. X. (2001). Fluvial landscape response time: How plausible is steady state denudation? *Am. J. Sci.*, 301:313–325.

Whipple, K. X. and Tucker, G. E. (1999). Dynamics of the stream-power river incision model: Implications for height limits of mountain ranges, landscape response timescales, and research needs. *Journal of Geophysical Research - Solid Earth*, 104(B8):17661–17674.

Willett, S., Beaumont, C., and Fullsack, P. (1993). Mechanical model for the tectonics of doubly vergent compressional orogens. *Geology*, 21:371–374.

Willett, S. D. (1992). Kinematic and dynamic growth and change of a Coulomb wedge. In McClay, K., editor, *Thrust Tectonics*, pages 19–31. Chapman and Hall.

Willett, S. D. (1999). Orogeny and orography: The effects of erosion on the structure of mountain belts. *J. Geophys. Res.*, 104:28957–28981.

Willett, S. D. and Brandon, M. T. (2002). On steady states in mountain belts. *Geological Society of America*, 30(2):175–178.

Wobus, C. W., Hodges, K. V., and Wipple, K. X. (2003). Has focused denudation sustained active thrusting at the Himalaya topographic front? *Geology*, 31(10):861–864.

Wolf, D. (1997). Friction in granular media. In *Physics of Dry Granular Media*, pages 441–464. NATO Advanced Study Unit, Kluwer Academic Publishers.

Zhang, D. and Whiten, W. J. (2001). Step size control for efficient discrete element simulation. *Minerals Engineering*, 14(10):1341–1346.